

# Universidad de Salamanca



## Facultad de Ciencias

Física Fundamental y Matemáticas

---

COLISIONES ENTRE DEFECTOS TOPOLÓGICOS DEL MODELO  
 $\phi^4$  VIBRACIONALMENTE EXCITADOS

---

## Joao Victor Queiroga Nunes

Tesis para obtener el grado de Doctor en Física

2023



# Publicaciones

La presente tesis doctoral constituye una defensa de tesis por compendio de trabajos publicados. Esta incluye tres trabajos originales publicados en revistas científicas cuyas referencias completas se detallan a continuación.

1. Alonso-Izquierdo, A., Nieto-Calzada, L.M. y Queiroga-Nunes, J. (2021). Scattering between wobbling kinks. *Physical Review D*, **103**, 045003.  
<https://doi.org/10.1103/PhysRevD.103.045003>  
Índice de impacto: 5.407.  
Cuartil: Q1 (Categoría: Physics, Particles and Fields, 6 de 29).  
Número de citas: 42 (google académico, 7 de mayo).
  2. Alonso-Izquierdo, A., Nieto-Calzada, L.M. y Queiroga-Nunes, J. (2022). Asymmetric scattering between kinks and wobblers. *Commun. Nonlinear Sci. Numer. Simul.* **107**, 106183.  
<https://doi.org/10.1016/j.cnsns.2021.106183>  
Índice de impacto: 5.296.  
Cuartil: Q1 (Categoría: Applied Mathematics, 5 de 265).  
Número de citas: 6 (google académico, 7 de mayo).
  3. Alonso-Izquierdo, A., Miguélez-Caballero, D., Nieto-Calzada, L.M. y Queiroga-Nunes, J. (2023). Wobbling kinks in a two-component scalar field theory: Interaction between shape model. *Physica D: Nonlinear Phenomena* **443**, 133590.  
<https://doi.org/10.1016/j.physd.2022.133590>  
Índice de impacto: 3.751.  
Cuartil: Q1 (Categoría: Applied Mathematics, 16 de 267); Q1 (Categoría: Mathematical Physics, 6 de 56).  
Número de citas: 7 (google académico, 7 de mayo).
- Alberto Alonso Izquierdo  
*Departamento de Matemática Aplicada, Universidad de Salamanca*  
*Casas del Parque 2, Salamanca 37008, España*  
*Instituto Universitario de Física Fundamental y Matemáticas (IUFFyM), Universidad de Salamanca*  
*Plaza de la Merced 1, Salamanca 37008, España*

- David Miguélez Caballero  
*Departamento de Física Teórica, Atómica y Óptica, Universidad de Valladolid*  
*Paseo de Belén s/n, Valladolid 47011, España*  
*Instituto de Matemáticas (IMUVA), Universidad de Valladolid*  
*Paseo de Belén s/n, Valladolid 47011, España*
  
- Joao Victor Queiroga Nunes  
*Departamento de Matemática Aplicada, Universidad de Salamanca*  
*Casas del Parque 2, Salamanca 37008, España*
  
- Luis Miguel Nieto Calzada  
*Departamento de Física Teórica, Atómica y Óptica, Universidad de Valladolid*  
*Paseo de Belén s/n, Valladolid 47011, España*  
*Instituto de Matemáticas (IMUVA), Universidad de Valladolid*  
*Paseo de Belén s/n, Valladolid 47011, España*

Nota: Los índices bibliográficos no accesibles en el año presente han sido referenciados al año anterior.

# Autorización de defensa por compendio de trabajos publicados

Conforme a lo descrito en el documento *PROCEDIMIENTO PARA LA PRESENTACIÓN DE LA TESIS DOCTORAL EN LA UNIVERSIDAD DE SALAMANCA EN EL FORMATO DE COMPENDIO DE ARTÍCULOS/PUBLICACIONES* de la Comisión de Doctorado y Posgrado publicado el 15 de febrero de 2013 sigue adjunto la autorización del Director de tesis y coautores para la presentación en esta modalidad, el informe de la Comisión Académica del Programa de Doctorado y la autorización de la Comisión de Doctorado y Posgrado de la Universidad para la tramitación en dicha modalidad.



VNIVERSIDAD  
D SALAMANCA

Alberto Alonso Izquierdo  
Departamento de Matemática Aplicada  
Facultad de CCAA  
Av. Filiberto Villalobos 119  
37007 -Salamanca (Spain)  
[alonsoiz@usal.es](mailto:alonsoiz@usal.es)

Dr. Alberto Alonso Izquierdo con DNI 04181918N, profesor Titular del Departamento de Matemática Aplicada de la Universidad de Salamanca:

HACE CONSTAR:

Que como director de la tesis doctoral de D. Joao Victor Queiroga Nunes con DNI Y7488526Q autorizo a presentar la tesis doctoral "Colisiones entre defectos topológicos del modelo  $\phi^4$  vibracionalmente excitados" mediante la modalidad de compendio de artículos al disponer de las siguientes publicaciones

1. Alonso-Izquierdo, A., Nieto-Calzada, L.M. y Queiroga-Nunes, J. (2021). Scattering between wobbling kinks. Physical Review D, 103, 045003.

<https://doi.org/10.1103/PhysRevD.103.045003>

2. Alonso-Izquierdo, A., Nieto-Calzada, L.M. y Queiroga-Nunes, J. (2022). Asymmetric scattering between kinks and wobblers. Commun. Nonlinear Sci. Numer. Simul. 107, 106183.

<https://doi.org/10.1016/j.cnsns.2021.106183>

3. Alonso-Izquierdo, A., Miguélez-Caballero, D., Nieto-Calzada, L.M. y Queiroga-Nunes, J. (2023). Wobbling kinks in a two-component scalar field theory: Interaction between shape modes. Physica D: Nonlinear Phenomena 443, 133590.

<https://doi.org/10.1016/j.physd.2022.133590>

Por todo ello firmo esta carta de autorización

Salamanca, a 20 de Abril de 2023

ALONSO IZQUIERDO ALBERTO - 04181918N  
Firmado digitalmente  
por ALONSO IZQUIERDO ALBERTO  
- 04181918N  
Fecha: 2023.04.17  
10:00:28 +02'00'

Alberto Alonso Izquierdo  
[alonsoiz@usal.es](mailto:alonsoiz@usal.es)



# Agradecimientos

Primeramente quiero agradecer a Dios por haberme dado un corazón nuevo dispuesto a creer y agradecer todo lo que Él ha hecho por mí, en mí y a través de mí. Asimismo, quiero agradecer por el fenomenal tutor Dr. Alberto Alonso Izquierdo que Él ha puesto en mi camino para guiarme y direccionarme en todo lo realizado a lo largo de este camino que culminó en esta tesis. Gracias por tu paciencia, por tu disponibilidad, por lo que me has transmitido como profesor y como persona. Las aportaciones, correcciones y conocimiento que me has dado han sido definitivamente claves para llevar a cabo esta tesis doctoral. Estoy enormemente agradecido por todo ello, Alberto.

A lo largo de esta jornada académica también he recibido la ayuda de muchas otras personas a las cuales quisiera nombrar en sincero agradecimiento. Gracias al Dr. Luis Miguel Nieto, quien me acogió con amabilidad y siempre estuvo disponible para ayudarme desde el principio. A mi esposa Gabriela, por apoyarme e impulsarme cada día con su amor y cariño. Todo tiene un sentido más lindo contigo, mi amor. A mis padres, Antonio y Sandra, quienes me han apoyado y educado con amor, y sacrificios, en todo hasta aquí. Este y todos los demás logros que gracias a Dios he logrado no hubieran sido posibles sin vosotros. No puedo olvidarme de mis hermanos, tíos y primos que me han apoyado y depositado en mí la confianza para seguir adelante en todo este camino. En especial, gracias a mis hermanas Sandrielly, Gabriela, a mi hermano Gabriel, a mi tío Jânio y a mis tías Carmen Lucia, Helena, Iolani, Luiza y Maria dos Anjos.

También quisiera agradecer a todos los profesores y amigos que durante mi etapa como estudiante han contribuido directa o indirectamente a mi formación. Espero haber podido retribuir a vosotros algo positivo a nivel profesional o personal.

Finalmente, quisiera expresar mi agradecimiento por el apoyo del proyecto QCAYLE, financiado por el Ministerio de Ciencia e Innovación de España y por la Unión Europea NextGenerationEU. Los trabajos publicados que conforman esta tesis doctoral hicieron uso de los recursos del centro de Supercomputación de Castilla y León (SCAYLE).





# Índice general

Agradecimientos	1
Introducción	6
<b>1. Defectos topológicos en teorías de campos escalares en (1+1)-dimensiones</b>	<b>10</b>
1.1. Defectos topológicos en teoría de campos escalares . . . . .	10
1.2. El Modelo $\phi^4$ . . . . .	16
1.3. Modelos de dos campos escalares . . . . .	18
1.4. El Modelo MSTB . . . . .	21
1.5. Colisiones entre kinks . . . . .	25
1.5.1. Simulaciones numéricas . . . . .	27
1.6. Contribución de los artículos presentados . . . . .	31
1.6.1. Contribución del artículo <i>Scattering between wobbling kinks</i> . . . . .	32
1.6.2. Contribución del artículo <i>Asymmetric scattering between kinks and wobblers</i> .	35
1.6.3. Contribución del artículo <i>Wobbling kinks in a two-component scalar field theory: Interaction between shape modes</i> . . . . .	39
1.7. Bibliografía . . . . .	43
<b>2. Scattering Between Wobbling Kinks</b>	<b>48</b>
<b>3. Asymmetric Scattering Between Kinks and Wobblers</b>	<b>65</b>
<b>4. Wobbling kinks in a two-component scalar field theory: Interaction between shape modes</b>	<b>80</b>
<b>5. Conclusiones</b>	<b>96</b>

# Índice de figuras

1.	Diagrama de velocidad final versus velocidad inicial en el proceso de scattering entre el kink y el antikink del modelo $\phi^4$ . Los colores identifican el numero de rebotes que han sufrido las soluciones antes de que se alejen. La línea discontinua en gris representa la velocidad final sin la transferencia de energía entre modos vibracionales tal que el proceso fuese completamente elástico. El régimen de resonancia está destacado en la parte superior izquierda. Figura tomada de [23]. . . . .	6
2.	Evolución de una solución kink estática que ha sido excitada por el modo cero (izquierda) y por el modo vibracional (derecha). En el primer caso puede observarse que la solución viaja con cierta velocidad mientras que en el segundo el tamaño del kink oscila periódicamente. . . . .	7
1.1.	Gráficos de las soluciones de tipo kink y antikink dibujadas sobre el potencial del modelo $\phi^4$ (izquierda) y de su densidad de energía (derecha). . . . .	16
1.2.	Gráfico del pozo de potencial asociado al operador Hessiano $H$ (1.37) para la solución kink en el modelo $\phi^4$ . En azul, la representación de los modos normales de este modelo. . . . .	17
1.3.	Gráficos de los estados ligados del operador Hessiano $H$ (1.37) para el modelo $\phi^4$ : modo cero identificado con el modo traslacional (izquierda) y modo excitado identificado con el estado vibracional (derecha). . . . .	18
1.4.	Gráficos del potencial del modelo MSTB para $\sigma = 0,5$ (izquierda) y $\sigma = 1,2$ (derecha). . . . .	23
1.5.	Gráficos del pozo de potencial del operador de fluctuaciones (1.70) para $\sigma = 1,2$ (izquierda) y espectro de fluctuaciones del modelo MSTB para $\sigma \in [0, 3]$ para los canales longitudinal y ortogonal (derecha). . . . .	24
1.6.	Gráficos de las soluciones del campo $K_1^\pm(x)$ (izquierda) y $K_2^\pm(x)$ (derecha) para el parámetro $\sigma = 0,5$ . . . . .	25
1.7.	Representación gráfica ilustrando la atracción mutua ejercida en una configuración kink y antikink con velocidad inicial nula y separados por una distancia $2L$ (izquierda) y colisión entre kink y antikink de modelo $\phi^4$ localizados en $x_0 = -5$ y $x_0 = 5$ , respectivamente, con velocidad inicial $v_0 \approx 0$ (derecha). . . . .	27

1.8.	Diagrama de velocidad final versus velocidad inicial en el proceso de scattering entre el kink y el antikink del modelo $\phi^4$ . Los colores identifican el numero de rebotes que han sufrido las soluciones antes de que se alejen. La línea discontinua en gris representa la velocidad final sin la transferencia de energía entre modos vibracionales y el proceso es elástico. El régimen de resonancia está destacado en la parte superior izquierda. Figura tomada de [23]. . . . .	29
1.9.	Diagrama de amplitud final versus velocidad inicial en el proceso de scattering entre el kink y el antikink del modelo $\phi^4$ . Los colores identifican el numero de rebotes que han sufrido las soluciones antes de que se alejen. Figura tomada de [23]. . . . .	31
1.10.	Diagrama de velocidades con ventanas de 1-rebote para diferentes valores de amplitud inicial $a_0 \in [0; 0, 1]$ . En este gráfico es posible observar como nuevas ventanas de reflexión son generadas dentro del régimen de resonancia y como la cola de reflexión oscila conforme la amplitud inicial de vibración aumenta. El código de colores ha sido utilizado para mostrar la evolución del gráfico conforme la amplitud inicial de vibración aumenta. Figura tomada de [23]. . . . .	34
1.11.	Diagrama de velocidades para los kinks vibrantes ampliada en el rango de velocidades $v_0 \in [0, 19; 0, 21]$ . En este gráfico es posible observar cómo ventanas de 2-rebotes se dividen en ventanas más estrechas conforme la amplitud inicial de vibración aumenta. El código de colores ha sido utilizado para mostrar la evolución del gráfico conforme la amplitud inicial de vibración aumenta. Figura tomada de [23]. . . . .	34
1.12.	Diagrama de velocidades para los kinks vibrantes con amplitud inicial $a_0 = 0, 2$ . El código de colores es utilizado para especificar el número de rebotes que sufren las soluciones antes que se alejen con velocidad final $v_f$ . Figura tomada de [23]. . . . .	35
1.13.	Diagrama de velocidades para los kinks vibrantes con fases opuestas y con amplitud inicial $a_0 = 0, 04$ (panel superior), $a_0 = 0, 1$ (panel del medio) y $a_0 = 0, 2$ (panel inferior). El código de colores es el mismo utilizado en el trabajo anterior para identificar el número de rebotes que sufren las soluciones antes que se alejen con velocidad final $v_f$ . Figura tomada de [43]. . . . .	37
1.14.	Diagrama de velocidades para las colisiones entre un kink vibrante con amplitud inicial $a_0 = 0, 1$ y antikink no excitado. El código de colores es el mismo utilizado en el trabajo anterior para identificar el número de rebotes que sufren las soluciones antes que se alejen con velocidad final $v_f$ . Figura tomada de [43]. . . . .	38
1.15.	Diagrama de velocidades para las colisiones entre un kink vibrante y antikink no excitado que destaca el surgimiento de ventanas de 1-rebote dentro del régimen de resonancia en el rango de amplitudes $a_0 \in [0; 0, 2]$ . Las líneas verticales identifican el conjunto de velocidades $v_0$ para las cuales la velocidad final es máxima dentro de las ventanas de 1-rebote siguiendo la fórmula (1.102). Figura tomada de [43]. . . . .	38
1.16.	Representación gráfica de la evolución del campo longitudinal (izquierda) y ortogonal (derecha) con una excitación inicial $a = 0, 6$ . Figura tomada de [38]. . . . .	40

- 1.17. Distribución espectral de la serie temporal obtenida calculando la componente longitudinal del campo en  $x_M$  (panel superior) y  $x_0$  (panel inferior) con la excitación inicial del campo ortogonal fijada en  $a_0 = 0, 1$ . Esta información se muestra para tres valores representativos de  $\sigma$ :  $\sigma = 1,2$  (izquierda),  $\sigma = 1,5$  (centro),  $\sigma = 2,5$  (derecha). Figura tomada de [38]. . . . 41
- 1.18. Distribución espectral de la serie temporal obtenida calculando la componente ortogonal del campo en  $x_M$  (panel superior) y  $x_0$  (panel inferior) con la excitación inicial del campo ortogonal fijada en  $a_0 = 0, 1$ . Esta información se muestra para tres valores representativos de  $\sigma$ :  $\sigma = 1,2$  (izquierda),  $\sigma = 1,5$  (centro),  $\sigma = 2,5$  (derecha). Figura tomada de [38]. . . . 41



# Introducción

En las últimas décadas, el interés en defectos topológicos (DT) embebidos en teoría de campos escalares reales ha crecido ampliamente y su investigación ha tomado un rol fundamental en la física no lineal [1–4]. Esto es debido a que los DT surgen en transiciones de fase o rupturas de simetrías y por ello son encontrados en muchos fenómenos de la naturaleza. A modo de ejemplo, podemos mencionar sus aplicaciones en propiedades de materiales en Materia Condensada [5–7], en modelos cosmológicos inflacionarios [8–10], en transmisión digital de señales en fibras ópticas de larga distancia [11–13], procesos físico-químicos en sistemas moleculares [14, 15], en bioquímica [16], entre otras ramas de la ciencia no lineal. No obstante, todavía no hay un método analítico satisfactorio para explicar la dispersión de defectos topológicos y muchas características de este proceso de colisiones sigue siendo una incógnita.

A partir de finales de la década de los 70 los estudios de colisiones entre defectos topológicos en el modelo  $\phi^4$  empezaron a surgir en la literatura. En las primeras referencias del tema [17–19] los autores estudiaron mediante simulaciones numéricas la colisión de un kink y un antikink del modelo  $\phi^4$  en (1,1)-dimensiones para diferentes valores de velocidad inicial. En los resultados se ha observado dos regímenes de dispersión: (1) estados ligados, llamados *bions*, en el que las soluciones quedan ligadas entre sí rebotando indefinidamente y (2) reflexión, en el que las soluciones terminan alejándose una de la otra. La característica más destacada en este proceso está en que esos dos regímenes quedan entrelazados para valores intermedios de velocidad inicial por una estructura fractal, ver Figura 1.

El régimen de presencia de biones mencionado anteriormente aparece por debajo de un valor crítico de velocidad inicial de colisión  $v_c$ . En este régimen las soluciones chocan, apenas se apartan

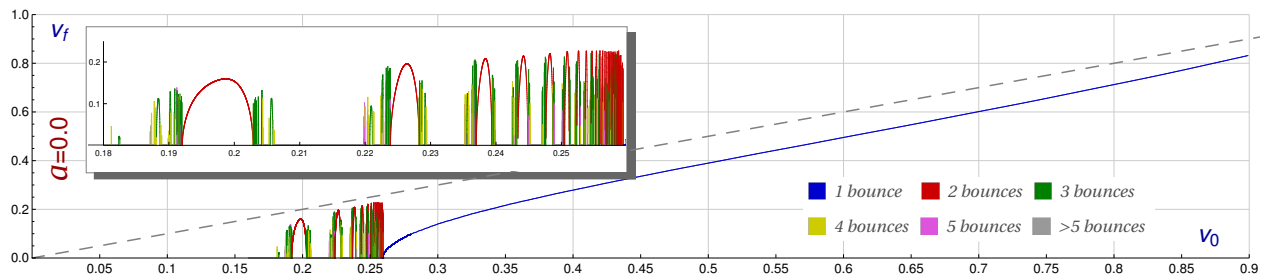


**Figura 1:** Diagrama de velocidad final versus velocidad inicial en el proceso de scattering entre el kink y el antikink del modelo  $\phi^4$ . Los colores identifican el número de rebotes que han sufrido las soluciones antes de que se alejen. La línea discontinua en gris representa la velocidad final sin la transferencia de energía entre modos vibracionales tal que el proceso fuese completamente elástico. El régimen de resonancia está destacado en la parte superior izquierda. Figura tomada de [23].

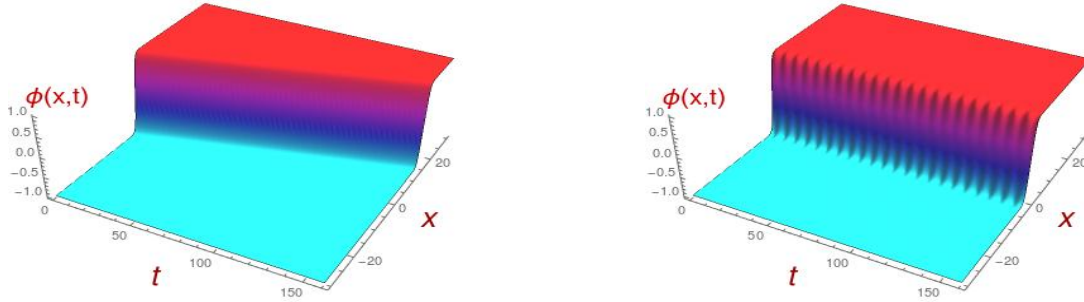


**Figura 2:** Evolución de una solución kink estática que ha sido excitada por el modo cero (izquierda) y por el modo vibracional (derecha). En el primer caso puede observarse que la solución viaja con cierta velocidad mientras que en el segundo el tamaño del kink oscila periódicamente.

y vuelven a rebotar una y otra vez sin llegar a escapar del potencial atractivo que las confinan, emitiendo radiación en cada nuevo rebote y por tanto disipando energía en el medio [20]. A partir de otro valor crítico de velocidad inicial  $v_r$  las soluciones chocan una única vez y se alejan sin volver a rebotar, dando lugar a una curva creciente casi lineal observada al final del diagrama de velocidades asociada a los procesos de scattering de las soluciones tipo kinks. A este valor crítico se le llama velocidad mínima de escape y en modelos de campos no integrables se cumple la desigualdad  $v_r > v_c$ .

En las colisiones entre kink y antikink del modelo  $\phi^4$  con velocidad inicial por encima del valor crítico  $v_c$  y por debajo de la velocidad de escape  $v_r$  las soluciones rebotan un número finito de veces hasta que finalmente se alejan. En la literatura este rango de valores de velocidad inicial es llamado régimen de resonancia. Podemos ver en el diagrama de velocidades como el patrón de ventanas de  $n$ -rebotes se replica indefinidamente con ventanas cada vez más estrechas, conforme la velocidad inicial se acerca a  $v_r$ , Figura 1. En esta figura las ventanas de  $n$ -rebotes están identificadas por colores. Se puede observar que ventanas de 2-rebotes (dibujadas en rojo) están rodeadas por ventanas de 3-rebotes (marcadas en verde) y estas a su vez son rodeadas por otras de 4-rebotes (dibujadas en amarillo) y así sucesivamente. Vale la pena mencionar también que no se ha encontrado ventanas de 1-rebote dentro del régimen de resonancia en colisiones del modelo  $\phi^4$ .

El modelo  $\phi^4$  pertenece a una clase de modelos de campos que son no integrables, lo que significa que su dinámica no está restringida por infinitas magnitudes conservadas [21, 22]. Debido a eso, la presencia de esta estructura fractal encontrada en el diagrama de velocidades encuentra su explicación en la transferencia de energía entre los modos normales de las soluciones.

Los kinks del modelo  $\phi^4$  presentan dos modos normales discretos: el modo cero y el modo vibracional. Las excitaciones en el modo cero de la solución estática causan una translación del kink o antikink en el espacio mientras que las excitaciones en el modo vibracional generan una vibración interna de la solución, ver Figura 2. Estas soluciones vibracionalmente excitadas son comúnmente llamadas en la literatura *wobbling kinks* o *wobblers*.

Por el mecanismo de transferencia de energía resonante mencionado anteriormente, en una coli-



sión entre un kink y un antikink del modelo  $\phi^4$ , parte de la energía cinética almacenada en el modo cero es transferida al modo vibracional en el impacto y tras ello dos soluciones vibracionalmente excitadas, o wobbling kinks, aparecen después del primer rebote. En una ventana de  $n$ -rebotes esta transferencia de energía entre los modos normales se da  $n - 1$  veces hasta que en la última redistribución de energía se transfiera suficiente energía al modo cero, permitiendo que las soluciones escapen del potencial atractivo que las confinaban. Por otra parte, en una colisión entre kink y antikink en que inicialmente las soluciones no tienen suficiente energía cinética, éstas no conseguirán escapar de la fuerza atractiva que las unen y rebotarán indefinidamente. Esto explica el régimen de formación de *bions* para velocidades iniciales de colisión por debajo de  $v_c$ .

Por otro lado, si la energía cinética inicial es suficientemente alta, independientemente de la redistribución de energía que suceda después del primer rebote las soluciones siempre serán capaces de superar el potencial atractivo y se reflejarán, lo que explica la cola de reflexión observada en el diagrama, en color azul, para velocidades superiores a  $v_r$ . Este mecanismo de transferencia de energía resonante también es observado para una gran variedad de modelos de campos escalares reales, entre los cuales podemos destacar generalizaciones del modelo  $\phi^4$  [24–29], el doble sine-Gordon [22,30–32], teorías de campos de dos componentes [33–38], en teorías de campos de mayores ordenes [39–41], etc. El interés de la comunidad científica en este tema sigue aumentando en los últimos años y nuevos aspectos del proceso de scattering salen a la luz en cada nueva publicación.

Entre los resultados más destacados en los últimos cuatro años en la parte teórica de scattering entre kinks podemos mencionar la observación de *oscillons* en la dispersión de multi-kinks [32, 42]; la repulsión y resonancia en las colisiones kink-antikink del modelo  $\phi^8$ , [40]; el surgimiento de nuevas ventanas de reflexión en el régimen de resonancia, así como la posibilidad de wobblers que presentan velocidad final mayor que la velocidad inicial de colisión [23, 43]; interacción entre los modos normales de vibración longitudinal y ortogonal en teorías de campos de dos componentes [38], etc.

Esta tesis doctoral proporciona resultados novedosos en el proceso de scattering entre kinks. La línea maestra que caracteriza las investigaciones en esta memoria corresponde con el estudio del comportamiento de los kinks que son excitados vibracionalmente, o como hemos dicho antes, el comportamiento de los llamados wobblers o wobbling kinks. Lo que se pretende es investigar cómo los modos vibracionales presentes en estas soluciones interactúan con otros, principalmente los modos traslacionales, lo que lleva a transformar energía vibracional en energía cinética, dando un impulso al kink viajero. Este estudio puede realizarse estudiando la colisión entre un wobbling kink y el correspondiente wobbling antikink como por ejemplo, en el paradigmático modelo  $\phi^4$ , y analizar las velocidades finales de los kinks y antikinks resultantes, así como su amplitud de vibración. Otra opción para estudiar la interacción entre estos modos es emplear modelos más complejos como, por ejemplo, modelos de dos o más campos escalares, donde podemos encontrar no sólo un modo vibracional sino varios, tanto en el canal longitudinal como en el ortogonal. Este tratamiento nos proporciona resultados sobre el funcionamiento de la dinámica de estos modos

normales de vibración y cómo la excitación de alguno de ellos desencadena la excitación de otros y de los mecanismo de emisión de radiación en forma de ondas planas.

Cada uno de los trabajos publicados que componen la presente tesis doctoral se centra en un escenario inicial específico: colisiones entre wobbling kinks, colisiones asimétricas entre kinks y wobblers, e interacción entre los modos normales de kinks en teorías de campos de dos componentes. Los resultados nos permiten entender cómo los parámetros de la configuración inicial influyen sobre el patrón fractal encontrado en el diagrama de velocidades y cómo pueden favorecer o desfavorecer el surgimiento de ventanas de reflexión en el régimen de resonancia.

En el Capítulo 1 introduciremos las nociones básicas sobre las teorías de campos escalares reales en (1,1)-dimensiones tales como el modelo  $\phi^4$  y el modelo MSTB, cuyas soluciones son ampliamente conocidas en la literatura. Veremos en detalle las condiciones de minimización de la energía que nos permite obtener soluciones analíticas en estos modelos. También estudiaremos la estabilidad lineal de las soluciones, identificando sus modos normales de vibración y de radiación, pasos fundamentales que cimientan las bases de los resultados destacados en la tesis. Además, investigamos la interacción entre soluciones en una configuración kink-antikink mediante simulaciones numéricas cuando son sometidos a procesos de scattering o colisión. Al final del Capítulo 1 se encuentra un resumen de la contribución y coherencia entre los artículos publicados que componen esta tesis doctoral. Por último y no menos importante se encuentran las referencias bibliográficas de esta tesis. Inevitablemente, esta relación de referencias se quedará corta por la amplitud de la literatura científica relacionada con este tema. Es pertinente pedir disculpas por aquellas que no aparecen, remarcando que se ha tratado de introducir la selección de referencias más relevantes para el tema de esta tesis. Para una relación más extensa se puede consultar la lista de referencias de cada artículo que conforma esta tesis doctoral.





# Capítulo 1

---

## Defectos topológicos en teorías de campos escalares en (1+1)-dimensiones

---

En la primera sección de este capítulo veremos una breve introducción a la definición de defectos topológicos así como ejemplos de fenómenos físicos en los que pueden ser encontrados. Tomando como centro de nuestra discusión los defectos de tipo kink revisaremos el ejemplo paradigmático del modelo  $\phi^4$ . Encontraremos las soluciones analíticas de este modelo utilizando el método BPS, que puede ser generalizado a modelos de varios campos y verificaremos la estabilidad de la solución con respecto a pequeñas perturbaciones, identificando los estados normales del kink. También introduciremos el modelo de dos campos MSTB que es una generalización natural del modelo  $\phi^4$  en dicho contexto. La solución kink del modelo  $\phi^4$  está embebido en este nuevo sistema. Un listado de las contribuciones de los artículos que conforman esta tesis también es incluido al final de este capítulo.

### 1.1. Defectos topológicos en teoría de campos escalares

Los defectos topológicos son soluciones de ecuaciones diferenciales de segundo orden no lineales en teorías de campos. Aparecen naturalmente en transiciones de fase. En general, las transiciones de fase son caracterizadas por un *parámetro de orden* que aumenta conforme las condiciones de contorno (por ejemplo, la temperatura) cambian el estado del sistema pudiendo generar defectos topológicos. Las transiciones de fase pueden ser clasificadas como de primer orden o de segundo orden.

En particular, una transición de fase de segundo orden ocurre cuando una ruptura de simetría cambia de manera continua el *parámetro de orden*, llevando el sistema a un estado de menor simetría. Podemos mencionar como ejemplo el crecimiento continuo de la magnetización en una transición de fase paramagnético - ferromagnético. Cuando los momentos magnéticos de los átomos de un

material no apuntan a una misma dirección, pero pueden ser alineados por un campo magnético externo decimos que el material presenta propiedades paramagnéticas. Inicialmente, un material paramagnético presenta una magnetización neta nula, debido a que la magnetización de cada átomo del material varía aleatoriamente por las fluctuaciones térmicas. Un material paramagnético con cierta temperatura alta  $T_H$  puede pasar a un estado ferromagnético al bajar de una temperatura  $T_C$ , en una transición de este tipo. En este caso, el desorden en la orientación de los spins de los átomos en el estado paramagnético es sustituido por el orden en el estado ferromagnético en que todos los spins apuntan a una misma dirección, lo que caracteriza la ruptura de simetría espacial del sistema. En ese ejemplo, la magnetización  $\mathbf{M}$  del material es el *parámetro de orden*. Se puede observar el aumento continuo de la magnetización conforme la temperatura del material disminuye.

En una situación real, debido a la finitud de la velocidad de propagación de la información, regiones del material suficientemente distantes tendrán diferentes temperaturas y elegirán diferentes direcciones de magnetización al alcanzar la temperatura  $T_C$ . Entre esas dos regiones distantes se forma una región de transición continua que las conecta o en otras palabras se forma un *defecto* topológico en el material. Defecto, porque, en este ejemplo, esta región no presenta ninguna de las direcciones de spin encontradas en las regiones de contorno.

Por otro lado, una transición de fase de primer orden está asociada a un cambio abrupto del *parámetro de orden* del sistema. La transición de fase de agua líquida en hielo es un ejemplo clásico de transición de primer orden. En el cambio de fase la entropía cambia abruptamente debido al cambio de calor latente cuando todo el agua se transforma en hielo. Transiciones de fase de primer orden con ruptura de simetría también tienen un papel importante en cosmología. De acuerdo con la bariogénesis, el universo primordial pasó por diversas transiciones de fase que dieron origen a los campos de fuerza actualmente conocidos. En los ejemplos mencionados de transiciones de fase y en muchas otras ramas de la física no lineal los defectos topológicos encontrados en modelos de teorías de campos son utilizados para explicar los fenómenos observados.

Los kinks son los defectos topológicos encontrados en teorías de campos escalares en (1,1)-dimensiones espacio-temporales. De hecho, el teorema de Derrick prohíbe la existencia de este tipo de soluciones de energía finita para dimensiones mayores. Estos aparecen como soluciones estáticas que conectan dos mínimos consecutivos del potencial asociado al campo escalar en modelos no lineales. La no linealidad de los modelos dificulta su tratamiento analítico, pero hay métodos para reducir el orden de las ecuaciones diferenciales, como el método BPS (del acrónimo Bogomolnyi-Prasad-Sommerfield) [44,45] del cual hablaremos más adelante, que permiten encontrar un conjunto de soluciones que satisfacen las ecuaciones de segundo orden originales.

A pesar de la aparente simplicidad de los modelos con soluciones tipo kink, estos son utilizados para describir una variedad de comportamientos de materiales magnéticos en materia condensada [46,47]. Cuando son embebidos en teorías con más dimensiones espaciales pueden aparecer como paredes de dominio (domain walls) en soluciones cristalinas [48] y en modelos fenomenológicos básicos de la estructura secundaria de proteínas [49]. Un modelo ampliamente conocido en la literatura

en que surgen soluciones tipo kink es el modelo  $\phi^4$  estándar. Este es descrito por una funcional llamada acción. En el espacio-tiempo Minkowskiano el funcional acción en (1,1)-dimensiones se escribe

$$S[\phi] = \int_{-\infty}^{\infty} d^2x \mathcal{L}(\phi, \partial_\mu \phi), \quad (1.1)$$

donde la densidad de lagrangiana se define como

$$\mathcal{L} = \frac{1}{2} g_{\mu\nu} \partial^\nu \phi \partial^\mu \phi - V(\phi). \quad (1.2)$$

La métrica adoptada en esta tesis es  $g_{00} = -g_{11} = 1$  y  $g_{01} = g_{10} = 0$ . En la ecuación anterior el término  $V(\phi)$  es la energía potencial asociada al modelo que depende únicamente del campo escalar. Por conveniencia la llamaremos de aquí en adelante potencial. A través del cálculo variacional se encuentran las ecuaciones de Euler-Lagrange

$$\partial_\mu \left( \frac{\partial \mathcal{L}}{\partial (\partial_\mu \phi)} \right) - \frac{\partial \mathcal{L}}{\partial \phi} = 0, \quad (1.3)$$

que determinan las soluciones del sistema. La ecuación (1.3) en un sistema en (1, 1)-dimensiones puede ser reescrita como

$$\frac{\partial^2 \phi}{\partial t^2} - \frac{\partial^2 \phi}{\partial x^2} + \frac{dV(\phi)}{d\phi} = 0. \quad (1.4)$$

Para el caso estático, en el cual el campo no depende del tiempo, la ecuación de movimiento (1.4) se reduce a la ecuación diferencial ordinaria

$$\frac{d^2 \phi(x)}{dx^2} = \frac{dV(\phi)}{d\phi}. \quad (1.5)$$

El teorema de Noether garantiza que si la acción (1.1) es invariante frente a una transformación de coordenadas, existirá una cantidad conservada asociada a esa invariancia [50]. Considerando una transformación infinitesimal general de las coordenadas del tipo  $x^\mu \rightarrow x'^\mu = x^\mu + \delta x^\mu$  en (1.1) obtenemos una nueva acción reescrita en función de las coordenadas transformadas dada por  $S' = S + \delta S$ . Visto de otra forma, podemos escribir que la variación de la acción frente a transformaciones infinitesimales en las coordenadas es

$$\delta S = \int d^2x' \mathcal{L}(\phi', \partial_\mu \phi', x'^\mu) - \int d^2x \mathcal{L}(\phi, \partial_\mu \phi, x^\mu), \quad (1.6)$$

donde el determinante Jacobiano de esa transformación es  $J = \det \left( \frac{\partial x'^\mu}{\partial x^\alpha} \right) = 1 + \partial_\mu \delta x^\mu + \mathcal{O}(\delta x^\mu)$  y si la acción es invariante, entonces  $\delta S = 0$ . Teniendo en cuenta que se ha tomado transformaciones infinitesimales, los términos de segundo orden pueden ser despreciados. Utilizando la ecuación de Euler-Lagrange (1.2) se puede reescribir (1.6) de la siguiente manera

$$\delta S = \int d^2x \partial_\mu \left[ \mathcal{L} \delta x^\mu - \frac{\partial \mathcal{L}}{\partial(\partial_\mu \phi)} \delta \phi \right] = 0. \quad (1.7)$$

que resulta en una integral en un contorno  $\Sigma$ . Sumando y restando los términos  $\frac{\partial \mathcal{L}}{\partial(\partial_\mu \phi)} (\partial^\nu \phi) \delta x_\nu$  a la ecuación anterior, se obtiene

$$\delta S = \int_\Sigma d\Sigma_\mu \left[ \frac{\partial \mathcal{L}}{\partial(\partial_\mu \phi)} \Delta \phi - T^{\mu\nu} \delta x_\nu \right] = 0, \quad (1.8)$$

donde la cantidad  $\Delta \phi \equiv \delta \phi + (\partial^\nu \phi) \delta x_\nu$  es la variación total del campo en el contorno  $\Sigma$  y el tensor

$$T^{\mu\nu} \equiv \frac{\partial \mathcal{L}}{\partial(\partial_\mu \phi)} \partial^\nu \phi - g_{\mu\nu} \mathcal{L}. \quad (1.9)$$

es una corriente conservada. La expresión (1.9) es llamada el tensor energía-momento. La componente temporal de este tensor es la densidad de energía del sistema. Para los casos estáticos en que el campo no depende del tiempo, la densidad de energía es igual en módulo a la densidad lagrangiana

$$\rho := -\mathcal{L} = \frac{1}{2} \phi'^2 + V(\phi), \quad (1.10)$$

donde  $\phi' = d\phi(x)/dx$ . La descomposición de Bogomolnyi permite encontrar soluciones analíticas para una clase especial de modelos en que el potencial es acotado inferiormente, pudiendo ser escrito como

$$V(\phi) = \frac{1}{2} W_\phi^2, \quad (1.11)$$

donde  $W_\phi = dW(\phi)/d\phi$ . La función  $W(\phi)$  es llamada superpotencial por analogía a los modelos que surgen en teorías supersimétricas. Sustituyendo el potencial escrito de esta forma en (1.10) se obtiene la energía total del sistema dada por

$$E = \int_{-\infty}^{\infty} dx \left[ \frac{1}{2} \phi'^2 + \frac{1}{2} W_\phi^2 \right], \quad (1.12)$$

que puede ser reescrita en la forma

$$E = \int_{-\infty}^{\infty} dx \left[ \frac{1}{2} (\phi' \mp W_\phi)^2 \pm \frac{dW(\phi)}{dx} \right]. \quad (1.13)$$

Los dos términos en (1.13) dan contribuciones positivas. El segundo de ellos será demostrado que es constante. Luego, la energía será mínima siempre que se cumpla la condición

$$\phi' = \pm W_\phi. \quad (1.14)$$

De esa manera, la energía total viene dada por



$$E_B = \int_{-\infty}^{\infty} dx \frac{dW(\phi)}{dx} = |W(\phi(\infty)) - W(\phi(-\infty))|. \quad (1.15)$$

si asumimos que el superpotencial  $W(\phi)$  es una función diferenciable.  $E_B$  se llama energía de Bogomolnyi. También se puede comprobar que el conjunto de soluciones que vienen de (1.14) satisfacen las ecuaciones de movimiento de segundo orden (1.5). Tomando la derivada en el espacio y utilizando la ecuación de primer orden (1.14) se obtiene que

$$\frac{d^2\phi}{dx^2} = \pm W_{\phi\phi}\phi' = W_{\phi\phi}W_{\phi} = \frac{dV(\phi)}{d\phi}. \quad (1.16)$$

Considerando una solución estática, se puede investigar la estabilidad lineal frente a perturbaciones de primer orden. Eso puede servir como guía para determinar si una solución es estable o si rápidamente decaerá a un estado de menor energía. Tomaremos una pequeña fluctuación alrededor de la solución estática como

$$\tilde{\phi}_K(t, x) = \phi_K(x) + \psi(t, x). \quad (1.17)$$

Aquí  $\phi_K$  representa la solución estática y  $\tilde{\phi}_K$  la solución estática perturbada por la fluctuación  $\psi$ . Expandiendo la ecuación de movimiento (1.4) hasta primer orden en  $\psi$  se tiene

$$\frac{\partial^2\psi}{\partial t^2} - \frac{\partial^2\psi}{\partial x^2} + U_S(x)\psi = 0, \quad (1.18)$$

donde

$$U_S(x) = \left. \frac{d^2V(\phi)}{d\phi^2} \right|_{\phi_K}. \quad (1.19)$$

Una vez que el potencial de estabilidad  $U(x)$  depende únicamente de  $x$ , se puede utilizar la separación de variables estándar para encontrar una solución a la ecuación diferencial (1.18) con el siguiente *ansatz*

$$\psi(t, x) = \sum_n a_n e^{i\omega_n t} \psi_{\omega_n^2}(x). \quad (1.20)$$

Con ese *ansatz* la ecuación de movimiento para la perturbación puede ser reescrita como una ecuación de tipo Schrodinger independiente del tiempo

$$H\psi_{\omega_n^2}(x) = \omega_n^2\psi_{\omega_n^2}(x), \quad (1.21)$$

donde

$$H = -\frac{d^2}{dx^2} + U_S(x). \quad (1.22)$$

Es posible observar en la ecuación (1.21) que los autovalores  $\omega_n^2$  deben ser necesariamente no

negativos para asegurar que la solución es estable. En caso contrario, el término  $e^{i\omega t}$  del *ansatz* (1.20) se convertiría en exponenciales reales que divergen rápidamente en el tiempo.

También se puede verificar que siempre existe un modo cero  $\psi_{\omega_0^2}$  con autovalor nulo, que corresponde a la primera derivada  $\psi_{\omega_0^2} = d\phi_K/dx$  de la solución estática en (1,1)-dimensiones, simplemente derivando la ecuación (1.5)

$$\left[ -\frac{d^2}{dx^2} + \frac{d^2V(\phi)}{d\phi^2} \right] \phi'_K(x) = 0, \quad (1.23)$$

que es la ecuación espectral (1.21) para  $\omega_0^2 = 0$ . Comparando (1.23) con (1.21) se obtiene que

$$\psi_0(x) = x_0 \phi'_K(x). \quad (1.24)$$

En la ecuación anterior,  $x_0$  es un factor de normalización. Dado que el modelo (1.5) es invariante frente a traslaciones, entonces si  $\phi_K(x)$  es una solución,  $\phi_K(x + x_0)$  también lo será. Por tanto, expandiendo el campo hasta primer orden en  $x_0$  se obtiene

$$\phi_K(x) \rightarrow \phi_K(x + x_0) = \phi_K(x) + x_0 \phi'_K(x), \quad (1.25)$$

de modo que el segundo término de la ecuación anterior corresponde a la velocidad del campo en la coordenada  $x$ . En general, se puede comprobar que en  $(D + 1)$ -dimensiones cualquier teoría invariante a transformaciones del tipo (1.25) tendrá  $D$  modos de traslación, uno asociado a cada dimensión espacial.

En modelos cuyo potencial es acotado inferiormente como en (1.11) el operador  $H$  de la ecuación tipo Schrodinger puede ser reescrito como

$$H = -\frac{d^2}{dx^2} + W_{\phi\phi}^2 + W_\phi W_{\phi\phi\phi}, \quad (1.26)$$

lo que motiva la definición del siguiente operador

$$S = -\frac{d}{dx} + W_{\phi\phi}. \quad (1.27)$$

Utilizando la ecuación de primer orden (1.14)  $H$  puede ser factorizado en función del operador  $S$  como sigue

$$H = S^\dagger S. \quad (1.28)$$

Sustituyendo (1.28) en (1.21) y aplicando  $\psi_{\omega_n^2}^\dagger$  por la izquierda se obtiene que

$$\omega_n^2 = \frac{\int dx |S\psi_{\omega_n^2}|^2}{\int dx |\psi_{\omega_n^2}|^2}, \quad (1.29)$$

de modo que es posible observar que los autovalores  $\omega_n^2$  en (1.29) serán siempre no negativos, lo

que garantiza la estabilidad lineal de las soluciones frente a pequeñas fluctuaciones y también que el modo cero es el estado ligado de menor energía del sistema. Además, el modo cero puede ser escrito en función del superpotencial como

$$\psi_0(x) = x_0 W_\phi(\phi_K). \quad (1.30)$$

## 1.2. El Modelo $\phi^4$

El modelo  $\phi^4$  estándar es un caso particular de los sistemas caracterizados por la densidad de lagrangiana (1.2). Este modelo está definido por el potencial

$$V(\phi) = \frac{\lambda^2}{2}(a^2 - \phi^2)^2, \quad (1.31)$$

donde  $a$  y  $\lambda$  son constantes que determinan respectivamente los puntos de mínimo de  $V(\phi)$  y la masa del campo. En un sistema con unidades naturales i.e.  $c = \hbar = 1$ , la densidad lagrangiana en (1.2) tiene dimensión de energía al cuadrado, y el campo  $\phi$  y las coordenadas son adimensionales. Por tanto, al nivel clásico se puede realizar una reescala en el campo tal que  $\phi \rightarrow a\phi$ , y en las coordenadas,  $x^\mu \rightarrow (a\lambda)^{-1}x^\mu$ , sin pérdida de generalidad. Esta reescala lleva el sistema a una densidad lagrangiana equivalente,  $\tilde{\mathcal{L}} \rightarrow \lambda^2 a^2 \mathcal{L}$ , pero que no modifica las ecuaciones de movimiento del sistema. Con todo eso, el potencial del  $\phi^4$  puede ser reescrito como

$$V(\phi) = \frac{1}{2}(1 - \phi^2)^2, \quad (1.32)$$

ver Figura (1.1). Se puede observar que el potencial del modelo  $\phi^4$  se encuadra en la clase especial de modelos cuyo potencial está acotado inferiormente. Comparando (1.32) con (1.11) se obtiene que el superpotencial para este modelo es dado por

$$W(\phi) = \phi - \frac{1}{3}\phi^3. \quad (1.33)$$

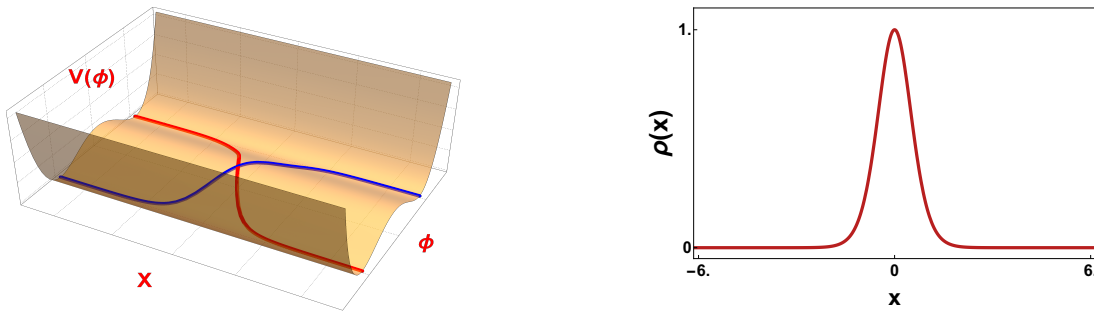


**Figura 1.1:** Gráficos de las soluciones de tipo kink y antikink dibujadas sobre el potencial del modelo  $\phi^4$  (izquierda) y de su densidad de energía (derecha).

Sustituyendo (1.32) en la ecuación de movimiento (1.14) se obtiene

$$\frac{d\phi}{dx} = \pm(1 - \phi^2). \quad (1.34)$$

Como fue demostrado en (1.16) las soluciones de esta ecuación de primer orden satisfacen la ecuación de segundo orden (1.5). Las soluciones estáticas no triviales para el campo vienen dadas por

$$\phi(x; x_0) = \pm \tanh(x - x_0), \quad (1.35)$$

donde la solución positiva es llamada kink y la solución negativa, antikink. En la Figura 1.1 se puede visualizar el comportamiento de estas soluciones sobre el potencial del modelo. En este escenario unidimensional la densidad de energía  $\rho(x)$  de la solución estática se identifica con la densidad lagrangiana, como en (1.10). Por tanto, para el modelo  $\phi^4$  se verifica que

$$\rho(x) = -\mathcal{L} = \text{sech}^4(x - x_0). \quad (1.36)$$

Integrando en todo el espacio, se obtiene que la energía total del modelo es  $E = 4/3$ .

El estudio de la estabilidad lineal de la solución kink del modelo  $\phi^4$  resulta en una ecuación tipo Schrodinger como ha sido visto en (1.21), donde el operador (1.22), tiene la forma

$$H = -\frac{d^2}{dx^2} + 4 - 6\text{sech}^2(x - x_0). \quad (1.37)$$

Este operador a su vez puede ser factorizado con el operador diferencial definido en (1.27), donde  $S = -d/dx + 2\phi$ . Como resultado no habrá modos normales negativos, lo que indica la estabilidad de las soluciones. Por otro lado, con el superpotencial (1.33) la energía de Bogomolnyi es dada por

$$E_B = |W(\phi(\infty)) - W(\phi(-\infty))| = 4/3, \quad (1.38)$$

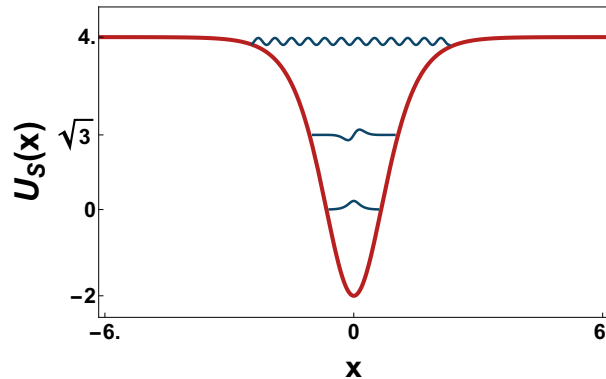


**Figura 1.2:** Gráfico del pozo de potencial asociado al operador Hessiano  $H$  (1.37) para la solución kink en el modelo  $\phi^4$ . En azul, la representación de los modos normales de este modelo.

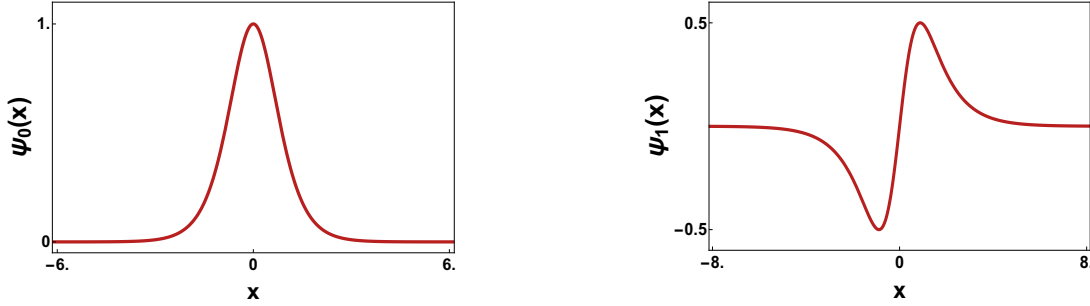


**Figura 1.3:** Gráficos de los estados ligados del operador Hessiano  $H$  (1.37) para el modelo  $\phi^4$ : modo cero identificado con el modo traslacional (izquierda) y modo excitado identificado con el estado vibracional (derecha).

que se identifica con la energía total de las soluciones kinks y antikinks. Como  $E_B$  es la mínima posible, se verifica que las soluciones no decaerán a un estado de menor energía y si es así, entonces las soluciones estáticas del modelo  $\phi^4$  definidas en (1.35) son estables.

En la Figura 1.2 se puede visualizar el pozo de potencial  $U_S$  asociado a  $H$ . La ecuación de Schrodinger con autovalor nulo,  $H\psi_0 = 0$ , permite encontrar el estado ligado de menor energía para la teoría. Como ha sido introducido en (1.24), este modo normal en el caso estático se identifica con el modo traslacional del campo, entonces  $\psi_0(x) = x_0 d\phi/dx$ . Sin añadir ninguna restricción al sistema se puede tomar el centro de la solución estática en  $x_0 = 0$ .

El modelo  $\phi^4$  presenta también un modo normal de vibración por encima del modo cero y que tiene un autovalor  $\omega^2 = 3$ . La correspondiente autofunción está asociada a vibraciones internas de la solución que modifican el tamaño del kink, por eso es llamado en la literatura como *shape mode* o modo vibracional. El espectro continuo de la teoría empieza a partir del valor umbral  $\omega^2 = 4$ . Los estados normales que se obtienen de la ecuación de Schrodinger tienen la forma

$$\psi_{\omega^2=0}(x) = \phi'_K(x) = \text{sech}^2(x), \quad (1.39)$$

$$\psi_{\omega^2=3}(x) = \sinh(x)\text{sech}^2(x), \quad (1.40)$$

$$\psi_{\omega^2=4}(x) = e^{iqx}[-1 - q^2 + 3 \tanh^2(x) - 3iq \tanh(x)]. \quad (1.41)$$

### 1.3. Modelos de dos campos escalares

La introducción anterior se aplica a modelos cuya densidad lagrangiana está definida por un único campo escalar. Las aplicaciones en varios escenarios de la ciencia no lineal, así como los métodos desarrollados para encontrar soluciones analíticas a esos problemas han favorecido el aumento de las investigaciones sobre esa clase de modelos en las últimas décadas. No obstante, en ellos la órbita de la solución estática en el espacio interno está limitada a un segmento de recta. Así también las

colisiones entre defectos topológicos están limitadas a una configuración compuesta de un kink y su par antisimétrico, el antikink. Esas limitaciones desaparecen en modelos cuya densidad lagrangiana incluye dos o más campos escalares reales. Las primeras referencias en este tema empezaron a surgir al final de los años setenta [4] y desde entonces una gran variedad de modelos ha recibido mucha atención en la literatura debido a las propiedades presentadas por los kinks en estos escenarios, tales como el modelo de Montonen–Sarker–Trullinger–Bishop (MSTB), del cual hablaremos más adelante. En cosmología la existencia de múltiples campos escalares puede influir en la anchura de las branas y en el contexto de la cosmología de mundos brana [51].

Encontrar soluciones analíticas en esa clase de modelos es significativamente más complicado que en modelos de un único campo escalar, lo que ha impulsado una investigación activa en ese tema [52–54]. En trabajos recientes se ha demostrado que en este tipo de sistemas se duplica el número de eventos que pueden encontrarse en la colisión entre dos kinks estables diferentes en el modelo MSTB [33, 34, 36]. En este modelo, los autores han investigado cómo los modos normales de vibración de un kink son excitados por la excitación inicial de otros modos [38].

La dinámica antes gobernada por un único campo escalar ahora es descrita en función de dos campos como

$$S[\phi] = \int_{-\infty}^{\infty} d^2x \mathcal{L}(\phi, \psi, \partial_\mu \phi, \partial_\mu \psi), \quad (1.42)$$

donde la densidad lagrangiana es

$$\mathcal{L} = \frac{1}{2} \partial_\mu \phi \partial^\mu \phi + \frac{1}{2} \partial_\mu \psi \partial^\mu \psi - U(\phi, \psi). \quad (1.43)$$

De manera similar a los modelos de un campo se considerará que el modelo de dos campos está embebido en un espacio-tiempo Minkowskiano de (1,1)-dimensiones cuya métrica está definida como  $g_{00} = -g_{11} = 1$  y  $g_{10} = g_{01} = 0$ . Cada campo es gobernado por una ecuación de movimiento que se obtiene aplicando el cálculo variacional a (1.42). Se llega a

$$\frac{\partial^2 \phi}{\partial t^2} - \frac{\partial^2 \phi}{\partial x^2} + \frac{\partial}{\partial \phi} U(\phi, \psi) = 0, \quad (1.44)$$

$$\frac{\partial^2 \psi}{\partial t^2} - \frac{\partial^2 \psi}{\partial x^2} + \frac{\partial}{\partial \psi} U(\phi, \psi) = 0, \quad (1.45)$$

que en el caso estático se reescriben como

$$\frac{d^2 \phi}{dx^2} = \frac{\partial}{\partial \phi} U(\phi, \psi), \quad (1.46)$$

$$\frac{d^2 \psi}{dx^2} = \frac{\partial}{\partial \psi} U(\phi, \psi). \quad (1.47)$$

Del teorema de Noether se obtiene el tensor energía-momento dado por

$$T^{\mu\nu} = \frac{\partial \mathcal{L}}{\partial(\partial_\mu \phi)} \partial^\nu \phi + \frac{\partial \mathcal{L}}{\partial(\partial_\mu \psi)} \partial^\nu \psi - g_{\mu\nu} \mathcal{L}. \quad (1.48)$$

La descomposición de Bogomolnyi introducida para modelos de un campo puede ser extendida para modelos de dos campos escalares. Considerando el caso en que el potencial es acotado inferiormente para ambos campos  $\phi$  y  $\psi$ , a veces es posible expresar el potencial en la siguiente forma

$$U(\phi, \psi) = \frac{1}{2}(W_\phi^2 + W_\psi^2), \quad (1.49)$$

donde  $W(\phi, \psi)$  es como antes el superpotencial de la teoría. Con el potencial escrito de esta forma, en el caso estático la energía total del modelo se reduce a

$$E = \frac{1}{2} \int_{-\infty}^{\infty} dx \left[ \left( \frac{d\phi}{dx} \right)^2 + \left( \frac{d\psi}{dx} \right)^2 + W_\phi^2 + W_\psi^2 \right]. \quad (1.50)$$

De manera conveniente se puede reescribir el integrando en (1.50) completando cuadrados, resultando en

$$E = \frac{1}{2} \int_{-\infty}^{\infty} dx \left( \frac{d\phi}{dx} \mp \frac{\partial W}{\partial \phi} \right)^2 + \frac{1}{2} \int_{-\infty}^{\infty} dx \left( \frac{d\psi}{dx} \mp \frac{\partial W}{\partial \psi} \right)^2 + E_B, \quad (1.51)$$

donde si  $W(\phi)$  es una función diferenciable

$$E_B = |W(\phi(\infty), \psi(\infty)) - W(\phi(-\infty), \psi(-\infty))|, \quad (1.52)$$

es la energía de Bogomolnyi. Por la condición de minimización de la energía (1.51) se obtiene las ecuaciones de primer orden

$$\frac{d\phi}{dx} = \pm \frac{\partial W}{\partial \phi}, \quad (1.53)$$

$$\frac{d\psi}{dx} = \pm \frac{\partial W}{\partial \psi}. \quad (1.54)$$

y por tanto, si se cumplen esas condiciones la energía total del sistema es la energía de Bogomolnyi i.e.  $E = E_B$ . Por eso, se puede esperar que las soluciones provenientes de esa descomposición sean estables frente a pequeñas fluctuaciones. Es importante mencionar también que la descomposición permite encontrar la energía total de la teoría sin conocer explícitamente sus soluciones.

Se puede verificar que las soluciones a las ecuaciones de primer orden en (1.53) y (1.54) también son soluciones a las ecuaciones de segundo orden (1.44) y (1.45). Derivando la ecuación de primer orden para  $\phi$  con signo positivo, por ejemplo, se obtiene

$$\frac{d^2 \phi}{dx^2} = W_{\phi\phi} \phi' + W_{\phi\psi} \psi'. \quad (1.55)$$

Utilizando las ecuaciones de primer orden se puede ver que

$$\frac{d^2\phi}{dx^2} = W_{\phi\phi}W_\phi + W_{\phi\psi}W_\psi = U_\phi, \quad (1.56)$$

que es la ecuación de segundo orden (1.44) en el caso estático. De forma completamente análoga se puede obtener la ecuación (1.45).

Con un análisis similar al realizado en la introducción al modelo de un campo escalar se puede estudiar la estabilidad de las soluciones en el modelo de dos campos. Aplicaremos pequeñas fluctuaciones en torno a las soluciones estáticas como

$$\tilde{\phi}_K(t, x) = \phi_K(x) + \eta(t, x), \quad (1.57)$$

$$\tilde{\psi}_K(t, x) = \psi_K(x) + \xi(t, x), \quad (1.58)$$

donde  $\phi_K$  y  $\psi_K$  son soluciones estáticas del modelo. Considerando una separación de variable en las fluctuaciones como sigue

$$\begin{pmatrix} \eta(t, x) \\ \xi(t, x) \end{pmatrix} = \sum_n a_n \begin{pmatrix} \eta_n(x) \\ \xi_n(x) \end{pmatrix} e^{i\omega_n t}, \quad (1.59)$$

es posible reescribir las ecuaciones de segundo orden expandiendo hasta primer orden en las perturbaciones en torno a las soluciones estáticas, resultando una ecuación tipo Schrodinger

$$H\Psi_{\omega_n^2}(x) = \omega_n^2\Psi_{\omega_n^2}(x). \quad (1.60)$$

donde

$$H = -\frac{d^2}{dx^2} + \begin{pmatrix} U_{\phi\phi} & U_{\phi\psi} \\ U_{\psi\phi} & U_{\psi\psi} \end{pmatrix} \quad \text{y} \quad \Psi_{\omega_n^2} = \begin{pmatrix} \eta_n(x) \\ \xi_n(x) \end{pmatrix}. \quad (1.61)$$

En [55] los autores definen el operador diferencial de primer orden

$$S = \begin{pmatrix} -d/dx + W_{\phi\phi} & W_{\phi\psi} \\ W_{\psi\phi} & -d/dx + W_{\psi\psi} \end{pmatrix}, \quad (1.62)$$

que permite factorizar el operador  $H = S^\dagger S$ . Si  $H$  es un operador no negativo, sus autovalores también lo serán. Por tanto, se verifica que las soluciones estáticas de (1.53) y (1.54) son estables en tal caso.

## 1.4. El Modelo MSTB

Una generalización natural del modelo  $\phi^4$  en teorías de dos campos escalares es el modelo MSTB. Este es una deformación del modelo sigma  $\mathcal{O}(2)$  lineal que preserva la existencia de dos



mínimos degenerados. El modelo es un caso particular de la densidad lagrangiana (1.43), cuyo potencial tiene la forma

$$U(\phi, \psi) = \frac{1}{2}(\phi^2 + \psi^2 - 1)^2 + \frac{1}{2}\sigma^2\psi^2, \quad (1.63)$$

ver Figura 1.4. De (1.44) y (1.45) se obtiene que las ecuaciones de movimiento para  $\phi$  y  $\psi$  en este modelo son respectivamente

$$\frac{\partial^2 \phi}{\partial t^2} - \frac{\partial^2 \phi}{\partial x^2} = 2\phi(1 - \phi^2 - \psi^2), \quad (1.64)$$

$$\frac{\partial^2 \psi}{\partial t^2} - \frac{\partial^2 \psi}{\partial x^2} = 2\psi(1 - \phi^2 - \psi^2 - \frac{1}{2}\sigma^2). \quad (1.65)$$

Este par de ecuaciones diferenciales de segundo orden acopladas resulta difícil de tratar analíticamente. Por tanto, consideraremos el caso estático en que ambos campos no dependen del tiempo. Con eso, las ecuaciones de movimiento pueden ser reescritas como

$$\frac{d^2 \phi}{dx^2} = 2\phi(\phi^2 + \psi^2 - 1), \quad (1.66)$$

$$\frac{d^2 \psi}{dx^2} = 2\psi(\phi^2 + \psi^2 + \frac{1}{2}\sigma^2 - 1), \quad (1.67)$$

y la densidad de energía de una configuración determinada por  $\Psi(x) = (\phi(x), \psi(x))$  es

$$\varepsilon = \frac{1}{2} \left( \frac{d\phi}{dx} \right)^2 + \frac{1}{2} \left( \frac{d\psi}{dx} \right)^2 + \frac{1}{2}(\phi^2 + \psi^2 - 1)^2 + \frac{1}{2}\sigma^2\psi^2. \quad (1.68)$$

Se puede verificar que las soluciones tipo kink y antikink del modelo  $\phi^4$  están embebidas en el conjunto de soluciones a estas ecuaciones de movimiento para el caso particular en que el campo  $\psi$  desaparece

$$K_1^\pm(x) = \begin{pmatrix} \pm \tanh(x) \\ 0 \end{pmatrix}, \quad (1.69)$$

donde se ha tomado el centro de la solución en  $x_0 = 0$ . Las soluciones tipo kink (1.69) son válidas para cualquier valor del parámetro  $\sigma$ , a pesar de que ese defecto topológico es inestable en el intervalo  $\sigma < 1$  [38]. El estudio de la estabilidad lineal lleva a la ecuación de Schrodinger introducida en (1.60). No existen métodos analíticos generales para encontrar soluciones al espectro de la ecuación de Schrodinger (1.60), pero para la solución estática (1.69) el operador  $H$  tiene la forma

$$H[K_1^\pm(x)] = \begin{pmatrix} -\frac{d^2}{dx^2} + 4 - 6\text{sech}^2(x) & 0 \\ 0 & -\frac{d^2}{dx^2} + \sigma^2 - 2\text{sech}^2(x) \end{pmatrix}, \quad (1.70)$$

que es una matriz diagonal. La ecuación de Schrodinger se reduce a dos problemas espectrales con potenciales de Poschl-Teller independientes entre si,  $U_S^\phi = 4 - 6\text{sech}^2(x)$  y  $U_S^\psi = \sigma^2 - 2\text{sech}^2(x)$ , ver

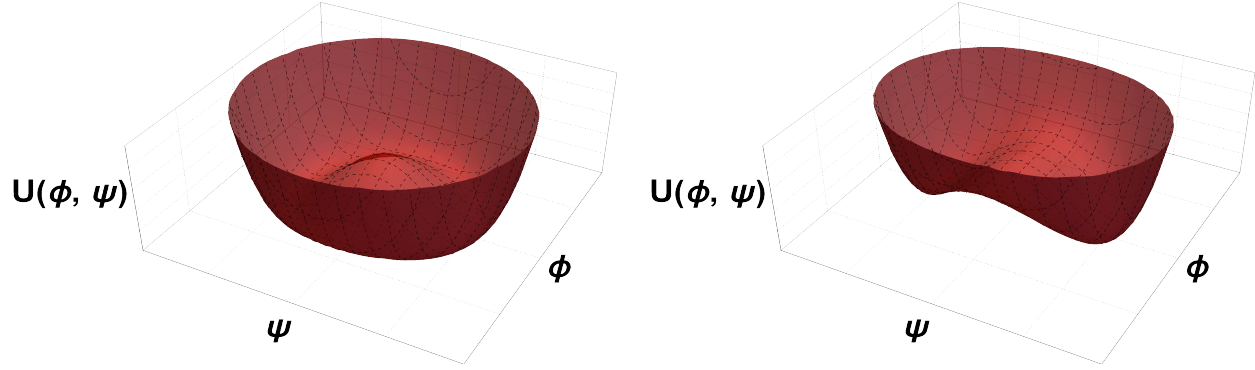


**Figura 1.4:** Gráficos del potencial del modelo MSTB para  $\sigma = 0,5$  (izquierda) y  $\sigma = 1,2$  (derecha).

Figura 1.5.

De forma similar al modelo  $\phi^4$ , el problema espectral tiene asociado los modos normales (1.39), (1.40) y (1.41). Por tanto, para la componente longitudinal a la solución kink (1.69), los modos normales toman la forma

$$\bar{F}_{\bar{\omega}_0^2=0}(x) = \left( \operatorname{sech}^2(x), 0 \right)^T, \quad (1.71)$$

$$\bar{F}_{\bar{\omega}_1^2=\sqrt{3}}(x) = \left( \operatorname{sech}(x) \tanh(x), 0 \right)^T, \quad (1.72)$$

$$\bar{F}_{\bar{\omega}_c^2=\sqrt{4}}(x) = \left( e^{iqx}(-1 - q^2 + 3 \tanh^2(x) - 3iq \tanh(x)), 0 \right)^T. \quad (1.73)$$

El problema espectral asociado al campo ortogonal  $\psi$  tiene un único estado ligado cuyo autovalor asociado es  $\hat{\omega}^2 = \sigma^2 - 1$ . La autofunción correspondiente a este autovalor es

$$\hat{F}_{\hat{\omega}_0^2=\sigma^2-1}(x) = \left( 0, \operatorname{sech}(x) \right)^T. \quad (1.74)$$

El espectro continuo de la fluctuación ortogonal empieza a partir del valor umbral  $\hat{\omega}^2 = \sigma^2 + q^2$ , donde  $q \in \mathbb{R}$ . Las autofunciones del espectro continuo vienen dadas por

$$\hat{F}_{\hat{\omega}_c^2=\sigma^2+q^2}(x) = \left( 0, e^{iqx}(q + i \tanh(x)) \right)^T. \quad (1.75)$$

Se puede visualizar en la Figura 1.5 el espectro del operador de fluctuaciones del canal longitudinal y ortogonal en función de  $\sigma$ . Se puede observar que para  $\sigma < 1$  los autovalores  $\hat{\omega}$  son negativos y por tanto las soluciones estáticas (1.69) son inestables. Por otro lado, para cualquier valor de  $\sigma \geq 1$  estas soluciones estáticas son estables.

En [34] el autor utiliza una transformación de coordenadas que permite reducir el orden de las

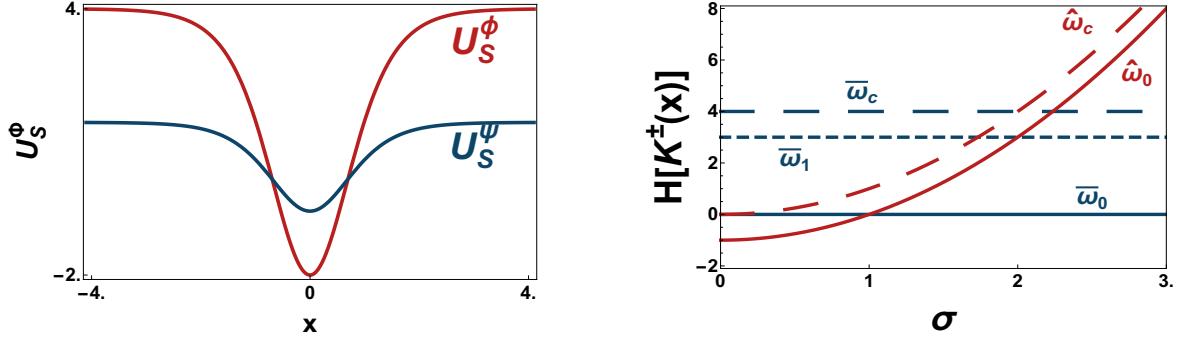


**Figura 1.5:** Gráficos del pozo de potencial del operador de fluctuaciones (1.70) para  $\sigma = 1, 2$  (izquierda) y espectro de fluctuaciones del modelo MSTB para  $\sigma \in [0, 3]$  para los canales longitudinal y ortogonal (derecha).

ecuaciones diferenciales (1.66) y (1.67). Utilizando la transformación de coordenadas elípticas como

$$\phi = \frac{1}{\sigma} uv, \quad (1.76)$$

$$\psi = \pm \frac{1}{\sigma} \sqrt{(u^2 - \sigma^2)(\sigma^2 - v^2)}, \quad (1.77)$$

las dos ecuaciones diferenciales de segundo orden se mapean en cuatro ecuaciones de primer orden

$$\frac{du}{dx} = (-1)^a \frac{u^2 - \sigma^2}{u^2 - v^2} (1 - u^2), \quad (1.78)$$

$$\frac{dv}{dx} = (-1)^b \frac{\sigma^2 - v^2}{u^2 - v^2} (1 - v^2), \quad (1.79)$$

donde  $a, b = 0, 1$  para soluciones tipo kink. Estas ecuaciones de primer orden se obtienen simplemente escribiendo la energía de este modelo en coordenadas elípticas (1.76) y (1.77) y reorganizando los términos según el procedimiento de Bogomolnyi. Considerando la solución  $u = 1$  de (1.78) en el régimen  $\sigma \in (0, 1)$ , la ecuación diferencial para la variable  $v$  se reduce a

$$\frac{dv}{dx} = (-1)^b (\sigma^2 - v^2), \quad (1.80)$$

que lleva a la solución  $v = (-1)^b \sigma \tanh[\sigma(x - x_0)]$ . Volviendo a las coordenadas cartesianas por la transformación de coordenadas (1.76) y (1.77) se obtiene las soluciones

$$\phi(x) = \pm \tanh(\sigma x), \quad (1.81)$$

$$\psi(x) = \pm \sqrt{1 - \sigma^2} \operatorname{sech}(\sigma x). \quad (1.82)$$

Entonces, la solución del campo es ahora dada por

$$K_2^\pm(x) = (\pm \tanh(\sigma x), \pm \sqrt{1 - \sigma^2} \operatorname{sech}(\sigma x))^T, \quad (1.83)$$

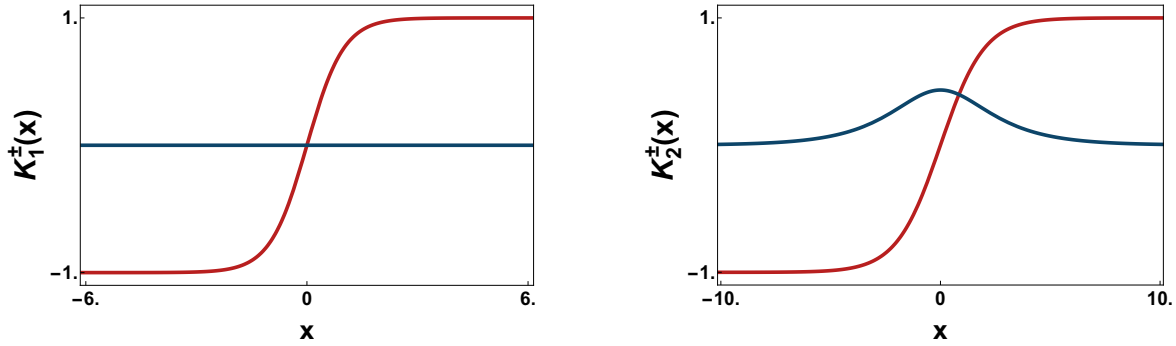


**Figura 1.6:** Gráficos de las soluciones del campo  $K_1^\pm(x)$  (izquierda) y  $K_2^\pm(x)$  (derecha) para el parámetro  $\sigma = 0,5$ .

ver Figura 1.6. Para esta solución, el operador de fluctuaciones toma la forma

$$H = \begin{pmatrix} -\frac{d^2}{dx^2} + 4 - 2(2 + \sigma^2)\text{sech}^2(\sigma x) & 4\sqrt{1 - \sigma^2}\text{sech}(\sigma x) \tanh(\sigma x) \\ 4\sqrt{1 - \sigma^2}\text{sech}(\sigma x) \tanh(\sigma x) & -\frac{d^2}{dx^2} + \sigma^2 + 2(2 - 3\sigma^2)\text{sech}^2(\sigma x) \end{pmatrix}. \quad (1.84)$$

El análisis espectral de dicho operador es analíticamente no abordable. No obstante, el análisis numérico indica que el problema espectral no presenta autovalores negativos de modo que la estabilidad lineal de esta solución se verifica [38]. El modo cero mencionado previamente es ahora

$$F^0(x) = (\bar{F}_{\omega_0^2}, \hat{F}_{\omega_0^2})^T = (\text{sech}^2(\sigma x), \pm\sigma\text{sech}(\sigma x) \tanh(\sigma x))^T. \quad (1.85)$$

También existe una familia de kinks no topológicos los cuales son inestables. No discutimos esas soluciones aquí dado que no son usados en los desarrollos futuros de la tesis, pero puede encontrarse su descripción en [34].

## 1.5. Colisiones entre kinks

En esta sección trataremos el scattering entre kinks, esto es, analizaremos eventos en los que estas soluciones son obligadas a viajar en una trayectoria de colisión entre ellas. Tras los procesos de colisión una gran variedad de fenómenos ha sido observado, entre las cuales podemos destacar aniquilación de soluciones, repulsión entre kinks, ventanas de resonancia, así como excitación de sus estados normales [23, 33, 40]. A pesar de que los eventos de colisiones entre defectos topológicos es de difícil tratamiento, una gran cantidad de simulaciones numéricas publicadas en la literatura proporcionan información que ayudan a entender estos fenómenos.

Antes de abordar la colisión entre kinks estudiaremos la fuerza de interacción entre ellos desde una perspectiva analítica. Como configuración inicial en este estudio tomaremos una superposición compuesta por un kink y un antikink del modelo  $\phi^4$  inicialmente en reposo, respectivamente, centrados en las posiciones  $x_0 = -L$  y  $x_0 = L$  y que podemos caracterizar por la expresión

$$\Phi(0, x) = \phi_K(x + L) + \phi_{\bar{K}}(x - L) - 1, \quad (1.86)$$

donde  $\phi_K(x + L)$  y  $\phi_{\bar{K}}(x - L)$  denotan las soluciones del tipo kink y antikink centradas en  $-L$  y  $L$ , respectivamente, vistas previamente. El término  $-1$  en (1.86) garantiza que  $\Phi(0, x)$  está bien definida, porque cuando  $x \rightarrow \pm\infty$  los campos tienden de manera asintótica al vacío. La fuerza que actúa sobre las configuraciones es la derivada temporal del momento lineal. Este se identifica con la componente  $01$  del tensor energía-momento (1.9), i.e.  $P = -T^{01} = \dot{\phi}\phi'$ . Entonces,

$$F = \dot{P} = - \int_{x_a}^{x_b} dx (\ddot{\phi}\phi' + \dot{\phi}\phi''). \quad (1.87)$$

La fuerza que actúa sobre el kink es caracterizada por los contornos  $x_a = -\infty$  y  $x_b = b$ . El campo en  $x = -\infty$  está en el estado de vacío y por tanto no contribuye a la fuerza. De las ecuaciones de movimiento,  $\ddot{\phi} = \phi'' - V(\phi)$  se obtiene

$$F = - \int_{-\infty}^b dx \left[ \phi''\phi' - \frac{dV}{d\phi}\phi' + \dot{\phi}\phi'' \right]. \quad (1.88)$$

que resulta en

$$F = - \left[ \frac{1}{2}\dot{\phi}^2 + \frac{1}{2}\phi'^2 - V(\phi) \right]_{-\infty}^b, \quad (1.89)$$

donde se ha considerado un punto en el intervalo entre el kink y el antikink  $-L \ll b \ll L$ . Dado que el antikink  $\phi_{\bar{K}}$  centrado en  $x = -L$  es el antisimétrico del kink  $\phi_K$  esta expresión también es válida en el otro extremo del intervalo. De esa manera, expandiendo el potencial hasta primer orden en torno al kink  $V(\phi) \approx V(\phi_K) + (1 + \phi_{\bar{K}})\frac{dV}{d\phi}(\phi_K)$  se puede reescribir la fuerza como [1]

$$F = \left[ -\frac{1}{2}\phi_{\bar{K}}'^2 + V(\phi_K) - \phi_K'\phi_{\bar{K}}' + (1 + \phi_{\bar{K}})\frac{dV}{d\phi}(\phi_K) \right]_{-\infty}^b. \quad (1.90)$$

Con la ecuación de segundo orden para el caso estático  $\phi'' = V_\phi$  y dado que para el modelo  $\phi^4$  es válida la ecuación de primer orden (1.14) la expresión anterior se reduce a

$$F = \left[ -\phi_K'\phi_{\bar{K}}' + (1 + \phi_{\bar{K}})\phi_K'' \right]_{-\infty}^b. \quad (1.91)$$

Utilizando las soluciones aproximadas  $\phi_K \simeq 1 - 2e^{-2(x+L)}$  y  $\phi_{\bar{K}} \simeq 1 - 2e^{2(x-L)}$  para la cola asintótica del kink nos lleva a la expresión

$$F = 32e^{-4L}. \quad (1.92)$$

Vale la pena mencionar que la fuerza es positiva en el kink situado en la posición  $x = -L$ . Por tanto, la fuerza entre el kink y antikink del modelo  $\phi^4$  es atractiva y disminuye exponencialmente con la distancia entre los centros de los defectos  $2L$ . De hecho, en una configuración kink y antikink

como en la Figura 1.7 para una distancia de separación finita se espera que las soluciones choquen para un tiempo suficientemente alto.

En los eventos de colisiones entre defectos topológicos es importante tener en cuenta la propiedad de integrabilidad de los sistemas físicos en los cuales las soluciones tipo defecto pertenecen. En modelos integrables, como el modelo seno-Gordon, las soluciones chocan una única vez y se reflejan con un desfase en sus velocidades. En estos modelos la dinámica de las soluciones está restringida por infinitas magnitudes conservadas, lo que no permite la transferencia de energía entre los modos normales de las soluciones. Por otro lado, en los modelos no integrables, como el modelo  $\phi^4$ , las soluciones pueden rebotar indefinidamente, reflejarse o rebotar un número finito de veces antes de que se aparten. Al contrario de los modelos integrables, el mecanismo de transferencia de energía entre los modos normales se produce en cada rebote para esta clase de modelos. Varias investigaciones han demostrado una gran variedad de comportamientos en las colisiones entre kink y antikink para modelos no integrables [22, 24–41]. Por tratarse de modelos con sistemas de ecuaciones diferenciales altamente no lineales, en estas referencias los autores han utilizado algoritmos específicos que simulan la evolución de las soluciones en estas ecuaciones.

### 1.5.1. Simulaciones numéricas

En esta sección describiremos las simulaciones numéricas y los resultados que motivaron la investigación de scattering con configuraciones iniciales simétricas y asimétricas entre kinks excitados del modelo  $\phi^4$ , así como la investigación de interacciones entre modos normales en la teoría de dos campos conocida como modelo MSTB. En las simulaciones numéricas presentes en esta tesis han sido utilizados diferentes métodos numéricos, entre ellos un método de diferencias finitas de segundo orden conservativo (la energía asociada al método numérico se mantiene constante en la simulación numérica). Este método es implícito aunque las ecuaciones no lineales puedan ser analíticamente

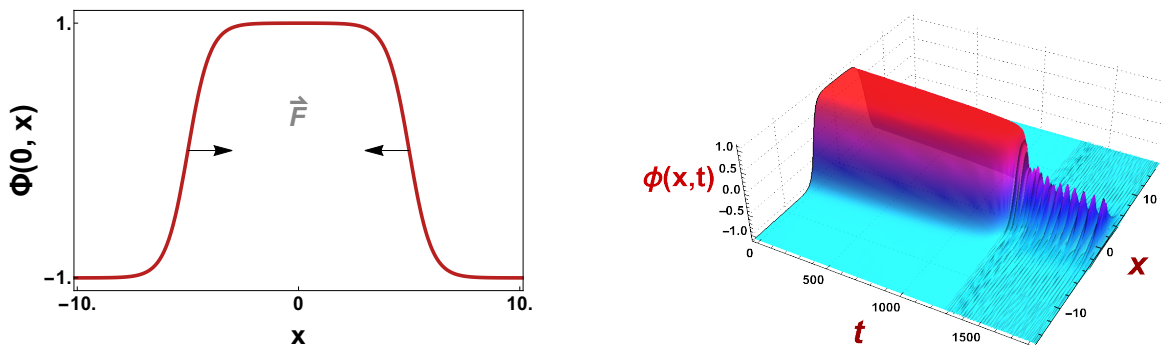


**Figura 1.7:** Representación gráfica ilustrando la atracción mutua ejercida en una configuración kink y antikink con velocidad inicial nula y separados por una distancia  $2L$  (izquierda) y colisión entre kink y antikink de modelo  $\phi^4$  localizados en  $x_0 = -5$  y  $x_0 = 5$ , respectivamente, con velocidad inicial  $v_0 \approx 0$  (derecha).

tratadas para acelerar el algoritmo en el caso del modelo  $\phi^4$ . Otro método usado corresponde a una discretización por diferencias finitas de cuarto orden (tanto en el espacio como en el tiempo) [56]. En todos los algoritmos se ha utilizado las condiciones de contorno de Mur. De esta manera, los efectos de la radiación no retornan al centro, porque las ondas planas son absorbidas en las fronteras de la malla.

La configuración inicial adoptada para las simulaciones de colisiones entre kinks del modelo  $\phi^4$  es conformada por la concatenación

$$\phi_K^{(\pm)}(t_0, -x_0, v_0; x) \cup \phi_K^{(\mp)}(t_0, x_0, -v_0; x), \quad (1.93)$$

donde se ha utilizado la notación

$$\phi_K^{(\pm)}(t_0, -x_0, v_0; x) \cup \phi_K^{(\mp)}(t_0, x_0, -v_0; x) \equiv \begin{cases} \text{si } x < 0, & \phi_K^{(\pm)}(t_0, -x_0, v_0; x), \\ \text{si } x \geq 0, & \phi_K^{(\mp)}(t_0, x_0, -v_0; x). \end{cases} \quad (1.94)$$

La solución  $\phi_K^{(\pm)}$  utilizada en (1.94) es la solución tipo kink estático del modelo  $\phi^4$  (1.35) impulsado por un *boost* de Lorentz como en

$$\phi_K^{(\pm)}(x_0, v_0; x, t) = \pm \tanh \left[ \frac{x - x_0 - v_0 t}{\sqrt{1 - v_0^2}} \right]. \quad (1.95)$$

Por simplicidad se ha tomado el centro de referencia en  $x = 0$  y los centros de las soluciones en las posiciones  $x = \pm x_0$ . Inicialmente los centros de los kinks se encuentran separados por una distancia  $d = 2x_0$  y se mueven con una velocidad inicial  $v_0$ . Esta es la velocidad del centro de la solución con respecto al centro de separación entre ambas soluciones. De hecho, la solución situada a la izquierda del centro de referencia tiene velocidad positiva y la situada a la derecha tiene velocidad negativa. Es importante destacar que la solución (1.94) satisface la ecuación de movimiento de segundo orden para  $x_0 \gg 0$ .

Las simulaciones numéricas fueron llevadas a cabo en el supercomputador Caléndula situado en el centro de supercomputación de Castilla y León (SCAYLE). La capacidad de procesamiento del Caléndula ha permitido reproducir el algoritmo para el rango de velocidades  $v_0 \in [0,1; 0,9]$  con saltos de velocidad  $\Delta v_0 = 0,00001$  dentro del régimen de resonancia y  $\Delta v_0 = 0,001$  en el régimen de reflexión y de estados ligados. Además, en las simulaciones numéricas se ha adoptado un intervalo espacial  $x \in [-100, 100]$  con los centros de las soluciones a una distancia  $d = 60$ .

La evolución de los centros de las soluciones ha sido capturada por el algoritmo, lo que ha permitido identificar las características de los kinks que colisionan, como por ejemplo el número de rebotes que han sufrido, así como la velocidad final en el caso en que las soluciones se apartan después de  $n$ -rebotes. Dada la simetría  $\mathbb{Z}_2$  del modelo, en una configuración simétrica, en que ambas soluciones tienen la misma velocidad y amplitud inicial, el análisis del proceso de scattering puede ser realizado sobre un único kink. Debido a la interacción entre los modos normales del kink se

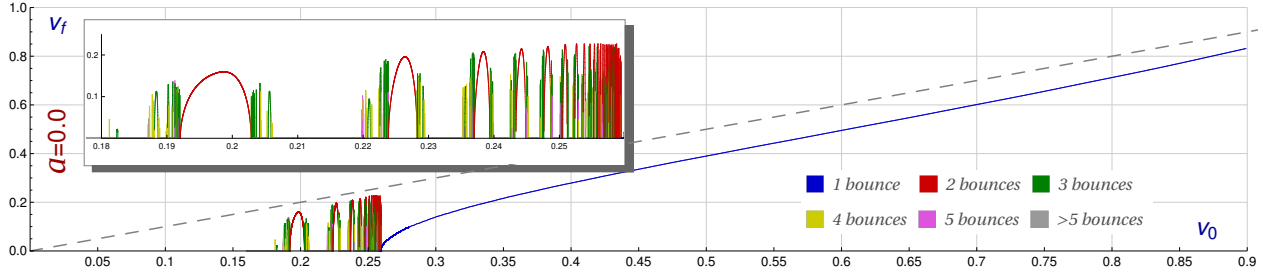


**Figura 1.8:** Diagrama de velocidad final versus velocidad inicial en el proceso de scattering entre el kink y el antikink del modelo  $\phi^4$ . Los colores identifican el número de rebotes que han sufrido las soluciones antes de que se alejen. La línea discontinua en gris representa la velocidad final sin la transferencia de energía entre modos vibracionales y el proceso es elástico. El régimen de resonancia está destacado en la parte superior izquierda. Figura tomada de [23].

espera una redistribución de energía entre los modos traslacional y vibracional. Debido a esto, la frecuencia de vibración y la correspondiente amplitud también fueron obtenidas numéricamente en cada punto de la evolución de las soluciones comparando el resultado numérico con el perfil de la solución no excitada. El punto de máxima desviación del kink excitado cuando es comparado con el kink no excitado puede ser obtenido analíticamente y ocurre en

$$x_M^{(\pm)} = \pm \operatorname{arccosh}(\sqrt{2}), \quad (1.96)$$

de modo que las simulaciones monitorizan la amplitud del modo vibracional en este punto dado que permite una mayor precisión en su estimación.

El resultado de la simulación de colisiones entre un kink y un antikink en el modelo puede ser visualizado en la Figura 1.8. En ella es posible observar la intrincada relación que existe entre la velocidad final y la velocidad inicial de colisión. En el diagrama de velocidades se observa dos regímenes de colisión: (1) estados ligados, llamados bion, que se forman para velocidades de colisión suficientemente bajas en los que los kinks después de la primera colisión no logran escapar de la fuerza atractiva que existe entre ellos y vuelven a colisionar indefinidamente, emitiendo radiación en cada nuevo rebote y (2) reflexión de kinks que aparece para velocidades suficientemente altas en que los kinks se apartan después del primer rebote con una velocidad final menor que la velocidad inicial. Es importante destacar que entre estos dos regímenes existe una secuencia de ventanas de  $n$ -rebotes que sigue una estructura fractal en que las soluciones rebotan un número finito de veces antes de que se reflejen con un velocidad final menor que la velocidad inicial.

El número de rebotes que sufren las soluciones sigue un patrón definido conforme la velocidad de colisión aumenta. Se puede verificar en el cuadro destacado en la Figura 1.8 que ventanas de 2 rebotes (dibujadas en rojo) están rodeadas por ventanas de 3 rebotes (marcadas en verde), estas a su vez están rodeadas por ventanas de 4 rebotes (dibujadas en amarillo) y así sucesivamente. Ese patrón se repite indefinidamente con ventanas más estrechas a medida que la velocidad inicial aumenta. El código de colores utilizado en la Figura 1.8 permite identificar dicho patrón.

La estructura fractal observada en el régimen de resonancia encuentra su explicación en el me-



canismo de transferencia de energía entre los modos normales de los kinks (1.39), (1.40) y (1.41). Los kinks se aproximan inicialmente con una energía cinética almacenada en el modo traslacional (1.39) y en la colisión parte de esta energía es transferida al modo vibracional (1.40) por el mecanismo de transferencia de energía resonante. Esto da lugar a soluciones vibracionalmente excitadas tras el primer rebote. Consecuentemente, en un proceso de  $n$ -rebotes ocurren  $(n - 1)$ -rebotes entre kinks vibrantes. Si tras el primer impacto las soluciones no tienen suficiente energía cinética para escapar la barrera atractiva, estas vuelven a colisionar dando lugar a una nueva redistribución de energía entre los modos normales. Esta situación vuelve a darse un número finito de veces dentro del régimen de resonancia hasta que las soluciones escapen con una velocidad final  $v_f$ . Este mecanismo de transferencia de energía resonante es un proceso universal y también ha sido encontrado en la dinámica de kinks de otros modelos de campos escalares como el modelo seno-Gordon modificado [22, 30–32, 42], y otros modelos de una y dos componentes [23, 25–29, 33–37, 40–43].

La excitación del modo vibracional ocasionada por el mecanismo de transferencia de energía también demuestra una intrincada correlación con la velocidad de colisión. En la Figura 1.9 se puede visualizar la amplitud final de vibración de las soluciones en función de la velocidad inicial  $v_0$ . En este gráfico es posible verificar que a partir del régimen de resonancia las soluciones presentan una amplitud final de vibración diferente de cero.

Es importante destacar que en la cola de reflexión (dibujada en azul en la Figura 1.9) la amplitud crece linealmente con la velocidad de colisión. Se ha demostrado que esta dependencia lineal de la amplitud final es independiente de la excitación inicial de los kinks [23]. La dependencia de la amplitud final de las soluciones dispersadas con respecto a la velocidad de colisión es dada aproximadamente por

$$a(v_0) = 0,084 + 0,34v_0. \quad (1.97)$$

Esta es una propiedad que resulta relevante para comprender el mecanismo de transferencia de energía una vez que las ventanas de  $n$ -rebotes pueden entenderse por la aplicación sucesiva del mecanismo de redistribución de energía. Por otro lado, en el régimen de resonancia vale la pena observar que en el pico de una ventana de  $n$ -rebotes, que es el punto en que los kinks se apartan con mayor velocidad final, las soluciones dispersadas presentan menor amplitud de vibración, lo que caracteriza una redistribución de energía entre los modos normales del kink. Dicho de otro modo, el punto en el que las soluciones se apartan con mayor velocidad es el punto en el que las soluciones presentan menor amplitud final de vibración. También ocurre lo contrario, para aquellas velocidades iniciales en el régimen de resonancia en las que la velocidad de escape es pequeña implicarán que su vibración interna será muy grande.

Debido a las propiedades mencionadas anteriormente se hace relevante investigar la dinámica de kinks excitados. Este estudio arroja luz sobre el fenómeno de transferencia de energía resonante una vez la amplitud de excitación final de los kinks depende directamente de la velocidad inicial de colisión. En este sentido los trabajos publicados que conforman esta tesis doctoral investigan

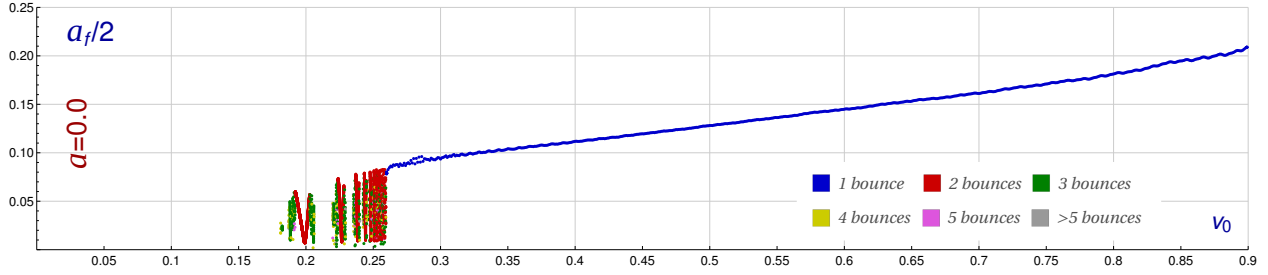


**Figura 1.9:** Diagrama de amplitud final versus velocidad inicial en el proceso de scattering entre el kink y el antikink del modelo  $\phi^4$ . Los colores identifican el número de rebotes que han sufrido las soluciones antes de que se alejen. Figura tomada de [23].

numéricamente colisiones entre kinks del modelo  $\phi^4$  vibracionalmente excitados en una variedad de escenarios. También se estudia la transferencia de energía entre modos normales en un modelo de dos campos, lo que permite estudiar este mecanismo en marcos más generales.

## 1.6. Contribución de los artículos presentados

En esta sección discutiremos las principales aportaciones de los artículos que componen esta tesis. Cada uno de los trabajos publicados se correlaciona con los demás, todos los cuales giran en torno al análisis del modo o modos vibracionales que se presentan en soluciones de tipo kink y de su interrelación con otros modos normales que pueden originar, como hemos visto, el mecanismo de transferencia de energía resonante, y la presencia de estructuras fractales en los diagramas de scattering.

En el primer artículo se investiga la estructura subyacente asociada a las colisiones simétricas entre kinks excitados del modelo  $\phi^4$ . La dependencia de la estructura fractal encontrada en el régimen de resonancia con respecto a la amplitud de excitación inicial de los kinks vibrantes es analizada.

Sobre el modelo  $\phi^4$ , se investiga en el segundo trabajo los siguientes puntos: (1) la estructura para colisiones asimétricas entre kinks vibrantes con fases opuestas y (2) colisiones entre kinks vibrantes y kinks no excitados. En el primer escenario se destaca el impacto de la diferencia de fase entre los kinks vibrantes y la amplitud inicial de vibración en el régimen de resonancia. En el segundo escenario se destaca el impacto de la amplitud de vibración de un kink excitado en el régimen de resonancia y la amplitud final del antikink no excitado inicialmente.

En el tercer trabajo publicado se investiga la interacción entre modos normales en el modelo de dos campos MSTB. Este modelo tiene la relevancia de que es la generalización natural del modelo  $\phi^4$  en modelos con dos campos, conservando la presencia de dos estados de vacío como en el modelo mencionado. Además, el kink del modelo  $\phi^4$  se encuentra embebido en este modelo más general cuando la componente ortogonal del campo es cero. Esto supone el estudio de los kinks vibracionalmente excitados en un ámbito más complejo, en el que las teorías involucran dos

campos escalares reales altamente acoplados con términos no lineales. Además, mientras que en el modelo  $\phi^4$ , sólo aparece un modo discreto masivo (*shape mode*) en este tipo de modelos pueden aparecer varios, los cuales además pueden estar asociados a fluctuaciones longitudinales (a lo largo de la trayectoria u órbita del kink) u ortogonales (a lo largo de caminos perpendiculares a dicha trayectoria). Por ello, parece pertinente antes de investigar la colisión de kinks multicomponente en estas teorías el estudio de cómo la energía puede pasar entre los distintos modos normales de vibración y afectar al mecanismo de transferencia de energía resonante.

### 1.6.1. Contribución del artículo *Scattering between wobbling kinks*

Como ha quedado claro de las secciones previas, las colisiones entre kinks del modelo  $\phi^4$  muestran una compleja estructura de resonancia, como se puede observar en la Figura 1.8. Los procesos de  $n$ -rebotes son conformados por  $(n - 1)$ -rebotes entre kinks vibrantes debido a la redistribución de energía que ocurre tras la primera colisión. De hecho, en un proceso de 2-rebotes el segundo rebote es un proceso de colisión entre dos kinks vibracionalmente excitados. En esta investigación, estudiaremos de manera directa las colisiones entre kinks vibrantes que nos permitirá comprender desde otra perspectiva la redistribución de energía entre los modos normales por la transferencia de energía resonante. Dada la intrínseca relación entre la velocidad de colisión y la amplitud final de las soluciones dispersadas, en el presente estudio han sido ejecutadas millones de simulaciones numéricas para diferentes valores de la velocidad inicial y de la amplitud inicial de excitación.

En una situación en que los kinks están inicialmente excitados la configuración adoptada para las simulaciones numéricas es dada por

$$\phi_{WK}^{(\pm)}(t, x; -x_0, v_0, \omega, a) \cup \phi_{WK}^{(\mp)}(t, x; x_0, -v_0, \omega, a) \equiv \begin{cases} \text{si } x < 0, & \phi_{WK}^{(\pm)}(t, x; -x_0, v_0, \omega, a), \\ \text{si } x \geq 0, & \phi_{WK}^{(\mp)}(t, x; x_0, -v_0, \omega, a), \end{cases} \quad (1.98)$$

Esta concatenación identifica una configuración compuesta por un kink vibrante, solución  $\phi_{WK}^{(+)}$ , (o antikink vibrante, solución  $\phi_{WK}^{(-)}$ ) a la izquierda y un antikink vibrante  $\phi_{WK}^{(-)}$  (o kink vibrante  $\phi_{WK}^{(+)}$ ) a la derecha. En la expresión anterior  $\phi_{WK}$  representa la solución tipo kink vibracionalmente excitada del modelo  $\phi^4$ , que explicamos abajo. La vibración inicial de la solución estática es dada por la excitación del primer estado excitado  $\psi_{\omega^2=3}(x)$  (1.40) que se encuentra por encima del modo cero  $\psi_{\omega^2=0}(x)$  (1.39). La frecuencia de vibración del kink excitado en (1.98) es la intrínseca del modo vibracional  $\omega_1 = \sqrt{3}$ . La amplitud inicial de excitación de los kinks vibrantes es controlada por el parámetro real  $a$ . Los centros de las soluciones están situados inicialmente en los puntos  $-x_0$  y  $x_0$ . De hecho, la distancia que separa los centros de ambas soluciones es  $d = 2x_0$ . La velocidad inicial con que viajan los centros de las soluciones es  $v_0$ , respecto al centro de la separación entre ambos. Debido a esto la solución excitada a la izquierda del centro de referencia tiene velocidad positiva y la solución excitada a la derecha del centro de referencia tiene velocidad negativa. Por simplicidad

se ha tomado el centro de referencia en  $x = 0$ . La velocidad inicial como es usual será considerada como una de las variables en nuestras simulaciones numéricas para estudiar su influencia en los procesos de scattering.

En una configuración simétrica entre kink y antikink los resultados obtenidos son independientes de la fase inicial de vibración de los kinks. Por lo considerado anteriormente, la solución excitada se obtiene perturbando el estado vibracional  $\psi_{\omega_1^2}$  (1.40) como en

$$\begin{aligned} \phi_{WK}^{(\pm)}(t, x; -x_0, v_0, \omega, a) = & \pm \tanh \left[ \frac{x - x_0 - v_0 t}{\sqrt{1 - v_0^2}} \right] \\ & \pm a \sin(\omega t) \operatorname{sech} \left[ \frac{x - x_0 - v_0 t}{\sqrt{1 - v_0^2}} \right] \tanh \left[ \frac{x - x_0 - v_0 t}{\sqrt{1 - v_0^2}} \right], \end{aligned} \quad (1.99)$$

La solución tipo kink es impulsada por un boost de Lorentz y vibra periódicamente en el tiempo con la frecuencia natural de vibración del primer modo excitado. La amplitud de excitación inicial de la solución es controlada por el parámetro real  $a$ . La novedad en este artículo, además de ser pionera en el estudio de las colisiones entre kinks vibrantes, es que esta amplitud ha sido considerada una variable en las simulaciones lo que nos ha permitido obtener una comprensión más profunda de los mecanismos de transferencia de energía entre los modos normales. Los resultados obtenidos empiezan a ser considerados como una pieza fundamental en las investigaciones recientes, como constata el alto número de citas obtenidas en poco tiempo.

En particular, las simulaciones para colisiones entre kinks excitados simétricos han sido reproducidas para valores de amplitud inicial en el rango  $a \in [0; 0,2]$  con saltos de  $\Delta a = 0,001$  en el rango  $a \in [0; 0,02]$ ,  $\Delta a = 0,01$  en el rango  $a \in (0,02; 0,1]$  y  $\Delta a = 0,1$  en el rango  $a \in (0,1; 0,2]$ . Asimismo, en las simulaciones se ha tomado el rango de velocidades  $v_0 \in [0,02; 0,9]$  con un paso de  $\Delta v_0 = 0,00001$  en el régimen de resonancia y de  $\Delta v_0 = 0,001$  en el resto de casos. De forma aproximada podemos decir que para tratar todas las posibles condiciones iniciales en el rango marcado se ha llevado a cabo más de  $10^6$  de simulaciones entre colisiones de kinks. Para llevar a cabo tal ingente cantidad de ejecuciones ha sido necesario usar el supercomputador Calendula ubicado en SCAYLE (<https://www.scayle.es/>). Esto ha permitido identificar el papel de la amplitud inicial de vibración en el patrón fractal encontrado en el régimen de resonancia.

En los resultados ha sido observado que en el proceso de scattering, parte de la energía almacenada en el modo vibracional es transferido al modo cero de los kinks y vice versa. Los resultados destacan la influencia de la amplitud en la estructura fractal encontrada en el régimen de resonancia que permite entender el mecanismo de transferencia de energía resonante. Debido a la simetría inicial de la configuración la vibración de los kinks presenta una interferencia constructiva en las colisiones lo que da lugar a nuevas ventanas de  $n$ -rebotes en el régimen de resonancia. Esto resulta en una estructura fractal más intrincada conforme la amplitud inicial de vibración aumenta.

El aumento de la complejidad de la estructura fractal dentro del régimen de resonancia ocurre

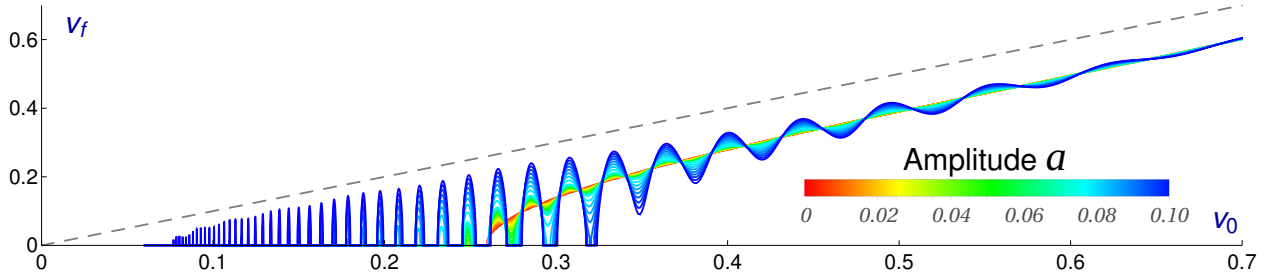


**Figura 1.10:** Diagrama de velocidades con ventanas de 1-rebote para diferentes valores de amplitud inicial  $a_0 \in [0; 0, 1]$ . En este gráfico es posible observar como nuevas ventanas de reflexión son generadas dentro del régimen de resonancia y como la cola de reflexión oscila conforme la amplitud inicial de vibración aumenta. El código de colores ha sido utilizado para mostrar la evolución del gráfico conforme la amplitud inicial de vibración aumenta. Figura tomada de [23].

principalmente por dos mecanismos: (1) la separación de la cola de reflexión y (2) el surgimiento espontáneo de nuevas ventanas de  $n$ -rebotes dentro del régimen de resonancia. El primer escenario ocurre debido a la oscilación de la cola de reflexión conforme la amplitud inicial  $a_0$  aumenta, ver Figura 1.10. Para valores suficientemente altos de la amplitud inicial la cola de reflexión toca el eje  $v_0$  del diagrama de velocidades, creando así una ventana de 1-rebote dentro del régimen de resonancia. Adicionalmente, en la brecha generada entre la ventana de 1-rebote y la cola de reflexión nuevas ventanas de  $n$ -rebotes, para  $n > 1$ , surgen espontáneamente. Este mecanismo también se replica para ventanas de  $n$ -rebotes, las cuales empiezan a oscilar según aumenta la amplitud inicial de vibración y se dividen en ventanas más estrechas, ver Figura 1.11. La brecha generada en la separación de estas ventanas es rellena por ventanas de  $(n + 1)$ -rebotes y así sucesivamente. El segundo mecanismo ocurre debido a la energía vibracional inicial de los kinks, lo que permite que para bajas velocidades las soluciones escapen del potencial atractivo, generando así nuevas ventanas de resonancia. De hecho, conforme la amplitud inicial aumenta nuevas ventanas de  $n$ -rebotes son observadas para cada vez menores velocidades de colisión.

Es importante destacar también que se ha observado que para valores suficientemente altos de la amplitud inicial las soluciones pueden eventualmente alejarse con velocidades mayores que

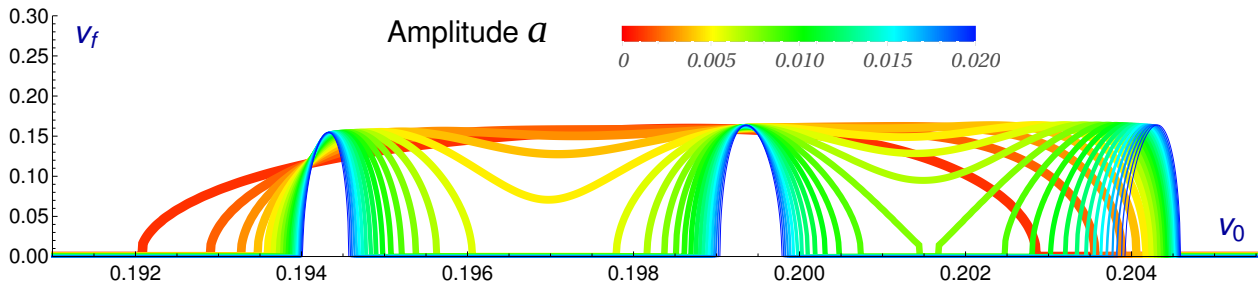


**Figura 1.11:** Diagrama de velocidades para los kinks vibrantes ampliada en el rango de velocidades  $v_0 \in [0, 19; 0, 21]$ . En este gráfico es posible observar cómo ventanas de 2-rebotes se dividen en ventanas más estrechas conforme la amplitud inicial de vibración aumenta. El código de colores ha sido utilizado para mostrar la evolución del gráfico conforme la amplitud inicial de vibración aumenta. Figura tomada de [23].

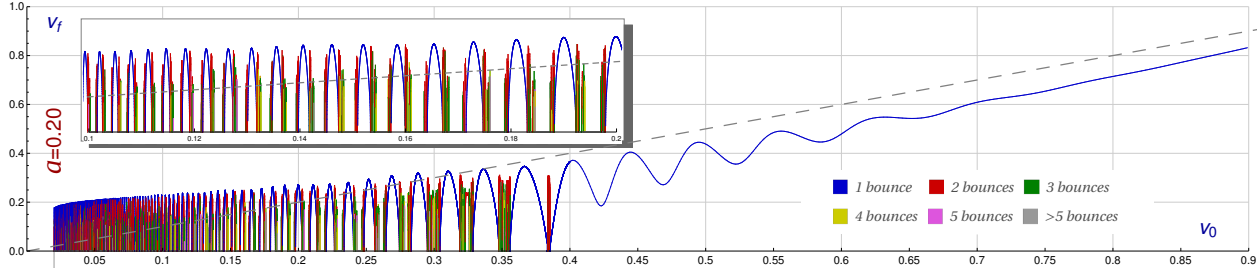


**Figura 1.12:** Diagrama de velocidades para los kinks vibrantes con amplitud inicial  $a_0 = 0,2$ . El código de colores es utilizado para especificar el número de rebotes que sufren las soluciones antes que se alejen con velocidad final  $v_f$ . Figura tomada de [23].

la velocidad de colisión, ver Figura 1.12. Esto sucede para altas amplitudes en un rango de bajas velocidades iniciales. De hecho, se puede concluir que en un proceso de  $n$ -rebotes la última colisión consiste en kinks fuertemente excitados acercándose uno al otro a bajas velocidades.

Los resultados de esta investigación sobre colisiones entre kinks vibracionalmente excitados revela nuevas propiedades en la interacción entre modos normales del modelo  $\phi^4$ . Esto abre nuevas posibilidades para la construcción de una teoría efectiva que pueda describir analíticamente el mecanismo de transferencia de energía entre modos normales. Además, las colisiones entre defectos topológicos vibracionalmente excitados puede ser investigado en otros modelos como el modelo  $\phi^6$  o incluso en modelos no estándar, como los modelos twin. En este sentido otros autores han replicado nuestro estudio en otros modelos como, por ejemplo, el modelo seno-Gordon doble, ver referencia [57].

### 1.6.2. Contribución del artículo *Asymmetric scattering between kinks and wobblers*

Tal y como hemos comentado previamente la estructura fractal encontrada en el diagrama de velocidades en colisiones entre kinks está asociada al mecanismo de transferencia de energía resonante entre el modo vibracional y el modo traslacional de las soluciones. Este mecanismo permite una gran variedad de procesos, entre ellos: formación de *bions*, ventanas de resonancia y reflexión. Esta característica particular en colisiones entre defectos topológicos se presenta en modelos en los cuales la energía puede ser transferida libremente de un modo normal al otro mientras una solución evoluciona.

Como fue mencionado en el trabajo anterior, en una colisión entre kinks del modelo  $\phi^4$  una redistribución de energía entre los modos normales ocurre, lo que da lugar a soluciones vibrantes tras el primer impacto. De hecho, en una ventana de resonancia de  $n$ -rebotes ocurren  $(n - 1)$  colisiones entre kinks vibrantes. De ahí la importancia de investigar los procesos de colisión entre estos objetos. Recientes publicaciones muestran que el método de coordenadas colectivas es una buena aproximación analítica al proceso de colisiones entre kinks. No obstante, a pesar de la extensa

literatura publicada en este tema todavía no hay un método analítico que describa este fenómeno con exactitud. Esta nueva perspectiva que utiliza kinks vibrantes en ruta de colisión en la configuración inicial de las simulaciones numéricas permite investigar diferentes aspectos de este proceso en una diversidad de modelos.

Como continuación directa del trabajo anterior, en este artículo investigamos las colisiones asimétricas entre kinks vibrantes. En el trabajo anterior el kink y antikink que colisionaban tenían idéntica configuración inicial, lo que resultaba en una interferencia constructiva entre los modos vibraciones en el punto de colisión. En el artículo que comentamos en esta sección, se ha investigado las colisiones asimétricas en dos escenarios distintos: (1) entre kinks vibrantes con fases opuestas y (2) entre un kink vibrante y un antikink no excitado. La elección de estos dos casos es evidentemente debida a que describen los casos más extremos, por ejemplo, en el primer artículo los wobblers colisionaban en fase, de modo que se espera que el comportamiento de los kinks vibrantes cuando chocan en contrafase describa la situación más distintiva del caso mencionado antes. Por otra parte, el segundo de los escenarios atiende a las colisiones en que la amplitud del modo vibracional asociado a los kinks que colisionan es la más dispar posible. De hecho, estos dos escenarios han permitido identificar, respectivamente, la interferencia destructiva entre los modos vibracionales debido a la diferencia de fase de los modos vibracionales asociados a las soluciones y la transferencia de energía del modo vibracional del kink al antikink. Las simulaciones numéricas han sido reproducidas para distintos valores de la amplitud inicial, siguiendo el mismo esquema marcado en la sección precedente.

De forma más específica, en esta investigación la configuración inicial está conformada por dos kinks excitados del modelo  $\phi^4$  que vibran con fases opuestas entre si

$$\phi_{WK}^{(\pm)}(t, x; -x_0, v_0, \omega, a, \delta) \cup \phi_{WK}^{(\mp)}(t, x; x_0, -v_0, \omega, a, \delta + \pi) \equiv \begin{cases} \text{si } x < 0, & \phi_{WK}^{(\pm)}(t, x; -x_0, v_0, \omega, a, \delta), \\ \text{si } x \geq 0, & \phi_{WK}^{(\mp)}(t, x; x_0, -v_0, \omega, a, \delta), \end{cases} \quad (1.100)$$

donde la solución excitada proviene de una perturbación del kink a través de una excitación del modo vibracional dada por

$$\begin{aligned} \phi_{WK}^{(\pm)}(t, x; -x_0, v_0, \omega, a, \delta) = & \pm \tanh \left[ \frac{x - x_0 - v_0 t}{\sqrt{1 - v_0^2}} \right] \\ & \pm a \sin(\omega t + \delta) \operatorname{sech} \left[ \frac{x - x_0 - v_0 t}{\sqrt{1 - v_0^2}} \right] \tanh \left[ \frac{x - x_0 - v_0 t}{\sqrt{1 - v_0^2}} \right]. \end{aligned} \quad (1.101)$$

Diferentes elecciones de los parámetros  $a$  y  $\delta$  permiten investigar diferentes procesos de colisiones entre kinks, como por ejemplo, kinks excitados simétricos y asimétricos, así como el scattering entre un kink excitado y un antikink no excitado. La vibración inicial del campo es controlada por un parámetro real  $a$  que determina la amplitud inicial del modo vibracional. La frecuencia de vibración

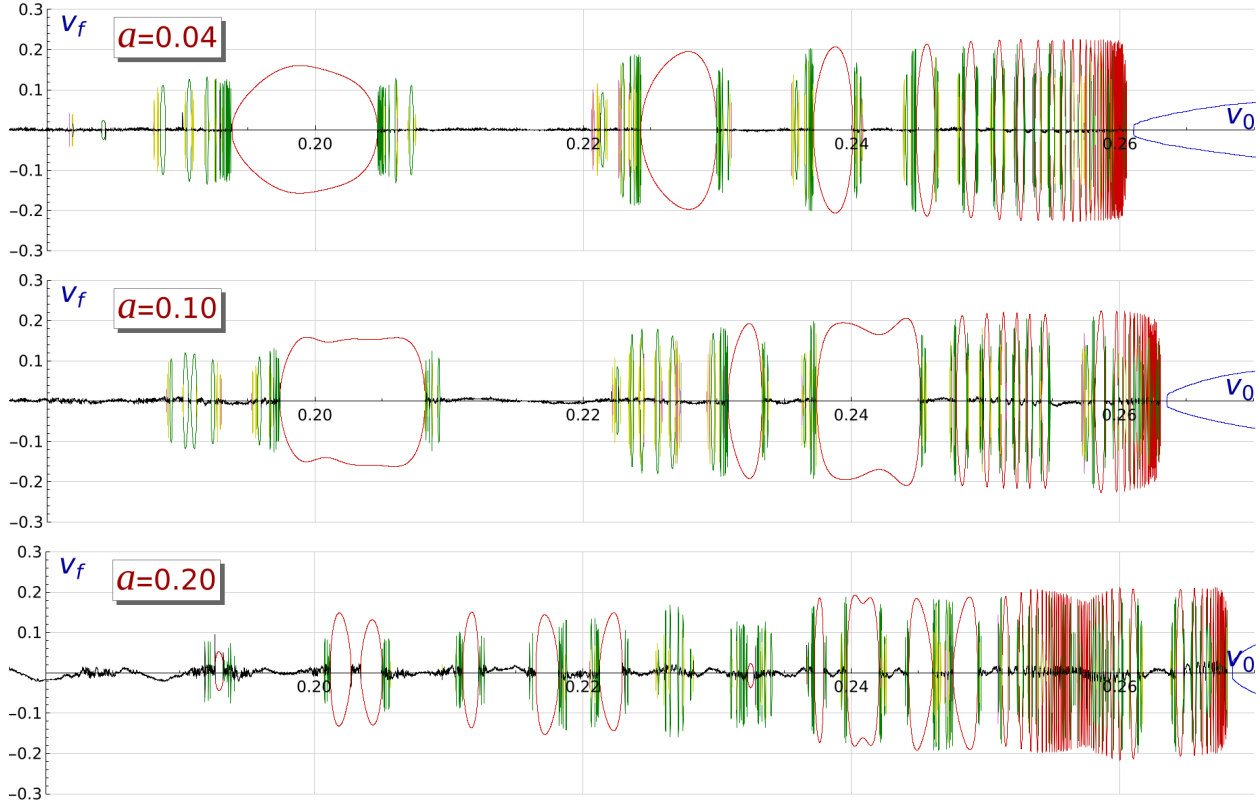


**Figura 1.13:** Diagrama de velocidades para los kinks vibrantes con fases opuestas y con amplitud inicial  $a_0 = 0,04$  (panel superior),  $a_0 = 0,1$  (panel del medio) y  $a_0 = 0,2$  (panel inferior). El código de colores es el mismo utilizado en el trabajo anterior para identificar el número de rebotes que sufren las soluciones antes que se alejen con velocidad final  $v_f$ . Figura tomada de [43].

del kink (1.100) es la frecuencia característica  $\omega_1 = \sqrt{3}$  del primer estado ligado por encima del modo cero. Téngase presente que el modo vibracional oscila periódicamente en el tiempo conforme a la función senoidal. La fase de vibración inicial del kink es determinado por el parámetro real  $\delta$ . Con la finalidad de investigar la máxima diferencia de fase entre las soluciones se ha tomado la fase del antikink, a la derecha del centro de referencia, como  $\delta + \pi$ . Las simulaciones numéricas de colisiones asimétricas entre kinks excitados fueron realizadas para diferentes valores de la amplitud  $a$  y velocidad inicial  $v_0$  tanto para el escenario de scattering entre kinks vibrantes con fases opuestas como para el scattering entre kink vibrante y antikink no excitado, siguiendo elecciones similares a las tomadas en el artículo anterior. De nuevo, el estudio al completo exige la ejecución de más de  $10^6$  simulaciones que han sido ejecutadas en el supercomputador Calendula de SCAYLE.

En ambos escenarios se ha observado los regímenes de formación de bion y de reflexión encontrados en la sección anterior. Entre ambos regímenes se encuentra la estructura fractal que se replica indefinidamente con ventanas más estrechas conforme aumenta la amplitud inicial de los kinks vibrantes. Otra propiedad a destacar es que dado que la configuración inicial es asimétrica, la velocidad final de los kinks resultantes después de la colisión son diferentes. Por esta razón, los diagramas de scattering son dibujados para velocidades positivas y negativas, especificando la



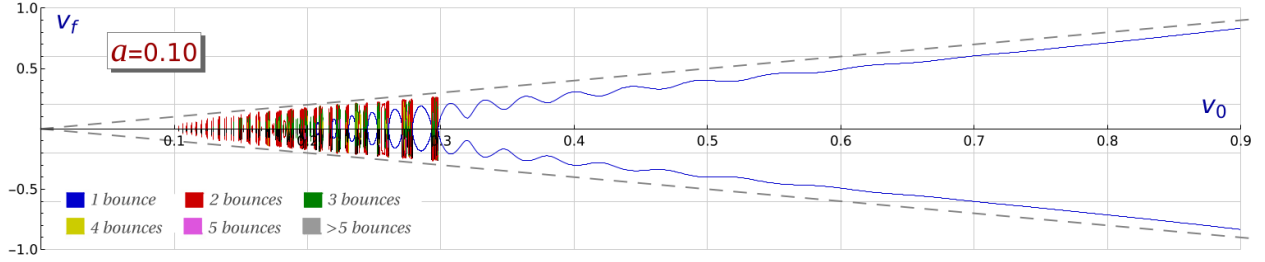


**Figura 1.14:** Diagrama de velocidades para las colisiones entre un kink vibrante con amplitud inicial  $a_0 = 0,1$  y antikink no excitado. El código de colores es el mismo utilizado en el trabajo anterior para identificar el número de rebotes que sufren las soluciones antes que se alejen con velocidad final  $v_f$ . Figura tomada de [43].

solución que viaja a la izquierda y a la derecha, esto también para mostrar las amplitudes finales de las soluciones.

En el primer escenario los resultados numéricos han permitido identificar el impacto de las fases de vibración de los kinks en la eficiencia de la transferencia de energía entre los modos normales, ver Figura 1.13. Se ha identificado una interferencia destructiva entre los modos vibracionales de las soluciones. De hecho, la estructura fractal parece ser menos intrincada que en el caso donde la interferencia constructiva tiene lugar.

Por otro lado, al considerar colisiones entre kinks excitados y no excitados se ha observado la transferencia de energía del modo vibracional a la solución no excitada inicialmente lo que se refleja en resultados similares a los obtenidos en la publicación anterior como, por ejemplo, la formación de ventanas de reflexión dentro del régimen de resonancia, ver Figura 1.14, aunque también presenta propiedades particulares asociadas al escenario estudiado en este caso.

Como hemos mencionado anteriormente, debido a la asimetría de la configuración inicial, las velocidades y amplitudes finales de las soluciones son diferentes. No obstante, en ambos escenarios mencionados anteriormente se ha observado que para un conjunto discreto de velocidades iniciales las velocidades y amplitudes finales son idénticas en ambas soluciones dispersadas. Este conjunto es aproximadamente independiente de la amplitud inicial de vibración. Usando un razonamiento

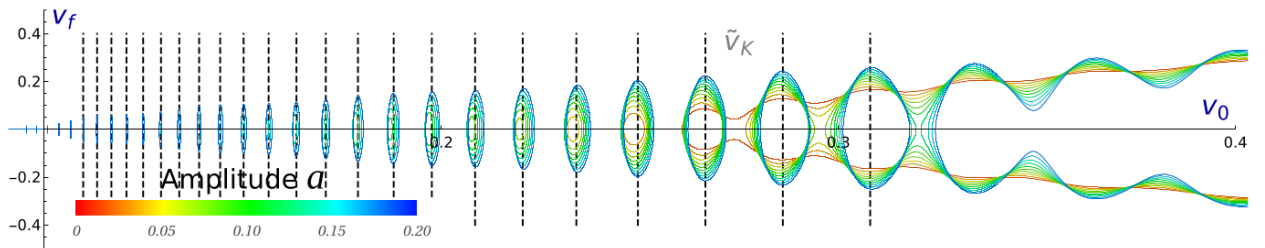


**Figura 1.15:** Diagrama de velocidades para las colisiones entre un kink vibrante y antikink no excitado que destaca el surgimiento de ventanas de 1-rebote dentro del régimen de resonancia en el rango de amplitudes  $a_0 \in [0; 0, 2]$ . Las líneas verticales identifican el conjunto de velocidades  $v_0$  para las cuales la velocidad final es máxima dentro de las ventanas de 1-rebote siguiendo la fórmula (1.102). Figura tomada de [43].

analítico puede demostrarse que los valores de velocidad inicial para los cuales los kinks se alejan con igual velocidad y amplitud final es dada por la expresión

$$f_k(v_0, T) = \frac{v_0 x_0 \omega}{\sqrt{\frac{k^2 T^2 v_0^2}{4c(x_0)^2} - \frac{T}{c(x_0)} k v_0 x_0 \omega \sqrt{1 - v_0^2} + x_0^2 \omega^2}}, \quad k \in \mathbb{Z}, \quad (1.102)$$

donde la constante  $c(x_0)$  es un factor de corrección que depende de la posición inicial del centro de las soluciones y  $T$  es la diferencia de fase entre las soluciones en el punto de colisión. Esta expresión también ha sido empleada para encontrar el conjunto de velocidades finales máximas dentro de las ventanas de reflexión en el scattering entre kinks vibrantes y antikinks no excitados, ver Figura 1.15

### 1.6.3. Contribución del artículo *Wobbling kinks in a two-component scalar field theory: Interaction between shape modes*

La dinámica de los kinks vibrantes desempeña un papel fundamental en el scattering entre soluciones del tipo kink. Esto es debido a la transferencia de energía resonante que genera una redistribución de energía tras cada impacto excitando así el modo vibracional del kink. Por ello, se encuentra en la literatura trabajos que investigan la evolución de estos objetos de manera aislada [58,59]. Para investigar el proceso de scattering entre kinks en teorías de campos multicomponentes es interesante investigar inicialmente la dinámica aislada de este tipo de soluciones. Para ello, se ha tomado el modelo MSTB, una generalización natural del modelo  $\phi^4$  investigado en los artículos precedentes en el contexto de teorías con dos o más campos.

Como hemos visto anteriormente en la Sección 1.4 la solución del tipo kink encontrada en el modelo  $\phi^4$  está embebida en el modelo MSTB y es estable en el rango  $\sigma \in [1, \infty)$ . Por otro lado, el espectro de pequeñas fluctuaciones para  $\sigma \geq 1$  tiene asociado los modos normales (1.39), (1.40) y (1.41) del kink del modelo  $\phi^4$  en la componente longitudinal y un modo vibracional en la componente ortogonal del campo como en

$$\hat{F}_{\sqrt{\sigma^2-1}}(x) = (0, \hat{\eta}_D(x))^t = (0, \text{sech}(x))^t, \quad (1.103)$$

además de los modos del continuo

$$\hat{F}_{\sqrt{\sigma^2+q^2}}(x) = (0, \hat{\eta}_q(x))^t = (0, e^{iqx}(q + i \tanh(x)))^t. \quad (1.104)$$

En este modelo de dos campos estamos interesados en estudiar la evolución de la solución kink cuando el modo vibracional ortogonal es excitado. Uno de los objetivos es conocer si el modo vibracional longitudinal es excitado y si procesos de radiación interfieren en la dinámica de interacción de los modos normales. En este caso, la configuración inicial es dada como

$$\tilde{K}(x, t; a) = \left( \phi_K(x), a \sin(\hat{\omega}t) \hat{\eta}_D(x) \right)^T, \quad (1.105)$$

donde  $\hat{\eta}_D(x)$  es el modo vibracional del campo ortogonal y  $\hat{\omega}$  el correspondiente autovalor, especificado en la ecuación (1.74). Debido a los términos no lineales que aparecen en las ecuaciones de evolución de segundo orden es presumible que los modos de vibración interactúen, y que la solución final esté compuesta por la solución kink en conjunto con perturbaciones procedentes de la excitación de distintos modos normales tanto en el canal longitudinal como en el ortogonal. Es por ello que la ecuación que caracteriza el estado final de la solución kink evolucionando en el tiempo será de la forma

$$\tilde{K}(x, t; a) = K^{(+)} + \sum_{\omega \in \text{Spec} \mathcal{H}} a_\omega \sin(\omega t + \varphi_\omega) F_\omega(x). \quad (1.106)$$

Las simulaciones numéricas son lanzadas con la configuración inicial indicada en (1.105) y se deja evolucionar por un tiempo largo. Para estudiar la excitación de los distintos modos de vibración se estudia la serie temporal obtenida de la diferencia entre la solución numérica y la solución estática (lo que representa la fluctuación del kink) en distintos puntos. Por ejemplo, la oscilación máxima del modo vibracional ortogonal ocurre en  $x_0 = 0$  mientras que el modo vibracional longitudinal lo es en el punto  $x_M$ , con

$$x_M = \pm \text{arccosh}(\sqrt{2}). \quad (1.107)$$

Por otro lado, los modos de radiación son analizados mediante series temporales construidas a partir de datos lejos del origen y cerca de la frontera de la simulación. Para estimar las amplitudes y frecuencias de estas series temporales se emplea un algoritmo de transformada de Fourier discreta.

Las simulaciones numéricas han sido reproducidas para diferentes valores del parámetro real  $\sigma$  y distintos valores de la amplitud inicial de excitación. En una primera aproximación los resultados han demostrado que las frecuencias excitadas son independientes del valor de la amplitud inicial. Por

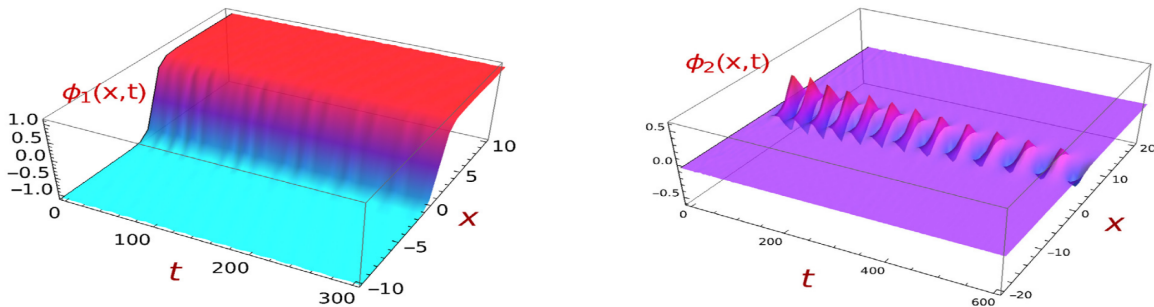


**Figura 1.16:** Representación gráfica de la evolución del campo longitudinal (izquierda) y ortogonal (derecha) con una excitación inicial  $a = 0,6$ . Figura tomada de [38].

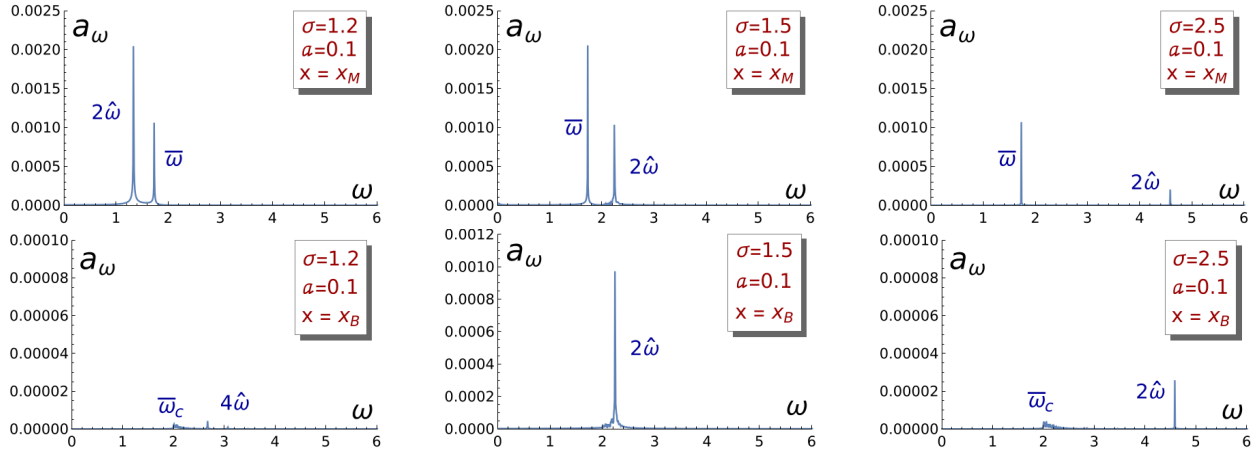


**Figura 1.17:** Distribución espectral de la serie temporal obtenida calculando la componente longitudinal del campo en  $x_M$  (panel superior) y  $x_0$  (panel inferior) con la excitación inicial del campo ortogonal fijada en  $a_0 = 0, 1$ . Esta información se muestra para tres valores representativos de  $\sigma$ :  $\sigma = 1,2$  (izquierda),  $\sigma = 1,5$  (centro),  $\sigma = 2,5$  (derecha). Figura tomada de [38].

ello, se ha tomado el valor fijo de amplitud inicial  $a_0 = 0,1$  como representativo del comportamiento global de estos sistemas.

Se ha podido constatar que la excitación inicial del modo normal ortogonal excita los demás modos de vibración, ver Figura 1.16. También se emite radiación tanto en el canal longitudinal como en el canal ortogonal para algunas frecuencias determinadas. En particular, en el canal longitudinal el wobbling kink emite radiación con una frecuencia igual al doble de la frecuencia asociada al modo vibracional ortogonal mientras que en el canal ortogonal la radiación tiene frecuencia igual a la suma de las frecuencias asociadas a los modos normales de vibración, ver Figuras 1.17 y 1.18. Esto demuestra que la energía puede ser transferida de un modo normal de vibración al otro entre

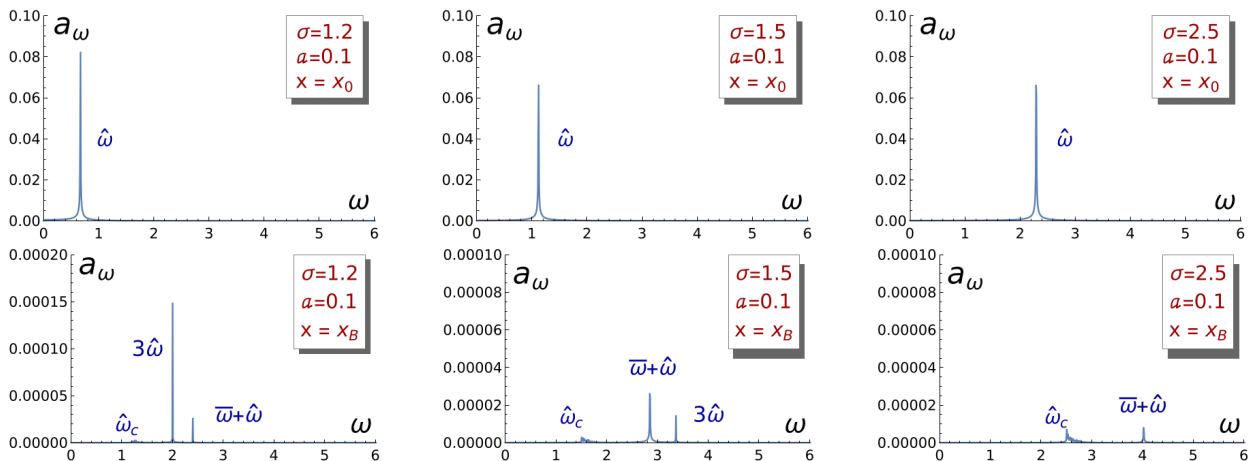


**Figura 1.18:** Distribución espectral de la serie temporal obtenida calculando la componente ortogonal del campo en  $x_M$  (panel superior) y  $x_0$  (panel inferior) con la excitación inicial del campo ortogonal fijada en  $a_0 = 0, 1$ . Esta información se muestra para tres valores representativos de  $\sigma$ :  $\sigma = 1,2$  (izquierda),  $\sigma = 1,5$  (centro),  $\sigma = 2,5$  (derecha). Figura tomada de [38].

las diferentes componentes del campo.

Utilizando teorías de expansión de perturbaciones se ha tratado analíticamente la interacción entre los modos normales para valores de  $\sigma > \sqrt{2}$ . Concretamente se ha utilizado las aproximaciones de Manton y Merabet y las aproximaciones de Barashenkov y Oxtoby. Ambas aproximaciones han presentado resultados similares y los términos no lineales que corresponden a la amplitud de excitación del modo continuo han sido identificados. Los resultados analíticos encontrados en estos desarrollos perturbativos reproducen los resultados numéricos.

## Bibliografía

- [1] Manton, N. y Sutcliffe, P. (2004). *Topological Solitons*. Cambridge: Cambridge University Press.
- [2] Shnir, Y.M. (2018). *Topological and non-topological solitons in scalar field theories*. Cambridge: Cambridge University Press.
- [3] Kevrekidis, P.G. y Cuevas-Maraver, J. (2019). *A Dynamical Perspective on the  $\phi^4$  Model: Past, Present and Future*. Nonlinear systems and complexity, vol. 26. Cham: Springer.
- [4] Rajaraman, R. (1982). *Solitons and Instantons*. Amsterdam: North-Holland.
- [5] Eschenfelder, A.H. (1981). *Magnetic Bubble Technology*. Berlin: Springer-Verlag.
- [6] Jona, F. y Shirane, G. (1993). *Ferroelectric crystals*. New York: Dover.
- [7] Strukov, B.A. y Levanyuk, A.P. (1998). *Ferroelectric phenomena in crystals: physical foundations*. Berlin: Springer-Verlag.
- [8] Vilenkin, A. y Shellard, E.P.S. (1994). *Cosmic strings and other topological defects*. Cambridge: Cambridge University Press.
- [9] Vachaspati, T. (2006). *Kinks and domain walls: an introduction to classical and quantum solitons*. Cambridge: Cambridge University Press.
- [10] Bazeia, D., Losano, L., Rodrigues, J.J., y Rosenfeld, R. (2008). First-order formalism for dark energy and dust. *The European Physical Journal C*, 55, 113-117. <https://doi.org/10.1140/epjc/s10052-008-0566-x>.
- [11] Agrawal, G.P. (1995). *Nonlinear Fiber Optics*. Academic Press, San Diego.
- [12] Schneider, T. (2004). *Nonlinear Optics in Telecommunications*. Springer-Verlag.
- [13] Mollenauer, L. F. y J. P. Gordon. (2006). *Solitons in Optical Fibers: Fundamentals and Applications*. Academic Press, Burlington.
- [14] Davydov, A.S. (1985). *Solitons in molecular systems*. Springer Dordrecht.
- [15] Bazeia, D. y Ventura, E. (1999). Topological twistons in crystalline polyethylene. *Chemical Physics Letters*, 303(3-4), 341-346. [https://doi.org/10.1016/S0009-2614\(99\)00171-2](https://doi.org/10.1016/S0009-2614(99)00171-2).
- [16] Yakushevich, L.V. (1998). *Nonlinear Physics of DNA*. John Wiley & Sons.
- [17] Sugiyama, T. (1979). Kink-Antikink Collisions in the Two-Dimensional  $\phi^4$  Model. *Progress of Theoretical Physics*, 61(5), 1550-1563. <https://doi.org/10.1143/PTP.61.1550>.

- [18] Campbell, D.K., Schonfeld, J.S. y Wingate C.A. (1983). Resonance structure in kink-antikink interactions in  $\phi^4$  theory. *Physica D: Nonlinear Phenomena*, 9(1-2), 1-32. [https://doi.org/10.1016/0167-2789\(83\)90289-0](https://doi.org/10.1016/0167-2789(83)90289-0).
- [19] Anninos, P., Oliveira, S. y Matzner, R.A. (1991). Fractal structure in the scalar  $\lambda(\phi^2 - 1)^2$  theory. *Physical Review D*, 44(4), 1147-1160. <https://doi.org/10.1103/PhysRevD.44.1147>.
- [20] Pereira, C.F.S., Luchini, G., Tassis, T. y Constantinidis, C.P. (2021). Some novel considerations about the collective coordinates approximation for the scattering of  $\phi^4$  kinks. *Journal of Physics A: Mathematical and Theoretical*, 54, 075701. <https://doi.org/10.1088/1751-8121/abd815>.
- [21] Babelon, O., Bernard, D. y Talon, M. (2003). *Introduction to Classical Integrable Systems*. Cambridge University Press.
- [22] Dorey, P., Gorina, A., Perapechka, I. et al. (2021). Resonance structures in kink-antikink collisions in a deformed sine-Gordon model. *J. High Energ. Phys.*, 145(9). [https://doi.org/10.1007/JHEP09\(2021\)145](https://doi.org/10.1007/JHEP09(2021)145).
- [23] Alonso-Izquierdo, A., Nieto, L.M., y Queiroga-Nunes, J. (2021). Scattering between wobbling kinks. *Phys. Rev. D*, 103, (4), 045003. <https://doi.org/10.1103/PhysRevD.103.045003>.
- [24] Simas, F.C., Gomes, A.R., Nobrega, K.Z. et al. (2016). Suppression of two-bounce windows in kink-antikink collisions. *J. High Energ. Phys.* 104. [https://doi.org/10.1007/JHEP09\(2016\)104](https://doi.org/10.1007/JHEP09(2016)104).
- [25] Bazeia, D., Mendonça, T.S., Menezes, R. et al. (2019). Scattering of compactlike structures. *Eur. Phys. J. C*, 79, 1000. <https://doi.org/10.1140/epjc/s10052-019-7519-4>.
- [26] Bazeia, D., Belendryasova, E. y Gani, V.A. (2017). Scattering of kinks in a non-polynomial model. *J. Phys.: Conf. Ser.*, 934, 012032. <https://doi.org/10.1088/1742-6596/934/1/012032>.
- [27] Bazeia, D., Belendryasova, E. y Gani, V.A. (2018). Scattering of kinks of the sinh-deformed  $\phi^4$  model. *Eur. Phys. J. C*, 78, 40. <https://doi.org/10.1140/epjc/s10052-018-5815-z>.
- [28] Bazeia, D., Gomes, A.R., Nobrega, K.Z. y Simas, C. (2019). Kink scattering in hyperbolic models. *International Journal of Modern Physics A*, 34(31), 1950200. <https://doi.org/10.1142/S0217751X19502002>.
- [29] Mohammadi, M. y Dehghani, R. (2021). Kink-antikink collisions in the periodic model. *Commun. Nonlinear Sci. Numer. Simulat.*, 94, 105575. <https://doi.org/10.1016/j.cnsns.2020.105575>.
- [30] Peyrard, M. y Campbell, D.K. (1983). Kink-antikink interactions in a modified sine-Gordon model. *Physica D: Nonlinear Phenomena*, 9(1-2), 33-51. [https://doi.org/10.1016/0167-2789\(83\)90290-7](https://doi.org/10.1016/0167-2789(83)90290-7).

- [31] Campbell, D.K. et al. (1986). Kink-antikink interactions in the double sine-Gordon equation. *Physica D: Nonlinear Phenomena*, 19(2), 160-205. [https://doi.org/10.1016/0167-2789\(86\)90019-9](https://doi.org/10.1016/0167-2789(86)90019-9).
- [32] Gani, V.A. et al. (2018). Scattering of the double sine-Gordon kinks. *Eur. Phys. J. C*, 78, 345. <https://doi.org/10.1140/epjc/s10052-018-5813-1>.
- [33] Alonso-Izquierdo, A. (2018). Reflection, transmutation, annihilation, and resonance in two-component kink collisions. *Phys. Rev. D*, 97, 045016. <https://doi.org/10.1103/PhysRevD.97.045016>.
- [34] Alonso-Izquierdo, A. (2019). Kink dynamics in the MSTB model. *Physica Scripta*, 94(8), 085302. <https://doi.org/10.1088/1402-4896/ab1184>.
- [35] Alonso-Izquierdo, A. (2018). Kink dynamics in a system of two coupled scalar fields in two space-time dimensions. *Physica D: Nonlinear Phenomena*, 365, 12-26. <https://doi.org/10.1016/j.physd.2017.10.006>.
- [36] Alonso-Izquierdo, A. (2019). Asymmetric kink scattering in a two-component scalar field theory model. *Commun. Nonlinear Sci. Numer. Simulat.*, 75, 200-219. <https://doi.org/10.1016/j.cnsns.2019.04.001>.
- [37] Alonso-Izquierdo, A. (2020). Non-topological kink scattering in a two-component scalar field theory model. *Commun. Nonlinear Sci. Numer. Simulat.*, 85, 105251. <https://doi.org/10.1016/j.cnsns.2020.105251>.
- [38] Alonso-Izquierdo, A. et al. (2023). Wobbling kinks in a two-component scalar field theory: Interaction between shape modes. *Physica D: Nonlinear Phenomena*, 443, 133590. <https://doi.org/10.1016/j.physd.2022.133590>.
- [39] Romańczukiewicz, T. (2017). Could the primordial radiation be responsible for vanishing of topological defects? *Physics Letters B*, 773, 295-299. <https://doi.org/10.1016/j.physletb.2017.08.045>.
- [40] Belendryasova, E. y Gani, V.A. (2019). Scattering of the  $\phi^8$  kinks with power-law asymptotics. *Commun. Nonlinear Sci. Numer. Simulat.*, 67, 414-426. <https://doi.org/10.1016/j.cnsns.2018.07.030>.
- [41] Christov, I.A. et al. (2021). Kink-antikink collisions and multi-bounce resonance windows in higher-order field theories. *Commun. Nonlinear Sci. Numer. Simulat.*, 97, 105748. <https://doi.org/10.1016/j.cnsns.2021.105748>.
- [42] Gani, V.A., Moradi-Marjaneh, A. y Saadatmand, D. (2019). Multi-kink scattering in the double sine-Gordon model. *Eur. Phys. J. C*, 79, 620. <https://doi.org/10.1140/epjc/s10052-019-7125-5>.



- [43] Alonso-Izquierdo, A., Nieto, L.M., y Queiroga-Nunes, J. (2022). Asymmetric scattering between kinks and wobblers. *Commun. Nonlinear Sci. Numer. Simulat.*, 102, 106183. <https://doi.org/10.1016/j.cnsns.2021.106183>.
- [44] Prasad, M. K. y Sommerfield, C. M. (1975). Exact Classical Solution for the 't Hooft Monopole and the Julia-Zee Dyon. *Phys. Rev. Lett.* 35, 760. <https://doi.org/10.1103/PhysRevLett.35.760>.
- [45] Bogomol'nyi, E. B (1976). The stability of classical solutions. *Sov. J. Nucl. Phys.* 24(4), 449-454.
- [46] Fradkin, E. (2013). *Field Theories of Condensed Matter Physics*. Cambridge: Cambridge University Press.
- [47] Belmonte-Beitia, J. et al. (2008). Localized Nonlinear Waves in Systems with Time- and Space-Modulated Nonlinearities. *Phys. Rev. Lett.* 100(16), 164102. <https://doi.org/10.1103/PhysRevLett.100.164102>.
- [48] Başar, G. y Dunne, G.V. (2008). Self-Consistent Crystalline Condensate in Chiral Gross-Neveu and Bogoliubov-de Gennes Systems. *Phys. Rev. Lett.* 100(20), 200404. <https://doi.org/10.1103/PhysRevLett.100.200404>.
- [49] Melnikov, D. y Neves, A.B.F. (2019). Chern-Simons-Higgs model as a theory of protein molecules. *Journal of Applied Physics* 126, 244701. <https://doi.org/10.1063/1.5137808>.
- [50] Noether, E. (1918). Invariante Variationsprobleme. *Nachr. d. König. Gesellsch. d. Wiss. zu Göttingen, Math-phys*, 235-257. <https://doi.org/10.48550/arXiv.physics/0503066>.
- [51] Bazeia, D. y Lobao Jr, A.S. (2022). Mechanism to control the internal structure of thick brane. *Eur. Phys. J. C*, 82, 579. <https://doi.org/10.1140/epjc/s10052-022-10546-z>.
- [52] Montonen, C. (1976). On solitons with an Abelian charge in scalar field theories: (I) Classical theory and Bohr-Sommerfeld quantization. *Nuclear Physics B*, 112(2), 349-357. [https://doi.org/10.1016/0550-3213\(76\)90537-X](https://doi.org/10.1016/0550-3213(76)90537-X).
- [53] Sarker, S., Trullinger, S.E. y Bishop, A.R. (1976). Solitary-wave solution for a complex one-dimensional field. *Physics Letters A*, 59(4), 255-258. [https://doi.org/10.1016/0375-9601\(76\)90784-2](https://doi.org/10.1016/0375-9601(76)90784-2).
- [54] Alonso-Izquierdo, A. et al (1998). Kink manifolds in (1+1)-dimensional scalar field theory. *Journal of Physics A: Mathematical and General*, 31(1) 209-229. <https://doi.org/10.1088/0305-4470/31/1/021>.
- [55] Bazeia, D. y Santos, M.M. (1996). Classical stability of solitons in systems of coupled scalar fields. *Physics Letters A*, 217(1), 28-30. [https://doi.org/10.1016/0375-9601\(96\)00305-2](https://doi.org/10.1016/0375-9601(96)00305-2).

- 
- [56] Kassam, A.K. y Trefethen, L.N. (2005). Fourth-Order Time-Stepping for Stiff PDEs. *SIAM Journal on Scientific Computing*, 26(4). <https://doi.org/10.1137/S1064827502410633>.
- [57] Campos, J.G.F y Mohammadi, A. (2021). Wobbling doble sine-Gordon kinks. *J. High Energ. Phys.* 67. [https://doi.org/10.1007/JHEP09\(2021\)067](https://doi.org/10.1007/JHEP09(2021)067).
- [58] Manton, N.S. y Merabet, H. (1997).  $\phi^4$  kinks - gradient flow and dynamics. *Nonlinearity*, 10, 3. <https://doi.org/10.1088/0951-7715/10/1/002>.
- [59] Barashenkov, I.V y Oxtoby, O.F. (2009). Wobbling kinks in  $\phi^4$  theory. *Phys. Rev. E* 80, 026608. <https://doi.org/10.1103/PhysRevE.80.026608>.



# Capítulo 2

---

## Scattering Between Wobbling Kinks

---

### Resumen

En el artículo que se muestra a continuación se investiga numéricamente colisiones entre kinks vibracionalmente excitados del modelo  $\phi^4$  estándar. La dependencia de las velocidades, amplitudes y frecuencias finales de las soluciones es discutida en términos de la velocidad y amplitud inicial de los kinks vibrantes. Se ha observado que la estructura fractal, ya observada en diagrama de scattering del modelo  $\phi^4$ , se vuelve más intrincada conforme la amplitud de vibración inicial aumenta debido a la emergencia de nuevas ventanas de resonancia y la fragmentación de las encontradas en colisiones entre kink y antikink no excitados. Fuera del régimen de resonancia la velocidad final del kink excitado muestra una dependencia lineal con la velocidad de colisión y aproximadamente independiente de la amplitud inicial. Además, para altos valores de la excitación inicial se observa que es posible que las soluciones se aparten con velocidad final mayor que la inicial. Esto sucede para pequeños valores de velocidad de colisión. Esto indica que en todos los eventos de  $n$ -rebotes la última colisión consiste en kinks fuertemente excitados acercándose uno al otro a bajas velocidades.

## Scattering between wobbling kinks

A. Alonso Izquierdo<sup>\*</sup> and J. Queiroga-Nunes<sup>†</sup>

*Departamento de Matematica Aplicada, Universidad de Salamanca,  
Casas del Parque 2, Salamanca 37008, Spain  
and IUFFyM, Universidad de Salamanca, Plaza de la Merced 1, Salamanca 37008, Spain*

L. M. Nieto<sup>‡</sup>

*Departamento de Física Teórica, Atómica y Óptica, Universidad de Valladolid, 47011 Valladolid, Spain  
and Instituto de Matemáticas (IMUVA), Universidad de Valladolid, Valladolid 47011, Spain*



(Received 9 August 2020; accepted 14 January 2021; published 4 February 2021)

In this paper the scattering between a wobbling kink and a wobbling antikink in the standard  $\phi^4$  model is numerically investigated. The dependence of the final velocities, wobbling amplitudes and frequencies of the scattered kinks on the collision velocity and on the initial wobbling amplitude is discussed. The fractal structure becomes more intricate due to the emergence of new resonance windows and the splitting of those arising in the nonexcited kink scattering. Outside this phase the final wobbling amplitude exhibits a linear dependence of the collision velocity, which is almost independent of the initial wobbling amplitude.

DOI: [10.1103/PhysRevD.103.045003](https://doi.org/10.1103/PhysRevD.103.045003)

### I. INTRODUCTION

Over the last 50 years, topological defects have played an essential role in explaining a wide variety of nonlinear phenomena arising in several physical contexts, including condensed matter [1–4], cosmology [5,6], optics [7–9], molecular systems [10,11], biochemistry [12], etc. This broad range of applications underlies the fact that topological defects are solutions of nonlinear partial differential equations, which behave as extended particles in the physical substrate. Solitons and kinks are paradigmatic examples of this type of solutions, which have been profusely studied both in physics and mathematics. They arise, respectively, in the sine-Gordon and  $\phi^4$  field theory models, which are endowed with two opposite properties: integrability versus nonintegrability. Curiously, kink scattering in nonintegrable systems exhibits a richer behavior than the one found for integrable systems. The study of the collision between kinks and antikinks in the  $\phi^4$  model was initially addressed in the seminal references [13–16]. The complex relation between the final velocity  $v_f$  of the scattered kinks and the initial collision velocity  $v_0$  was

displayed in these papers. There exist two different scattering channels: bion formation and kink reflection. In the first case a bound state (called bion) is formed, where kink and antikink collide and bounce back over and over emitting radiation in every impact. In the second case, kink and antikink emerge after the impact and move away with a certain velocity  $v_f$ . If the initial collision velocity  $v_0$  is low enough, a bion is always formed while for large velocities  $v_0$  the kinks are reflected. However, the most striking feature in this scheme is that the transition between the two previously described regimes is characterized by a sequence of initial velocity windows with a fractal structure where the kinks collide several times before definitely escaping, see Fig. 1. The fractal nature displayed by this final velocity versus initial velocity diagram is twofold: (i) the first two-bounce window arises approximately in the range  $v_0 \in [0.1920, 0.2029]$  and it is infinitely replicated by progressively narrower windows up to the beginning of the one-bounce kink reflection regime at (approximately)  $v_0 \approx 0.26$ , see Fig. 1. (ii) Two-bounce windows are surrounded by three-bounce windows, and these ones, in turn, are surrounded by four-bounce windows and so on. Consequently, the previously mentioned diagram displays three clearly differentiated parts: the first one corresponds to zero velocity where the bion state is formed, the second part approximately occurs in the interval  $[0.19, 0.26]$ , where the fractal structure emerges, and the third one refers to the one-bounce kink reflection regime, characterized by a continuous increasing curve starting at zero final velocity, which we shall call the one-bounce tail. Notice that there is no one-bounce windows in the fractal region.

<sup>\*</sup>alonsoiz@usal.es

<sup>†</sup>luismiguel.nieto.calzada@uva.es

<sup>‡</sup>queiroga.nunes@usal.es

*Published by the American Physical Society under the terms of the Creative Commons Attribution 4.0 International license. Further distribution of this work must maintain attribution to the author(s) and the published article's title, journal citation, and DOI. Funded by SCOAP<sup>3</sup>.*

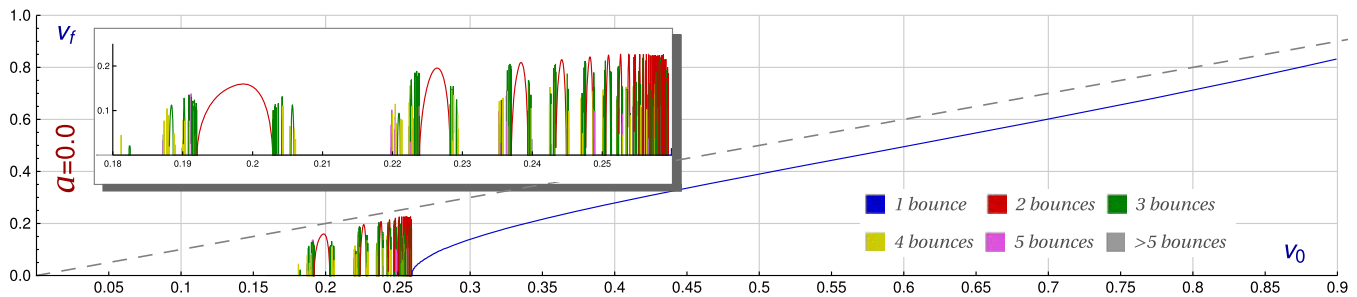


FIG. 1. Final velocity  $v_f$  of the scattered kinks as a function of the initial collision velocity  $v_0$  of the colliding kinks. The final velocity of a bion is assumed to be zero. The color code is used to specify the number of bounces suffered by the kinks before escaping. The resonance window has been enlarged and inserted in the figure.

The presence of the  $n$ -bounce windows can be explained by means of the resonant energy transfer mechanism. As it is well known the second order small kink fluctuation operator involves two discrete eigenfunctions: a zero mode (which generates an infinitesimal translational movement of the kink) and a shape mode (an infinitesimal perturbation associated with the internal vibration of the kink). The presence of these modes is the consequence of two different evolutions: (a) the kink travels with constant velocity and (b) the kink vibrates by changing its size. This last behavior defines the so-called wobbling kink. The previously mentioned mechanism allows an energy exchange between the zero and shape kink modes. For example, a kink and an antikink could approach each other with initial velocity  $v_0$ , collide, and bounce back. The impact could excite the shape mode, which would absorb a part of the kinetic energy. As a consequence, a wobbling kink and a wobbling antikink would emerge after the collision and move away. If the kinetic energy of the resulting kinks was not large enough to make the kinks escape, then they would end up approaching and colliding again. The new impact would cause a redistribution of the energy among the zero and vibrational modes. It is clear that the wobbling kinks play an important role in the fractal structure of the  $n$ -bounce windows. In this sense the present study is important to understand the  $n$ -bounce scattering since after the first collision a wobbling kink and a wobbling antikink emerge with, in general, higher amplitudes than the initial one. A part of the vibrational energy could return to the zero mode making it possible for the kinks to move away and eventually escape. This describes a two-bounce kink scattering event. In general, a  $n$ -bounce event arises when the resulting kinks need to collide  $n$  times before escaping. It is worthwhile to mention that the resonant energy transfer mechanism does not arise for the soliton scattering in the sine-Gordon model. It is assumed that the reason for this is the lack of vibrational (shape) modes in this model. However, this mechanism and other related phenomena are present in a large variety of one-component scalar field theory models, such as in the double sine-Gordon model [17–23], in deformed  $\phi^4$  models [24–33], in  $\phi^6$  models

[34–39], and in other more complex models [40–46]. Kink dynamics has also been analyzed in coupled two-component scalar field theory models, see [47–54]. The effect of impurities, defects, or inhomogeneities on kink dynamics has been discussed in several models, see Refs. [55–68]. The previous description constitutes an heuristic explanation of the resonant energy transfer mechanism, although this phenomenon has revealed to be more complicated than expected. It has been proved that it can be triggered by the discrete eigenfunctions of combined kink configurations when kink and antikink are close enough and also by quasinormal modes [41,69–71]. This complexity turns the search for an analytical explanation of this phenomenon into a very elusive problem. Indeed, the collective coordinate method was initially introduced in [13] to explain the kink dynamics in the  $\phi^4$  model and was used later on to explain the resonant energy transfer mechanism in a satisfactory way. However, the presence of typographical errors in the original paper has been proved [72]. The corrected terms were not sufficient to make the collective coordinate approach fit the data outcome of the scattering process using the harmonic approximation. A recent paper [73] shows that the inclusion of more terms, up to second order, in the effective Lagrangian improves the fit between analytical and simulation data.

Another important topic in this context is the study of the evolution of the wobbling kink in the  $\phi^4$  model. This issue was initially discussed by Getmanov [74], who interpreted the wobbling kink as a bound state of three nonoscillatory kinks. Some perturbation expansion schemes have been employed to explore the properties of the wobbling kinks, see for example [48,60,75–78]. These publications show that the amplitude  $a(t)$  of the wobbling mode at fourth order in the expansion decays. As a consequence the wobbling kink emits radiation. When  $a(0)$  is small, the decay becomes appreciable only after long times  $t \sim |a(0)|^{-2}$ , see [75,76].

In this paper we shall investigate the scattering between wobbling kinks. This analysis is interesting for several reasons. The original kink scattering problem, where the

resonant energy transfer mechanism was initially discovered, involves the collisions of wobbling kinks after the first impact. In other words, a  $n$ -bounce scattering process presumably includes  $n - 1$  wobbling kink collisions. For example, in a two-bounce event the kinks collide and a part of the kinetic energy is transferred to the vibrational mode, such that the second collision is a wobbling kink scattering process. Indeed, this last impact causes the more (at first sight) astonishing phenomenon, the two kinks acquire more velocity than they initially had before colliding. For this reason, the study of the wobbling kink scattering can bring new insight in the original problem, particularly those one-bounce events, where the amplitude and velocity of colliding wobbling kinks can be monitored. This allows us to study the resonant energy transfer mechanism in a more direct way. Obviously, the major part of the results displayed in this paper comes from numerical analysis due to the previously mentioned fact that there are no satisfactory analytical methods to study this problem.

The organization of this paper is as follows: in Sec. II the theoretical background of the  $\phi^4$  model is introduced. The study of the kink and its linear stability leads us to the description of the wobbling kinks. The kink-antikink scattering is also discussed. Section III is devoted to the numerical analysis of the wobbling kink scattering. Here we shall address the scattering between weakly wobbling kinks and the scattering between strongly wobbling kinks in two different subsections. The distinction underlies the fact that the amplitude of the wobbling kinks decreases in the course of time. This effect is small for weakly wobbling kinks. So, we can assume in our numerical experiments that the amplitude of these kinks does not significantly change in the interval in which they are initially approaching before the collision. Finally, some conclusions are drawn in Sec. IV.

## II. THE $\phi^4$ MODEL AND THE KINK-ANTIKINK SCATTERING

The dynamics of the  $\phi^4$  model in  $(1 + 1)$  dimensions is governed by the action

$$S = \int d^2x \mathcal{L}(\partial_\mu \phi, \phi), \quad (1)$$

where the Lagrangian density  $\mathcal{L}(\partial_\mu \phi, \phi)$  is of the form

$$\mathcal{L}(\partial_\mu \phi, \phi) = \frac{1}{2} \partial_\mu \phi \partial^\mu \phi - V(\phi), \quad V(\phi) = \frac{1}{2} (\phi^2 - 1)^2. \quad (2)$$

The use of dimensionless variables and Einstein summation convention is assumed in (1) and (2). The Minkowski metric  $g_{\mu\nu}$  has been chosen as  $g_{00} = -g_{11} = 1$  and

$g_{12} = g_{21} = 0$ . The solutions of this model verify the nonlinear partial differential equation

$$\frac{\partial^2 \phi}{\partial t^2} - \frac{\partial^2 \phi}{\partial x^2} = -\frac{dV}{d\phi} = -2\phi(\phi^2 - 1), \quad (3)$$

which derives from the Euler-Lagrange equations associated with the functional (1). The energy-momentum conservation laws imply that the total energy and momentum

$$E[\phi] = \int dx \left[ \frac{1}{2} \left( \frac{\partial \phi}{\partial t} \right)^2 + \frac{1}{2} \left( \frac{\partial \phi}{\partial x} \right)^2 + V(\phi) \right],$$

$$P[\phi] = - \int dx \frac{\partial \phi}{\partial t} \frac{\partial \phi}{\partial x} \quad (4)$$

are system invariants. The integrand of the total energy  $E[\phi]$

$$\varepsilon[\phi(x)] = \frac{1}{2} \left( \frac{\partial \phi}{\partial t} \right)^2 + \frac{1}{2} \left( \frac{\partial \phi}{\partial x} \right)^2 + V(\phi)$$

is the energy density of a configuration  $\phi(x)$ . Time and space independent solutions of (3) are  $\phi_V = \pm 1$ . Therefore, the set  $\mathcal{M}$  of the vacua in this model is  $\mathcal{M} = \{-1, 1\}$ . Finite energy static solutions of (3) are of the form

$$\phi_K^{(\pm)}(x; x_0) = \pm \tanh(x - x_0), \quad (5)$$

which are called kink/antikink (+/-) and connect the two elements of the set  $\mathcal{M}$ . The kink/antikink energy density  $\varepsilon[\phi_K^{(\pm)}(x; x_0)] = \text{sech}^4(x - x_0)$  is localized around the point  $x = x_0$ , which represents the center of the kink (the value where the field profile vanishes and the energy density is maximal). The Lorentz invariance can be used to construct traveling kinks/antikinks in the form

$$\phi_K^{(\pm)}(t, x; x_0, v_0) = \pm \tanh \left[ \frac{x - x_0 - v_0 t}{\sqrt{1 - v_0^2}} \right]. \quad (6)$$

Obviously, the kink center  $x_C$  for (6) moves in the real line following the expression  $x_C = x_0 + v_0 t$ , such that  $v_0$  is interpreted as the kink velocity.

Now, in order to examine the linear stability of the solution, we consider fluctuations around the static kink/antikink solution (5) by adding a small perturbation as

$$\tilde{\phi}_K^{(\pm)}(t, x; x_0) = \phi_K^{(\pm)}(x; x_0) + \psi(t, x; x_0). \quad (7)$$

Expanding the equation of motion (3) up to first order in  $\psi$  and using the standard separation of variables ansatz,

$$\psi(t, x; x_0) = a e^{i\omega t} \psi_{\omega^2}(x; x_0),$$

results the Schrödinger-like equation

$$\left[-\frac{d^2}{dx^2} + U(x)\right]\psi_{\omega^2}(x; x_0) = \omega^2\psi_{\omega^2}(x; x_0), \quad (8)$$

where

$$U(x) = \frac{d^2V}{d\phi^2}\Big|_{\phi_K^{(\pm)}} = 4 - 6\text{sech}^2(x - x_0).$$

Equation (8) has one zero mode, one excited mode with eigenvalue  $\omega^2 = 3$ , and a continuous spectrum on the threshold value  $\omega^2 = 4$ , whose eigenfunctions are given by

$$\begin{aligned} \psi_{\omega^2=0}(x; x_0) &= \text{sech}^2(x - x_0) = \frac{\partial\phi_K}{\partial x}, \\ \psi_{\omega^2=3}(x; x_0) &= \sinh(x - x_0)\text{sech}^2(x - x_0), \\ \psi_{\omega^2=4+q^2}(x; x_0) &= e^{iq(x-x_0)}[-1 - q^2 + 3\text{tanh}^2(x - x_0) \\ &\quad - 3iq \tanh(x - x_0)]. \end{aligned}$$

The zero mode  $\psi_{\omega^2=0}$  describes an infinitesimal translation of the static kink (5) or, in other words, an infinitesimal evolution of the traveling kink (6). The shape mode  $\psi_{\omega^2=3}(x; x_0)$  describes a vibrational state of the kink/antikink whose width oscillates with frequency  $\omega = \sqrt{3}$ . For small amplitudes  $a$ , a traveling wobbling kink/antikink  $\phi_{\text{WK}}^{(\pm)}$  is described by the expression

$$\begin{aligned} \phi_{\text{WK}}^{(\pm)}(t, x; x_0, v_0, a) &= \pm \tanh\left[\frac{x - x_0 - v_0 t}{\sqrt{1 - v_0^2}}\right] \\ &\quad + a e^{i\omega t} \sinh\left[\frac{x - x_0 - v_0 t}{\sqrt{1 - v_0^2}}\right] \\ &\quad \times \text{sech}^2\left[\frac{x - x_0 - v_0 t}{\sqrt{1 - v_0^2}}\right], \end{aligned} \quad (9)$$

which is a good approximation up to first order. The maximum deviation of the wobbling kink (9) from the kink (6) takes places at the points

$$x_M^{(\pm)} = x_C \pm \sqrt{1 - v_0^2} \text{arccosh}\sqrt{2}, \quad (10)$$

where  $x_C$  is the kink center. The same result applies to the antikink. The deviation at these points is given by half the wobbling amplitude

$$|\phi_{\text{WK}}(x_M^{(\pm)}) - \phi_K(x_M^{(\pm)})| = \frac{1}{2}|a|. \quad (11)$$

We shall analyze the evolution of the kink/antikink at these points to study the excitation of the shape mode in the kink scattering processes. For larger amplitude  $a$  higher order corrections in  $\psi$  need to be taken into account. Then the magnitude  $a$  becomes a function of the time variable.

Indeed, it has been proved that the amplitude  $a(t)$  of the wobbling mode at fourth order in the expansion decays following the expression

$$|a(t)|^2 = \frac{|a(0)|^2}{1 + \omega\xi_I|a(0)|^2 t}, \quad (12)$$

where  $\xi_I$  is a constant and  $\omega = \sqrt{3}$ . When  $a(0)$  is small, the decay becomes appreciable only after a long time  $t \sim |a(0)|^{-2}$ , see [75,76].

The scattering between a kink and an antikink [whose shape eigenfunctions are unexcited, i.e.,  $a = 0$  in (9)] has been thoroughly analyzed in the physical and mathematical literature. In this case, a kink and antikink, which are well separated, are pushed together with initial collision velocity  $v_0$ . Taking into account the spatial reflection symmetry of the system, the kink can be located at the left of the antikink or vice versa. Such an initial configuration at  $t = t_0$  can be characterized by the concatenation

$$\begin{aligned} &\phi_K^{(\pm)}(t_0, x, x_0, v_0) \cup \phi_K^{(\mp)}(t_0, x, -x_0, -v_0) \\ &= \begin{cases} \phi_K^{(\pm)}(t_0, x, x_0, v_0) & \text{if } x < 0 \\ \phi_K^{(\mp)}(t_0, x, -x_0, -v_0) & \text{if } x \geq 0 \end{cases} \end{aligned} \quad (13)$$

for a large enough  $x_0$ . Two different scattering channels have been found in this situation:

- (1) Bion formation: in this case, kink and antikink approach each other, then collide and bounce back. After the impact an exchange of energy from the translational mode to the shape and continuous modes takes place in such a way that the kinetic energy of these two kinks is not big enough to allow them to escape. Therefore, they approach each other again, collide, and bounce back over and over. This is a long living bound kink-antikink state called ‘‘bion.’’
- (2) Kink reflection: now, kink and antikink approach each other, collide, and bounce back. After the impact a redistribution of the energy among the normal modes occurs. After colliding a finite number  $n$  of times, kink and antikink emerge and move away with final velocity  $v_f$ . These processes will be referred to as  $n$ -bounce scattering events.

If we plot the final velocity  $v_f$  of the scattered kinks as a function of the initial collision velocity  $v_0$  we find the diagram displayed in Fig. 1. Here, it is assumed that the final velocity for a bion state is zero. It is clear that the bion formation regime arises for low enough values of the collision velocity  $v_0$ . On the other hand, if  $v_0$  is greater than 0.25988 then kink and antikink reflect each other after colliding once (blue curve in Fig. 1). We will refer to this piece of curve as ‘‘the one-bounce tail.’’ Note that a color code has been used in Fig. 1 to specify the number of



collisions that the kinks suffer before escaping. The convention used in this work is that the zeroes of the evolving configuration determine the presence of kink/antikink solutions. In every collision the two zeroes (which specify the centers of kink and antikink) disappear. Therefore, the number of bounces can be measured by the number of these periods where the evolving solution does not vanish. A surprising fractal pattern turns up in the interval  $[0.18, 0.25988]$ , where the bion formation and kink reflection regimes are interlaced (see enlarged area in Fig. 1).

As previously mentioned, after the first collision in a  $n$ -bounce scattering process the following collisions involve wobbling kinks due to the fact that the first impact usually excites the shape mode of the initially colliding kinks. It is difficult to monitor the velocities and amplitudes of the resulting kinks after the first impact in an  $n$ -bounce event because the period of time between bounces is usually very short. For this reason, it seems reasonable to directly investigate the collision between wobbling kinks. In this situation the velocity and amplitude of the colliding and scattered wobbling kinks can be monitored, at least, in the one-bounce processes. In any case, this type of scattering events can provide us with a lot of information about the resonant energy transfer mechanism.

### III. SCATTERING BETWEEN WOBBLING KINKS

The goal of this paper is to analyze the scattering between wobbling kinks. In order to accomplish this task we shall employ numerical approaches based on the discretization of the partial differential equation (3). The numerical procedure used in this paper corresponds to an energy conservative second-order finite difference algorithm implemented with Mur boundary conditions. The effect of radiation in the simulation is controlled by this algorithm because the linear plane waves are absorbed at the boundaries. As an alternative method to verify the reliability of the previous numerical scheme, the algorithm described in [79] by Kassam and Trefethen has been employed. This scheme is spectral in space and fourth order in time and was designed to solve the numerical instabilities of the exponential time-differencing Runge-Kutta method introduced in [80]. The initial settings for our scattering experiments are described by two initially well separated wobbling kinks which are pushed together with initial collision velocity  $v_0$ . This situation is characterized by the concatenation

$$\begin{aligned} & \phi_{\text{WK}}^{(\pm)}(t_0, x, x_0, v_0, a) \cup \phi_{\text{WK}}^{(\mp)}(t_0, x, -x_0, -v_0, a) \\ &= \begin{cases} \phi_{\text{WK}}^{(\pm)}(t_0, x, x_0, v_0, a) & \text{if } x < 0 \\ \phi_{\text{WK}}^{(\mp)}(t_0, x, -x_0, -v_0, a) & \text{if } x \geq 0 \end{cases}, \end{aligned} \quad (14)$$

where  $x_0$  is large enough and

$$\begin{aligned} & \phi_{\text{WK}}^{(\pm)}(t, x; x_0, v_0, a) \\ &= \pm \tanh\left(\frac{x - x_0 - v_0 t}{\sqrt{1 - v_0^2}}\right) \\ &\quad \pm a \sin(\omega t) \operatorname{sech}\left(\frac{x - x_0 - v_0 t}{\sqrt{1 - v_0^2}}\right) \tanh\left(\frac{x - x_0 - v_0 t}{\sqrt{1 - v_0^2}}\right) \end{aligned} \quad (15)$$

has been chosen to comply with the initial condition  $\phi_{\text{WK}}^{(\pm)}(0, x; x_0, v_0, a) = \phi_{\text{K}}^{(\pm)}(0, x, x_0, v_0)$ . This involves a particular choice of the initial phase in the vibration of the shape mode. It has been checked that this does not alter the global properties discussed in this section. The configuration (14) consists of a wobbling kink/antikink with center  $-x_0$  located at the left side of an wobbling antikink/kink with center  $x_0$ . It is clear that if  $x_0 \gg 0$  and  $a \ll 1$  the partial differential equation (3) is verified by (14) with high accuracy. The initial conditions for our problem can be derived from (14) by simply taking  $t = 0$ , that is,  $\phi(0, x; x_0, v_0, a)$  and  $\frac{\partial \phi}{\partial t}(0, x; x_0, v_0, a)$  define the starting point of the numerical algorithm.

We remark that (15) has been used to construct the initial conditions of our numerical simulations. We will discuss now the range of validity of this procedure. Perturbation theory can be used to obtain approximations of the evolving wobbling kink up to some order in a small parameter  $\epsilon$ . The expression

$$\begin{aligned} & \phi_{\text{WK}}(x, t) \\ &= \tanh x + \epsilon(C \operatorname{sech}^2 x + A e^{i\omega t} \operatorname{sech} x \tanh x) + o(\epsilon^2), \end{aligned} \quad (16)$$

where  $\psi_0 = \operatorname{sech}^2 x$  is the zero mode and  $\psi_\omega = \operatorname{sech} x \tanh x$  is the shape mode of the kink fluctuation operator (8), is an approximation of the traveling wobbling kink up to second order in the parameter  $\epsilon$  [75]. This approximation assumes that two physical magnitudes must be small, the traveling velocity  $v_0$  and the wobble amplitude  $a$ . For example, the expansion of the boosted kink

$$\phi_K(x, t) = \tanh\left(\frac{x - v_0 t}{\sqrt{1 - v_0^2}}\right) \approx \tanh x - t v_0 \operatorname{sech}^2 x + o(v_0^2)$$

reveals that the factor  $\epsilon C$  in (16) must be equal to  $-t v_0$ . This implies that, in general,  $v_0$  must be small. However, the initial conditions in our problem can be determined by the behavior of the solution for  $t \approx 0$ , so the perturbation parameter  $\epsilon C = -t v_0$  is small for all the velocities  $v_0$  in this limit. On the other hand, the expansion of the boosted solution (15)

$$\begin{aligned} & \phi_{\text{WK}}(x, t) \approx \tanh x - t v_0 \operatorname{sech}^2 x \\ &\quad + a \sin(\omega t) \operatorname{sech} x \tanh x + \dots \end{aligned}$$

reproduces formula (16). This means that (9) verifies the equations of motion up to second order in the small parameters  $a$  and  $v_0$ . The expression (9) is a good approximation for small  $a$  and  $v_0$ . In order to check the reliability of the numerical approach for larger initial velocities, the evolution of a single wobbling kink configuration starting with the previous initial conditions has been systematically analyzed by means of numerical simulations. No substantial changes in the evolution of the wobbling solution were detected. It is assumed that the difference between the correct and approximate initial conditions is dissipated by means of a very small radiation emission in a very short period of time at the beginning of the simulation and that this does not affect the later evolution.

The configuration (14) is invariant under a spatial reflection transformation  $x \mapsto -x$ , as it is also the evolution equation (3), so all the scattering processes will preserve this symmetry. This means that we can extract all the scattering information by analyzing the features of only one of the scattered kinks. In particular, our numerical experiments have been carried out in a spatial interval  $x \in [-100, 100]$  where the kink and antikink centers are initially separated by a distance  $d = 2x_0 = 60$ . These kink centers have been monitored during the evolution, as well as the number of bounces suffered by the topological defects. In the kink reflection regime this information is used to work out the final velocity of the scattered kinks by employing a linear regression when the kinks are far enough apart from each other. This scheme has been performed for a range of initial velocities  $v_0$  usually covering the interval  $v_0 \in [0.1, 0.9]$  with initial velocity steps  $\Delta v_0 = 0.001$ , which is decreased to  $\Delta v_0 = 0.00001$  in the resonance range. These data allow us to study the dependence of the separation velocity of the scattered kinks as a function of the collision velocity  $v_0$ , which can be graphically represented by means of diagrams similar to Fig. 1. Once the position and the velocity of the kink centers have been determined, the wobbling amplitude and frequency are also estimated. To do this, the difference between the numerical profile and a nonexcited traveling kink, both of them with the same center  $x_C$  and velocities  $v_f$ , is evaluated at the points  $x_M^\pm$  for every time step in the simulation. The choice of these points underlies the fact that the shape fluctuation has its maximum/minimum values at the points  $x_M^\pm$ . The time series constructed in this way were analyzed by using a fast Fourier transform algorithm.

In order to explore the dependence of the final velocity on the initial wobbling amplitude of the colliding kinks the previously described numerical scheme has been replicated for different values of the amplitude  $a$  considered in the initial configuration. In these numerical experiments we considered only positive values of  $a$ . Negative values of  $a$  are simply related with the positive ones by adding a phase in the argument of the oscillatory factor  $\sin(\omega t)$  in (15). To get a better understanding of the phenomena associated

with this type of scattering processes it is convenient to distinguish two different regimes which depend on the magnitude of the amplitude  $a$ . They are determined as follows:

- (1) Scattering between weakly wobbling kinks: this scenario comprises those scattering processes where the initial amplitude  $a$  of the colliding wobbling kinks is  $|a| < 0.05$ . In these cases the amplitude decay effect is assumed to be negligible such that the wobbling amplitude of the evolving kinks at the time of impact is approximately equal to the initial one. It is clear that this kind of events allows a better control on the variables of the scattering problem. The mechanisms that begin to deform the velocity diagram with respect to the pattern found in Fig. 1 when  $a$  is increased can already be perceived in these cases. These novel behaviors will be discussed in Sec. III A.
- (2) Scattering between strongly wobbling kinks: the more intense phenomena are expected to take place when the wobbling amplitudes of the colliding kinks are relatively large. We assumed that these cases are determined by the condition  $|a| \geq 0.1$ . Now, the amplitude decay suffered by the wobbling kinks in the time period lapsed between the beginning of the simulation and the kink collision [approximately  $d/(2v_0)$ ] could be significant. Therefore, it is difficult to estimate the value of the wobbling amplitude immediately before the impact, which is from our point of view the more significant variable. Despite this fact, this type of events plays an essential role in the resonance mechanism and for this reason it will be discussed in Sec. III B. We shall analyze the dependence of some scattering parameters on the initial wobbling amplitude of our numerical experiments taking into account that the value of the collision amplitude will be smaller than the initial one. Obviously, the higher the initial magnitude is, the higher the collision amplitude is.

### A. Scattering between weakly wobbling kinks

In this section, we shall consider the scattering of kinks whose initial wobbling amplitudes  $a$  are small. As previously mentioned, it is assumed that in these cases the decay of the wobbling amplitude is a residual effect. Thus, the magnitude of the wobbling amplitude of the kinks just before colliding must be approximately equal to the initial one. This first regime of kink scattering has been numerically investigated in the initial wobbling amplitude range  $a \in [0, 0.05]$  taking an amplitude step  $\Delta a = 0.001$  for  $0 \leq a \leq 0.02$  and  $\Delta a = 0.01$  for  $a > 0.02$ . A characteristic velocity diagram is displayed in Fig. 2, where the dependence of the final velocity  $v_f$  of the scattered kinks on the initial collision velocity  $v_0$  is graphically represented for the initial wobbling amplitude  $a = 0.02$ . Although this value is

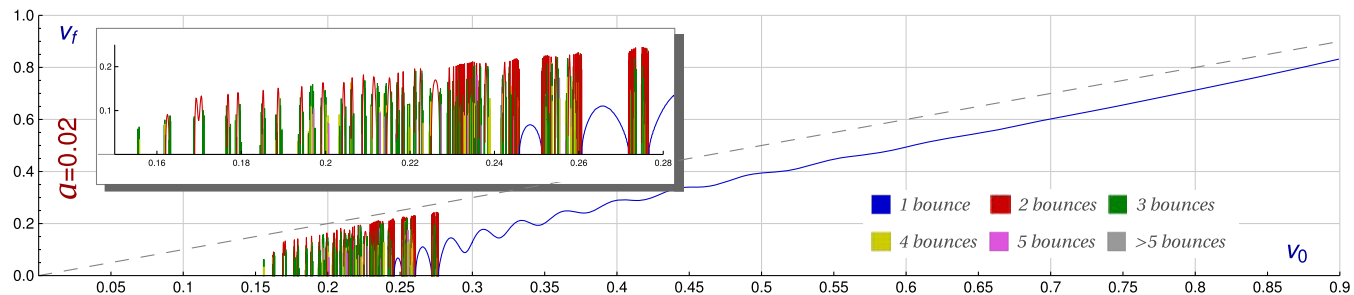


FIG. 2. Final velocity  $v_f$  of the scattered kinks as a function of the initial collision velocity  $v_0$  of the colliding wobbling kinks with initial amplitude  $a = 0.02$ . The final velocity of a bion is assumed to be zero. The color code is used to specify the number of bounces suffered by the kinks before escaping. The resonance window has been zoomed and inserted in the figure.

relatively small the diagram displayed in Fig. 2 introduces novel features with respect to the classical diagram shown in Fig. 1.

It can be observed that the complexity of the fractal structure grows as the initial wobbling amplitude  $a$  increases. A first sign of this fact is that the fractal structure interval is widened as  $a$  increases. For example, this interval is approximately  $[0.155, 0.277]$  for the case  $a = 0.02$ , whereas it is approximately  $[0.18, 0.26]$  for

the case  $a = 0$ . A second indicator is the growth in the number of resonance windows. Indeed, this effect is caused by a resonance window splitting mechanism, which is illustrated in Fig. 3. Before examining this process it is worthwhile to bring our attention to another novel property of the diagram in Fig. 2: the presence of isolated one-bounce windows in the fractal structure, which, in turn, are surrounded by other  $n$ -bounce windows with  $n \geq 2$ . This feature does not arise in the classical velocity diagram with

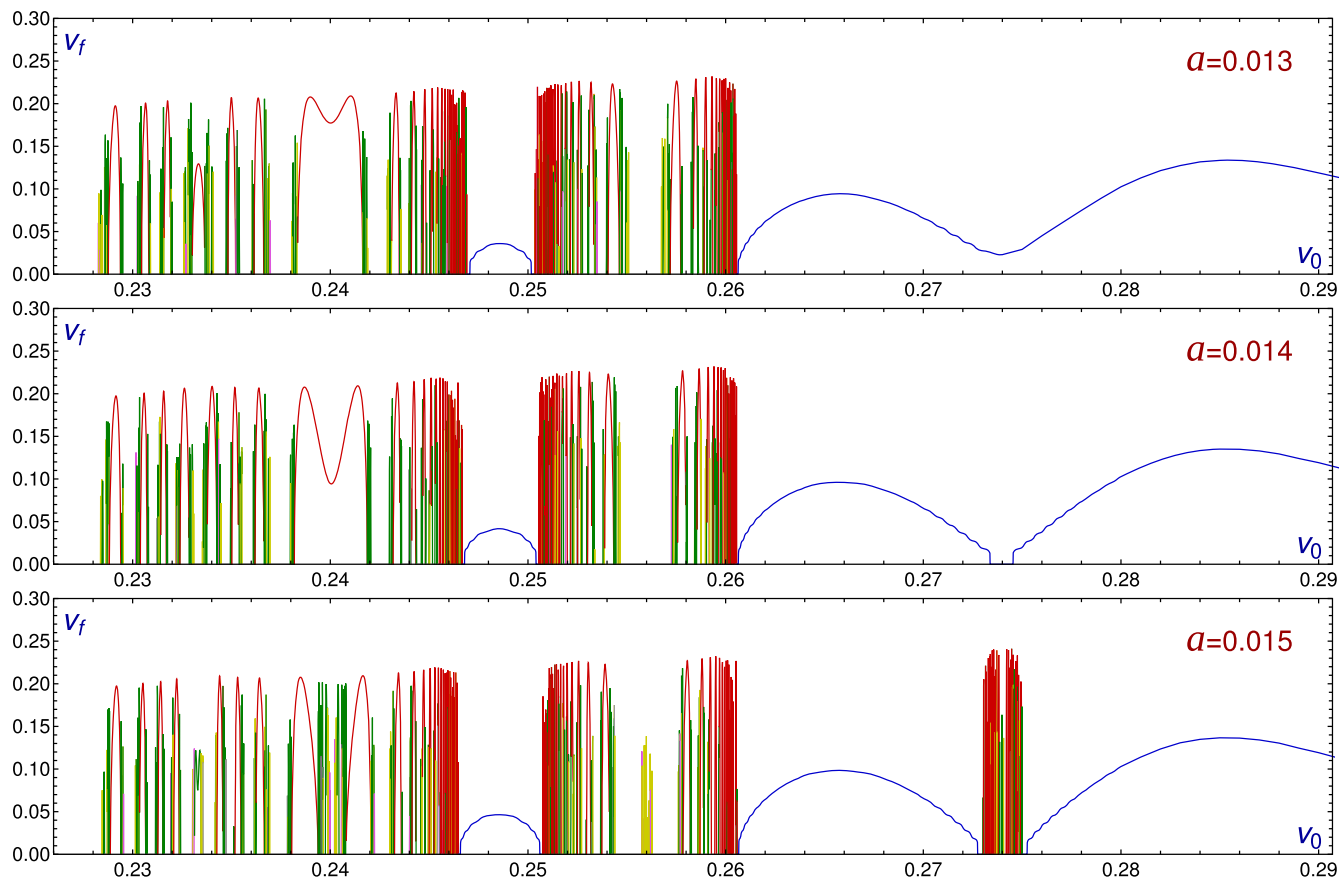


FIG. 3. Velocity diagrams for the wobbling kink scattering with initial amplitudes  $a = 0.013$ ,  $a = 0.014$ , and  $a = 0.015$  for the initial velocity interval  $v_0 \in [0.2260, 0.2907]$ . This sequence of graphics illustrates the formation of isolated one-bounce windows and the two-bounce window splitting mechanism.

zero initial energy on the shape mode displayed in Fig. 1 and seems to originate from two different procedures. Figure 2 shows the existence of two isolated one-bounce windows approximately in the intervals  $[0.246, 0.251]$  and  $[0.261, 0.272]$ , each of them generated by different channels. They are described as follows:

- (1) One-bounce reflection tail splitting: this process is based on the oscillatory behavior of the one-bounce tail arising for large initial velocities and represented by blue curves in Figs. 1 and 2. For  $a = 0$  this one-bounce tail is a monotonically increasing function (see Fig. 1). However, this curve ceases to follow that behavior and begins to oscillate as the amplitude  $a$  grows (see Fig. 2). The amplitude of these oscillations becomes bigger as the value of  $a$  grows, overall at the beginning of the one-bounce tail. When the amplitude  $a$  is large enough the minima of the previously mentioned oscillations can intercept the  $v_0$  axis, reaching a zero final velocity. As a consequence an isolated one-bounce window arises and the gap between this window and the one-bounce tail is filled with new  $n$ -bounce windows. This phenomenon can be triggered repeatedly as  $a$  increases giving rise to several isolated one bounce windows embedded in the resonance regime. The previously described mechanism can be visualized in Fig. 3, where final velocity versus initial velocity diagrams have been plotted for three close initial amplitudes:  $a = 0.013$ ,  $a = 0.014$ , and  $a = 0.015$ . We can observe the formation of an isolated one-bounce window approximately in the interval  $v_0 \in [0.26, 0.273]$ .
- (2) Spontaneous emergence in the resonance phase: the other process, instead, is characterized by the appearance of windows inside the resonance interval. In these new windows the wobbling kinks collide only once before escaping. The additional energy stored in the shape mode carried by the excited kinks allows them to escape in initial velocity windows where this was not possible before. For example, the formation of the first window of this kind happens

approximately for  $a = 0.011$  around the value  $v_0 = 0.249$ . As the value of  $a$  increases the width of these windows widens. Indeed, this first window can be observed in Fig. 3 for the initial amplitudes  $a = 0.013$ ,  $a = 0.014$ , and  $a = 0.015$ . The second window of this class arises for  $a = 0.030$  around  $v_0 = 0.233$ . From here the number of the windows grows enormously (see Fig. 4).

Figure 4 illustrates the combined effect of the previously mentioned processes of production of isolated one-bounce reflection windows. This figure shows the evolution of the velocity diagrams associated to one-bounce events as the initial wobbling amplitude  $a$  increases from  $a = 0$  (red curve) to  $a = 0.1$  (dark blue curve). For the sake of clarity,  $n$ -bounce processes with  $n \geq 2$  are not included in this plot. Together with the reflection tail splitting and the spontaneous emergence processes, another curious behavior is displayed in Fig. 4; the oscillations of final versus initial velocity curves for different values of the amplitude  $a$  have common nodes, they intersect each other at the same points (at least in a large degree of approximation).

Now, let us return to the previously mentioned resonance window splitting mechanism. If we observe Fig. 3 around the initial velocity  $v_0 = 0.24$ , we will witness the split of a two-bounce window into other two narrower two-bounce windows. As before, the gap between these two new two-bounce windows is occupied by new  $n$ -bounce windows with  $n > 2$ . To emphasize the behavior of this novel feature, the evolution of the first two-bounce window found in the classical velocity diagram for  $a = 0$  (see Fig. 1) as the value of the wobbling amplitude  $a$  increases is shown in Fig. 5. It can be observed that the initial two-bounce window  $v_0 \in [0.1920, 0.2028]$  (represented by a red curve) gives rise to three new two-bounce windows  $v_0 \in [0.1940, 0.1946]$ ,  $v_0 \in [0.1990, 0.1998]$ , and  $v_0 \in [0.2039, 0.2046]$  (represented by blue curves) for  $a = 0.02$ . This process is repeated for the majority of the resonance windows as the initial wobbling amplitude grows escalating the complexity of the fractal pattern in the resonance phase.

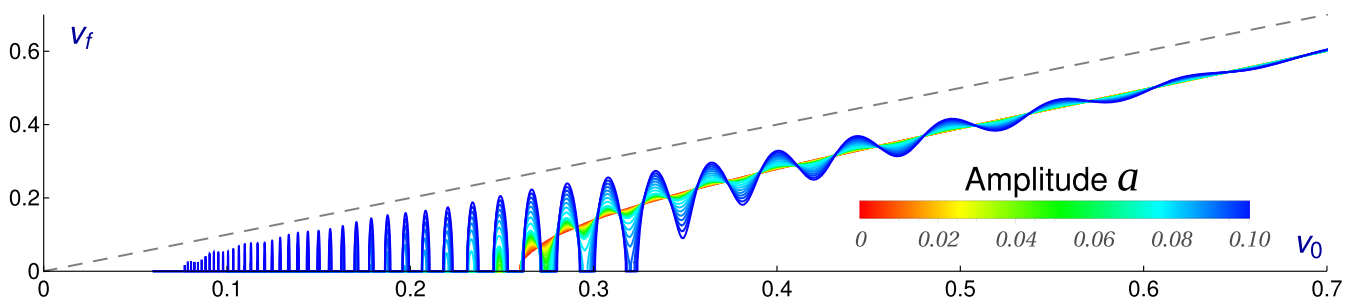


FIG. 4. Velocity diagram associated with one-bounce scattering events for initial wobbling amplitudes ranging in the interval  $a \in [0, 0.10]$ . This graphics illustrates the formation of isolated one-bounce windows. For the sake of clarity,  $n$ -bounce processes with  $n \geq 2$  have not been included in this figure.

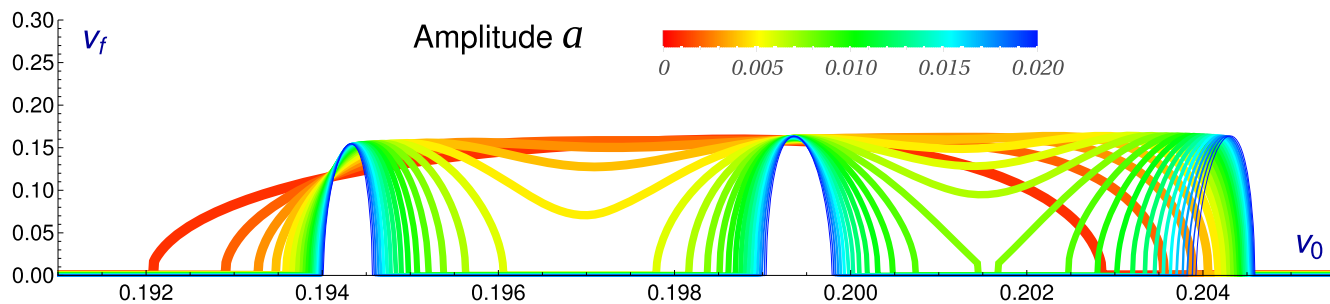


FIG. 5. Evolution of the first two-bounce window found in the velocity diagram for  $a = 0$  (red curve) as the value of the initial wobbling amplitude increases up to  $a = 0.02$  (dark blue curves). For the sake of clarity, only two-bounce scattering events have been included in this graphics.

Note that the formation of isolated one-bounce windows leads to an ambiguity in the concept of the critical velocity  $v_c$ . This term was introduced in the context of kink-antikink scattering [14,19] and was defined as the lowest velocity at which the one-bounce reflection regime takes place, or alternatively, the lowest velocity at which the one-bounce tail starts and no more bion states or more multibounces are observed. These two definitions coincide when the two colliding kinks are not wobbling because there is only one (blue) piece of one-bounce curve (see Fig. 1), but they can differ in other cases. In order to remove this ambiguity we shall distinguish these two velocities, referring to the first one as the one-bounce reflection minimum escape velocity  $v_r$ , whereas the second one will be called one-bounce tail minimum escape velocity  $v_t$ . Since more energy in the vibrational mode means that more energy can be released to the translation mode in the scattering process through the resonant energy transfer mechanism, it is expected that one-bounce windows become more prevalent as the value of the wobbling amplitude  $a$  grows. Consequently, it is presumed that the velocity  $v_r$  is a decreasing function of the amplitude  $a$ . On the other hand, the isolated one-bounce window

formation previously explained implies that the velocity  $v_t$  must grow as the amplitude  $a$  increases. In the transition from initial amplitude  $a_0 = 0$  to  $a_0 = 0.014$  the escape velocity  $v_t$  is observed to increase logarithmically; however, this pattern is broken by the existence of a discontinuity due to the formation of the first isolated one-bounce window from the reflection tail.

After discussing the features of the velocity diagram as a function of the initial amplitude  $a$ , we shall illustrate some particular processes. In Fig. 6 (left) a wobbling kink and a wobbling antikink with collision velocity  $v_0 = 0.285$  and initial amplitude  $a = 0.02$  approach each other, collide, bounce back, and move away with final velocity  $v_f = 0.144805$  and wobbling amplitude  $a_f = 0.175462$  after the collision. These dynamical parameters are the same for the kink and the antikink, which is in agreement with spatial reflection symmetry. Once they do not collide back after the first bounce the energy stored in the vibrational mode remains there and propagates within the kinks. The process displayed in Fig. 6 (right) describes a three-bounce event with initial velocity  $v_0 = 0.25737$  and amplitude  $a = 0.02$ . In this case, the scattered kink and antikink travel away

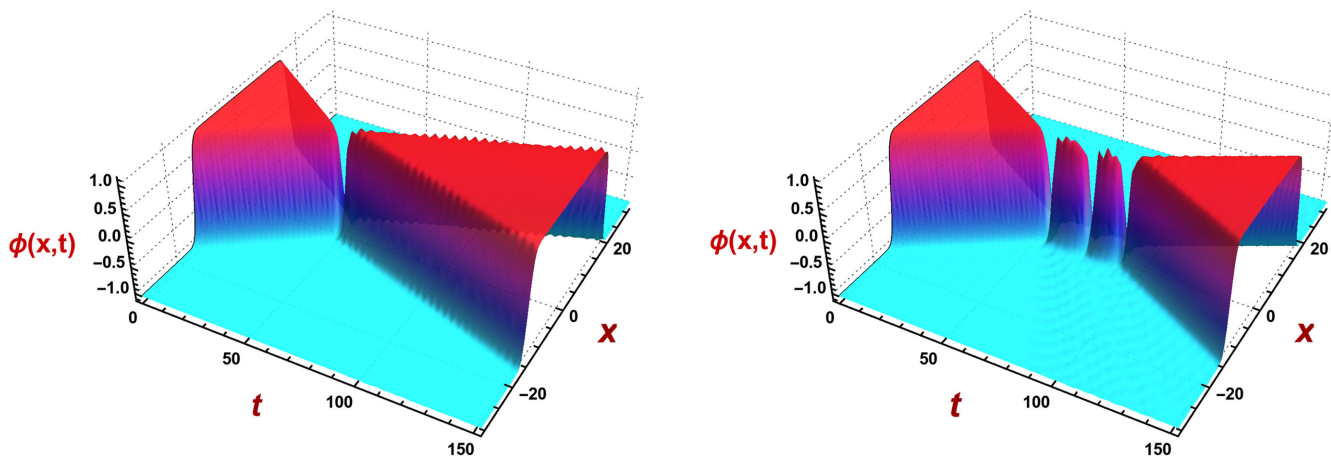


FIG. 6. Scattering processes between two wobbling kinks with initial amplitude  $a_0 = 0.02$  and collision velocities  $v_0 = 0.285$  (left) and  $v_0 = 0.25737$  (right). The final velocities and wobbling amplitudes for these events are, respectively,  $v_f = 0.144805$ ,  $a_f = 0.175462$  and  $v_f = 0.219$ ,  $a_f = 0.003085$ .

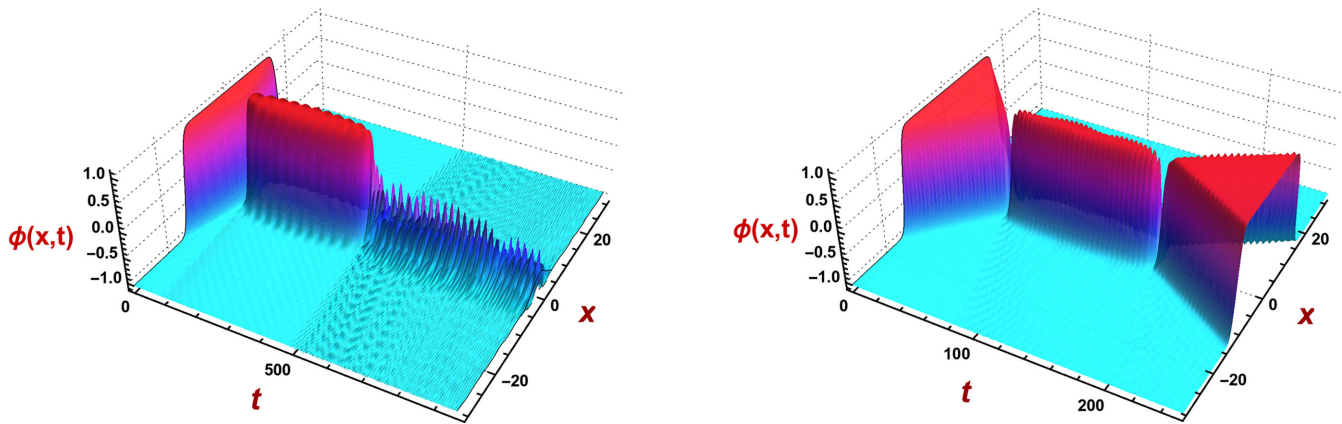


FIG. 7. Scattering processes between two wobbling kinks with initial velocities and amplitudes  $v_0 = 0.24691$ ,  $a = 0.013$  (left) and  $v_0 = 0.27420$ ,  $a = 0.015$  (right). In the first case a bion state is formed whereas in the second case the scattered kinks have  $v_f = 0.147041$  and  $a_f = 0.15351$ .

with velocity  $v_f = 0.219$  and wobbling amplitude  $a_f = 0.003085$ . We can see the resonant energy transfer mechanism in action in these cases. In the one-bounce event the outcome amplitude  $a_f$  is bigger than the initial amplitude  $a$ , which evinces an energy transfer from the translational mode to the shape mode being the final separation velocity  $v_f$  less than the initial one  $v_0$ . On the other hand, in the three-bounce process this mechanism takes place three times redistributing the energy between the kinetic and vibrational energy pools after every collision. Clearly, in the first impact the shape mode gains energy at the expense of the zero mode, which finally recovers part of that energy in the third collision allowing the kinks to escape. Note that radiation emission is also involved in these processes.

In Fig. 7 we have decided to illustrate the behavior of two extreme scattering events, which are near to metastable configurations. In the first process, left plot, kink and antikink approach each other with initial velocity  $v_0 = 0.24691$  and wobbling amplitude  $a = 0.013$ , collide and bounce back. For a long time, they apparently remain motionless at a fixed distance. In this particular simulation this situation takes approximately 400 time units in the dimensionless coordinates introduced in Sec. II. Finally, the lumps end up approaching again to form a bion state. In the second simulation Fig. 7 (right) the kinks initially travel with velocity  $v_0 = 0.27420$  and wobbling amplitude  $a = 0.015$ ; after colliding the kink and antikink remain in a similar quasimetastable state, which was previously described, although in this case after the second collision the kinks are able to escape with final velocity  $v_f = 0.147041$  and wobbling amplitude  $a_f = 0.15351$ . This type of scattering events are difficult to monitor because there will always be processes whose metastable phase will last more than any simulation time. Indeed, this is the reason for the gap in the velocity diagram introduced in Fig. 3 (middle) around  $v_0 = 0.274$ .

Clearly, in the previous simulations the wobbling mode is strongly excited after the first collision. This is a general pattern as we can observe in Fig. 8, which exhibits the final wobbling amplitude of the scattered kinks after the last collision as a function of the initial velocity  $v_0$  for two different values of the initial wobbling amplitude  $a = 0.0$  and  $a = 0.02$ . The analysis of these data, specially for the one-bounce events, can lead to a very valuable information to understand the resonant energy transfer mechanism. One-bounce events can be considered as elementary processes in the kink scattering because  $n$ -bounce events can be understood as a reiteration of  $n$  one-bounce events. The most surprising fact is that the final amplitude for the one-bounce processes is almost independent of the initial wobbling amplitude of the colliding kinks. We can observe that this magnitude follows a linear dependence on  $v_0$  very approximately, which can be fitted by the expression

$$a(v_0) = 0.084 + 0.34v_0. \quad (17)$$

What is clear from Fig. 8 is that all the one-bounce events produce a strong excitation of the wobbling mode, which in all the cases range approximately in the interval  $a_f \in [0.15, 0.4]$ . Obviously, the more the impact velocity of the colliding kinks is, the more excited the scattered kinks become. For moderate collision impact the final wobbling amplitude is in the range  $a_f \in [0.15, 0.25]$ . A first consequence of this high vibrational excitation in one-bounce scattering events for initially weakly wobbling kinks is that the  $n$ -bounce events in this regime necessarily involve the scattering of strongly wobbling kinks in one or several of the intermediate collision processes (at least in the second one). A second consequence is that the direction of energy transfer in these one-bounce events is always from kinetic energy to vibrational energy. Notice that the final velocity  $v_f$  of the scattered kinks in one-bounce events displayed in Fig. 2 is always less than the initial velocity  $v_0$ .

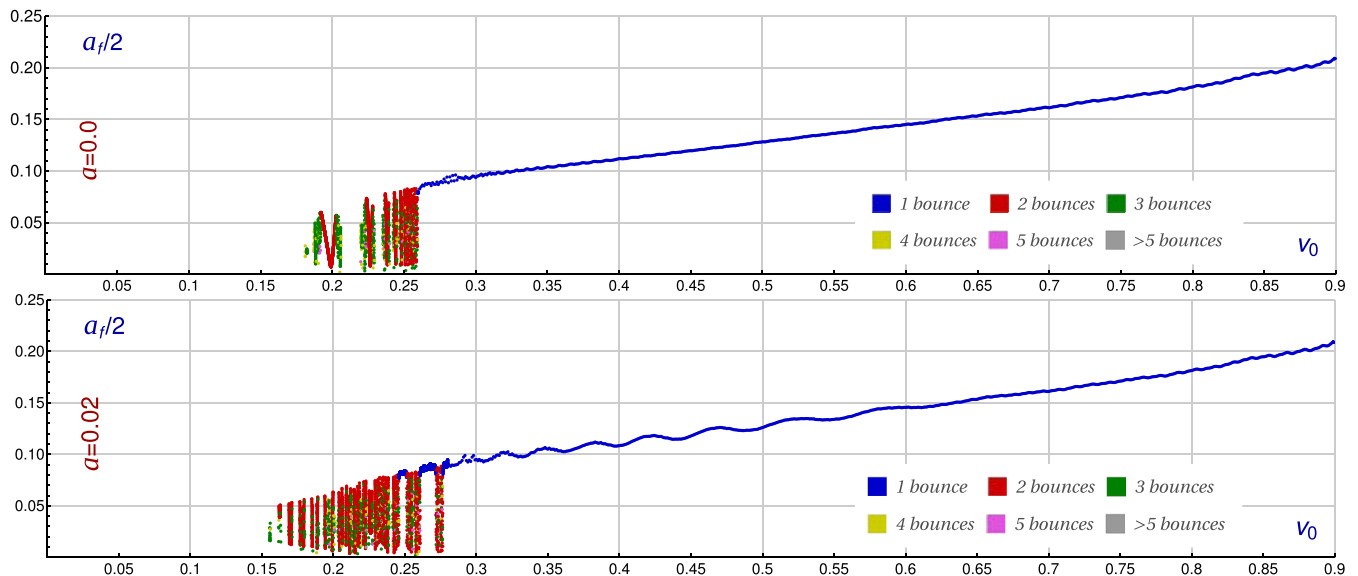


FIG. 8. Wobbling half-amplitude  $a_f/2$  [maximum deviation from the nonexcited kink (11)] of the scattered kinks after the last impact as a function of the collision velocity for the initial amplitude  $a = 0$  (top panel) and  $a = 0.02$  (bottom panel). The same color code employed in the previous figures is used to specify the number of bounces suffered by the kinks before escaping.

The isolated one-bounce windows found in this regime prove that there exist some initial velocity intervals where less energy is transferred to the shape mode, which allows the kinks keep enough kinetic energy to escape. The reverse processes must involve the scattering between strongly wobbling kinks.

The wobbling frequency  $\omega_f$  of the scattered kinks has also been analyzed. Note that the shape mode coming from

the second order small kink fluctuation operator expressed in (8) vibrates with the frequency  $\omega = \sqrt{3}$ . It seems reasonable to assume that this frequency is kept constant at least by the time the scattered kinks are far away. Figure 9 shows this magnitude as a function of the initial velocity  $v_0$  for the wobble amplitudes  $a = 0$  and  $a = 0.02$ . The color solid curves describe the frequencies measured in the inertial system attached to the kink center. We can observed

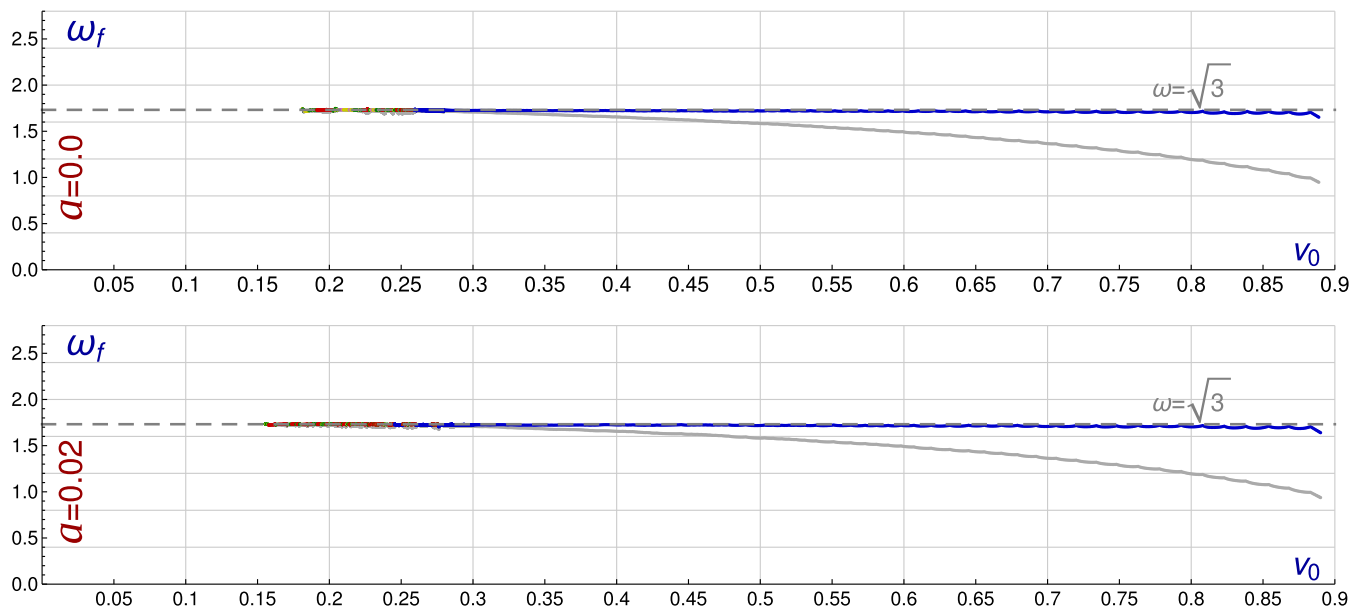


FIG. 9. Wobbling frequency of the scattered kinks after the last impact as a function of the collision velocity for the initial amplitude  $a = 0$  (top panel) and  $a = 0.02$  (bottom panel). The color solid curves determine the frequencies measured in the inertial system attached to the kink center, whereas the gray curves use the motionless inertial system. The same color code employed in previous figures is used to specify the number of bounces suffered by the kinks before escaping.

that the previously mentioned behavior is confirmed. The gray solid curves determine the frequencies measured in the motionless inertial system. The two curves are related by the relativistic transverse Doppler effect [75].

As previously mentioned in this section, the scattering between strongly wobbling kinks is always present in the resonance phenomenon because, independently of the initial velocity  $v_0$ , the second collision will involve a strongly wobbling kink scattering event. For this reason, the next section will be devoted to discuss the properties of this kind of more violent events. We shall emphasize the deviations of this new scenario from that introduced in the present section.

### B. Scattering between strongly wobbling kinks

This class of kink scattering processes is characterized by a relatively large value of the initial wobbling amplitude, which is assumed to be  $|a| \geq 0.1$ . In this section this regime has been analyzed for events with an initial amplitude  $a$  in the interval  $a \in [0.1, 0.2]$  by taking an amplitude step  $\Delta a = 0.01$ . As usual we shall begin by examining the dependence of the final velocity  $v_f$  of the scattered kinks on the initial velocity  $v_0$ . This function has been plotted in Fig. 10 for the particular cases  $a = 0.1$  and  $a = 0.2$ , which exhibits the representative properties of this regime. The global behavior of these velocity diagrams is similar to that described in Sec. III A, see Fig. 2, although they include important differences.

First of all, the fractal structure becomes even more intricate than the scenario found in Sec. III A. The interval where the resonance phenomenon takes place keeps

widening as  $a$  grows. In addition to this, when the value of  $a$  is large enough the number of isolated one-bounce windows explodes and the sequence of these windows forms a fractal structure clustered near the origin of the graphics (see bottom panel in Fig. 10). The initial velocities  $v_0$  around the peak of these windows can define initial velocity intervals where the scattered kinks move faster than the colliding kinks,  $v_f > v_0$ . In these cases a part of the vibrational kink energy accumulated in the shape mode is transferred to the kinetic energy, which becomes bigger than its initial value. It can be observed that this phenomenon occurs for low initial velocities and ceases to happen for high values (when the kinetic energy is large). For example, for  $a = 0.2$  the height of the windows in the resonance phase exceeds the elastic limit approximately when  $v_0 < 0.34$ . Obviously, as the value of the initial amplitude  $a$  increases this threshold velocity grows, because the vibrational energy becomes bigger. This scenario is a fundamental link in the chain of the resonant energy transfer mechanism because it allows relatively slow scattered wobbling kinks to escape in a multiple bounce event in the last collision by transferring vibrational energy to the kinetic energy pool. Figure 11 illustrates this kind of processes: a kink and antikink with initial velocity  $v_0 = 0.1506$  and wobbling amplitude  $a = 0.2$  approach each other and collide only once before escaping. As we can see, the scattered kink and antikink move away with final velocity  $v_f = 0.246454$  while its wobbling amplitude is approximately  $a = 0.0215$ . The final outcome in this event is that the kink and antikink are sped up whereas its wobbling is softened.

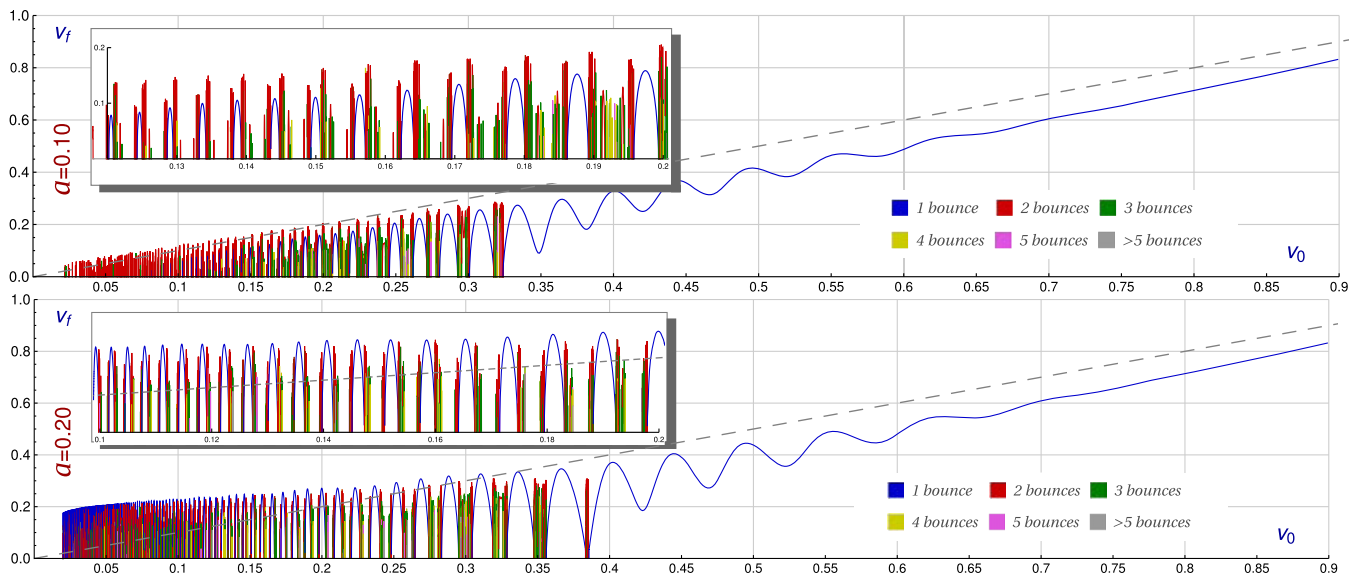


FIG. 10. Final velocity  $v_f$  of the scattered kinks as a function of the initial collision velocity  $v_0$  of the colliding wobbling kinks with initial amplitudes  $a = 0.1$  (top panel) and  $a = 0.2$  (bottom panel). The final velocity of a bion is assumed to be zero. The color code is used to specify the number of bounces suffered by the kinks before escaping. The part of the resonance window has been zoomed and inserted in the figure.



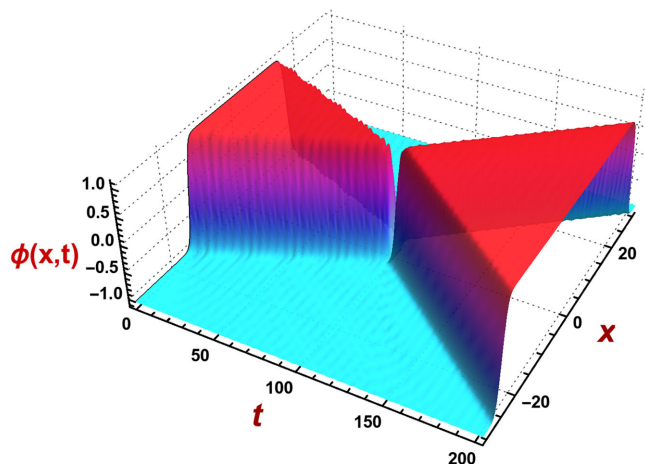


FIG. 11. Scattering between two wobbling kinks with initial amplitude  $a_0 = 0.2$  and collision velocity  $v_0 = 0.1406$ . The final velocity  $v_f$  of the scattered kinks is  $v_f = 0.246454$ , so the kinks move faster after the collision.

Figure 7 (right) represents a two-bounce kink scattering process, which was introduced in Sec. III A. Here, kink and antikink approach each other with initial velocity  $v_0 = 0.2742$  while vibrating with amplitude  $a = 0.015$ . Notice, thus, that the first collision is a weakly wobbling kink scattering event. As we know, after this first impact an important part of the kinetic energy is devoted to excite the shape mode and emit radiation, such that the resulting kink and antikink move very slowly but vibrate intensely. In

these circumstances, the attraction force between the kink and the antikink makes them approach again. This evolution is now described by a strongly wobbling kink scattering event. The lumps collide and bounce back, but now the resonant energy transfer mechanism is reversed and the kink and antikink velocities are large enough to let them escape. They travel away with final velocity  $v_f = 0.147041$  and final wobbling amplitude  $a = 0.153513$ . Figure 6 (right) represents a three-bounce kink scattering process, where a similar behavior takes place, although the intermediate stages are much shorter. They finally move away with velocity  $v_f = 0.219006$  and wobbling amplitude  $a = 0.00308$ .

The behavior of the final wobbling amplitude  $a_f$  as a function of the initial velocity is plotted in Fig. 12. The amplitude can undergo important fluctuations when the initial velocity varies, which increases as the value of  $a$  grows. These oscillations can be observed, for example, in the one-bounce reflection tail. The range of the wobbling amplitudes found in these cases is similar to that described in Sec. III A for weakly wobbling kink scattering processes. The minima of these fluctuations can reach very low values. In the resonance phase these oscillations are more accentuated for these one-bounce events than in the previous regime. Obviously, the detailed behavior of the amplitude in the resonance phase is completely particular for every value of  $a$  due to the presence of the fractal structure. Besides, the dependence of the final frequency  $\omega_f$  on the initial velocity  $v_0$  completely resembles the result found in Sec. III A (see Fig. 13).

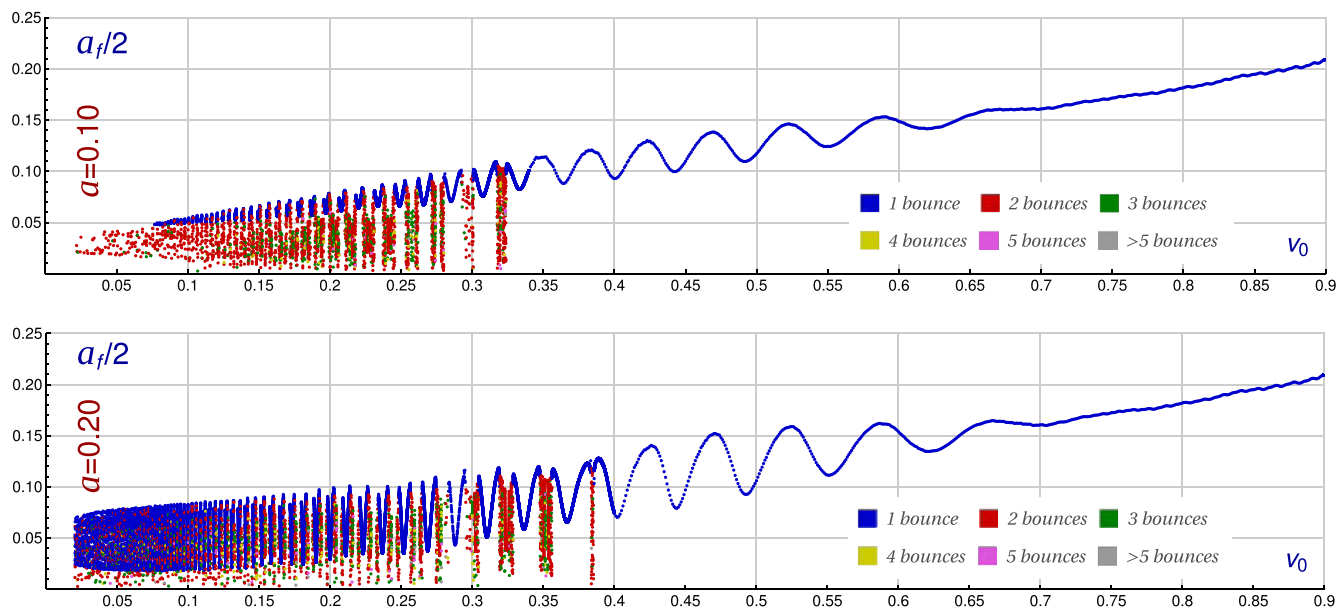


FIG. 12. Wobbling half-amplitude  $a_f/2$  [maximum deviation from the nonexcited kink (11)] of the scattered kinks after the last impact as a function of the collision velocity  $v_0$  for the initial amplitude  $a = 0.1$  (top panel) and  $a = 0.2$  (bottom panel). The same color code employed in previous figures is used to specify the number of bounces suffered by the kinks before escaping.

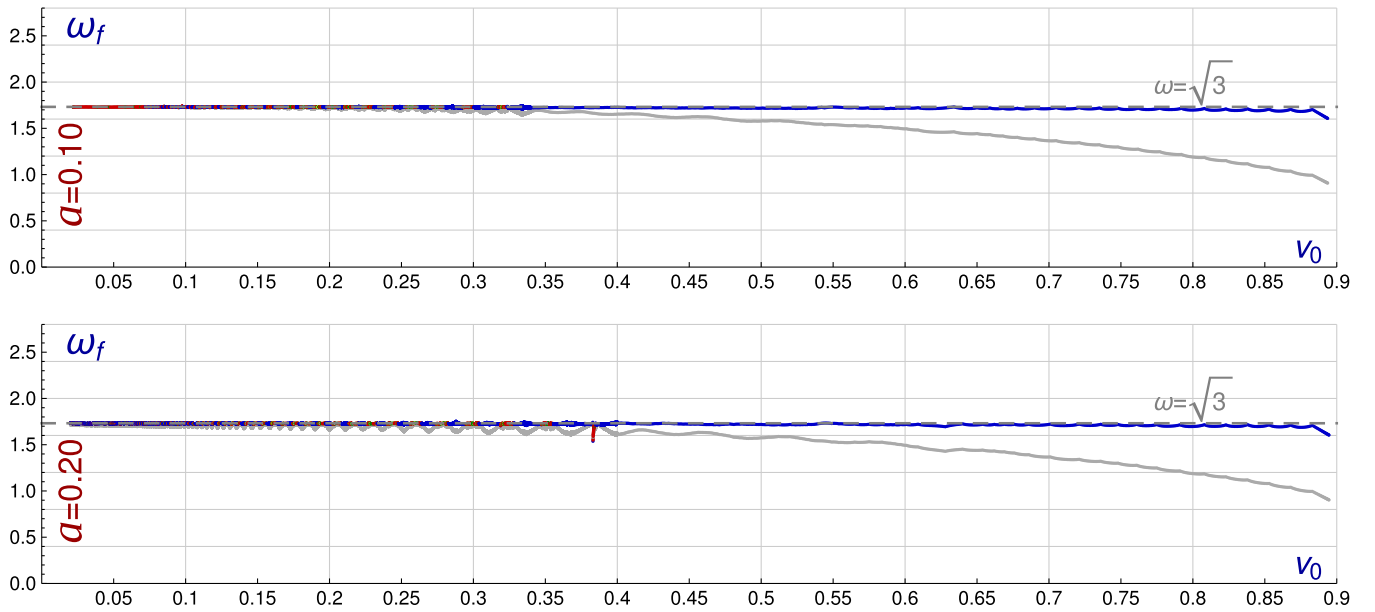


FIG. 13. Wobbling frequency of the scattered kinks after the last impact as a function of the collision velocity  $v_0$  for the initial amplitude  $a = 0$  (top panel) and  $a = 0.02$  (bottom panel). The color solid curves determine the frequencies measured in the inertial system attached to the kink center, whereas the gray curves use the motionless inertial system. The same color code as in previous figures is used to specify the number of bounces suffered by the kinks before escaping.

#### IV. CONCLUSIONS AND FURTHER COMMENTS

In this paper we have addressed the scattering between wobbling kinks in the  $\phi^4$  model. In addition to its intrinsic interest the study of these processes can give us some insight into the resonant energy transfer mechanism. We must take into account that two traveling nonexcited kinks become wobbling kinks after the first collision due to the energy exchange between the translational mode and the shape mode. In this sense, a  $n$ -bounce scattering process can be considered as the reiteration of  $n$  one-bounce collisions, most of them between wobbling kinks. In this work the influence of the collision velocity and the initial wobbling amplitude on the scattering processes have been directly investigated. The fractal structure arising in the resonance regime of the final versus initial velocity diagram becomes more intricate as the value of the initial wobbling amplitude of the colliding kinks increases. This growing complexity is caused by two different mechanisms: the one-bounce reflection tail splitting and the spontaneous emergence of resonance windows. The first case is produced by the oscillations of the one-bounce reflection tail when the initial wobbling amplitude grows. When the amplitude is large enough, this tail can intercept the  $v_0$  axis, creating an isolated one-bounce window in the resonance regime. The gap between this new window and the one-bounce tail is filled with new  $n$ -bounce windows, with  $n > 1$ . The same phenomenon is replicated for  $n$ -bounce windows, which are broken up into narrower new  $n$ -bounce windows, and as before the gap between them is occupied with  $N$ -bounce windows, with  $N > n$ . The second

mechanism is directly triggered by the extra energy carried by the initially excited shape mode of the wobbling kinks. New bounce windows emerge for ever-smaller initial velocities as the value of the amplitude increases. As a consequence, the fractal structure interval becomes larger as  $a$  grows. On the other hand, the final wobbling amplitude of the scattered kinks involve very approximately a linear dependence on the initial velocity outside the resonance phase, although some oscillations arise for large enough values of the initial amplitude. one-bounce events between weakly wobbling kinks always give rise to strongly wobbling kinks moving away. On the other hand, weakly wobbling kinks can emerge from the collision between strongly wobbling kinks only for relatively small values of the initial velocity.

It is worthwhile to mention that for strongly wobbling kink collisions there exist one-bounce windows where the scattered kinks will travel faster than the colliding kinks. This occurs for relatively low values of the initial velocity. This behavior implies that the last collision in every  $n$ -bounce scattering event with  $n > 1$  must involve the presence of strongly wobbling kinks approaching each other at a relatively low speed. In a multiple bounce scattering process the kinks approach each other and bounce back again and again until the next collision velocity and wobbling amplitude fall into one of the previously mentioned one-bounce windows. In the bion formation regime the successive collisions are not able to excite the shape mode enough to trigger this escape manoeuvre.

The research introduced in the present work opens some possibilities for future investigations. An inherent goal of

this paper is to bring insight into the interaction of the shape and zero modes when a kink and an antikink collide. It would be very interesting to construct an effective finite-dimensional dynamical system (for example, by means of the collective coordinate approach), which is able to quantitatively explain the results found in this paper. This would allow us to get a better understanding of the resonance phenomenon and the connection between chaos and the fractal pattern arising in the velocity diagrams. On the other hand, the scattering between wobbling kinks can be numerically explored in other models. For example, the  $\phi^6$  model involves a similar resonance regime as the  $\phi^4$  model, although it does not present vibrational eigenstates in the second order small fluctuation operator. The characteristics of the scattered wobbling kinks can be analyzed to study their influence on the resonant energy transfer mechanism. Alternatively, a twin model to the  $\phi^6$  model involving internal modes can be constructed, and we could compare the scattering processes of the twin model with those of the standard  $\phi^6$  model. In this way the role played

by the shape modes in the collision process could be carefully examined. Moreover, many other different topological defects (kinks in the double sine-Gordon model, deformed  $\phi^4$  models, hybrid and hyperbolic models, etc) could be studied in the new perspective presented here.

### ACKNOWLEDGMENTS

A. A.-I. acknowledges the Junta de Castilla y León for financial support under Grants No. BU229P18 and No. SA067G19. L. M. N. acknowledges the Junta de Castilla y León and FEDER Projects for financial support under Grants No. VA057U16, No. VA137G18, and No. BU229P18. J. V. Q.-N. acknowledges the financial support of Santander Group under scholarship program UVa—Santander Iberoamerica+Asia. This research has made use of the high performance computing resources of the Castilla y León Supercomputing Center (SCAYLE, www.scayle.es), financed by the European Regional Development Fund (ERDF).

- 
- [1] A. R. Bishop, J. A. Krumhansl, and S. E. Trullinger, *Physica (Amsterdam)* **1D**, 1 (1980).
  - [2] A. H. Eschenfelder, *Magnetic Bubble Technology* (Springer-Verlag, Berlin, 1981).
  - [3] F. Jona and G. Shirane, *Ferroelectric Crystals* (Dover, New York, 1993).
  - [4] B. A. Strukov and A. P. Levanyuk, *Ferroelectric Phenomena in Crystals: Physical Foundations* (Springer-Verlag, Berlin, 1998).
  - [5] A. Vilenkin and E. P. S. Shellard, *Cosmic Strings and Other Topological Defects* (Cambridge University Press, Cambridge, England, 1994).
  - [6] T. Vachaspati, *Kinks and Domain Walls: An Introduction to Classical and Quantum Solitons* (Cambridge University Press, Cambridge, England, 2006).
  - [7] L. F. Mollenauer and J. P. Gordon, *Solitons in Optical Fibers—Fundamentals and Applications* (Academic Press, Burlington, 2006).
  - [8] T. Schneider, *Nonlinear Optics in Telecommunications* (Springer, Heidelberg, 2004).
  - [9] G. P. Agrawal, *Nonlinear Fiber Optics* (Academic Press, San Diego, 1995).
  - [10] A. S. Davydov, *Solitons in Molecular Systems* (D. Reidel, Dordrech, 1985).
  - [11] D. Bazeia and E. Ventura, *Chem. Phys. Lett.* **303**, 341 (1999).
  - [12] L. V. Yakushevich, *Nonlinear Physics of DNA* (Wiley-VCH, Weinheim, 2004).
  - [13] T. Sugiyama, *Prog. Theor. Phys.* **61**, 1550 (1979).
  - [14] D. K. Campbell, J. S. Schonfeld, and C. A. Wingate, *Physica (Amsterdam)* **9D**, 1 (1983).
  - [15] P. Anninos, S. Oliveira, and R. A. Matzner, *Phys. Rev. D* **44**, 1147 (1991).
  - [16] A. E. Kudryavtsev, *JETP Lett.* **22**, 82 (1975).
  - [17] J. Shiefman and P. Kumar, *Phys. Scr.* **20**, 435 (1979).
  - [18] M. Peyrard and D. K. Campbell, *Physica (Amsterdam)* **9D**, 33 (1983).
  - [19] D. K. Campbell, M. Peyrard, and P. Sodano, *Physica (Amsterdam)* **19D**, 165 (1986).
  - [20] V. A. Gani and A. E. Kudryavtsev, *Phys. Rev. E* **60**, 3305 (1999).
  - [21] B. A. Malomed, *Phys. Lett.* **136A**, 395 (1989).
  - [22] V. A. Gani, A. M. Marjaneh, A. Askari, E. Belendryasova, and D. Saadatmand, *Eur. Phys. J. C* **78**, 345 (2018).
  - [23] V. A. Gani, A. M. Marjaneh, and D. Saadatmand, *Eur. Phys. J. C* **79**, 620 (2019).
  - [24] F. C. Simas, A. R. Gomes, K. Z. Nobrega, and J. C. R. E. Oliveira, *J. High Energy Phys.* **09** (2016) 104.
  - [25] A. R. Gomes, F. C. Simas, K. Z. Nobrega, and P. P. Avelino, *J. High Energy Phys.* **10** (2018) 192.
  - [26] D. Bazeia, E. Belendryasova, and V. A. Gani, *J. Phys. Conf. Ser.* **934**, 012032 (2017).
  - [27] D. Bazeia, E. Belendryasova, and V. A. Gani, *Eur. Phys. J. C* **78**, 340 (2018).
  - [28] D. Bazeia, A. R. Gomes, and K. Z. Nobrega, and Fabiano C. Simas, *Int. J. Mod. Phys. A* **34**, 1950200 (2019).
  - [29] C. Adam, K. Oles, T. Romanczukiewicz, and A. Wereszczynski, *Phys. Rev. Lett.* **122**, 241601 (2019).
  - [30] T. Romanczukiewicz and Y. Shnir, *Some Recent Developments on Kink Collisions and Related Topics: A Dynamical Perspective on the  $\phi^4$  Model* (Springer, Cham, 2019).

- [31] C. Adam, K. Oles, T. Romanczukiewicz, and A. Wereszczynski, *Phys. Rev. D* **101**, 105021 (2020).
- [32] M. Mohammadi and R. Dehghani, *Commun. Nonlinear Sci. Numer. Simul.* **94**, 105575 (2021).
- [33] H. Yan, Y. Zhong, Y. X. Liu, and K. Maeda, *Phys. Lett. B* **807**, 135542 (2020).
- [34] T. Romanczukiewicz, *Phys. Lett. B* **773**, 295 (2017).
- [35] H. Weigel, *J. Phys. Conf. Ser.* **482**, 012045 (2014).
- [36] V. A. Gani, A. E. Kudryavtsev, and M. A. Lizunova, *Phys. Rev. D* **89**, 125009 (2014).
- [37] D. Bazeia, A. R. Gomes, K. Z. Nobrega, and F. C. Simas, *Phys. Lett. B* **793**, 26 (2019).
- [38] F. C. Lima, F. C. Simas, K. Z. Nobrega, and A. R. Gomes, *J. High Energy Phys.* **10** (2019) 147.
- [39] A. M. Marjaneh, V. A. Gani, D. Saadatmand, S. V. Dmitriev, and K. Javidan, *J. High Energy Phys.* **07** (2017) 028.
- [40] T. S. Mendona and H. P. de Oliveira, *Braz. J. Phys.* **49**, 914 (2019).
- [41] E. Belendryasova and V. A. Gani, *Commun. Nonlinear Sci. Numer. Simul.* **67**, 414 (2019).
- [42] Y. Zhong, X. L. Du, Z. C. Jiang, Y. X. Liu, and Y. Q. Wang, *J. High Energy Phys.* **02** (2020) 153.
- [43] D. Bazeia, A. R. Gomes, K. Z. Nobrega, and F. C. Simas, *Phys. Lett. B* **803**, 135291 (2020).
- [44] I. C. Christov, R. J. Decker, A. Demirkaya, V. A. Gani, P. G. Kevrekidis, and R. V. Radomskiy, *Phys. Rev. D* **99**, 016010 (2019).
- [45] I. C. Christov, R. J. Decker, A. Demirkaya, V. A. Gani, P. G. Kevrekidis, A. Khare, and A. Saxena, *Phys. Rev. Lett.* **122**, 171601 (2019).
- [46] I. C. Christov, R. J. Decker, A. Demirkaya, V. A. Gani, P. G. Kevrekidis, and A. Saxena, [arXiv:2005.00154](https://arxiv.org/abs/2005.00154).
- [47] A. Halavanau, T. Romanczukiewicz, and Ya. Shnir, *Phys. Rev. D* **86**, 085027 (2012).
- [48] T. Romanczukiewicz, *Acta Phys. Pol. B* **39**, 3449 (2008).
- [49] A. Alonso-Izquierdo, *Phys. Rev. D* **97**, 045016 (2018).
- [50] A. Alonso-Izquierdo, *Phys. Scr.* **94**, 085302 (2019).
- [51] A. Alonso-Izquierdo, *Physica (Amsterdam)* **365D**, 12 (2017).
- [52] A. Alonso-Izquierdo, *Commun. Nonlinear Sci. Numer. Simul.* **75**, 200 (2019).
- [53] A. Alonso-Izquierdo, *Commun. Nonlinear Sci. Numer. Simul.* **85**, 105251 (2020).
- [54] L. A. Ferreira, P. Klimas, and W. J. Zakreswski, *J. High Energy Phys.* **01** (2019) 020.
- [55] Z. Fei, Y. Kivshar, and L. Vazquez, *Phys. Rev. A* **45**, 6019 (1992).
- [56] Z. Fei, Y. S. Kivshar, and L. Vazquez, *Phys. Rev. A* **46**, 5214 (1992).
- [57] R. H. Goodman, P. J. Holmes, and M. I. Weinstein, *Physica (Amsterdam)* **161D**, 21 (2002).
- [58] R. H. Goodman and R. Haberman, *Phys. D* **195**, 303 (2004).
- [59] B. A. Malomed, *Physica (Amsterdam)* **15D**, 385 (1985).
- [60] B. A. Malomed, *J. Phys. A* **25**, 755 (1992).
- [61] K. Javidan, *J. Phys. A* **39**, 10565 (2006).
- [62] D. Saadatmand and K. Javidan, *Phys. Scr.* **85**, 025003 (2012).
- [63] D. Saadatmand and K. Javidan, *Braz. J. Phys.* **43**, 48 (2013).
- [64] D. Saadatmand, S. V. Dmitriev, D. I. Borisov, P. G. Kevrekidis, M. A. Fatykhov, and K. Javidan, *Commun. Nonlinear Sci. Numer. Simul.* **29**, 267 (2015).
- [65] D. Saadatmand, D. I. Borisov, P. G. Kevrekidis, K. Zhou, and S. V. Dmitriev, *Commun. Nonlinear Sci. Numer. Simul.* **56**, 62 (2018).
- [66] C. Adam, T. Romanczukiewicz, and A. Wereszczynski, *J. High Energy Phys.* **3** (2019) 131.
- [67] C. Adam, K. Oles, J. M. Queiruga, T. Romanczukiewicz, and A. Wereszczynski, *J. High Energy Phys.* **07** (2019) 150.
- [68] M. A. Lizunova, J. Kager, S. de Lange, and J. van Wezel, [arXiv:2007.04747](https://arxiv.org/abs/2007.04747).
- [69] P. Dorey, K. Mersh, T. Romanczukiewicz, and Y. Shnir, *Phys. Rev. Lett.* **107**, 091602 (2011).
- [70] P. Dorey and T. Romanczukiewicz, *Phys. Lett. B* **779**, 117 (2018).
- [71] J. G. F. Campos and A. Mohammadi, *Eur. Phys. J. C.* **80**, 352 (2020).
- [72] I. Takiy and H. Weigel, *Phys. Rev. D* **94**, 085008 (2016).
- [73] C. F. S. Pereira, G. Luchini, T. Tassis, and C. P. Constantinidis, [arXiv:2004.00571v2](https://arxiv.org/abs/2004.00571v2).
- [74] B. S. Getmanov, *JETP Lett.* **24**, 291 (1976).
- [75] I. V. Barashenkov and O. F. Oxtoby, *Phys. Rev. E* **80**, 026608 (2009).
- [76] I. V. Barashenkov, in *The Continuing Story of the Wobbling Kink*, edited by P. Kevrekidis and J. Cuevas-Maraver, *A Dynamical Perspective on the  $\phi^4$  Model. Nonlinear Systems and Complexity* Vol. 26 (Springer, Cham, 2018).
- [77] H. Segur, *J. Math. Phys. (N.Y.)* **24**, 1439 (1983).
- [78] N. S. Manton and H. Merabet, *Nonlinearity* **10**, 3 (1997).
- [79] A. K. Kassam and L. N. Trefethen, *SIAM J. Sci. Comput.* **26**, 1214 (2005).
- [80] S. M. Cox and P. C. Matthews, *J. Comput. Phys.* **176**, 430 (2002).



# Capítulo 3

---

## Asymmetric Scattering Between Kinks and Wobblers

---

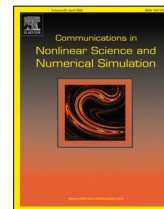
### Resumen

En el trabajo que se muestra a continuación se investiga numéricamente la estructura de la información de scattering procedente de colisiones asimétricas entre kinks vibracionalmente excitados y no excitados del modelo  $\phi^4$  estándar. Inicialmente se investiga la colisión entre kinks vibrantes con fases opuestas. En el diagrama de velocidades se observa una estructura fractal de menor complejidad que la encontrada en la sección precedente debido a la interferencia destructiva entre las vibraciones de los kinks con fases opuestas. En un segundo escenario se investiga las colisiones entre kinks vibrantes y kinks no excitados. En este caso, se observa la transferencia de la excitación del kink vibrante al kink no excitado lo que se traduce en resultados similares al trabajo anterior. Las simulaciones numéricas destacan la dependencia de las velocidades y amplitudes finales en términos de la velocidad y amplitud inicial de vibración de los kinks. Además, debido a la asimetría presente en la configuración inicial las velocidades y amplitudes finales de los kinks vibrantes son diferentes. No obstante, para una secuencia de velocidades iniciales, tanto las velocidades y amplitudes finales coinciden. Esto es aproximadamente independiente de la amplitud de vibración inicial. Esto demuestra que la fase de oscilación inicial del kink vibrante tiene un papel fundamental en las propiedades de colisión entre estos objetos.



Contents lists available at ScienceDirect

# Communications in Nonlinear Science and Numerical Simulation

journal homepage: [www.elsevier.com/locate/cnsns](http://www.elsevier.com/locate/cnsns)

Research paper

## Asymmetric scattering between kinks and wobblers

A. Alonso-Izquierdo<sup>a,b,\*</sup>, L.M. Nieto<sup>c</sup>, J. Queiroga-Nunes<sup>a,b</sup><sup>a</sup> Departamento de Matematica Aplicada, Universidad de Salamanca, Casas del Parque 2, 37008 Salamanca, Spain<sup>b</sup> IUFFyM, Universidad de Salamanca, Plaza de la Merced 1, 37008 Salamanca, Spain<sup>c</sup> Departamento de Física Teórica, Atómica y Óptica, and IMUVA, Universidad de Valladolid, 47011, Valladolid, Spain

### ARTICLE INFO

#### Article history:

Received 7 October 2021

Received in revised form 2 December 2021

Accepted 5 December 2021

Available online 11 December 2021

#### Keywords:

Kink scattering

Wobbling kinks

Non-linear Klein–Gordon equation

Resonant energy transfer mechanism

### ABSTRACT

The asymmetric scattering between wobblers and kinks in the standard  $\phi^4$  model is numerically investigated in two different scenarios. First, the collision between wobblers with opposite phases is analyzed. Here, a destructive interference between the shape modes of the colliding wobblers takes place at the impact time. The second scenario involves the scattering between a wobbler and an unexcited kink. In this case the energy transfer from the wobbler to the kink can be examined. The dependence of the final velocities and wobbling amplitudes of the scattered wobblers on the collision velocity and on the initial wobbling amplitude is discussed. Both situations lead to very different fractal structures in the velocity diagrams.

© 2021 Elsevier B.V. All rights reserved.

## 1. Introduction

The scattering between kinks has become a very popular research topic in recent decades because of its astonishing properties [1–3]. The study of the collisions between kinks and antikinks in the  $\phi^4$  model was initially addressed in the seminal Refs. [4–6]. As it is well known, only two different scattering channels arise: *bion formation* (where kink and antikink collide and bounce back over and over emitting radiation in every impact) and *kink reflection* (where kink and antikink collide and bounce back a finite number of times before moving away from one another). These two channels are predominant, respectively, for low and large values of the initial collision velocity. In these studies there emerges the fascinating property that the two previously mentioned channels are infinitely interlaced in the transition between these regimes, giving rise to a fractal structure embedded in the final versus initial velocity diagram. Kink reflection included in this region involves scattering processes where kink and antikink collide and bounce back a finite number of times before definitely separating. This kink dynamics could have important consequences for physical applications where the presence of these topological defects allows us to understand certain non-linear phenomena. Kinks (and topological defects in general) occur in a wide variety of physical disciplines, such as Condensed Matter [7–9], Cosmology [10,11], Optics [12–14], molecular systems [15,16], Biochemistry [17], etc.

The appearance of a fractal structure in the velocity diagram describing kink scattering for the  $\phi^4$  model is based on the existence of an internal vibrational mode (the shape mode) associated with the kink solutions. The presence of this massive mode together with the zero mode triggers a *resonant energy transfer mechanism*, which allows the redistribution of the energy between the kinetic and vibrational modes when kinks collide. Usually, in a scattering event the kink and

\* Corresponding author at: Departamento de Matematica Aplicada, Universidad de Salamanca, Casas del Parque 2, 37008 Salamanca, Spain.  
E-mail address: [alonsoiz@usal.es](mailto:alonsoiz@usal.es) (A. Alonso-Izquierdo).

the antikink approach each other and collide. A certain amount of kinetic energy is transferred to the shape mode, such that kink and antikink become wobblers (kinks whose shape modes are excited), which try to escape from each other. If the kinetic energy of each wobbler is not large enough both of them end up approaching and recolliding. This process can continue indefinitely or end after a finite number of collisions. In the last case, enough vibrational energy returned back to the zero mode as kinetic energy, which allows the wobblers separate. This mechanism and related phenomena have been thoroughly analyzed in a large variety of models [18–70], revealing the enormous complexity of these events and the difficulty to explain this phenomenon analytically. The *collective coordinate approach* has indeed been used to accomplish this task, reducing the field theory to a finite dimensional mechanical system, where the separation between the kinks and the wobbling amplitudes of the shape modes are promoted to dynamical variables. This method has been progressively improved, see for example [3,4,71,72] and references therein, and recently, a reliable description of kink scattering in the  $\phi^4$  model has been achieved in the reflection-symmetric case [73], by introducing into this scheme the removal of a coordinate singularity in the moduli space and choosing the appropriate initial conditions.

As mentioned, after the first collision the initially unexcited kink and antikink become wobblers, so in a  $n$ -bounce scattering process the subsequent  $n - 1$  collisions can be understood to be scattering processes between two wobblers. This observation justifies interest in collisions between these objects. The evolution of a single wobbler has been studied by perturbations by various authors, see [74–76] and references therein. Scattering between wobblers in the  $\phi^4$  model was discussed in [77] for space reflection symmetry. This situation is relevant to the original kink scattering problem where mirror symmetry is preserved. The goal of these investigations is to bring insight into the resonant energy transfer mechanism by means of numerical analysis of the scattering solutions derived from the corresponding the Klein–Gordon partial differential equations. In this context it is worthwhile mentioning that the scattering of wobblers in the double sine–Gordon model has been studied by Campos and Mohammadi [78].

In this paper we shall continue this line of research by investigating asymmetric scattering between wobblers in two different scenarios, which we consider representative in this context. The scattering processes addressed in previous works involve wobblers which evolve with the same phase. This implies that constructive interference between the shape modes associated to each wobbler takes place at the collision. In this work we propose to analyze the scattering between wobblers with opposite phases, such that destructive interference between the vibrational modes now occurs at impact. The second scenario is described by the collision between a wobbler and an unexcited kink. This allows us to monitor the transfer of vibrational energy from the wobbler to the kink. We will show that the fractal structures associated with resonance phenomenon in these two cases display very different patterns. The motivation to explore these new scenarios is twofold. From a theoretical point of view, this analysis provides us with new data on the behavior of the resonance phenomenon. In this article it will be shown that the difference between the wobbling phases associated with the colliding wobblers on impact determines the efficiency of energy transfer between the different eigenmodes. The collective coordinate method could be used to examine this framework by considering initial configurations in which the wobbling phases of the moving wobblers are arbitrary. On the other hand, the scattering between wobblers seems to be the natural situation found in a real physical application where non-linear phenomena are explained by the presence of kinks. During the creation of kinks in a phase transition, the vibrational and zero modes of these topological defects will be excited. Therefore, the relevant physical scenario must involve the presence of wobbling kinks that collide with each other with different initial conditions. In a real physical material it is difficult to observe if the energy lumps (described by topological defects) involve vibrational modes and if they are excited or not. However, as it will be shown in this paper, if a scattering process is detected where the final velocities of two scattered extended particles are greater than the collision velocities, then it is clear that the vibration modes must play a relevant role in these phenomena. In this sense, the differences in the fractal structures and, in general, the differences between the velocity diagrams associated with different initial conditions could provide us with an image of the phenomena that occur in real applications.

The organization of this paper is as follows: in Section 2 the theoretical background of the  $\phi^4$  model together with the analytical description of kinks and wobblers is introduced. Kink–antikink scattering is also discussed, which allows us to describe the numerical methods to study the problem. Section 3 is dedicated to study scattering between wobblers with opposite phase, whereas the collision between a wobbler and an unexcited kink is addressed in Section 4. Finally, some conclusions are drawn in Section 5.

## 2. The $\phi^4$ model: kinks and wobblers

The dynamics of the  $\phi^4$  model in (1+1) dimensions is governed by the action

$$S = \int d^2x \mathcal{L}(\partial_\mu \phi, \phi) \quad , \tag{1}$$

where the Lagrangian density  $\mathcal{L}(\partial_\mu \phi, \phi)$  is of the form

$$\mathcal{L}(\partial_\mu \phi, \phi) = \frac{1}{2} \partial_\mu \phi \partial^\mu \phi - V(\phi) \quad \text{with} \quad V(\phi) = \frac{1}{2}(\phi^2 - 1)^2 \quad . \tag{2}$$

The use of dimensionless field and coordinates, as well as Einstein summation convention, are assumed in expressions (1) and (2). Here, the Minkowski metric  $g_{\mu\nu}$  has been set as  $g_{00} = -g_{11} = 1$  and  $g_{12} = g_{21} = 0$ . Therefore, the non-linear



Klein–Gordon partial differential equation

$$\frac{\partial^2 \phi}{\partial t^2} - \frac{\partial^2 \phi}{\partial x^2} = -2\phi(\phi^2 - 1) \tag{3}$$

characterizes the time-dependent solutions of this model. The energy–momentum conservation laws imply that the total energy and momentum

$$E[\phi] = \int dx \left[ \frac{1}{2} \left( \frac{\partial \phi}{\partial t} \right)^2 + \frac{1}{2} \left( \frac{\partial \phi}{\partial x} \right)^2 + V(\phi) \right] \quad , \quad P[\phi] = - \int dx \frac{\partial \phi}{\partial t} \frac{\partial \phi}{\partial x} \quad , \tag{4}$$

are system invariants. The kinks/antikinks (+/−)

$$\phi_k^{(\pm)}(t, x; x_0, v_0) = \pm \tanh \left[ \frac{x - x_0 - v_0 t}{\sqrt{1 - v_0^2}} \right] \tag{5}$$

are traveling solutions of (3), whose energy density is localized around the kink center  $x_c = x_0 + v_0 t$  (the value where the field profile vanishes). The parameter  $v_0$  can be interpreted as the kink velocity. Is well known that the solutions (5) are topological defects because they asymptotically connect the two elements of the set of vacua  $\mathcal{M} = \{-1, 1\}$ . These solutions have a normal mode of vibration. When this mode is excited the size of these solutions (called *wobbling kinks* or *wobblers*) periodically oscillate with frequency  $\omega = \sqrt{3}$ . This fact has been numerically checked and has been analytically proved in the linear regime. The spectral problem

$$\mathcal{H} \psi_{\omega^2}(x) = \omega^2 \psi_{\omega^2}(x)$$

of the second order small fluctuation operator associated with the static kink/antikink,

$$\mathcal{H} = - \frac{d}{dx^2} + 4 - 6 \operatorname{sech}^2(x - x_0), \tag{6}$$

involves the shape mode

$$\psi_{\omega^2=3}(x; x_0) = \sinh(x - x_0) \operatorname{sech}^2(x - x_0)$$

with eigenvalue  $\omega^2 = 3$ . The discrete spectrum of the operator (6) is completed with the presence of a zero mode

$$\psi_{\omega^2=0}(x; x_0) = \operatorname{sech}^2(x - x_0) = \left. \frac{\partial \phi_k^{(+)}}{\partial x} \right|_{t=0, v_0=0} \quad ,$$

whereas the continuous spectrum emerges at the threshold value  $\omega^2 = 4$ .

As a result of this linear analysis, the expression

$$\phi_W^{(\pm)}(t, x; x_0, v_0, \omega, a, \delta) = \pm \tanh \left[ \frac{x - x_0 - v_0 t}{\sqrt{1 - v_0^2}} \right] + a \sin(\omega t + \delta) \operatorname{sech} \left[ \frac{x - x_0 - v_0 t}{\sqrt{1 - v_0^2}} \right] \tanh \left[ \frac{x - x_0 - v_0 t}{\sqrt{1 - v_0^2}} \right] \tag{7}$$

is a good approximation of a traveling wobbler in the linear regime  $a \ll 1$ . Note that  $\phi_W^{(-)}(t, x)$  describes a *wobbling antikink* (or *antiwobbler*).

The maximum deviation of the wobbler (7) from the kink (5) takes place at the points

$$x_M^{(\pm)} = x_c \pm \sqrt{1 - v_0^2} \operatorname{arccosh} \sqrt{2} \quad , \tag{8}$$

where the relation

$$\left| \phi_W(x_M^{(\pm)}) - \phi_k(x_M^{(\pm)}) \right| = \frac{1}{2} |a|$$

holds. An optimized numerical strategy to measure the wobbling amplitude of a traveling wobbler is to monitor the profile of these solutions at the points (8). By using fourth order perturbation theory in the expansion parameter  $a$ , it has been proven that  $a$  depends on time,  $a = a(t)$ , and decays following the expression

$$|a(t)|^2 = \frac{|a(0)|^2}{1 + \omega \xi_l |a(0)|^2 t}, \tag{9}$$

where  $\xi_l$  is a constant. However, when the initial wobbling amplitude  $a(0)$  is small, the decay is very slow and becomes appreciable only after a long time  $t \sim |a(0)|^{-2}$  [74,75].

The scattering between a kink and an antikink has been thoroughly analyzed in the physical and mathematical literature during the last decades. A kink and antikink which are well separated are pushed together with initial collision velocity  $v_0$ . Taking into account the spatial reflection symmetry of the system the kink can be located at the left of

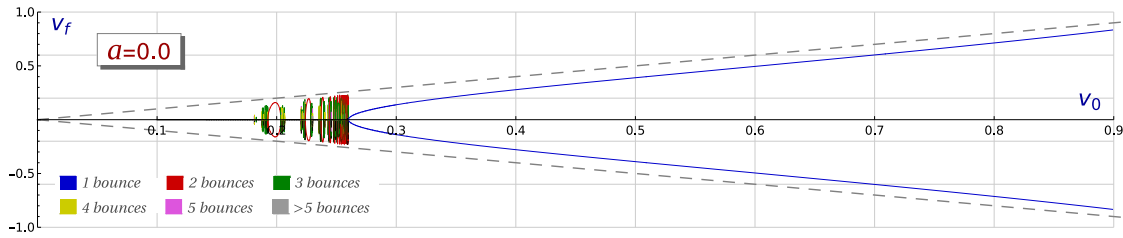


**Fig. 1.** Final versus initial velocity diagram for the kink–antikink scattering. The final velocity of the bion is assumed to be zero in this context. The color code is used to specify the number of bounces suffered by the kinks before escaping.

the antikink or vice versa. For very small values of the time  $t$  (with respect to the impact time), the latter scenario is characterized by the concatenation

$$\Phi_{KK}(t, x; x_0, v_0) = \phi_K^{(\pm)}(t, x; x_0, v_0) \cup \phi_K^{(\mp)}(t, x; -x_0, -v_0) \tag{10}$$

for  $x_0 \gg 0$ , where we have introduced the notation

$$\phi_K^{(\pm)}(t, x; x_0, v_0) \cup \phi_K^{(\mp)}(t, x; -x_0, -v_0) \equiv \begin{cases} \phi_K^{(\pm)}(t, x; x_0, v_0) & \text{if } x \leq 0, \\ \phi_K^{(\mp)}(t, x; -x_0, -v_0) & \text{if } x > 0. \end{cases} \tag{11}$$

The initial separation between the kink and the antikink is equal to  $2x_0$ . The configuration (10) defines the initial conditions of the scattering problem. As it is well known, there exist two different scattering channels in this case: (1) *bion formation*, where kink and antikink end up colliding and bouncing back over and over again, and (2) *kink reflection*, where kink and antikink collide, bounce, and finally recede with respective final velocities  $v_{f,L}$  and  $v_{f,R}$  in the opposite direction to which they were initially traveling. These scattering regimes are predominant, respectively, for low and high values of the initial velocity  $v_0$ . In Fig. 1 the two final velocities  $v_{f,L}$  and  $v_{f,R}$  are plotted as a function of the incident velocity  $v_0$ .

From the spatial reflection symmetry exhibited by the initial configuration (10) it is clear that  $v_{f,L} = -v_{f,R}$  and that the velocity of a bion must be zero. Therefore, the velocity diagram in Fig. 1 is symmetric with respect to the  $v_0$ -axis. In the next sections we shall address asymmetric scattering events where this symmetry is lost and  $|v_{f,L}| \neq |v_{f,R}|$  in general. The fascinating property found in this scattering problem is that the transition between the two previously mentioned regimes is ruled by a fractal structure where the bion formation and the kink reflection regimes are infinitely interlaced. The kink reflection windows included in this initial velocity interval involve scattering processes where kink and antikink collide and bounce back a finite number of times exchanging energy between the zero and shape modes before definitely moving away. These processes involve the so called *resonant energy transfer mechanism*.

For the previously mentioned  $n$ -bounce processes (with  $n \geq 2$ ) it is clear that after the first impact the subsequent collisions correspond to scattering processes between wobblers because, in general, the collision between kinks causes the excitation of their shape modes. Taking into account the spatial reflection symmetry of the problem, the wobbling amplitudes and phases of the colliding wobblers are equal. Therefore, these events are characterized by an initial configuration of the form

$$\Phi_{WW}(t, x; x_0, v_0, \omega, a, \delta) = \phi_W^{(\pm)}(t, x; x_0, v_0, \omega, a, \delta) \cup \phi_W^{(\mp)}(t, x; -x_0, -v_0, \omega, a, \delta). \tag{12}$$

This scattering problem was studied numerically in [77]. By mirror symmetry, it can be assumed that the phases of the shape modes of the traveling wobblers are also the same at the impact time, so constructive interference takes place in the collision. As a consequence, it is found that the fractal pattern enlarges and becomes more complex as the value of the initial wobbling amplitude  $a$  increases. Another interesting property in this context is the emergence of isolated 1-bounce windows, which are not present in the original kink–antikink scattering. It is clear that the scattering between wobblers characterized by the initial configuration (12) is relevant in studying the resonant energy transfer mechanism in this problem. However, because of the spatial reflection symmetry of this type of processes, wobblers transfer the same amount of energy to each other at the collision, that is, the scattered wobblers travel away with the same final speeds and wobbling amplitudes. In this work we are interested in analyzing more general scattering events where the energy transfer mechanism becomes asymmetric with respect to the traveling wobblers.

The first type of processes which could involve novel properties in this framework is the collision between two wobblers with opposite phase. This scenario can be characterized by the initial configuration

$$\Phi_{W\tilde{W}}(t, x; x_0, v_0, \omega, a, \delta) = \phi_W^{(\pm)}(t, x; x_0, v_0, \omega, a, \delta) \cup \phi_{\tilde{W}}^{(\mp)}(t, x; -x_0, -v_0, \omega, a, \pi + \delta). \tag{13}$$

We have employed the notation  $W\tilde{W}$  as subscript of  $\Phi$  in (13) simply to emphasize that the wobblers have different initial phases and to distinguish this configuration from (12). In this case it is assumed that the wobblers evolve preserving a phase difference of  $\pi$ , giving place to destructive interference in the excitation of the shape modes of each wobbler when they collide. It is expected that the final versus initial velocity diagrams associated to these scattering events will be

affected by this fact and that they will be very different from those found in the constructive interference scenario (12), analyzed in [77].

Another important situation which deserves attention is the scattering between a wobbler and a kink. These asymmetric events can be characterized by the initial configuration

$$\Phi_{WK}(t, x; x_0, v_0, \omega, a, \delta) = \phi_W^{(\pm)}(t, x; x_0, v_0, \omega, a, \delta) \cup \phi_K^{(\mp)}(t, x; -x_0, -v_0), \tag{14}$$

where without loss of generality the non-excited antikink/kink  $\phi_K^{(\mp)}(t, x; -x_0, -v_0)$  has been placed to the right of the wobbler/antiwobbler. This situation allows us to analyze how the vibrational energy is transferred to the non-excited kink in a better way than previously.

In order to study the scattering between kinks and wobblers in the two previously described scenarios, in the present work we shall employ numerical approaches based on the discretization of the partial differential Eq. (3) with different initial conditions determined by the configurations (13) and (14). The particular numerical scheme used here is a fourth-order explicit finite difference algorithm implemented with fourth-order Mur boundary conditions, which has been designed to address non-linear Klein–Gordon equations, see the Appendix in [54]. The linear plane waves are absorbed at the boundaries in this numerical scheme avoiding that radiation is reflected in the simulation contours. To rule out the presence of spurious phenomena attributable to the use of a particular numerical algorithm, a second numerical procedure is used to validate the results. This double checking has been carried out by means of an energy conservative second-order finite difference algorithm with Mur boundary conditions.

As previously mentioned, the initial settings for our scattering simulations are described by single solutions (kinks or wobblers) which are initially well separated, and are pushed together with initial collision velocity  $v_0$ . This situation is characterized by the concatenation (13) for the scattering between wobblers with opposite phase and by (14) for the scattering between a wobbler and a kink, both of them with  $x_0 \gg 0$ . These configurations verify the partial differential Eq. (3) in a very approximate way for very small values of the time when  $x_0 \gg 0$  and  $a \ll 1$ . Therefore,  $\Phi(t = 0)$  and  $\frac{\partial \Phi}{\partial t}(t = 0)$  provide the initial conditions of our scattering problem.

In particular, our numerical simulations have been carried out in a spatial interval  $x \in [-100, 100]$  where the centers of the single solutions are initially separated by a distance  $d = 2x_0 = 30$ . Simulations have been performed for  $v_0 \in [0.04, 0.9]$  with initial velocity step  $\Delta v_0 = 0.001$ , which is decreased to  $\Delta v_0 = 0.00001$  in the resonance interval.

At this point it is worthwhile mentioning that the expression (7) is only an approximation of the exact wobbler solution. When this expression is employed as initial condition in the Klein–Gordon Eq. (3) a small amount of radiation is emitted for a very small period of time. In this time interval the approximate solution (7) decays to the exact wobbler. When considering a traveling wobbler, this radiation emission can cause a very small change in its velocity. This effect takes place when  $\delta \neq 0, \pi$  in the expression (7) and it is maximized for  $\delta = \pm\pi/2$ . In order to avoid this effect we shall implement initial conditions by setting  $\delta = 0$  in the configurations (13) and (14). By taking this restriction we guarantee that the traveling wobbler involved in (14) continues to move with velocity  $v_0$  after the initial radiation emission. As mentioned above, this effect is very small and unnoticeable in the final versus initial velocity diagrams. However, we shall analyze the velocity difference of the resulting wobblers and in this context it is better to avoid this influence. On the other hand, for the values  $\delta = 0$  or  $\delta = \pi$  the decay of the approximation (7) to the real wobbler induces a very small variation in its wobbling amplitude. This effect also is very small and does not affect the global properties of the scattering processes discussed in this paper. An alternative scheme to implement initial configurations (14) with non-vanishing initial phases is to find an approximately equivalent configuration with vanishing phase. This can be obtained, for example, taking into account that

$$\phi_W^{(\pm)}(t, x; x_0, v_0, \omega, a, \delta) = \phi_W^{(\pm)}\left(t - \frac{\delta}{\omega}, x; x_0 - \frac{\delta v_0}{\omega}, v_0, \omega, a, 0\right) .$$

### 3. Scattering between wobblers with opposite phases

In this section we shall analyze the asymmetric scattering between two wobblers whose shape modes have the same amplitude but they have opposite phases with respect to our inertial system, which is located at the center of mass. In this context, a wobbler and an anti-wobbler approach each other with initial velocity  $v_0$  and  $-v_0$ , respectively. They evolve preserving the phase difference of  $\pi$  and collide giving place to a destructive interference between the shape modes of the involved wobblers. Fig. 2 shows the final versus initial velocity diagrams for three representative values of the initial wobbling amplitude,  $a = 0.04$ ,  $a = 0.1$ , and  $a = 0.2$ .

Unsurprisingly, the only scattering channels to emerge in this new scenario are still bion formation and kink reflection. As before, the former is predominant for small values of the initial velocity  $v_0$ , while the latter is found for large values. However, these velocity diagrams display some important differences regarding the scattering of wobblers addressed in [77], where the corresponding shape modes have the same phase and a constructive interference occurs in the collision. In this new context, the destructive interference avoids the emergence of isolated 1-bounce windows (at least for non-extreme values of  $a$ ), as can be observed in Figs. 2 and 3. The suppression of this mechanism implies that the fractal structure width does not increase.

In Fig. 3 the evolution of the fractal pattern can be visualized as the value of the initial amplitude  $a$  increases. First, we can observe that the value of the critical velocity  $v_c$  varies very slowly as the initial amplitude  $a$  grows. For instance,

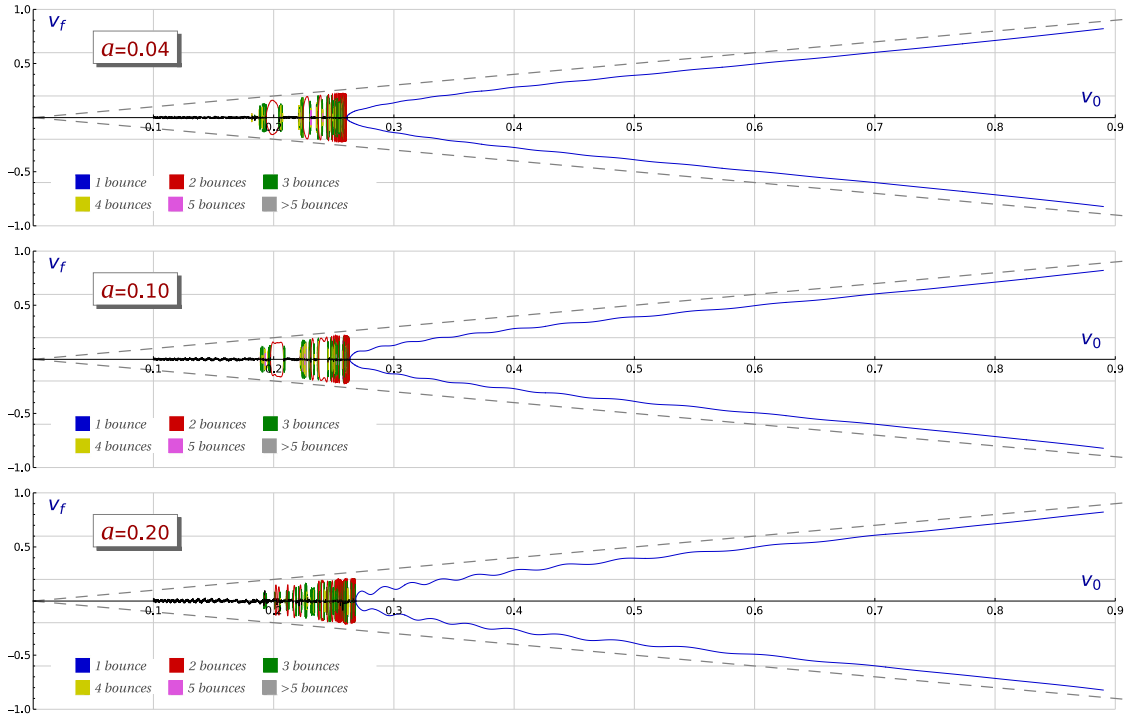


**Fig. 2.** Final versus initial velocity diagram for the scattering between two wobblers with opposite phase for the values of the wobbling amplitude  $a = 0.04$ ,  $a = 0.1$  and  $a = 0.2$ . The color code is used to specify the number of bounces suffered by the kinks before escaping. The black curves determine the final velocity of the bion formed for low initial velocities.

$v_c \approx 0.2601$  for  $a = 0.02$ , whereas  $v_c \approx 0.2681$  for  $a = 0.2$ , following a linear dependence in  $a$  for intermediate values. Second, it can be seen that the 2-bounce windows are deformed as the value of  $a$  increases and get broken up into smaller 2-bounce windows. The first 2-bounce window shown in Fig. 3 for  $a = 0.04$  can be used to illustrate this mechanism. This window gets distorted when  $a = 0.12$  and split into two pieces for  $a = 0.14$ . In turn, one of these pieces is divided again into two new 2-bounce windows for  $a = 0.20$ . Third, spontaneous generation of  $n$ -bounce windows with  $n \geq 2$  can also be identified in the sequence of graphics included in Fig. 3. For instance, for  $a = 0.12$  a small 3-bounce window spontaneously emerges in the interval  $[0.21585, 0.2174]$ , which was occupied by the bion formation regime for previous values of  $a$ . Subsequently, this window is split into two parts, resulting in a 2-bounce window in the middle for  $a = 0.14$ , which is surrounded by new  $n$ -bounce windows. This new 2-bounce window gets bigger as  $a$  increases and finally splits into two new 2-bounce windows once more, as one can see from the graphics for  $a = 0.20$ . This window generation mechanism could explain the clustering of 2-bounce windows that arise around the  $v_0 = 0.2566$  value for  $a = 0.20$ .

Another important characteristic of this type of scattering processes is that the final velocities of the scattered wobblers are different. This behavior is not surprising because the initial configuration (13) is not symmetric. Recall that the initial wobbling phases of the colliding wobblers are different. This velocity difference is very small, and therefore not noticeable in the velocity diagrams shown in Fig. 2. In order to emphasize this feature we define the magnitude

$$\Delta v_f = |v_{f,R}| - |v_{f,L}|, \tag{15}$$

as the difference between the final speed  $|v_{f,R}|$  of the rightward traveling wobbler and the final speed  $|v_{f,L}|$  of the leftward traveling wobbler. Positive values of  $\Delta v_f$  imply that the wobbler scattered to the right travels faster than the wobbler scattered to the left, whereas negative values describe the reverse situation. In Fig. 4, the magnitude  $\Delta v_f$  is plotted as a function of the initial velocity  $v_0$  and the wobbling amplitude  $a$ . There, we can see that  $\Delta v_f$  has oscillating behavior, which means that there are alternating initial velocity windows in which the wobbler traveling from the left travels faster than the wobbler traveling from the right and vice versa. The amplitudes of the oscillations exhibited by  $\Delta v_f$  increase as the value of the parameter  $a$  increases. This is reasonable because the vibrational energy stored in the shape mode is greater for bigger values of  $a$  and the resonant energy transfer mechanism may deflect a greater amount of this energy into the kinetic energy pool. However, the most remarkable property exhibited by Fig. 4 is that the zeros of  $\Delta v_f$ , the initial velocity values for which the two wobblers disperse with the same velocity, are approximately independent of the initial amplitude  $a$ . This behavior is precisely followed for sufficiently large values of  $v_0$ , where the effect of the resonance regime is not noticed (approximately for  $v_0 \geq 0.3$  in Fig. 4).

In Table 1, the zeros  $\tilde{v}_k$  of the final velocity difference  $\Delta v_f$  (explicitly computed for the case  $a = 0.04$ ) are shown in the non-resonance regime. The values  $\tilde{v}_k$  correspond to the nodes of the oscillations found in Fig. 4, which have been indicated

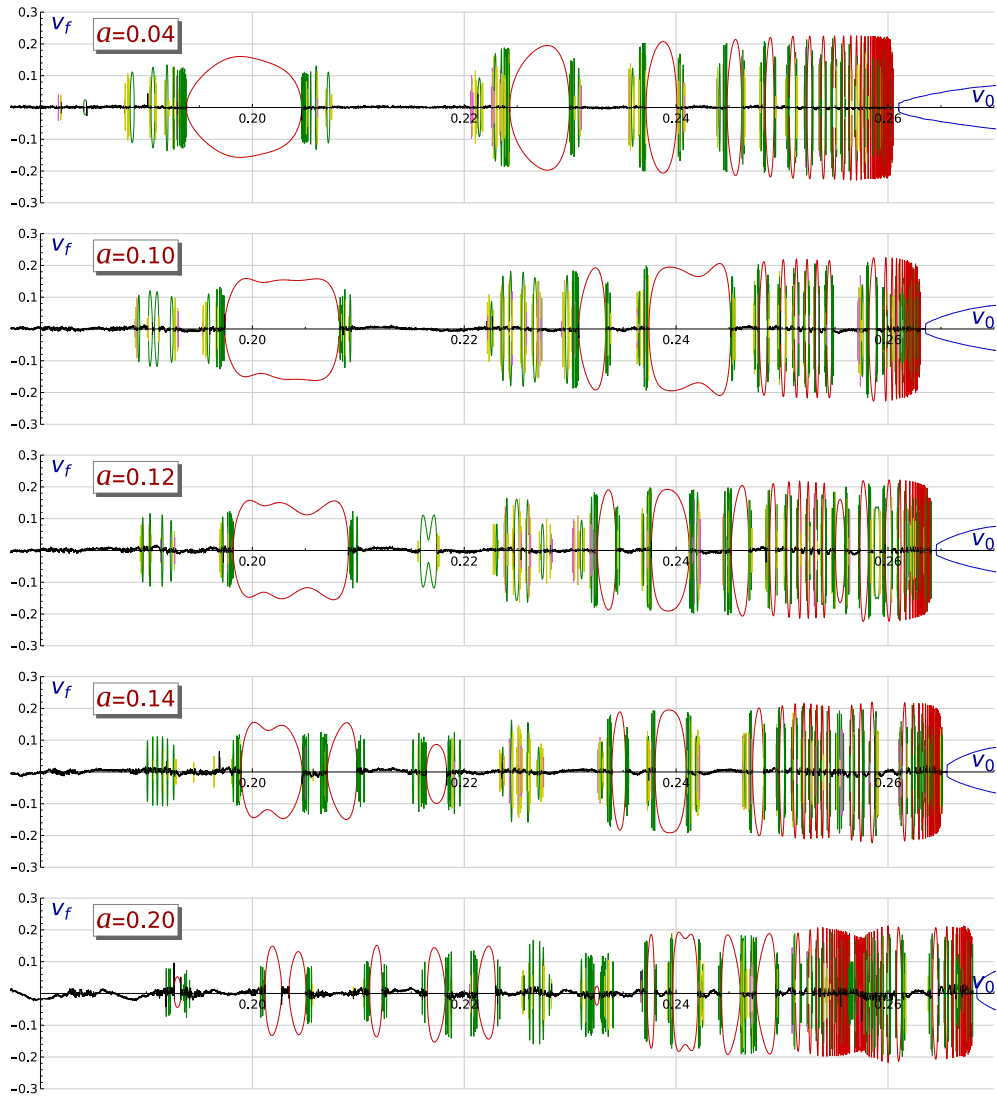


Fig. 3. Evolution of the fractal pattern found in the velocity diagrams associated to the scattering between wobblers with opposite phases as a function of the initial wobbling amplitude  $a$ .

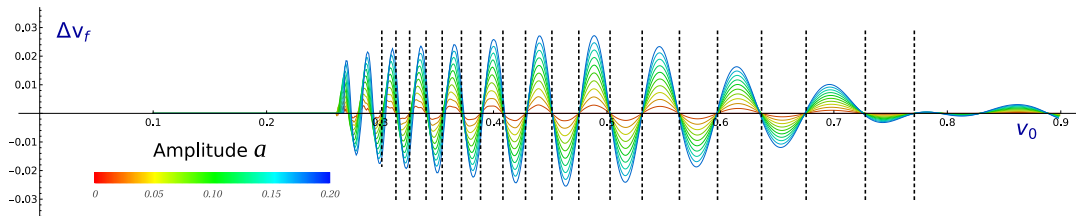


Fig. 4. Final velocity difference  $\Delta v_f$  of the scattered wobblers as a function of the collision velocity  $v_0$  and the initial wobbling amplitude  $a$  for the scattering of two wobblers with opposite phase. Recall that  $\Delta v_f = 0$  for  $a = 0$  due to spatial reflection symmetry. For the sake of clarity,  $n$ -bounce processes with  $n \geq 2$  have not been included in the plot. The vertical dashed lines mark the zeros  $\tilde{v}_k$  of the final velocity difference  $\Delta v_f$ .

by means of vertical dashed lines. The location of these points seems to depend mainly on the value of the wobbling phase when the collision between the wobblers occurs. This conjecture is heuristically supported by the following simple argument. Remember that  $x_0$  denotes the initial position of the kink center, while  $\omega$  represents the wobbling frequency. As previously discussed, the values  $x_0 = 15$  and  $\omega = \sqrt{3}$  have been implemented for our numerical simulations. Let  $v_0$  be the initial wobbler approach velocity. In the point particle approximation the collision would happen at the time  $t_l = \frac{x_0}{v_0}$ . We must bear in mind that there are several factors in the actual dynamics which break the precision of this assumption. For example, the interaction between the kinks and/or wobblers can make the collision velocity  $v_0$  vary. We shall assume

**Table 1**

Comparison between the zeros  $\tilde{v}_k$  of the final velocity difference  $\Delta v_f$  and the values  $V_k = f_k(v_0, \pi)$  obtained by using Eq. (17) for the scattering between wobblers with opposite phase and initial wobbling amplitude  $a = 0.04$ .

$k$	$\tilde{v}_k$	$V_k$
0	0.301538	0.301538
1	0.313991	0.313224
2	0.326057	0.325797
3	0.340542	0.339354
4	0.354757	0.354006
5	0.371738	0.369877
6	0.388575	0.387110
7	0.408291	0.405864
8	0.428219	0.426323
9	0.451464	0.448689
10	0.475173	0.473188
11	0.502713	0.500069
12	0.531044	0.529591
13	0.563882	0.562022
14	0.597459	0.597606
15	0.636259	0.636531
16	0.675558	0.678857
17	0.727740	0.724418
18	0.770909	0.772667

that the phase of the wobbler at the instant  $t_i$  can be expressed as

$$\varphi(v_0) = c(x_0) \frac{x_0}{v_0} \omega \sqrt{1 - v_0^2} + \delta.$$

where  $c(x_0)$  is a correction factor which is included to incorporate the previously mentioned behavior. The main assumption in this case is that  $c(x_0)$  does not depend on  $v_0$ . If we think about the initial impact velocity  $v$  as variable, then it makes sense to consider  $\varphi(v) = c(x_0) \frac{x_0}{v} \omega \sqrt{1 - v^2} + \delta$ . Those phenomena depending only on the wobbling phase must exhibit the periodicity

$$\varphi(v_0) - \varphi(v) = T k, \quad k \in \mathbb{Z}, \tag{16}$$

where  $T$  is the periodicity associated to our problem. In general,  $T = 2\pi$  but in the present scenario where we are interested in the zeros  $\tilde{v}_k$  of  $\Delta v_f$  the symmetry of the initial configuration leads to the choice  $T = \pi$ . From (16) we conclude that the discrete set of velocities

$$f_k(v_0, T) = \frac{v_0 x_0 \omega}{\sqrt{\frac{k^2 T^2 v_0^2}{4c(x_0)^2} - \frac{T}{c(x_0)} k v_0 x_0 \omega \sqrt{1 - v_0^2} + x_0^2 \omega^2}}, \quad k \in \mathbb{Z}, \tag{17}$$

must share similar features. The nodes  $\tilde{v}_k$  of  $\Delta v_f$  can be found approximately by using Eq. (17). In Table 1 (third column) the values  $V_k = f_k(v_0, \pi)$ , obtained by using formula (17) taking as initial input  $v_0 = \tilde{v}_0 = 0.301538$ , are included. The value  $c(x_0)$  has been adjusted to  $c(x_0) = 0.465$ . The comparison between the data allows us to conclude that the previous conjecture is satisfied at least for intermediate values of the initial velocity. Of course, the nonlinear nature of the problem makes the argument only an approximation to the actual behavior. This is clear for very large values of the collision velocity. In this regime the amplitudes of the oscillations of  $\Delta v_f$  are very attenuated compared to intermediate values of  $v_0$ . For these cases radiation can play a predominant role in the scattering processes.

At this point it is worthwhile mentioning that the zeros  $\tilde{v}_k$  introduced in Table 1 have been computed when  $\delta = 0$  in the initial configuration (13). The particular location of these points depends on the initial phase  $\delta$  introduced in (13), although it is clear that the same pattern is periodically reproduced for the values  $\delta + kT$  with  $k \in \mathbb{Z}$ .

Now that the final velocities of the scattered wobblers have been examined, we shall analyze the behavior of the wobbling amplitude of these evolving topological defects. In Fig. 5, the oscillation amplitudes of the wobblers moving to the left and to the right are represented as a function of the initial velocity  $v_0$  and the initial amplitude  $a$ . There it can be seen that this magnitude oscillates with respect to kink–antikink scattering. The variation of these oscillations increase with parameter  $a$ . Furthermore, the amplitudes of the resulting wobblers decrease. When the oscillation amplitude of the wobbler moving to the left reaches a maximum as a function of the initial velocity  $v_0$ , the oscillation amplitude of the wobbler moving to the right is minimized and vice versa. The asymmetry of the initial configuration (13) causes the wobblers to vibrate at different amplitudes in general. On the other hand, there are some points in the graphs shown in Fig. 5 where the amplitudes of the two wobblers coincide. Surprisingly, these points coincide with the zeros  $\tilde{v}_k$  of the final velocity difference  $\Delta v_f$  (as we can observed by means of the vertical dashed lines plotted in Fig. 5). In conclusion, for the initial velocities  $\tilde{v}_k$  the scattered wobblers travel with the same velocity and vibrate with the same wobbling amplitude.

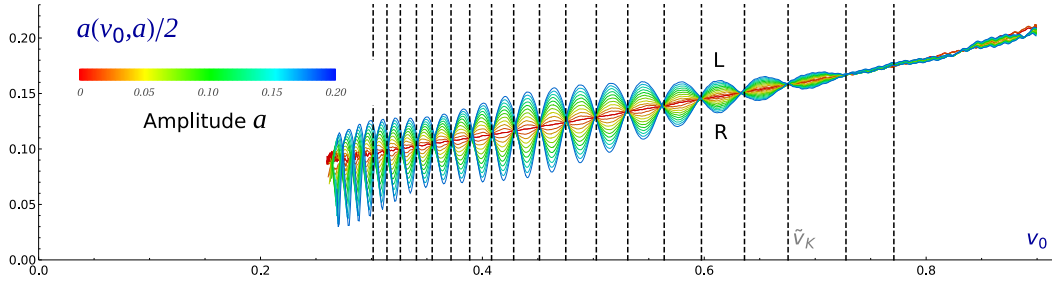


**Fig. 5.** Graphics of the final wobbling amplitudes of the wobblers scattered to the left and to the right as a function of the initial velocity  $v_0$  and the initial amplitude  $a$ . For the sake of clarity,  $n$ -bounce processes with  $n \geq 2$  have not been included. The vertical dashed lines mark the zeros  $\tilde{v}_k$  of the final velocity difference  $\Delta v_f$ . The letters  $L$  and  $R$  label the smooth amplitude functions associated with wobblers traveling left and right, respectively.

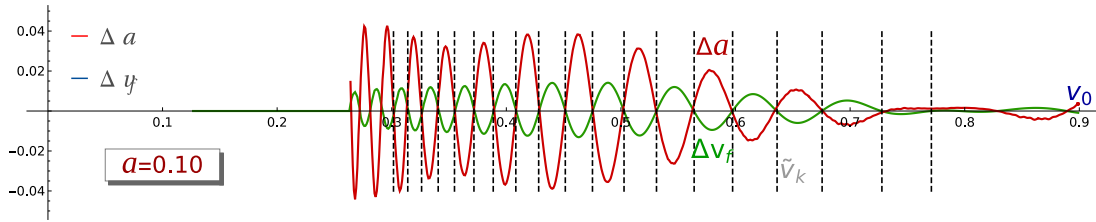


**Fig. 6.** Graphics of  $\Delta v_f$  (final velocity difference) and  $\Delta a$  (final wobbling amplitude difference) as functions of the initial collision velocity  $v_0$  for the scattering between wobblers with opposite phase with  $a = 0.10$ .  $n$ -bounce processes with  $n \geq 2$  have not been included. The vertical dashed lines mark the zeros  $\tilde{v}_k$  of  $\Delta v_f$ .

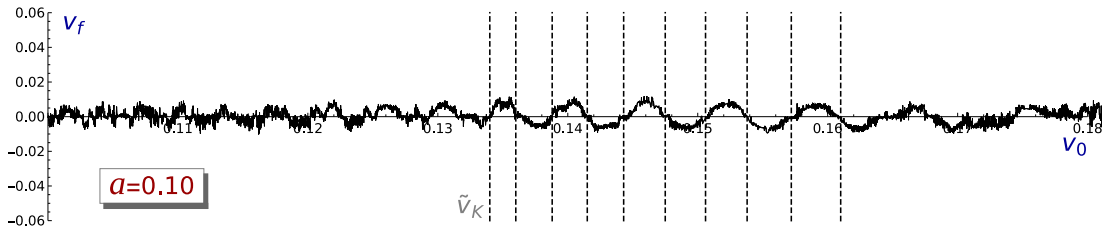


**Fig. 7.** Final bion velocity as a function of the initial velocity  $v_0$  in the interval  $v_0 \in [0.10, 0.18]$  for the scattering between two wobblers with opposite phase and the initial wobbling amplitude  $a = 0.10$ . The vertical dashed lines mark some of the nodes of the curve.

In order to explore the relation between the final velocity and the final wobbling amplitude of the scattered wobblers, we define the amplitude difference

$$\Delta a = \frac{1}{2} [a_{f,R} - a_{f,L}] , \tag{18}$$

where  $a_{f,R}$  and  $a_{f,L}$  are, respectively, the final oscillation amplitudes of the wobblers moving to the right and to the left.  $\Delta a > 0$  means that the wobbler scattered to the right vibrates more strongly than that moving to the left, whereas  $\Delta a < 0$  describes the opposite situation. Fig. 6 shows simultaneously the final velocity and the amplitude differences  $\Delta v_f$  and  $\Delta a$ , as functions of the initial velocity  $v_0$  for the particular value  $a = 0.10$ . It can be seen that when one scattered wobbler gains more kinetic energy than the other, it obtains less vibrational energy, and vice versa. The values  $\tilde{v}_k$  are interpreted as the collision velocities for which the final velocities and the wobbling amplitudes of the scattered wobblers are the same.

Finally, another consequence of the asymmetry of these scattering events is that the bion (formed as a bound state between the two colliding wobblers) can now move with certain final non-vanishing velocity after the impact. This velocity will be very small and for this reason it is sometimes difficult to compute its magnitude numerically. In Fig. 7 the region of the velocity diagram introduced in Fig. 2 for  $a = 0.10$  with  $v_0 \in [0.10, 0.18]$  has been enlarged to illustrate the behavior of the bion velocity. Again, we find an oscillating pattern, clearly seen in Fig. 7 for the interval  $v_0 \in [0.13, 0.16]$ . Also, it turns out that the formula (17) still governs this oscillating behavior. In the previously mentioned range of  $v_0$ , vertical dashed lines have been plotted to approximately mark the location of the nodes of the bion velocity. The values used correspond to the initial velocities  $v_1 \approx 0.134$ ,  $v_2 \approx 0.1364$ ,  $v_3 \approx 0.1388$ ,  $v_4 \approx 0.1415$ ,  $v_5 \approx 0.1443$ ,  $v_6 \approx 0.1475$ ,  $v_7 \approx 0.1506$ ,  $v_8 \approx 0.1538$ ,  $v_9 \approx 0.1572$  and  $v_{10} \approx 0.161$ , which can be approximately reproduced by (17).

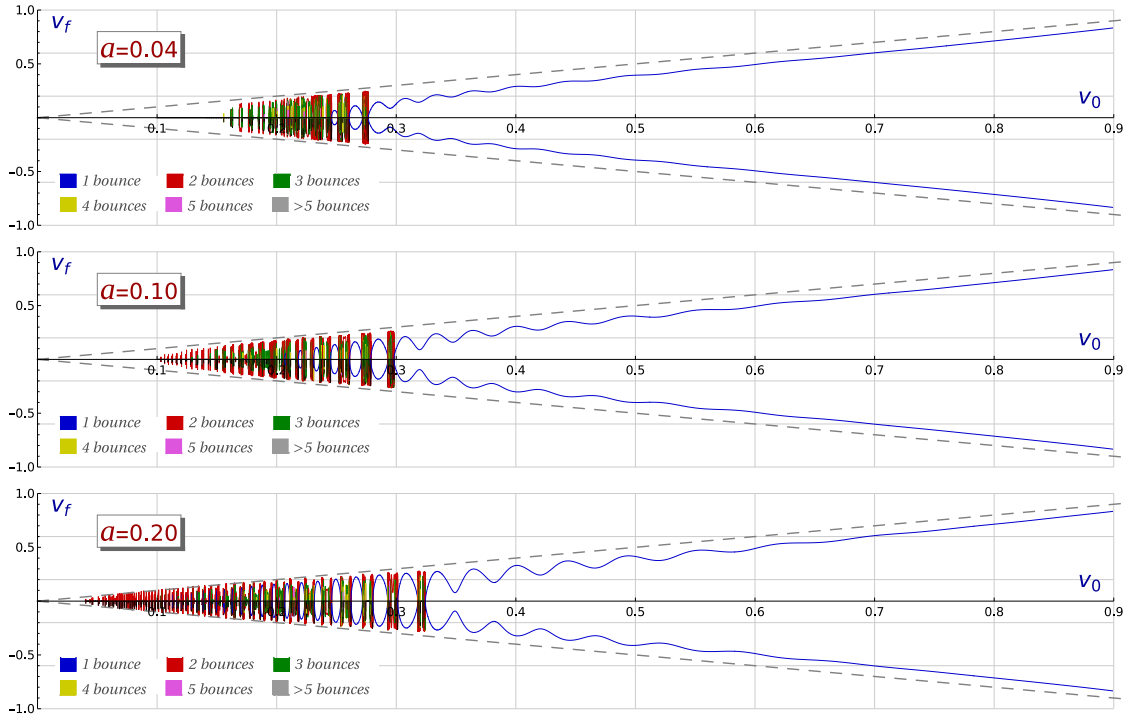


**Fig. 8.** Final versus initial velocity diagram for the wobbler–antikink scattering for the values of the wobbling amplitude  $a = 0.04$ ,  $a = 0.10$  and  $a = 0.20$ . The color code is used to specify the number of bounces suffered by the kinks before escaping.

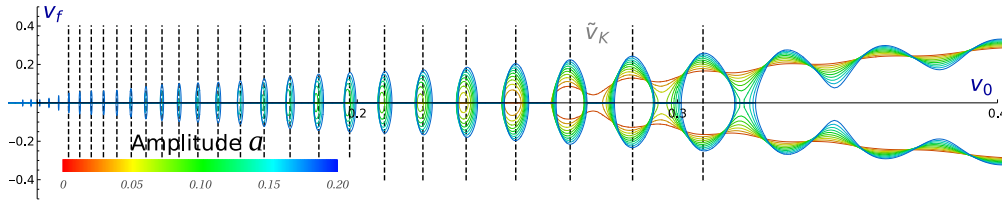


**Fig. 9.** Velocity diagrams for the wobbler–antikink scattering showing the emergence and location of the isolated 1-bounce windows as the value of the wobbling amplitude increases. The vertical dashed lines mark the values of  $v_0$  at the center of the 1-bounce windows for the extreme case  $a = 0.2$ . For the sake of clarity,  $n$ -bounce processes with  $n \geq 2$  have not been included.

#### 4. Scattering between a kink and a wobbler

In this section we shall study the scattering between a wobbler and a kink. This scenario is characterized by the concatenation (14). With the first choice of signs, this configuration describes a wobbler and an antikink which travel respectively with velocities  $v_0$  and  $-v_0$ . The rightward traveling wobbler and the leftward traveling antikink approach each other, collide, and bounce back. As usual, the *formation of a bion* and the *reflection of the solutions* complete the list of possible scattering channels. In the reflection regime, the initially unexcited antikink becomes an anti-wobbler after the collision because, in general, the shape mode of this solution is excited. Therefore, after the impact two wobblers emerge moving away with different final velocities in our inertial system. The goal of this study is to analyze the transfer of the vibrational and kinetic energies between the resulting wobblers. The dependence of the final velocities of the scattered extended particles on the initial velocity  $v_0$  has been graphically represented in Fig. 8 for the cases  $a = 0.04$ ,  $a = 0.1$ , and  $a = 0.2$ .

Some of the most relevant characteristics described in [77] for the scattering between wobbling kinks are also found in the present framework, such as the emergence of isolated 1-bounce windows and the growing complexity of the fractal pattern as the initial amplitude  $a$  of the originally rightward-traveling wobbler increases. It is also worthwhile mentioning the presence of oscillations in the 1-bounce tail arising for large values of the initial velocity. However, these features are less accentuated in this scenario. The reason for this behavior lies in the fact that the constructive interference is maximized when the wobblers with the same wobbling phase collide. In particular, we can observe the existence of two isolated 1-bounce windows for the case  $a = 0.04$ . They occupy approximately the region  $[0.2458, 0.2522] \cup [0.2607, 0.2717]$ . For  $a = 0.1$  six of these windows can be identified in  $[0.2068, 0.2085] \cup [0.2183, 0.2214] \cup [0.2310, 0.2358] \cup [0.2452, 0.2521] \cup [0.2610, 0.2709] \cup [0.2787, 0.2925]$ . Finally, the number of these



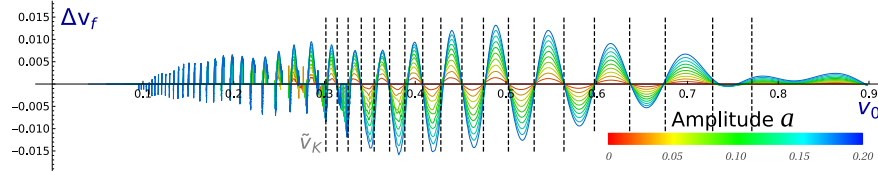


**Fig. 10.** Final velocity difference  $\Delta v_f$  of the scattered wobblers as a function of the collision velocity  $v_0$  and the initial wobbling amplitude  $a$  for the scattering of a wobbler and a kink.  $n$ -bounce processes with  $n \geq 2$  have not been included. The vertical dashed lines mark the zeros  $\tilde{v}_k$  of  $\Delta v_f$  displayed in Table 1.

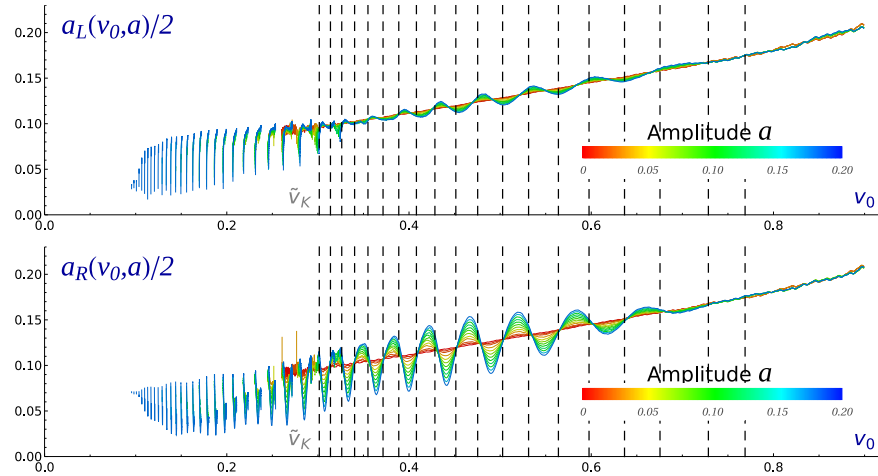


**Fig. 11.** Final wobbling amplitudes  $a_L$  and  $a_R$  of the wobblers scattered to the left (top) and to the right (bottom) as a function of the initial velocity  $v_0$  and the initial wobbling amplitude  $a$  of the colliding wobbler. The vertical dashed lines mark the zeros  $\tilde{v}_k$  of  $\Delta v_f$  displayed in Table 1.

windows explodes as the initial amplitude  $a$  grows. This can be observed in the velocity diagram for  $a = 0.2$  in Fig. 8. Some of the widest 1-bounce windows in this case arise in the set of intervals  $[0.2067, 0.2108] \cup [0.2185, 0.2234] \cup [0.2315, 0.2375] \cup [0.2460, 0.2535] \cup [0.2621, 0.2717] \cup [0.2804, 0.2928] \cup [0.3012, 0.3179]$ . From the list of 1-bounce windows above, it can be verified that once an isolated 1-bounce window emerges its location is approximately fixed (although its width grows slightly) as the initial wobbling amplitude  $a$  increases. This behavior can be checked in Fig. 9. Note that the deviation from the rule described above is a small translation of the center of these windows. In Fig. 9 the vertical dashed lines mark the values of the initial velocity which determine the centers of the 1-bounce windows for the extreme case  $a = 0.2$ . Once again, these velocities approximately follow relation (17), which reveals that the role of the phase of the evolving shape mode is predominant in this phenomenon.

The velocity diagrams shown in Fig. 8 also have some distinctive properties of their own. Because the scattering processes introduced in this section are asymmetric, the final velocities of the resulting wobblers are different, as well as their wobbling amplitudes. In order to illustrate this feature more clearly, the difference  $\Delta v_f$  between the final speeds of the scattered wobblers is plotted for different values of the wobbling amplitude  $a$  in Fig. 10. For the sake of simplicity, only 1-bounce events have been included in Fig. 10. As in the case of the scattering between wobblers with opposite phase discussed in Section 3, the zeros of this function  $\Delta v_f$  are approximately independent of the initial amplitude  $a$  and, indeed, coincide with the zeros  $\tilde{v}_k$  introduced in Table 1 in Section 3. This behavior underlies the fact that the initially rightward wobbler defined in the configuration (14) has the same initial conditions as those given by the configuration (13).

In Fig. 11 the final wobbling amplitudes of the scattered wobblers are plotted as a function of the initial velocity  $v_0$  and the initial wobbling amplitude  $a$ . Recall that  $a_L(v_0, a)$  and  $a_R(v_0, a)$  represent, respectively, the final wobbling amplitudes of the resulting leftward and rightward traveling wobblers after the collision. We can observe that the shape modes of the scattered wobblers become excited and its amplitudes are similar as a function of the initial velocity, oscillating around the values found for the kink–antikink scattering events (with  $a = 0$ ). However, the amplitude of these oscillations is much bigger for the final rightward traveling wobbler.

To illustrate the role of the zeros  $\tilde{v}_k$  of the final velocity difference  $\Delta v_f$  shown in Table 1 in this scenario, the functions  $\Delta v_f$  and  $\Delta a$  have been represented simultaneously for the case  $a = 0.10$  in Fig. 12. As in the scattering between wobblers with opposite phase, the values  $\tilde{v}_k$  determine the initial velocities for which the final velocities and the final wobbling amplitudes are the same for the both scattered wobblers.

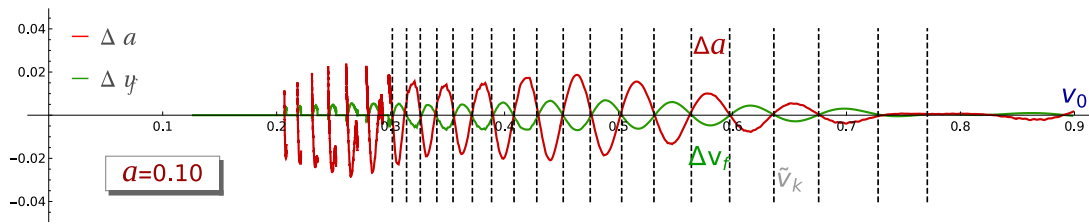


**Fig. 12.** Graphics of  $\Delta v_f$  (final velocity difference) and  $\Delta a$  (final wobbling amplitude difference) as a function of the initial collision velocity  $v_0$  for the scattering between a wobblers and an antikink with  $a = 0.10$ .  $n$ -bounce processes with  $n \geq 2$  have not been included. The vertical dashed lines mark the zeros  $\tilde{v}_k$  of  $\Delta v_f$ .

### 5. Conclusions

This paper delves into the study on the scattering between wobbling kinks initially addressed in [77]. Here, we have investigated the asymmetric scattering between kinks and wobblers (kinks whose shape mode is excited) in the standard  $\phi^4$  model. In particular, two different scenarios in this context have been considered: (a) the scattering between wobblers with opposite phases, and (b) the scattering between a wobblers and an unexcited antikink. Both cases exhibit the usual bion formation and reflection regimes, which are infinitely interlaced forming a fractal structure embedded in the final versus initial velocity diagram. However, the first case involves destructive interference of the shape modes in the collision. As a consequence, the growth in the complexity of the fractal pattern is smaller than that found in [77], where the colliding wobbling kinks travel with the same phase leading to constructive interference at the impact. For example, the emergence of isolated 1-bounce windows is not found in this new case (at least for moderate values of the initial wobbling amplitude  $a$ ), although the splitting of  $n$ -bounce widows is present. On the other hand, the kink scattering in the second scenario displays similar features (although more attenuated) than to those found in [77].

Due to the asymmetry of the initial configurations (13) and (14), the final velocities and wobbling amplitudes of the scattered wobblers are different in general. However, there is a sequence of initial velocities for which both the final velocities and wobbling amplitudes coincide. These values are almost independent of the initial wobbling amplitude  $a$  when the initial wobbling phase considered in (13) and (14) is fixed. Besides, the values of these velocities approximately follow the expression (17). This means that the phase associated to the shape modes of the evolving wobblers at the collision instant plays a predominant role in the scattering properties of these objects. Indeed, (17) allows obtaining values of the initial velocities which share similar features. For example, this expression has been used in the second scenario to predict the location of the maxima of the isolated 1-bounce windows. Finally, it is also worthwhile mentioning the results displayed in Figs. 6 and 12. It can be verified that systematically when a scattered wobblers gains more kinetic energy than the other, it obtains less vibrational energy and vice versa.

The research introduced in the present work opens up some possibilities for future work. For example, the  $\phi^6$  model possess a resonance regime similar to the  $\phi^4$  model, although it does not present vibrational eigenstates in the second-order small fluctuation operator. The characteristics of scattered wobbling kinks can be analyzed to study their influence on the resonant energy transfer mechanism. Alternatively, you can build a model twin to the  $\phi^6$  model that involves internal modes. By doing this, we could compare the scattering processes of the twin model with those of the standard  $\phi^6$  model. In this way, it will be possible to examine the role that shape modes play in the collision process. Furthermore, many other different topological defects (kinks in the double sine-Gordon model, deformed  $\phi^4$  models, hybrid and hyperbolic models, etc.) could be studied in the new perspective presented here. Work in these directions is in progress. Another interesting line of research to explore is the application of the *collective coordinate method* in this asymmetric frame. This study could provide further evidence for the validity of the *resonant energy transfer mechanism* as addressed in [73], or the need to introduce new degrees of freedom to broaden the applicability of this analytical approach.

### CRedit authorship contribution statement

**A. Alonso-Izquierdo:** Conceptualization, Methodology/Study design, Validation, Formal analysis, Investigation, Resources, Writing – original draft, Writing – review & editing, Visualization. **L.M. Nieto:** Conceptualization, Methodology/Study design, Validation, Formal analysis, Investigation, Resources, Writing – original draft, Writing – review & editing, Visualization. **J. Queiroga-Nunes:** Conceptualization, Methodology/Study design, Validation, Formal analysis, Investigation, Resources, Writing – original draft, Writing – review & editing, Visualization.

### Declaration of competing interest

The authors declare that they have no known competing financial interests or personal relationships that could have appeared to influence the work reported in this paper.

## Acknowledgments

We acknowledge support of QCAYLE project, financed by the European Union-NextGenerationEU, and Spanish MCIN grant PID2020-113406GB-I0. We also thank Prof. M.L. Glasser for his careful reading of the manuscript. A. Alonso-Izquierdo acknowledges the Junta de Castilla y León, Spain for financial support under grants SA067G19. This research has made use of the high performance computing resources of the Castilla y León Supercomputing Center (SCAYLE, [www.scayle.es](http://www.scayle.es)), financed by the European Regional Development Fund (ERDF).

## References

- [1] Manton N. Topological solitons. Cambridge: Cambridge University Press; 2004.
- [2] Shnir YM. Topological and non-topological solitons in scalar field theories. Cambridge: Cambridge University Press; 2018.
- [3] Kevrekidis PG, Cuevas-Maraver J, editors. A Dynamical perspective on the  $\phi^4$  model. Nonlinear systems and complexity, vol. 26, Cham: Springer; 2019.
- [4] Sugiyama T. Progr Theoret Phys 1979;61:1550.
- [5] Campbell DK, Schonfeld JS, Wingate CA. Physica D 1983;9:1.
- [6] Anninos P, Oliveira S, Matzner RA. Phys Rev D 1991;44:1147.
- [7] Eschenfelder AH. Magnetic bubble technology. Berlin: Springer-Verlag; 1981.
- [8] Jona F, Shirane G. Ferroelectric crystals. New York: Dover; 1993.
- [9] Strukov BA, Levanyuk AP. Ferroelectric phenomena in crystals: physical foundations. Berlin: Springer-Verlag; 1998.
- [10] Vilenkin A, Shellard EPS. Cosmic strings and other topological defects. Cambridge: Cambridge University Press; 1994.
- [11] Vachaspati T. Kinks and domain walls: an introduction to classical and quantum solitons. Cambridge: Cambridge University Press; 2006.
- [12] Mollenauer LF, Gordon JP. Solitons in optical fibers—fundamentals and applications. Burlington: Academic Press; 2006.
- [13] Schneider T. Nonlinear optics in telecommunications. Heidelberg: Springer; 2004.
- [14] Agrawal GP. Nonlinear fiber optics. San Diego: Academic Press; 1995.
- [15] Davydov AS. Solitons in molecular systems. Dordrech: D. Reidel; 1985.
- [16] Bazeia D, Ventura E. Chem Phys Lett 1999;303:341.
- [17] Yakushevich LV. Nonlinear physics of DNA. Weinheim: Wiley-VCH; 2004.
- [18] Shiefman J, Kumar P. Phys Scr 1979;20:435.
- [19] Peyrard M, Campbell DK. Physica D 1983;9:33.
- [20] Goodman RH, Haberman R. SIAM J Appl Dyn Syst 2005;4:1195.
- [21] Gani VA, Kudryavtsev AE. Phys Rev E 1999;60:3305.
- [22] Malomed BA. Phys Lett A 1989;136:395.
- [23] Gani VA, Marjaneh AM, Askari A, Belendryasova E, Saadatmand D. Eur Phys J C 2018;78:345.
- [24] Gani VA, Marjaneh AM, Saadatmand D. Eur Phys J C 2019;79:620.
- [25] Simas FC, Gomes AR, Nobrega KZ, Oliveira JCRE. J High Energy Phys 2016;9:104.
- [26] Gomes AR, Simas FC, Nobrega KZ, Avelino PP. J High Energy Phys 2018;10:192.
- [27] Bazeia D, Belendryasova E, Gani VA. J Phys Conf Ser 2017;934:012032.
- [28] Bazeia D, Belendryasova E, Gani VA. Eur Phys J C 2018;78:340.
- [29] Bazeia D, Gomes AR, Nobrega KZ, Simas FC. Internat J Modern Phys A 2019;34:1950200.
- [30] Adam C, Oles K, Romanczukiewicz T, Wereszczynski A. Phys Rev Lett 2019;122:241601.
- [31] Romanczukiewicz T, Shnir Y. Some recent developments on kink collisions and related topic: A dynamical perspective on the  $\phi^4$  model. Cham: Springer; 2019.
- [32] Adam C, Oles K, Romanczukiewicz T, Wereszczynski A. Phys Rev D 2020;101:105021.
- [33] Mohammadi M, Dehghani R. Commun Nonlinear Sci Numer Simul 2021;94:105575.
- [34] Yan H, Zhong Y, Liu YX, Maeda K. Phys Lett B 2020;807:135542.
- [35] Romanczukiewicz T. Phys Lett B 2017;773:295.
- [36] Weigel H. J Phys Conf Ser 2014;482:012045.
- [37] Gani VA, Kudryavtsev AE, Lizunova MA. Phys Rev D 2014;89:125009.
- [38] Bazeia D, Gomes AR, Nobrega KZ, Simas FC. Phys Lett B 2019;793:26.
- [39] Lima FC, Simas FC, Nobrega KZ, Gomes AR. J High Energy Phys 2019;10:147.
- [40] Marjaneh AM, Gani VA, Saadatmand D, Dmitriev SV, Javidan K. J High Energy Phys 2017;07:028.
- [41] Belendryasova E, Gani VA. Commun Nonlinear Sci Numer Simul 2019;67:414.
- [42] Zhong Y, Du XL, Jiang ZC, Liu YX, Wang YQ. J High Energy Phys 2020;02:153.
- [43] Bazeia D, Gomes AR, Nobrega KZ, Simas FC. Phys Lett B 2020;803:135291.
- [44] Christov IC, Decker RJ, Demirkaya A, Gani VA, Kevrekidis PG, Radomskiy RV. Phys Rev D 2019;99:016010.
- [45] Christov IC, Decker RJ, Demirkaya A, Gani VA, Kevrekidis PG, Khare A, et al. Phys Rev Lett 2019;122:171601.
- [46] Christov IC, Decker RJ, Demirkaya A, Gani VA, Kevrekidis PG, Saxena A. Commun Nonlinear Sci Numer Simul 2021;97:105748.
- [47] Halavanau A, Romanczukiewicz T, Shnir Ya. Phys Rev D 2012;86:085027.
- [48] Romanczukiewicz T. Acta Phys Polon B 2008;39:3449.
- [49] Alonso-Izquierdo A. Phys Rev D 2018;97:045016.
- [50] Alonso-Izquierdo A. Phys Scr 2019;94:085302.
- [51] Alonso-Izquierdo A. Physica D 2017;365:12.
- [52] Alonso-Izquierdo A. Commun Nonlinear Sci Numer Simul 2019;75:200.
- [53] Alonso-Izquierdo A. Commun Nonlinear Sci Numer Simul 2020;85:105251.
- [54] Alonso-Izquierdo A, Gonzalez Leon MA, Martin Vaquero J, de la Torre Mayado M. Commun Nonlinear Sci Numer Simul 2021;103:106011.
- [55] Ferreira LA, Klimas P, Zakreswski WJ. J High Energy Phys 2019;01:020.
- [56] Goodman RH, Holmes PJ, Weinstein MI. Physica D 2002;161:21.
- [57] Goodman RH, Haberman R. Physica D 2004;195:303.
- [58] B.A. Malomed. Physica D 1985;15:385.
- [59] Malomed BA. J Phys A: Math Gen 1992;25:755.
- [60] Saadatmand D, Dmitriev SV, Borisov DI, Kevrekidis PG, Fatykhov MA, Javidan K. Commun Nonlinear Sci Numer Simul 2015;29:267.
- [61] Saadatmand D, Borisov DI, Kevrekidis PG, Zhou K, Dmitriev SV. Commun Nonlinear Sci Numer Simul 2018;56:62.

- [62] Manton NS, Merabet H. *Nonlinearity* 1997;10:3.
- [63] Adam C, Romanczukiewicz T, Wereszczynski A. *J High Energy Phys* 2019;3:131.
- [64] Adam C, Oles K, Queiruga JM, Romanczukiewicz T, Wereszczynski A. *J High Energy Phys* 2019;07:150.
- [65] Adam C, Oles K, Romanczukiewicz T, Wereszczynski A. *Phys Rev E* 2020;102:062214.
- [66] Dorey P, Mersh K, Romanczukiewicz T, Shnir Y. *Phys Rev Lett* 2011;107:091602.
- [67] Dorey P, Romanczukiewicz T. *Phys Lett B* 2018;779:117.
- [68] Mohammadi M, Dehghani R. *Commun Nonlinear Sci Numer Simul* 2021;94:105575.
- [69] Campos JGF, Mohammadi A. *Eur Phys J C* 2020;80:352.
- [70] Blanco-Pillado JJ, Jimenez-Aguilar D, Urrestilla J. *J Cosmol Astropart Phys* 2021;01:027.
- [71] Takyi I, Weigel H. *Phys Rev D* 2016;94:085008.
- [72] Pereira CFS, Luchini G, Tassis T, Constantinidis CP. *J Phys A* 2021;54:075701.
- [73] Manton NS, Oles K, Romanczukiewicz T, Wereszczynski A. *Phys Rev Lett* 2021;127:071601.
- [74] Barashenkov IV, Oxtoby OF. *Phys Rev E* 2009;80:026608.
- [75] Barashenkov IV. The continuing story of the wobbling kink. In: Kevrekidis P, Cuevas-Maraver J, editors. *A dynamical perspective on the  $\phi^4$  model. Nonlinear systems and complexity*, vol. 26, Cham: Springer; 2019.
- [76] Segur H. *J Math Phys* 1983;24:1439.
- [77] Alonso-Izquierdo A, Queiroga-Nunes J, Nieto LM. *Phys Rev D* 2021;103:045003.
- [78] Campos JGF, Mohammadi A. Wobbling double sine-Gordon kinks. 2021, arXiv:2103.04908.



# Capítulo 4

---

## Wobbling kinks in a two-component scalar field theory: Interaction between shape modes

---

### Resumen

En este trabajo la interacción entre los modos normales de los kinks vibrantes en el modelo de dos campos escalares MSTB es investigada. En este modelo el espectro de pequeñas fluctuaciones de segundo orden del kink presenta dos modos normales de vibración asociados a la componente longitudinal y ortogonal del campo. Se observa que la excitación inicial del modo vibracional de la componente ortogonal da lugar a la excitación de otros modos normales del canal longitudinal. En esta componente se verifica que el kink emite radiación con el doble de la frecuencia de vibración del campo ortogonal (no la frecuencia de la componente longitudinal como en el modelo  $\phi^4$ ). Esto demuestra que la energía del modo vibracional del canal ortogonal puede ser transferida a otros modos normales del campo. La radiación emitida por la segunda componente presenta dos frecuencias dominantes: una es igual a tres veces la frecuencia de vibración del campo ortogonal y otra se identifica con la suma de las frecuencias de vibración del kink longitudinal y de la componente ortogonal del campo. Las propiedades de interacción entre estos modos normales son descritas analíticamente por medio de teorías de expansión de perturbaciones. Se utilizan las aproximaciones de Manton y Merabet [58] y las de Barashenkov y Oxtoby [59]. Ambos métodos aproximativos presentan resultados similares y los términos no lineales que corresponden a la excitación de los modos de radiación son identificados.



# Wobbling kinks in a two-component scalar field theory: Interaction between shape modes

A. Alonso-Izquierdo<sup>a,b,\*</sup>, D. Miguélez-Caballero<sup>c</sup>, L.M. Nieto<sup>c</sup>, J. Queiroga-Nunes<sup>a,b</sup>

<sup>a</sup> Departamento de Matemática Aplicada, Universidad de Salamanca, Casas del Parque 2, 37008 Salamanca, Spain

<sup>b</sup> IUFFyM, Universidad de Salamanca, Plaza de la Merced 1, 37008 Salamanca, Spain

<sup>c</sup> Departamento de Física Teórica, Atómica y Óptica, and IMUVA, Universidad de Valladolid, 47011, Valladolid, Spain

## ARTICLE INFO

### Article history:

Received 13 September 2022

Accepted 4 November 2022

Available online 11 November 2022

Communicated by V.M. Perez-Garcia

### Keywords:

Topological solitons

Wobbling kinks

Two-component scalar field theory

Perturbation theory

Radiation emission

## ABSTRACT

In this paper the interaction between the shape modes of the wobbling kinks arising in the family of two-component MSTB scalar field theory models is studied. The spectrum of the second order small kink fluctuation in this model has two localized vibrational modes associated to longitudinal and orthogonal fluctuations with respect to the kink orbit. It has been found that the excitation of the orthogonal shape mode immediately triggers the longitudinal one. In the first component channel the kink emits radiation with twice the orthogonal wobbling frequency (not the longitudinal one as happens in the  $\phi^4$ -model). The radiation emitted in the second component has two dominant frequencies: one is three times the frequency of the orthogonal wobbling mode and the other is the sum of the frequencies of the longitudinal and orthogonal vibration modes. This feature is explained analytically using perturbation expansion theories.

© 2022 Elsevier B.V. All rights reserved.

## 1. Introduction

Topological defects have played an essential role over the last decades to describe phase transitions in cosmology [1,2], superconductivity in modern condensed matter [3], protein folding [4,5], cluster of living species [6,7] and molecular systems [8,9], just to quote a few application areas. Kinks are the simplest form of a topological defect solution in  $(1 + 1)$ -dimensions and they naturally arise in a variety of scalar field models, all of them sharing the essential feature of living in non-linear scenarios [10,11]. Two paradigmatic examples in this context are the sine-Gordon and the  $\phi^4$ -models. On the one hand, the sine-Gordon model is an integrable system that presents solitary wave solutions, called solitons. In fiber optics these solutions have been widely used to describe traveling digital signals over long haul fibers [12–14]. On the other hand, the  $\phi^4$ -model is a non-integrable system that present solitary wave solutions called kinks. These solutions are stable under small fluctuations. In addition to the translational mode they have one localized vibrational mode, which is referred to as *the shape mode*. In kink-antikink collisions energy can be transferred from one of these modes to the other. This *resonant energy transfer mechanism* is responsible for the fractal structure found in the final versus initial velocity diagrams and the  $n$ -bounce window distribution,

see [15–35]. This complex pattern arises in a wide variety of non-integrable models: the double sine-Gordon model [36–43], the  $\phi^6$ -model [44–49], the  $\phi^8$ -model [50–53], non-polynomial models [54–57], two-component scalar field theories [58–68], etc. In each of the previously cited works different aspects of the kink scattering are explored: resonance phenomena, long range forces, kink collisions with boundaries, impurities or defects, evolution of Bogomolnyi–Prasad–Sommerfield defects without intersoliton forces, presence of spectral walls, etc.

In the kink-antikink scattering, the wobbling kinks or wobblers (kinks whose vibrational or shape mode has been excited) play an essential role in the previous scattering processes because after the first collision the shape mode is excited and kinks becomes wobblers. For this reason, the evolution of single wobbling kinks has been thoroughly studied both analytically and numerically [69–73]. In the  $\phi^4$ -model it has been found that while vibrating with wobbling frequency  $\bar{\omega} = \sqrt{3}$  these solutions emit radiation with frequency  $2\bar{\omega} = 2\sqrt{3}$ , that is, twice the natural vibrational frequency. This behavior has been analytically explained by employing perturbation theory in several works, see [70–73]. For example, Manton and Merabet [71] obtained the decay law of the wobbling amplitude by using a Lindstedt–Poincaré method. In the same context, Barashenkov and Oxtoby [72] employ a perturbation expansion which remains uniform to all orders by introducing a hierarchy of space and times scales. Furthermore, the collision between wobbling kinks has been investigated in the  $\phi^4$ -model [74,75] and the double sine-Gordon model [76].

\* Corresponding author at: Departamento de Matemática Aplicada, Universidad de Salamanca, Casas del Parque 2, 37008 Salamanca, Spain.

E-mail address: [alonsoiz@usal.es](mailto:alonsoiz@usal.es) (A. Alonso-Izquierdo).

A natural generalization of the  $\phi^4$ -model to theories involving several coupled scalar fields is given by the one-parameter family of the Montonen–Sarker–Trullinger–Bishop (MSTB) models. This system is a deformation of the  $O(2)$  linear sigma model preserving the existence of two discrete vacua. It has been the focus of study by many researchers for decades [77–89]. A brief description of the main works concerning the family of MSTB models is introduced in [90]. The usual kink (found in the one-component  $\phi^4$ -model) is embedded in these two-component scalar field theories. For the model parameter  $\sigma$  in the interval  $\sigma \in (1, \infty)$  the spectrum of the second-order small kink fluctuation operator implies the existence of a longitudinal vibrational mode (the usual shape mode found in the  $\phi^4$ -model) and an orthogonal vibrational mode, whose eigenfrequencies are, respectively, given by  $\bar{\omega} = \sqrt{3}$  and  $\hat{\omega} = \sqrt{\sigma^2 - 1}$ . This implies that the kink can vibrate in two different channels, periodically affecting the energy distribution of the extended particle described by this topological defect. In this work we will investigate the interaction between the vibrational modes of the kink in the MSTB model when the orthogonal shape mode is initially excited. It has been checked that in these circumstances the longitudinal shape mode is immediately triggered although it was initially unexcited. A surprising result is that the kink does not emit radiation with frequency  $2\bar{\omega}$  in the longitudinal channel, as found in the  $\phi^4$ -model, but with frequency  $2\hat{\omega}$ , that is, twice the frequency of the orthogonal shape mode. In the orthogonal channel, the frequencies of the emitted radiation are given by  $\bar{\omega} + \hat{\omega}$  and  $3\hat{\omega}$ . In order to elucidate this behavior numerical and analytical approaches have been employed in this paper. This analysis can shed light on the energy transfer mechanism in scattering processes involving kinks in both one-component and two-component scalar field theory models.

The organization of this paper is as follows: in Section 2 the theoretical background of the MSTB model is introduced. The spectrum of the second order small kink fluctuation operator is thoroughly discussed. The eigenfunctions of the longitudinal and orthogonal shape modes are analytically identified. Section 3 describes the problem addressed in this work: the evolution of a kink whose orthogonal shape mode has been initially excited. This problem is also numerically studied in this Section. The frequencies of the radiation reaching the simulation boundary are determined. The dependence of the amplitude of these eigenmodes on the model parameter  $\sigma$  is also discussed. In the next two sections, the above numerical results are explained analytically by applying perturbation expansion theories. In fact, in Section 4 the procedure introduced by Manton and Merabet in [71] is used, and in Section 5 the technique developed by Barashenkov and Oxtoby in [72] will be applied to our problem. Finally, the conclusions of this work are summarized in Section 6.

## 2. The kink in the MSTB model: stability and two shape modes

The dynamics of the one-parameter family of MSTB models is governed by the action

$$S = \int d^2x \left[ \frac{1}{2} \partial_\mu \phi \partial^\mu \phi + \frac{1}{2} \partial_\mu \psi \partial^\mu \psi - U(\phi, \psi) \right], \quad (2.1)$$

where the potential function  $U(\phi, \psi)$  is determined by the fourth-degree polynomial

$$U(\phi, \psi) = \frac{1}{2}(\phi^2 + \psi^2 - 1)^2 + \frac{1}{2}\sigma^2\psi^2. \quad (2.2)$$

As usual,  $\phi, \psi : \mathbb{R}^{1,1} \rightarrow \mathbb{R}$  are dimensionless real scalar fields and the Minkowski metric is taken as  $(g_{\mu\nu}) = \text{diag}\{1, -1\}$ . Each member of this family of models is characterized by the value of the coupling constant  $\sigma$  that appears in (2.2), which belongs to

the interval  $\sigma \in [0, \infty)$ . The field equations in this case are given by the following system of coupled nonlinear partial differential equations of the nonlinear Klein–Gordon type:

$$\frac{\partial^2 \phi}{\partial t^2} - \frac{\partial^2 \phi}{\partial x^2} = 2\phi(1 - \phi^2 - \psi^2), \quad (2.3)$$

$$\frac{\partial^2 \psi}{\partial t^2} - \frac{\partial^2 \psi}{\partial x^2} = 2\psi \left( 1 - \phi^2 - \psi^2 - \frac{1}{2}\sigma^2 \right). \quad (2.4)$$

Solutions of Eqs. (2.3) and (2.4) involve a kink variety with a very rich structure. The usual kink solution that arises in the  $\phi^4$ -model

$$\phi_K(x) = \tanh x \quad (2.5)$$

and its antikink are embedded into this two-component scalar field theory model as

$$K^{(\pm)}(x) = (\pm \phi_K(x), 0)^t = (\pm \tanh x, 0)^t. \quad (2.6)$$

Here and throughout this article we assume that the center of the kink is at the origin,  $x = 0$ , but it could be located at another point  $x_C \in \mathbb{R}$ , which would be achieved with a simple translation in (2.5). The signs in (2.6) distinguish between the kink (+) and the antikink (−). The solution (2.6) arises for any value of the model parameter  $\sigma$  although this topological defect is unstable for  $\sigma < 1$ , as we will see below. In this regime, a pair of two nonzero component topological kinks arise, which are less energetic than the kinks (2.6) and become linearly stable. In addition to these solutions, a one-parametric family of non-topological kinks emerges for each vacua in the model, see [85,86,90]. In this paper, however, we are interested in the regime  $\sigma \geq 1$ , where the one nonzero component kink (2.6) is the only topological defect and is stable. This statement can be checked by analyzing the evolution of a perturbation of the static kink (2.6) of the form

$$\tilde{K}(x, t; \omega, a) = K^{(\pm)}(x) + a e^{i\omega t} F_\omega(x), \quad (2.7)$$

where  $a$  is a small real parameter. This leads to the spectral problem

$$\mathcal{H} F_\omega(x) = \omega^2 F_\omega(x), \quad (2.8)$$

where  $\mathcal{H}$  is the second order small fluctuation operator

$$\mathcal{H} = \begin{pmatrix} \mathcal{H}_{11} & 0 \\ 0 & \mathcal{H}_{22} \end{pmatrix} = \begin{pmatrix} -\frac{d^2}{dx^2} + 4 - 6 \text{sech}^2 x & 0 \\ 0 & -\frac{d^2}{dx^2} + \sigma^2 - 2 \text{sech}^2 x \end{pmatrix}. \quad (2.9)$$

From the expression (2.7) it is clear that the solution (2.6) is stable only if the eigenvalues of the operator (2.9) are not negative. Note that (2.9) is a diagonal matrix differential operator. The spectral problem (2.8) in this case consists of two exactly solvable spectral problems (independent of each other) corresponding to Schrödinger operators  $\mathcal{H}_{11}$  and  $\mathcal{H}_{22}$  with Pöschl–Teller potential wells. Taking into account that the orbit of the kink solution (2.6) is located on the  $\phi$ -axis of the internal plane, perturbations of the form

$$\bar{F}_\omega(x) = (\bar{\eta}(x), 0)^t$$

characterize longitudinal fluctuations on the kink while those of the form

$$\hat{F}_\omega(x) = (0, \hat{\eta}(x))^t$$

determine orthogonal or transverse fluctuations of (2.6). As mentioned above, these types of perturbations are decoupled in this case, so that the spectrum of (2.9) is described as follows:



- **Longitudinal eigenmodes:** It can be checked that the operator (2.9) involves two discrete longitudinal eigenfunctions. These states are the zero mode

$$\bar{F}_0(x) = (\bar{\eta}_0(x), 0)^t = (\text{sech}^2 x, 0)^t \quad (2.10)$$

and the so-called shape mode

$$\bar{F}_{\sqrt{3}}(x) = (\bar{\eta}_D(x), 0)^t = (\text{sech } x \tanh x, 0)^t \quad (2.11)$$

whose eigenvalue is given by  $\bar{\omega}^2 = 3$ . This means that the kink when excited by this longitudinal shape mode vibrates with frequency  $\bar{\omega} = \sqrt{3}$ . It can be checked that the maximum deviation of this vibrating kink (or wobbler) from the static kink (2.6) happens at the points

$$x_M^{(\pm)} = \pm \text{arccosh } \sqrt{2}. \quad (2.12)$$

The longitudinal continuous spectrum emerges on the threshold value  $\bar{\omega}_c^2 = 4$ , that is,  $\bar{\omega}_q^2 = 4 + q^2$  with  $q \in \mathbb{R}$ . The corresponding eigenfunctions read

$$\begin{aligned} \bar{F}_{\sqrt{4+q^2}}(x) &= (\bar{\eta}_q(x), 0)^t \\ &= \left( e^{iqx}[-1 - q^2 + 3 \tanh^2 x - 3iq \tanh x], 0 \right)^t. \end{aligned} \quad (2.13)$$

The relations (2.10), (2.11) and (2.13) are also employed to define respectively the functions  $\bar{\eta}_0(x)$ ,  $\bar{\eta}_D(x)$  and  $\bar{\eta}(x)$ . Obviously, the spectrum of the longitudinal fluctuations is the same as that found for the one-component kink in the  $\phi^4$ -model because, as previously mentioned, this kink is embedded in the MSTB model. Indeed,  $\bar{\eta}_D(x)$  is the usual shape mode that turns a static kink into a wobbling kink, see [70–75]. As we will see below, in the MSTB model the kink can also vibrate in the orthogonal direction through a vibrational mode, which we will continue to call *shape mode*.

- **Orthogonal eigenmodes:** In this case, the spectrum of orthogonal fluctuations contains only a discrete eigenvalue  $\hat{\omega}^2 = \sigma^2 - 1$ , whose eigenfunction is

$$\hat{F}_{\sqrt{\sigma^2-1}}(x) = (0, \hat{\eta}_D(x))^t = (0, \text{sech } x)^t. \quad (2.14)$$

This orthogonal vibrational or shape mode maximally vibrates at the point

$$x_0 = 0 \quad (2.15)$$

with frequency  $\hat{\omega} = \sqrt{\sigma^2 - 1}$  if  $\sigma > 1$ . Note that if  $\sigma < 1$  the kink (2.6) becomes unstable because the eigenvalue  $\hat{\omega}^2$  is negative. In this case the kink (2.6) decays to one of the previously mentioned less energetic two non-null component kinks which arise in this regime. An interesting remark is that for  $\sigma = 1$  the solution (2.6) has two zero modes despite the fact that it is the only kink present in the model and, therefore, it is not a member of a one-parametric family of solutions. This is a very singular situation. Of course, this model parameter value defines a phase transition where a family of non-topological kinks starts to emerge, see [90]. Finally, the orthogonal continuous spectrum verifies the dispersion relation  $\hat{\omega}_q^2 = \sigma^2 + q^2$ ,  $q \in \mathbb{R}$ , with eigenfunctions

$$\hat{F}_{\sqrt{\sigma^2+q^2}}(x) = (0, \hat{\eta}_q(x))^t = (0, e^{iqx}(q + i \tanh x))^t, \quad (2.16)$$

which emerge on the threshold value  $\hat{\omega}_c^2 = \sigma^2$ .

The structure of the spectrum of (2.8)–(2.9) depends on the value of the coupling constant  $\sigma$ . In Fig. 1 the eigenfrequencies  $\omega$  derived from the spectrum of the operator (2.9) are represented as functions of the model parameter  $\sigma$  by solid lines. The longitudinal eigenfrequencies are shown in Fig. 1(a) while the orthogonal

ones are shown in Fig. 1(b). For later purposes, some discrete eigenfrequencies combinations have also been represented in Fig. 1 by dashed curves. In particular, the values  $2\bar{\omega}$ ,  $2\hat{\omega}$ ,  $4\hat{\omega}$  and  $\bar{\omega} + 2\hat{\omega}$  are included in the first graph and  $\bar{\omega} + \hat{\omega}$ ,  $|\bar{\omega} - \hat{\omega}|$  and  $3\hat{\omega}$  in the second. This allows us to distinguish two significant values of  $\sigma$ , which will play a relevant role later. Specifically we have the following:

- $\sigma_1 = \sqrt{2} \approx 1.41421$ . For  $\sigma > \sigma_1$  the relation  $2\hat{\omega} > \bar{\omega}_c$  holds, that is, twice the frequency  $\hat{\omega}$  of the orthogonal shape mode can be found as an eigenfrequency in the continuous longitudinal spectrum, see Fig. 1(a). On the other hand, if  $\sigma < \sigma_1$  the inequality  $2\hat{\omega} < \bar{\omega}_c$  holds, which means that there is no radiation with this frequency in the first component.
- $\sigma_2 = \frac{1}{2}\sqrt{7} \approx 1.32288$ . For  $\sigma = \sigma_2$  the equality  $2\hat{\omega} = \bar{\omega}$  is verified, that is, twice the frequency of the orthogonal shape mode coincides with the frequency of the longitudinal shape mode. Also note that  $3\hat{\omega} = \bar{\omega} + \hat{\omega}$  and  $\hat{\omega} = \bar{\omega} - \hat{\omega}$  are also valid, see Fig. 1(b).

It is worth anticipating that these values of  $\sigma$  will become especially important later on because just in  $\sigma_1$  and  $\sigma_2$  there are divergences in the radiation amplitudes that will be calculated in Sections 4 and 5.

### 3. Interaction between the normal modes of vibration

In this section we will analyze the interaction between the shape modes described above, which allow the kink solution (2.6) to vibrate in a longitudinal or orthogonal channel. This interaction is governed by the nonlinear Klein–Gordon Eqs. (2.3)–(2.4). The coupling between the field components present in the different terms of the MSTB potential (2.2) implies that the excitation of one of the eigenmodes can excite other different vibrational or radiation modes. For our case, it is clear that orthogonal modes cannot be triggered by longitudinal modes. If the second field component vanishes,  $\psi = 0$ , then the problem reduces to the usual one-component  $\phi^4$ -model and the second component  $\psi$  is not affected by kink evolution. Here, we will address the reverse situation, that is, we will discuss how the longitudinal modes are affected when the orthogonal shape mode  $\hat{F}(x)$  of the static kink (2.6) is excited. In this scenario, the initial configuration can be characterized by the linear approximation

$$\tilde{K}(x, t; a) = K^{(+)}(x) + a \sin(\hat{\omega}t) \hat{F}_{\sqrt{\sigma^2-1}}(x) \quad (3.1)$$

derived from linear stability analysis. By construction, this is a good approximation when  $a$  is small. Using (2.6) and (2.14), the expression (3.1) can be written in components as

$$\begin{aligned} \tilde{K}(x, t; a) &= \left( \phi_K(x), a \sin(\hat{\omega}t) \hat{\eta}_D(x) \right)^t \\ &= \left( \tanh x, a \sin(\sqrt{\sigma^2 - 1} t) \text{sech } x \right)^t. \end{aligned} \quad (3.2)$$

After the excited kink (3.1)–(3.2) has evolved sufficiently, we expect other eigenmodes to become excited, so that eventually the kink is more accurately described by the expression<sup>1</sup>:

$$\tilde{K}(x, t; a) = K^{(+)}(x) + \sum_{\omega \in \text{Spec } \mathcal{H}} a_\omega \sin(\omega t + \varphi_\omega) F_\omega(x), \quad \text{for } t \gg 0 \quad (3.3)$$

<sup>1</sup> Recall that for the usual  $\phi^4$ -model, the kink evolves by vibrating through the initially excited shape mode channel while emitting radiation with twice the  $\bar{\omega}$  wobbling frequency. Using the notation employed in (3.3) this would mean  $a_{2\bar{\omega}} \neq 0$  and  $a_{2\hat{\omega}} \neq 0$ . Note that in this case the frequency  $2\bar{\omega}$  is embedded in the continuous spectrum.

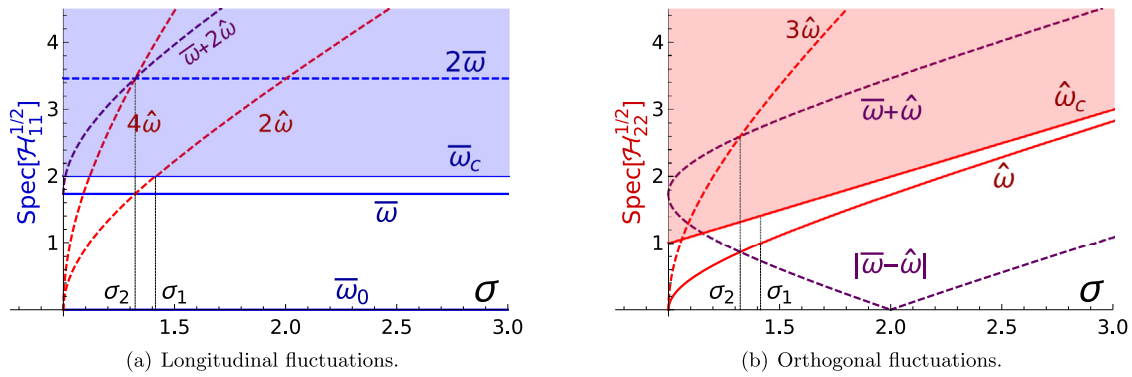


**Fig. 1.** Solid lines are the eigenfrequencies  $\omega$  (the square root of the eigenvalues of the operator (2.9)) associated to the longitudinal (a) and orthogonal (b) fluctuations as a function of the coupling constant  $\sigma$ . Some combinations of these eigenfrequencies that will be relevant later are also included (dashed lines).

which is a generalization of (2.7) and (3.1).

In the following sections we will study the problem proposed in this work from two different perspectives. On the one hand, we will use numerical analysis to extract the spectral information associated with the excitation of the different eigenmodes of the evolving kink. For example, Fig. 2 shows the evolution of the two-component kink solution when the orthogonal shape mode has been initially excited with amplitude  $a = 0.6$ . The value of  $a$  has been chosen high enough to better visualize the behavior of the fields in the graphics. We can clearly see that the initial excitation of the orthogonal shape mode  $\hat{F}(x)$  causes an almost immediate excitation of the longitudinal shape mode  $\bar{F}(x)$ . Note the small ripples around the center of the kink in the first plot. Another characteristic that is shown in Fig. 2 is that the amplitude of the orthogonal shape mode decreases as time passes. As mentioned above, this behavior is expected since this also occurs in the evolution of the wobbling kink in the one-component  $\phi^4$ -model. As a consequence, some radiation is emitted in this process. As stated above, in the  $\phi^4$  model plane waves are generated with a frequency of  $2\bar{\omega}$ . In our model, radiation can propagate through both components of the found as field. Furthermore, the kink (2.6) can vibrate with two different wobbling frequencies  $\bar{\omega}$  and  $\hat{\omega}$ . For this reason it is difficult to anticipate the frequencies of the radiation emitted by the excited kink (3.1). On the other hand, in Sections 4 and 5 two analytical approaches based on the perturbation expansion theory will be introduced. We will use two different techniques that have been employed by Manton and Merabet [71] and by Barashenkov and Oxtoby [72] in the analysis of the wobbling kink in the  $\phi^4$ -model. This study will be applied to the predominant regime  $\sigma \in (\sigma_1, \infty)$ , see Fig. 1. This will allow us to obtain an analytical understanding of the numerical results and of the mechanism involved in the interaction between the different eigenmodes. The  $\sigma \in (1, \sigma_1)$  regime implies much more complex dynamics, where added frequencies start to come into play due to couplings between higher order terms.

### 3.1. Numerical simulations

As mentioned before, in this section we will perform numerical simulations to gain a global understanding of the problem. This is characterized by a static kink whose orthogonal shape mode is initially excited with a certain initial amplitude  $a$  and evolves fulfilling the partial differential Eqs. (2.3) and (2.4). These equations will be discretized using an explicit fourth-order finite difference algorithm implemented with fourth-order Mur boundary conditions, which has been designed to deal with non-linear Klein-Gordon equations (see the Appendix in [66]). The initial conditions are easily implemented from the initial configuration (3.2) with  $t = 0$ . The simulations have been executed in the

spatial interval  $x \in [-100, 100]$  for a time range  $t \in [0, 1200]$ . The space and time intervals have been chosen to correctly estimate the spectral data associated with the vibrations of the fields using a fast Fourier transform algorithm. Different choices of space and time intervals have also been considered giving similar results. The spectral analysis mentioned above has been applied to time series obtained by evaluating the field components of the solutions at different points in space. This procedure is justified by the fact that the shape modes are localized and the estimation of their frequencies and amplitudes is optimized using different points  $x_i$ . The choice of these points is specified as follows:

1. Spectral information for time series evaluated at  $x = x_0 = 0$ . The vibration of the orthogonal shape mode  $\hat{F}(x)$  is most pronounced at the origin of the spatial axis, see (2.14). The time series extracted by evaluating the second field at this point allows us to assess, for example, the resulting amplitude of the orthogonal shape mode  $\hat{F}(x)$  associated with the evolving kink. Note that the first field component in this solution always vanishes at  $x_0$ .
2. Spectral information for time series evaluated at  $x = x_M^{(+)}$ . The amplitude of the longitudinal shape eigenmode is maximized at these points, see (2.11) and (2.12). The spectral analysis at the point  $x_M^{(+)}$  defines an optimized method to assess the excitation of this vibration channel. In contrast to the point  $x_0$ , which can be considered the source of the radiation emitted by the vibrating kink, some continuous eigenmodes propagating from the origin can be detected here.
3. Spectral information for time series evaluated at  $x = x_B$  with  $x_B$  representing a spacial value near the limits of the simulation. The set of radiation modes emitted by the wobbling kink can be identified by the fluctuations away from the kink center  $x_c$ . This makes it possible to identify the frequencies of the radiation emitted in both the longitudinal and orthogonal channels.

The spectral analysis of the time series corresponding to the points  $x_0, x_M^{(+)}$  and  $x_B$  is shown in the following figures for various values of the coupling constant  $\sigma$  and for the value of the initial amplitude  $a = 0.1$ . It has been verified that for other values of  $a$  in the range  $(0, 0.6]$  the results are very similar. For this reason the particular value  $a = 0.1$  can be considered as a representative case of the problem we are dealing with. Obviously, the resulting spectral information depends on the value of the model parameter  $\sigma$ . In the following figures, the results for the particular values  $\sigma = 1.2, \sigma = 1.5$  and  $\sigma = 2.5$  are illustrated. These cases describe the wide variety of behaviors that arise in this problem. Some of the most interesting features are set out in the following list:

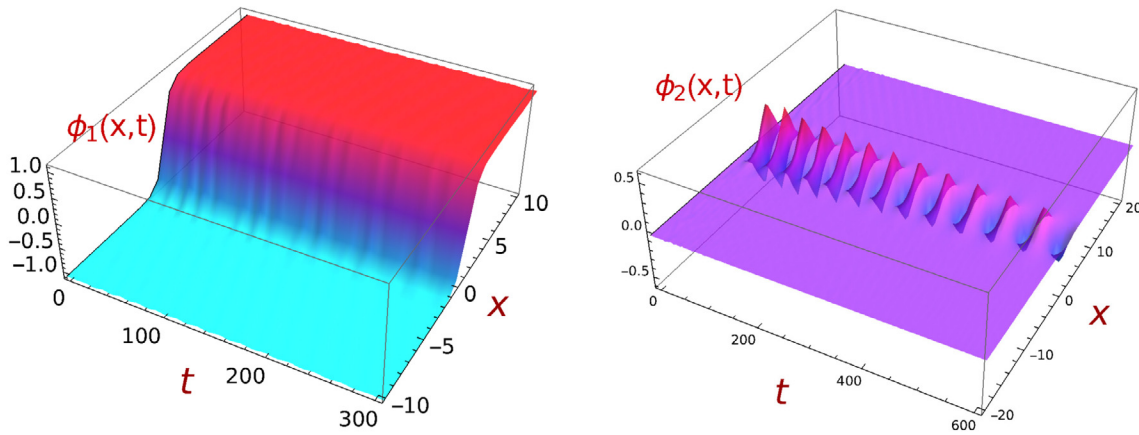


**Fig. 2.** Evolution of the first (left) and second (right) field components of the kink (2.6) initially excited by the orthogonal shape mode  $\widehat{F}(x)$ (2.14) with amplitude  $a = 0.6$ .

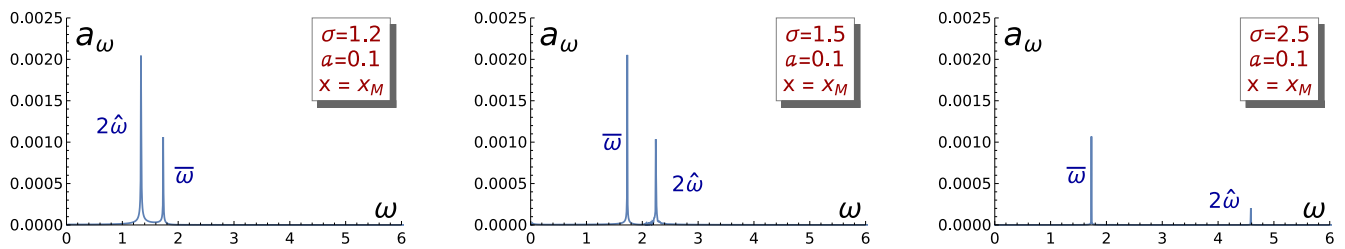


**Fig. 3.** Spectral distribution of the time series obtained by evaluating the first field component at the point  $x_M^{(+)}$  for the evolving kink with initial orthogonal shape mode amplitude  $a = 0.1$ . This information is displayed for three representative values of the model parameter:  $\sigma = 1.2$  (left),  $\sigma = 1.5$  (middle), and  $\sigma = 2.5$  (right).

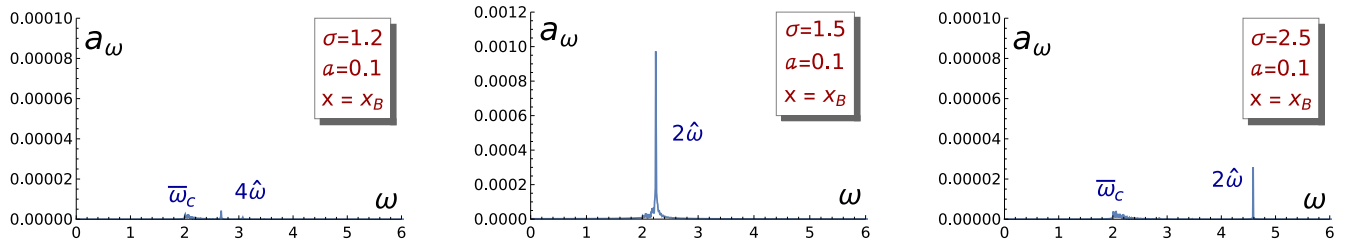


**Fig. 4.** Spectral distribution of the time series obtained by evaluating the first field component at the point  $x_B$  for the evolving kink with initial orthogonal shape mode amplitude  $a = 0.1$ . This information is shown for three representative values of model parameter:  $\sigma = 1.2$  (left),  $\sigma = 1.5$  (middle) and  $\sigma = 2.5$  (right).

- **Fig. 3** represents the amplitude  $a_\omega$  of the different longitudinal eigenmodes  $\widehat{F}_\omega(x)$  as a function of the frequency  $\omega$  when the time series are evaluated at the point  $x_M$ , which is the optimum point to assess the excitation of the longitudinal shape mode  $\widehat{F}_{\bar{\omega}}(x)$ . You can see that this mode is excited even though it initially was not. The first field component evaluated at this point also involves a vibration with frequency  $2\widehat{\omega}$ . To check if it is a localized fluctuation or corresponds to a radiation mode, the spectral analysis must be carried out far from the center of the kink. This is discussed in the next point.
- **Fig. 4** shows the spectral distribution of the radiation emitted in the first component channel that reaches the limits of the simulations. In practice, the time series in this case are constructed at a point  $x_B$  (far from the center of the kink). In the one-component  $\phi^4$ -model, nonlinearity causes the emission of radiation with frequency  $2\bar{\omega}$ . An unexpected novelty appears in our model: radiation is also emitted but its frequency is not  $2\bar{\omega}$  but  $2\widehat{\omega}$ , that is, twice the frequency of the orthogonal shape mode. This behavior can be observed in **Fig. 4** (center and right) for the model parameters  $\sigma = 1.5$  and  $\sigma = 2.5$ . Note that the frequency  $2\widehat{\omega}$  is embedded in

the longitudinal continuous spectrum for  $\sigma > \sigma_1 = \sqrt{2}$  which includes the cases mentioned above. The amplitude of the excited eigenmodes depends on the value of the model parameter  $\sigma$ . This can be partly explained by the fact that higher frequencies are more difficult to excite and that the eigenvalues associated with the orthogonal eigenfluctuations depend on  $\sigma$ . The case  $\sigma = 1.2$  shown in **Fig. 4** (left) does not satisfy the previous inequality, so there is no continuous longitudinal eigenfunction with frequency  $2\widehat{\omega}$ . Instead, a continuous eigenmode with frequency  $4\widehat{\omega}$  can be identified, albeit very slightly excited. Clearly, this indicates that higher order nonlinear terms are involved in the emission of this radiation. On the other hand, note that the frequency  $\bar{\omega}$  observed in **Fig. 3** is not present here because this massive eigenmode is localized around the kink center.

- The pattern found in **Fig. 5** is different. The spectral analysis is applied, in this case, on time series obtained by the values of the second field component extracted from our simulations computed at the kink center  $x_0 = 0$ . By symmetry, this point can be considered the source of the radiation emitted by the wobbling kink. For this reason, the plots included

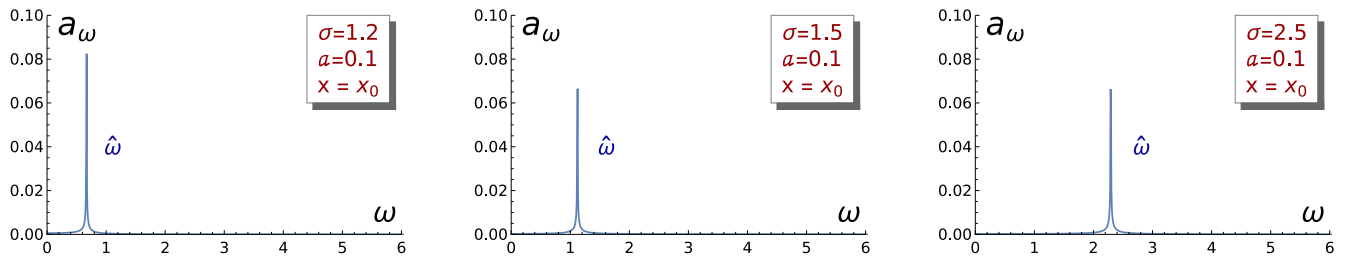


**Fig. 5.** Spectral distribution of the time series obtained by evaluating the second field component at the point  $x_0$  for the evolving kink with initial orthogonal shape mode amplitude  $a = 0.1$ . This information is shown for three representative values of model parameter:  $\sigma = 1.2$  (left),  $\sigma = 1.5$  (middle) and  $\sigma = 2.5$  (right).

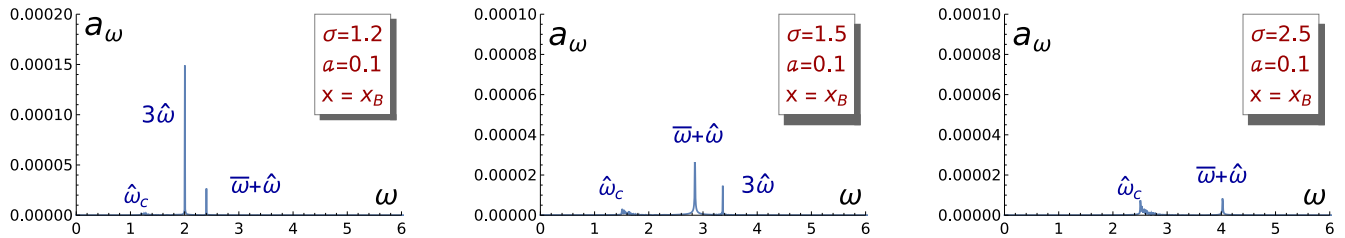


**Fig. 6.** Spectral distribution of the time series obtained by evaluating the second field component at the point  $x_B$  for the evolving kink with initial orthogonal shape mode amplitude  $a = 0.1$ . This information is shown for three representative values of model parameter:  $\sigma = 1.2$  (left),  $\sigma = 1.5$  (middle) and  $\sigma = 2.5$  (right).

in Fig. 5 show that the orthogonal shape mode (initially excited by construction) continues to be excited over time. However, the amplitude of this localized vibration seems to follow a non-trivial behavior. We will return to this point later.

- To identify the spectral distribution of the radiation emitted in the channel of the second component of the field, the time series associated with this component must be evaluated at a point  $x_B$  far from the center of the kink. Fig. 6 illustrates the results found in this case. The most remarkable fact in these plots is that radiation with frequencies  $\bar{\omega} + \hat{\omega}$  (i.e. the sum of the frequencies of the two shape modes) and  $3\hat{\omega}$  is detected at the simulation bounds. Note that for  $\sigma = 1.2$  shown in Fig. 6 (left), the most excited continuous eigenmode involves the frequency  $3\hat{\omega}$ , which is the lowest of the two frequencies mentioned above. In the rest of the graphs this situation is reversed. In fact, for  $\sigma = 2.5$  this amplitude becomes very small.

In the previous figures, the spectral information of our problem has been described for three specific values of the model parameter  $\sigma$ . In order to have a global understanding of the excitation process of the different eigenmodes, the previous spectral analysis has been carried out for values of  $\sigma$  in the interval  $\sigma \in [1, 5]$  with a parameter step  $\Delta\sigma = 0.01$ . As before, the initial amplitude of the orthogonal shape mode in these simulations has been chosen as  $a = 0.1$ . The results have been summarized in Figs. 7 and 8.

The graphs show the set of frequencies that are excited as a function of the model parameter  $\sigma$ . These frequencies are represented by a pixel with a grayscale pattern, where black is assigned to the most excited frequency for each  $\sigma$ . For the rest of frequencies (less excited) the intensity of gray represents the ratio between the amplitude associated with this frequency and that corresponding to the predominant frequency mentioned above. If a frequency involves negligible amplitude, it is represented by a white pixel. We can observe the following characteristics:

- Fig. 7 (left) shows that  $2\hat{\omega}$  and  $\bar{\omega}$  are the frequencies of the excited longitudinal eigenmodes at the point  $x_M$ . We can see that if  $\sigma \in (1, \sigma_2)$  then the kink vibrates predominantly with the frequency  $2\hat{\omega}$  but for  $\sigma > \sigma_2$  the wobbling frequency  $\bar{\omega}$

is dominant. This behavior seems to favor the less energetic eigenmode.

- Fig. 8 (left) confirms that the orthogonal shape mode is the only excited mode of the evolving kink when evaluated at the origin in the channel of the second field component. Remember that the origin can be considered as the emission source of the radiation and therefore no frequencies in the orthogonal continuous spectrum are found in the spectral analysis for this point.
- Fig. 7 (right) characterizes the frequencies of the radiation moving away from the simulation through the first field component. For  $\sigma > \sigma_1$ , the wobbling kink emits radiation with a frequency  $2\hat{\omega}$ , though when it becomes too energetic, the radiation frequency changes to the longitudinal threshold value  $\bar{\omega}_c$ . This happens approximately for  $\sigma > 3$ . For  $\sigma < \sigma_1$ , the previous frequency  $2\hat{\omega}$  is not included in the continuous spectrum. In this regime, the radiation can propagate with frequencies close to the threshold value  $\bar{\omega}_c$  but also with frequencies  $4\hat{\omega}$  or  $\bar{\omega} + 2\hat{\omega}$ . This behavior appears to be a consequence of the interaction between the shape modes at the higher order.
- Finally, Fig. 8 (right) shows that if  $\sigma > \sigma_2$  the radiation propagating in the channel of the second field component has a dominant frequency  $\bar{\omega} + \hat{\omega}$  which is progressively replaced by values close to the threshold value  $\bar{\omega}_c$  when the previous one is high enough. On the other hand, for  $\sigma < \sigma_2$  the vibrating kink emits radiation with frequency  $3\hat{\omega}$  which in this regime is easier to excite because it is less energetic than for higher values of  $\sigma$ .

Figs. 7 and 8 show that only a few eigenmodes are excited in the evolution of a kink initially excited by the orthogonal shape mode. It is also interesting to investigate the dependence of the amplitude of these eigenmodes on the value of the parameter  $\sigma$ . Fig. 9 (left) represents this dependence for the longitudinal shape eigenmode (evaluated at the point  $x_M$ ) for the usual value  $a = 0.1$ . Note that for small values of  $\sigma$  the amplitude  $a_{\bar{\omega}}$  is almost insignificant but for  $\sigma \approx 1.32$ , when the frequency  $2\hat{\omega}$  coincides with the frequency  $\bar{\omega}$  of the longitudinal shape mode, the amplitude exhibits a peak with amplitude  $a_{\bar{\omega}} \approx 0.03$ . Finally, the amplitude goes asymptotically to the constant value  $a_{\omega} = 0.001$ .

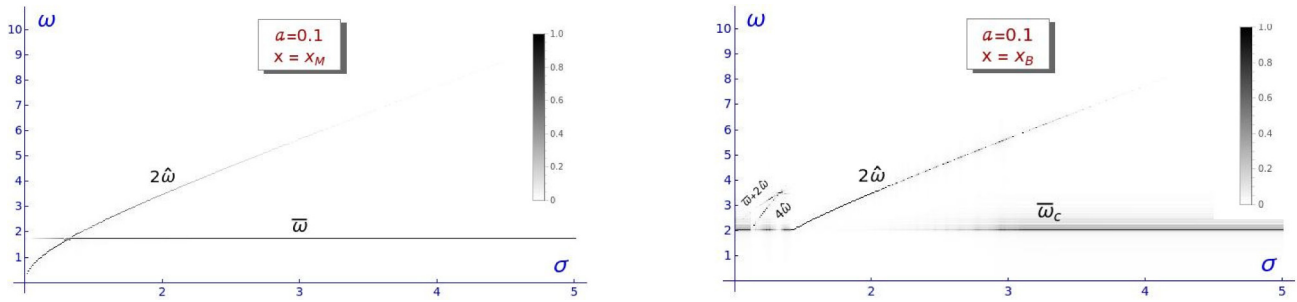


**Fig. 7.** Frequencies of the excited longitudinal eigenmodes at  $x = x_M$  (left) and  $x = x_B$  (right) when the static kink is initially excited by the orthogonal shape mode with amplitude  $a = 0.1$ .

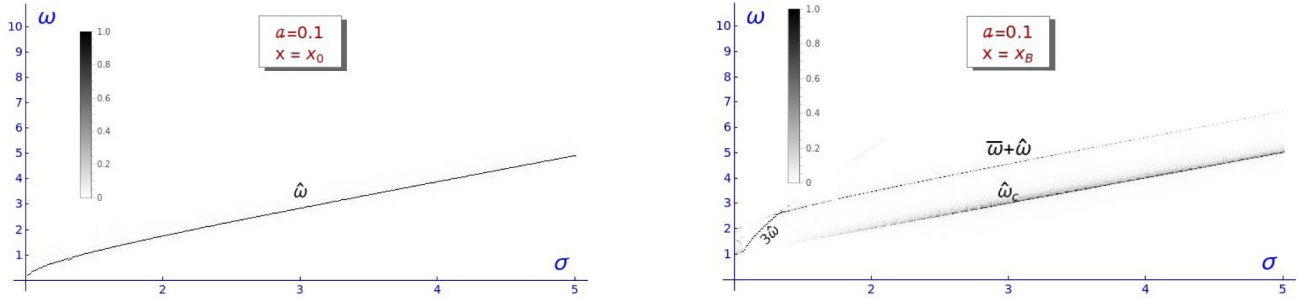


**Fig. 8.** Frequencies of the excited orthogonal eigenmodes at  $x = x_0$  (left) and  $x = x_B$  (right) when the static kink is initially excited by the orthogonal shape mode with amplitude  $a = 0.1$ .

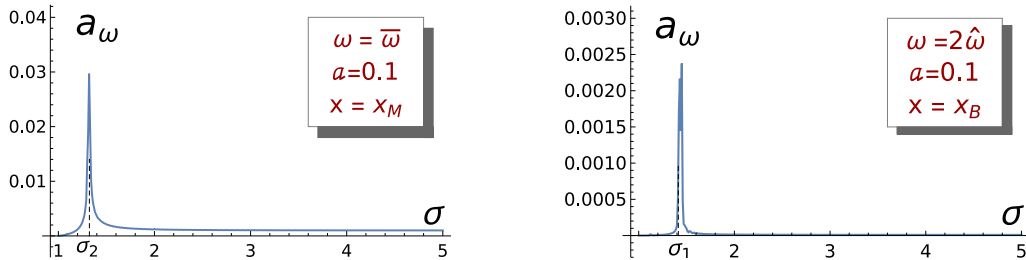


**Fig. 9.** Amplitudes of longitudinal shape mode, evaluated at  $x_M$  (left), and of the longitudinal continuous mode with frequency  $2\hat{\omega}$ , evaluated at  $x_B$  (right), as a function of the model parameter  $\sigma$ .

On the other hand, the amplitude of the longitudinal radiation mode with frequency  $2\hat{\omega}$  that escapes from the simulation is maximized for the value  $\sigma \approx 1.44$  when this frequency crosses the threshold value  $\bar{\omega}_c$  associated with the continuous longitudinal spectrum. At this point, the amplitude reaches approximately the value 0.0024, see Fig. 9 (right).

Fig. 10 (left) represents the amplitude  $a_{\hat{\omega}}$  of the orthogonal shape mode as a function of the model parameter  $\sigma$ . Here, the amplitude is almost constant  $a = 0.1$  although some depressions can be identified around the previously mentioned values  $\sigma = 1.32$  and  $\sigma = 1.46$ , where the amplitude of other frequencies is maximized. Fig. 10 (center) represents the amplitude of the orthogonal radiation eigenmodes with frequency  $\bar{\omega} + \hat{\omega}$ . The peak of this graph arises at the value  $\sigma = 1.32$ . Finally, Fig. 10 (right) represents the amplitude of the eigenmode with frequency  $3\hat{\omega}$ . Here, we find that this eigenmode is highly excited for  $\sigma < 1.36$ , showing two peaks located at  $\sigma = 1.068$  and  $\sigma = 1.32$ . After that, the amplitude decreases.

In the next two sections, perturbation expansion theory will be used to explain some of the surprising results found in the present section. In particular, we will apply the techniques of Manton & Merabet [71] and Barashenkov & Oxtoby [72] to our problem. Obviously, some modifications of these two approaches will be implemented because we are dealing with a two-

component field theory model with a particular initial setting. The results found in each case will be compared. In particular, we are very interested in understanding the suppression mechanism of longitudinal radiation emission with frequency  $2\bar{\omega}$ . We remember that in the  $\phi^4$ -model radiation with this frequency was emitted, however in our extended model it is replaced by longitudinal radiation with frequency  $2\hat{\omega}$ . Another feature which will be examined is the presence of orthogonal radiation with frequency  $\bar{\omega} + \hat{\omega}$  and, more surprisingly, with frequency  $3\hat{\omega}$  at the same scale. This means that the radiation emission in the latter case is not a higher order effect in the perturbation expansion, but must be explained in the same order as the previous frequency. The explanation of this behavior lies in the interaction between the longitudinal and orthogonal shape modes in the problem presented in the present section.

#### 4. Perturbative approach: Manton and Merabet approach

As previously mentioned, in [71] Manton and Merabet applied a perturbation expansion to the  $\phi^4$ -model to explain the emission of radiation by a wobbling kink with twice its natural vibration frequency, and they also estimate the decay rate of the wobbling amplitude due to this process. In the sequel we will follow the essence of this method to analyze the system we are dealing with.

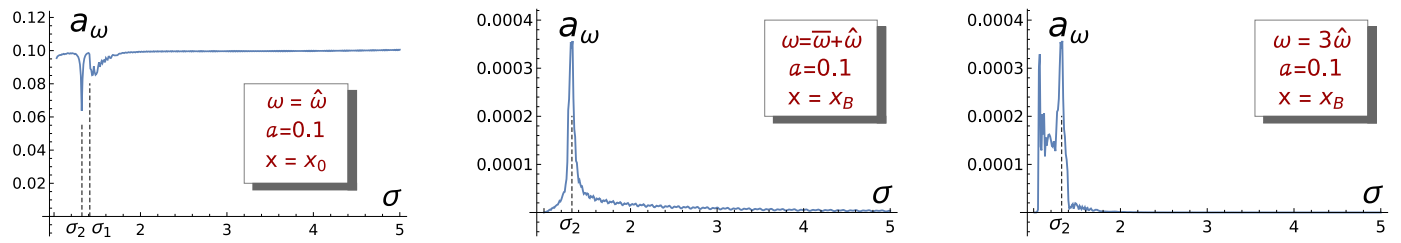


**Fig. 10.** Amplitudes of orthogonal shape mode evaluated at  $x_0$  (left) and of the orthogonal continuous mode with frequency  $\bar{\omega} + \hat{\omega}$  evaluated at  $x_B$  (right) as a function of the model parameter  $\sigma$ .

In this case, the components of the fields will be written as

$$\begin{aligned}\phi(x, t) &= \phi_K(x) + \bar{a}(t) \bar{\eta}_D(x) + \bar{\eta}(x, t), \\ \psi(x, t) &= \hat{a}(t) \hat{\eta}_D(x) + \hat{\eta}(x, t),\end{aligned}\quad (4.1)$$

where  $\phi_K(x)$ ,  $\bar{\eta}_D(x)$  and  $\hat{\eta}_D(x)$  where defined respectively in (2.5), (2.11) and (2.14). The time dependent functions  $\bar{a}(t)$  and  $\hat{a}(t)$  respectively describe the evolution of the amplitudes of the longitudinal and orthogonal shape modes. On the other hand, the space and time dependent functions  $\bar{\eta}(x, t)$  and  $\hat{\eta}(x, t)$  determine the evolution of the longitudinal and orthogonal radiation eigenmodes. For the sake of clarity, from now on the variables on which both the functions  $\bar{a}$  and  $\hat{a}$  and the eigenfunctions  $\bar{\eta}_D$ ,  $\hat{\eta}_D$ ,  $\bar{\eta}$ , and  $\hat{\eta}$  depend, are not written explicitly. Thus, if we substitute the expression (4.1) into the field Eqs. (2.3) and (2.4) we find

$$\begin{aligned}\bar{\eta}_D(3\bar{a} + \bar{a}_{tt}) + \bar{\eta}_{tt} - \bar{\eta}_{xx} + \bar{\eta}(6\phi_K^2(x) - 2) + 6\bar{a}^2\bar{\eta}_D^2(\bar{\eta} + \phi_K(x)) \\ + 6\bar{a}\bar{\eta}\bar{\eta}_D(\bar{\eta} + 2\phi_K(x)) + 2\bar{a}^3\bar{\eta}_D^3 + 6\bar{\eta}^2\phi_K(x) + 2\bar{\eta}^3 + 2\bar{\eta}\bar{\eta}^2 \\ + 2\bar{a}\bar{\eta}^2\eta_D + 4\bar{a}\bar{\eta}\hat{\eta}\hat{\eta}_D + 4\bar{a}\hat{a}\hat{\eta}\hat{\eta}_D\hat{\eta}_D + 2\hat{a}^2\bar{\eta}\hat{\eta}_D^2 \\ + 2\bar{a}\hat{a}^2\bar{\eta}_D\hat{\eta}^2 + 2\hat{\eta}^2\phi_K(x) + 4\hat{a}\hat{\eta}\hat{\eta}_D\phi_K(x) + 2\hat{a}^2\hat{\eta}_D^2\phi_K(x) = 0\end{aligned}$$

for the first component, and

$$\begin{aligned}\hat{\eta}_D(\hat{a}_{tt} + (\sigma^2 - 1)\hat{a}) + (\sigma^2 - 2)\hat{\eta} + 2\hat{\eta}^2\hat{\eta} + 2\hat{\eta}^3 + 4\bar{a}\hat{\eta}\hat{\eta}\hat{\eta}_D \\ + 2\hat{a}^2\hat{\eta}\hat{\eta}_D^2 + 2\hat{a}\hat{\eta}^2\hat{\eta}_D + 6\hat{a}\hat{\eta}^2\hat{\eta}_D + 4\bar{a}\hat{a}\hat{\eta}\hat{\eta}_D\hat{\eta}_D \\ + 2\hat{a}^2\hat{a}\hat{\eta}_D^2\hat{\eta}_D + 6\hat{a}^2\hat{\eta}\hat{\eta}_D^2 + 2\hat{a}^3\hat{\eta}_D^3 + 4\hat{\eta}\hat{\eta}\phi_K(x) \\ + 4\bar{a}\hat{\eta}\hat{\eta}_D\phi_K(x) + 4\bar{a}\hat{\eta}\hat{\eta}_D\phi_K(x) + 4\bar{a}\hat{a}\hat{\eta}_D\hat{\eta}_D\phi_K(x) \\ + 2\hat{\eta}\phi_K^2(x) + \hat{\eta}_{tt} - \hat{\eta}_{xx} = 0\end{aligned}\quad (4.3)$$

for the second one. In the problem at hand, we assume that the amplitude of the orthogonal shape mode is small, so we can neglect terms of the form  $a^3$ ,  $\eta^2$ ,  $\eta a$ , etc. in (4.2) and (4.3), where  $a$  stands for either  $\bar{a}$  or  $\hat{a}$  and  $\eta$  stands for  $\bar{\eta}$  or  $\hat{\eta}$ . Furthermore, the amplitudes of the emitted radiation are assumed to be much smaller than those associated with the shape modes. Under these assumptions Eqs. (4.2) and (4.3) reduce to

$$\begin{aligned}\bar{\eta}_D(3\bar{a} + \bar{a}_{tt}) + \bar{\eta}_{tt} - \bar{\eta}_{xx} + \bar{\eta}(6\phi_K^2(x) - 2) + 6\bar{a}^2\bar{\eta}_D^2\phi_K(x) \\ + 2\bar{a}^2\hat{\eta}_D^2\phi_K(x) \approx 0\end{aligned}\quad (4.4)$$

and

$$\begin{aligned}\hat{\eta}_D(\hat{a}_{tt} + (\sigma^2 - 1)\hat{a}) + \hat{\eta}_{tt} - \hat{\eta}_{xx} + (-2 + \sigma^2 + 2\phi_K^2(x))\hat{\eta} \\ + 4\bar{a}\hat{a}\hat{\eta}_D\hat{\eta}_D\phi_K(x) \approx 0.\end{aligned}\quad (4.5)$$

The projection of (4.4) onto the longitudinal shape mode  $\bar{\eta}_D$  leads to the relation

$$\bar{a}_{tt} + 3\bar{a} + \frac{9}{16}\pi\bar{a}^2 + \frac{3}{8}\pi\hat{a}^2 = 0,\quad (4.6)$$

while the projection of (4.5) onto the orthogonal shape mode  $\hat{\eta}_D$  yields

$$\hat{a}_{tt} + (\sigma^2 - 1)\hat{a} + \frac{1}{4}\pi\bar{a}\hat{a} = 0.\quad (4.7)$$

On the other hand, substituting (4.6) in (4.4) we get that the equation for the longitudinal radiation component  $\bar{\eta}$  is

$$\begin{aligned}\bar{\eta}_{tt} - \bar{\eta}_{xx} + (6\phi_K^2(x) - 2)\bar{\eta} + \left[6\bar{\eta}_D^2\phi_K(x) - \frac{9}{16}\pi\bar{\eta}_D\right]\bar{a}^2 \\ + \left[2\hat{\eta}_D^2\phi_K(x) - \frac{3}{8}\pi\bar{\eta}_D\right]\hat{a}^2 = 0,\end{aligned}\quad (4.8)$$

while substituting (4.7) in (4.5) we get for the orthogonal component  $\hat{\eta}$  the equation

$$\hat{\eta}_{tt} - \hat{\eta}_{xx} + (\sigma^2 - 2 + 2\phi_K^2(x))\hat{\eta} + \left[4\bar{\eta}_D\phi_K(x) - \frac{\pi}{4}\right]\hat{\eta}_D\bar{a}\hat{a} = 0.\quad (4.9)$$

The problem addressed in this work is characterized by the excitation of the orthogonal shape mode while the longitudinal remains initially unexcited. We are interested in analyzing the mechanism of energy transfer between the shape modes and the emission of radiation in this process. It is clear that the quadratic term  $\hat{a}^2$  arising in (4.6) implies the subsequent excitation of the longitudinal shape mode since the evolution of  $\bar{a}$  is forced by this term. Therefore, we can assume that at first-order the amplitude  $\hat{a}$  of the orthogonal shape mode follows the expression

$$\hat{a}(t) = \hat{a}_0 \sin(\hat{\omega}t) = \hat{a}_0 \sin(\sqrt{\sigma^2 - 1}t).\quad (4.10)$$

If we substitute (4.10) into (4.6) and the initial conditions  $\bar{a}(0) = \bar{a}_t(0) = 0$  are implemented, then the evolution of the amplitude  $\bar{a}(t)$  of the longitudinal mode is given by

$$\begin{aligned}\bar{a}(t) = \frac{\pi\hat{a}_0^2}{16} \left[ -1 + \frac{4(\sigma^2 - 1)}{4\sigma^2 - 7} \cos(\sqrt{3}t) \right. \\ \left. - \frac{3}{4\sigma^2 - 7} \cos(2\sqrt{\sigma^2 - 1}t) \right].\end{aligned}\quad (4.11)$$

We can see that the above formula anticipates that  $\sigma = \sigma_1 = \sqrt{7}/2$  is special because for precisely that value the denominators in (4.11) cancel. We can check in Figs. 9 and 10 that for this value of the coupling constant  $\sigma$  the amplitude of the longitudinal shape mode exhibits an abrupt peak. In this case a resonance arises between the frequencies  $\bar{\omega}$  and  $2\hat{\omega}$ . However, in this article we will not deal with this particular case because we are interested in the more general interval  $\sigma > \sigma_1 = \sqrt{2}$  where the value  $2\hat{\omega}$  enters into resonance with the continuous frequencies in the longitudinal channel.

From (4.11) it is clear that  $\bar{a} \sim O(\hat{a}^2)$ , i.e. the scales of the amplitudes of the shape modes are different. Taking into account that

$$(\hat{a}(t))^2 = \frac{1}{2}\hat{a}_0^2(1 - \cos(2\hat{\omega}t)) = \frac{1}{2}\hat{a}_0^2(1 - \cos(2\sqrt{\sigma^2 - 1}t))$$

and that the response of  $\bar{\eta}$  to the time-independent source is itself time-independent and carries no energy, then the non-trivial evolution of longitudinal radiation is governed by the equation

$$\bar{\eta}_{tt} - \bar{\eta}_{xx} + (6\phi_K^2(x) - 2)\bar{\eta} = f(x)e^{i2\hat{\omega}t},\quad (4.12)$$

which has been derived from the second-order truncation of (4.8) in  $\hat{a}_0$ . This means that terms involving  $\bar{a}^2(t)$  in (4.8) have been

ignored because  $\bar{a} \sim O(\hat{a}^2)$ , as mentioned above. At this point it is necessary to clarify that, in order to simplify the tedious calculations that must be carried out, we have decided to use imaginary exponentials in (4.12). But in fact, at the end of the calculation, only the real part of the solutions of (4.12) will be relevant, so this choice does not affect the final results of this section. In fact, the function  $f(x)$  of (4.12) has the following expression:

$$f(x) = \frac{1}{2} \hat{a}_0^2 \left( 2 \hat{\eta}_D^2 \phi_K(x) - \frac{3}{8} \pi \bar{\eta}_D \right) = -\frac{1}{2} \hat{a}_0^2 \left( \frac{3}{8} \pi \operatorname{sech} x \tanh x - 2 \operatorname{sech}^2 x \tanh x \right). \quad (4.13)$$

In these circumstances it can be assumed that the function describing the longitudinal radiation has the form

$$\bar{\eta}(x, t) = \bar{\eta}(x) e^{i2\hat{\omega}t}, \quad (4.14)$$

which leads to the following ordinary differential equation:

$$-\bar{\eta}''(x) + [-2 + 6\phi_K^2(x) - 4\hat{\omega}^2] \bar{\eta}(x) = f(x). \quad (4.15)$$

A similar argument is used to obtain an ordinary differential equation for the orthogonal component. The expression (4.9) contains the product of the amplitudes

$$\begin{aligned} \bar{a}(t)\hat{a}(t) &= \frac{\pi \hat{a}_0^3 (17 - 8\sigma^2)}{32(4\sigma^2 - 7)} \sin(\hat{\omega}t) + \frac{\pi \hat{a}_0^3 (\sigma^2 - 1)}{8(4\sigma^2 - 7)} \sin[(\bar{\omega} + \hat{\omega})t] \\ &\quad - \frac{\pi \hat{a}_0^3 (\sigma^2 - 1)}{8(4\sigma^2 - 7)} \sin[(\bar{\omega} - \hat{\omega})t] \\ &\quad - \frac{3\pi \hat{a}_0^3}{32(4\sigma^2 - 7)} \sin(3\hat{\omega}t), \end{aligned} \quad (4.16)$$

that contains sinusoidal functions with four different frequencies:

$$\omega_1 = \hat{\omega}, \quad \omega_2 = 3\hat{\omega}, \quad \omega_3 = \bar{\omega} + \hat{\omega}, \quad \text{and} \quad \omega_4 = \bar{\omega} - \hat{\omega}. \quad (4.17)$$

Note the presence, a priori unexpected, of  $\omega_2$ , three times the natural vibration frequency  $\hat{\omega}$  of the orthogonal shape mode. Due to the linearity of (4.9), the effect of each term in (4.16) on the radiation solution can be studied separately. Therefore, the emission of radiation with frequency  $\omega_\ell$  can be examined by analyzing the following four partial differential equations in complex form

$$\hat{\eta}_{tt} - \hat{\eta}_{xx} + (\sigma^2 - 2 + 2\phi_K^2(x))\hat{\eta} = g_\ell(x)e^{i\omega_\ell t}, \quad (4.18)$$

where

$$\begin{aligned} g_1(x) &= -\frac{\hat{a}_0^3 \pi (8\sigma^2 - 17)(\pi - 16 \operatorname{sech} x \tanh^2 x) \operatorname{sech} x}{128(4\sigma^2 - 7)}, \\ g_2(x) &= -\frac{\hat{a}_0^3 3\pi (\pi - 16 \operatorname{sech} x \tanh^2 x) \operatorname{sech} x}{128(4\sigma^2 - 7)}, \\ g_3(x) = -g_4(x) &= \frac{\hat{a}_0^3 \pi (\sigma^2 - 1)(\pi - 16 \operatorname{sech} x \tanh^2 x) \operatorname{sech} x}{32(4\sigma^2 - 7)}. \end{aligned}$$

As before, it is assumed that for each frequency  $\omega_\ell$  this orthogonal radiation can be written as

$$\hat{\eta}(x, t) = \hat{\eta}(x) e^{i\omega_\ell t},$$

which leads to the four ordinary differential equations

$$-\hat{\eta}''(x) + (\sigma^2 - 2 + 2\phi_K^2(x) - \omega_\ell^2)\hat{\eta}(x) = g_\ell(x), \quad \ell = 1, 2, 3, 4. \quad (4.19)$$

Now Eqs. (4.15) and (4.19) will be solved to determine the radiation emission of the shape modes in each channel. As mentioned above, this study will be carried out in the  $\sigma > \sigma_1$  regime

where twice the frequency of the orthogonal shape mode is included in the longitudinal continuous spectrum. We explicitly recall the notation introduced in (2.13) for the first component of the continuous longitudinal eigenfunctions:

$$\bar{\eta}_q(x) = e^{iqx} (-1 - q^2 + 3\phi_K^2(x) - 3iq\phi_K(x)). \quad (4.20)$$

From the dispersion relation, we have that  $q = \sqrt{\omega^2 - 4}$  with  $|\omega| \geq 2$ . Note that the Wronskian associated with these solutions

$$\bar{W}_q = W[\bar{\eta}_q(x), \bar{\eta}_{-q}(x)] = -2iq(q^2 + 1)(q^2 + 4)$$

is constant. The solution of (4.15) that describes the radiation emitted from the origin with frequency  $2\hat{\omega}$  is given by the expression

$$\bar{\eta}(x) = -\frac{\bar{\eta}_{-q_1}(x)}{\bar{W}_{q_1}} \int_{-\infty}^x \bar{\eta}_{q_1}(\xi) f(\xi) d\xi - \frac{\bar{\eta}_{q_1}(x)}{\bar{W}_{q_1}} \int_x^{\infty} \bar{\eta}_{-q_1}(\xi) f(\xi) d\xi, \quad (4.21)$$

where  $q_1 = \sqrt{(2\hat{\omega})^2 - 4} = 2\sqrt{\sigma^2 - 2}$ . The asymptotic behavior of (4.21) can be identified analytically and turns out to be

$$\bar{\eta}(x) \xrightarrow{x \rightarrow \infty} e^{-iq_1 x} \hat{a}_0^2 \frac{\pi}{16} \frac{q_1(2 + 3iq_1 - q_1^2)}{(q_1^2 + 1) \sinh \frac{\pi q_1}{2}}.$$

Multiplying the above result by  $e^{i2\hat{\omega}t}$  and using (4.14) we get  $\bar{\eta}(x, t)$ . Then, taking only its real part, which is what really interests us, it can be determined that the behavior of the longitudinal radiation of frequency  $2\hat{\omega}$  turns out to be

$$\begin{aligned} \bar{\eta}(x, t) \xrightarrow{x \rightarrow \infty} &\frac{\pi \sqrt{\sigma^2 - 2}}{4 \sinh(\pi \sqrt{\sigma^2 - 2})} \sqrt{\frac{\sigma^2 - 1}{4\sigma^2 - 7}} \hat{a}_0^2 \cos(2\hat{\omega}t - q_1 x + \delta_1), \\ \delta_1 &= \arctan\left(\frac{3q_1}{2 - q_1^2}\right). \end{aligned} \quad (4.22)$$

Therefore, the amplitude of the radiation emitted with frequency  $2\hat{\omega}$  in the longitudinal channel is

$$a_{2\hat{\omega}} = \frac{\pi \sqrt{\sigma^2 - 2}}{4 \sinh(\pi \sqrt{\sigma^2 - 2})} \sqrt{\frac{\sigma^2 - 1}{4\sigma^2 - 7}} \hat{a}_0^2. \quad (4.23)$$

It can be checked from (4.23) that  $a_{2\hat{\omega}} \sim O(\hat{a}_0^2)$ .

The asymptotic behavior of orthogonal radiation can be obtained in a similar way for each frequency  $\omega_\ell$  in (4.17). In this case, the second component of the orthogonal continuous eigenmodes is

$$\hat{\eta}_{q_\ell}(x) = e^{iq_\ell x} (q_\ell + i\phi_K(x)),$$

with  $q_\ell = \sqrt{\omega_\ell^2 - \sigma^2}$  such that  $|\omega_\ell| > \sigma$ . The Wronskian associated to this case is given by

$$\hat{W}_{q_\ell} = W[\hat{\eta}_{q_\ell}(x), \hat{\eta}_{-q_\ell}(x)] = 2iq_\ell(q_\ell^2 + 1).$$

Now the radiation emitted from the origin with frequency  $\omega_\ell$  is determined by the general formula

$$\begin{aligned} \hat{\eta}_{\omega_\ell}(x) &= -\frac{\hat{\eta}_{-q_\ell}(x)}{\hat{W}_{q_\ell}} \int_{-\infty}^x \hat{\eta}_{q_\ell}(\xi) g_\ell(\xi) d\xi \\ &\quad - \frac{\hat{\eta}_{q_\ell}(x)}{\hat{W}_{q_\ell}} \int_x^{\infty} \hat{\eta}_{-q_\ell}(\xi) g_\ell(\xi) d\xi, \end{aligned}$$

which allows us to obtain the following asymptotic behavior for  $\hat{\eta}_{\omega_\ell}(x)$ :

$$\hat{\eta}_{3\hat{\omega}}(x) \xrightarrow{x \rightarrow \infty} -e^{-iq_2 x} \frac{3\pi^2 \hat{a}_0^3}{128(4\sigma^2 - 7)} \frac{q_2^3 (q_2 - i)}{i(q_2^2 + 1) \sinh \frac{\pi q_2}{2}},$$

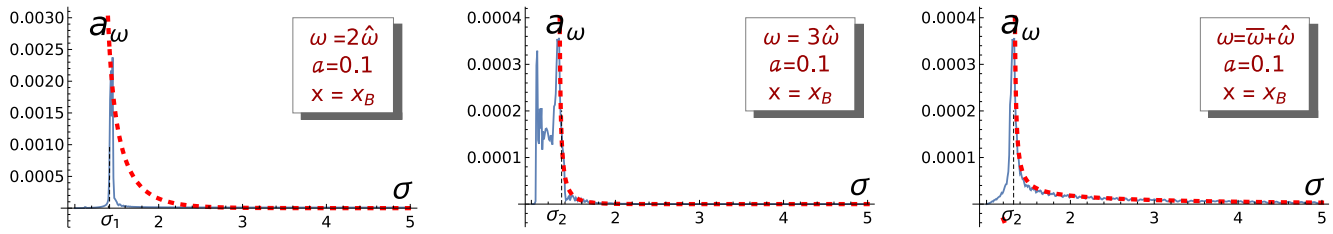


**Fig. 11.** Comparison between the numerical and analytical results for the dependence on the parameter  $\sigma$  of the amplitudes of the radiation emitted with frequencies  $2\hat{\omega}$ ,  $3\hat{\omega}$  and  $\bar{\omega} + \hat{\omega}$ . The red dashed curves represent the theoretical responses (4.23) and (4.26).

$$q_2 = \sqrt{8\sigma^2 - 9}, \quad (4.24)$$

$$\hat{\eta}_{\bar{\omega}+\hat{\omega}}(x) \xrightarrow{x \rightarrow \infty} e^{-iq_3 x} \frac{\pi^2 \hat{a}_0^3 (\sigma^2 - 1)}{32(4\sigma^2 - 7)} \frac{q_3^3 (q_3 - i)}{i(q_3^2 + 1) \sinh \frac{\pi q_3}{2}},$$

$$q_3 = \sqrt{2 + 2\sqrt{3}\sqrt{\sigma^2 - 1}}. \quad (4.25)$$

Note that the frequency  $\omega_4 = \bar{\omega} - \hat{\omega}$  has not been considered in this calculation because in the regime  $\sigma > \sigma_1$  its value is under the orthogonal continuous spectrum. Again, taking the imaginary part of the previous expressions, we obtain the physically relevant solutions, which are

$$\begin{aligned} \hat{\eta}_{3\hat{\omega}}(x, t) &\xrightarrow{x \rightarrow \infty} \frac{3\pi^2 \hat{a}_0^3}{128(4\sigma^2 - 7)} \frac{q_2^3}{\sqrt{q_2^2 + 1} \sinh \frac{\pi q_2}{2}} \\ &\quad \times \sin(\omega_2 t - q_2 x + \delta_2), \quad \delta_2 = \arctan(q_2), \\ \hat{\eta}_{\bar{\omega}+\hat{\omega}}(x, t) &\xrightarrow{x \rightarrow \infty} -\frac{\pi^2 \hat{a}_0^3 (\sigma^2 - 1)}{32(4\sigma^2 - 7)} \frac{q_3^3}{\sqrt{q_3^2 + 1} \sinh \frac{\pi q_3}{2}} \\ &\quad \times \sin(\omega_3 t - q_3 x + \delta_3), \quad \delta_3 = \arctan(q_3), \end{aligned}$$

so the amplitudes of the radiation with frequencies  $\bar{\omega} + \hat{\omega}$  and  $3\hat{\omega}$  are written as

$$\begin{aligned} a_{3\hat{\omega}} &= \frac{3\pi^2 \hat{a}_0^3}{128(4\sigma^2 - 7)} \frac{q_2^3}{\sqrt{q_2^2 + 1} \sinh \frac{\pi q_2}{2}}, \\ a_{\bar{\omega}+\hat{\omega}} &= \frac{\pi^2 \hat{a}_0^3 (\sigma^2 - 1)}{32(4\sigma^2 - 7)} \frac{q_3^3}{\sqrt{q_3^2 + 1} \sinh \frac{\pi q_3}{2}}. \end{aligned} \quad (4.26)$$

Fig. 11 shows the analytical results found at (4.23) and (4.26) for the amplitudes of the radiation emitted with frequencies  $2\hat{\omega}$ ,  $3\hat{\omega}$  and  $\bar{\omega} + \hat{\omega}$ , and are compared with the numerical results shown in Section 3. It can be seen that the dependence of these amplitudes on the model parameter  $\sigma$  is very well adjusted for the last two frequencies in the interval  $\sigma > \sigma_1$ . Furthermore, the divergences in the radiation amplitudes occur for the same values of the parameter  $\sigma$ .

#### 4.1. Amplitude decay law

It is well known that the average power radiated in a period by a wave of the form  $\eta = A \cos(\omega t - qx + \delta)$  is  $\langle P \rangle = -\frac{1}{2} A^2 \omega q$ , but as this radiation is emitted both to the right and to the left of the real line, then the power emitted would be doubled, that is,  $\langle P_{total} \rangle = -A^2 \omega q$ . In the previous section we have seen that at distances far from the origin of coordinates in the first field radiation is emitted with frequency  $2\hat{\omega}$  while in the second field the frequencies are  $3\hat{\omega}$  and  $\bar{\omega} + \hat{\omega}$ . Hence, rewriting the amplitudes described by the formulas (4.23) and (4.26) as

$$a_{2\hat{\omega}} = \hat{a}_0^2 A_{2\hat{\omega}}, \quad a_{3\hat{\omega}} = \hat{a}_0^3 A_{3\hat{\omega}}, \quad a_{\bar{\omega}+\hat{\omega}} = \hat{a}_0^3 A_{\bar{\omega}+\hat{\omega}}, \quad (4.27)$$

and taking into account that the radiation is emitted both from the right and from the left, we obtain that the average power

radiated by the system is

$$\begin{aligned} \langle P \rangle &= \frac{dE}{dt} = -(\hat{a}_0^4 A_{2\hat{\omega}}^2 (2\hat{\omega}) q_1 + \hat{a}_0^6 A_{3\hat{\omega}}^2 (3\hat{\omega}) q_2 \\ &\quad + \hat{a}_0^6 A_{\bar{\omega}+\hat{\omega}}^2 (\bar{\omega} + \hat{\omega}) q_3). \end{aligned} \quad (4.28)$$

On the other hand, in the previous Section we have considered that the differential equation that describes the dynamics of  $\hat{a}$  is approximately

$$\hat{a}_{tt} + \hat{\omega}^2 \hat{a} \approx 0, \quad (4.29)$$

that is, we consider that the orthogonal discrete vibrational mode behaves as a harmonic oscillator at each point in space. Therefore, we are going to assume that the energy density of this vibration is given by the expression

$$\mathcal{E} = \frac{1}{2} \hat{\omega}^2 (\hat{a}_0 \hat{\eta}_D)^2. \quad (4.30)$$

Integrating this last expression over the whole space, we obtain that the corresponding total energy will be  $E = \hat{\omega}^2 \hat{a}_0^2$ . As for the discrete mode of the first field, it will not be considered because we are going to assume that we are working for very long times, in which this vibration has already been excited and, therefore, the energy of the orthogonal discrete mode will be inverted only in terms of exciting radiation. If we now take into account the formula (4.28) and neglect the sixth order terms, we arrive at the differential equation

$$-\hat{\omega}^2 \frac{d\hat{a}_0^2}{dt} \approx \hat{a}_0^4 A_{2\hat{\omega}}^2 2\hat{\omega} q_1, \quad (4.31)$$

whose solution is

$$\hat{a}_0^2(t) \approx \frac{\hat{a}_0^2(0)}{1 + \frac{2q_1 A_{2\hat{\omega}}^2}{\hat{\omega}} \hat{a}_0^2(0) t}. \quad (4.32)$$

Function (4.32) directly gives us the decay law of the orthogonal discrete mode amplitude which, as we saw in Fig. 2, shows a clear decrease in the value of this amplitude as time progresses.

In the next Section we will calculate another decay law for this same amplitude which, despite not being exactly the same, will have a very similar form to the one calculated here. This discrepancy in the amplitude decay of the discrete vibration modes also occurred in the study of the  $\phi^4$  model in [71–73] and in fact the law obtained in this section has a very similar form to those calculated in these references. Finally, we can highlight that, although we have not considered the sixth-order terms in (4.28), they show that the orthogonal channel radiation influences the time evolution of  $\hat{a}_0$ , although to a lesser extent than the radiation emitted in the parallel channel.

#### 5. Perturbative approach: Barashenkov and Oxtoby procedure

Barashenkov and Oxtoby employed a more formal approach using perturbation theories in [72] to address the same problem. In this Section, the perturbation theory will be applied to our



problem following precisely the procedure described in [72]. As usual, the starting point is given by Eqs. (2.3) and (2.4). Taking into account the scenario described in Section 3, the following expansions of the fields about the kink are proposed

$$\begin{aligned} \phi &= \phi_0 + \epsilon^2 \phi_2 + \epsilon^4 \phi_4 + \dots, \\ \psi &= \epsilon \psi_1 + \epsilon^3 \psi_3 + \dots, \end{aligned} \quad (5.1)$$

where  $\epsilon$  is a formal small real parameter. In addition to this expansion, a sequence of stretched spaces and times will also be used:

$$X_n \equiv \epsilon^n x, \quad T_n \equiv \epsilon^n t. \quad (5.2)$$

In the limit  $\epsilon \rightarrow 0$  the variables  $X_n$  and  $T_n$  become independent. The derivatives with respect to the original variables can also be expanded into the new ones as follows:

$$\frac{\partial}{\partial x} = \partial_{x_0} + \epsilon \partial_{x_1} + \epsilon^2 \partial_{x_2} + \dots, \quad \text{with} \quad \partial_{x_n} \equiv \frac{\partial}{\partial X_n}, \quad (5.3)$$

$$\frac{\partial}{\partial t} = \partial_{t_0} + \epsilon \partial_{t_1} + \epsilon^2 \partial_{t_2} + \dots, \quad \text{with} \quad \partial_{t_n} \equiv \frac{\partial}{\partial T_n}. \quad (5.4)$$

If we substitute the expressions (5.1)–(5.4) in (2.3)–(2.4) we obtain a hierarchy of equations for the fields  $\phi_k$  and  $\psi_k$  for different orders in the  $\epsilon$ -expansion, which we will consider in some detail below.

### 5.1. Zero order approximation: $\phi_0$

In zero order approximation, the following relation

$$\partial_{T_0, T_0} \phi_0 - \partial_{X_0, X_0} \phi_0 - 2 \phi_0 (1 - \phi_0)^2 = 0$$

must be verified. As expected, the kink/antikink solution (2.5)

$$\phi_0(X_0) = \pm \phi_K(X_0) = \pm \tanh X_0 \quad (5.5)$$

meets the above condition and is considered the solution in this order.

### 5.2. First order approximation: $\psi_1$

In the first order approximation, Eq. (2.3) gives us the relation

$$\partial_{T_0, T_1} \phi_0 - \partial_{X_0, X_1} \phi_0 = 0,$$

which is checked automatically because as we have seen  $\phi_0$  in (5.5) is independent of  $T_0$ ,  $X_1$  and  $T_1$ . On the other hand, the second Klein–Gordon Eq. (2.4) leads to

$$(\partial_{T_0, T_0} - \partial_{X_0, X_0} - 2 + \sigma^2 + 2 \phi_0^2) \psi_1 = 0,$$

which corresponds to the spectral problem for the orthogonal channel, see (2.9). Therefore,

$$\psi_1 = \widehat{A}(X_1, \dots; T_1, \dots) e^{i\widehat{\omega} T_0} \widehat{\eta}_D(X_0) + \text{c.c.} + \widehat{\eta}(X_0, T_0),$$

where we recall that  $\widehat{\eta}_D(X_0) = \text{sech } X_0$  and  $\widehat{\omega} = \sqrt{\sigma^2 - 1}$ . As usual, the abbreviation c.c. indicates the complex conjugate of the previous expression, and

$$\widehat{\eta}(X_0, T_0) = \int_{-\infty}^{\infty} \widehat{R}(q) e^{i\widehat{\omega}_q T_0} \widehat{\eta}_q(X_0) dq + \text{c.c.}$$

is a wave packet traveling in the second field component, with orthogonal continuous eigenfunctions  $\widehat{\eta}_q(x)$  defined on (2.16), and  $\widehat{\omega}_q = \sqrt{\sigma^2 + q^2}$ , as defined in (2.16). Taking into account that the problem we are dealing with only involves the initial excitation of the orthogonal shape mode, the field component  $\psi_1$  is assumed to be

$$\psi_1 = \widehat{A}(X_1, \dots; T_1, \dots) e^{i\widehat{\omega} T_0} \text{sech } X_0 + \text{c.c.} \quad (5.6)$$

### 5.3. Second order approximation: $\phi_2$

In the second order approximation, the following condition on  $\psi_1$

$$\partial_{T_0, T_1} \psi_1 - \partial_{X_0, X_1} \psi_1 = 0$$

is found. Plugging (5.6) into the previous relation we have

$$\partial_{T_1} \widehat{A} = 0, \quad \partial_{X_1} \widehat{A} = 0,$$

which implies that the amplitude  $\widehat{A}$  does not depend on the slow variables  $X_1$  and  $T_1$ , that is,

$$\widehat{A} = \widehat{A}(X_2, \dots; T_2, \dots).$$

On the other hand, the condition extracted in this order for the field component  $\phi_2$  reduces to

$$[\partial_{T_0, T_0} - \partial_{X_0, X_0} - 2 + 6\phi_0^2] \phi_2 = -2 \phi_0 \psi_1^2 = \overline{F}_2, \quad (5.7)$$

where

$$\begin{aligned} \overline{F}_2 &= -4|\widehat{A}|^2 \text{sech}^2 X_0 \tanh X_0 - 2\widehat{A}^2 \text{sech}^2 X_0 \tanh X_0 e^{i2\widehat{\omega} T_0} + \text{c.c.} \\ &= \overline{F}_2^{(0)} + \overline{F}_2^{(1)} e^{i2\widehat{\omega} T_0} + \text{c.c.} \end{aligned}$$

The solution of the homogeneous equation associated with (5.7) can be written as

$$\phi_{2H} = C \overline{\eta}_0(X_0) + \overline{A} e^{i\overline{\omega} T_0} \overline{\eta}_D(X_0) + \text{c.c.} + \overline{\eta}(X_0, T_0), \quad (5.8)$$

where  $\overline{\eta}_0(X_0) = \text{sech}^2 X_0$ ,  $\overline{\eta}_D(X_0) = \text{sech } X_0 \tanh X_0$  and  $\overline{\omega} = \sqrt{3}$  as explained in Section 2. Besides,

$$\overline{\eta}(X_0, T_0) = \int_{-\infty}^{\infty} \overline{R}(q) e^{i\overline{\omega}_q T_0} \overline{\eta}_q(X_0) dq + \text{c.c.} \quad (5.9)$$

represents a wave packet evolving in the longitudinal channel, where  $\overline{\eta}_q$  is given by formula (2.13) with dispersion relation  $\overline{\omega}_q = \sqrt{4 + q^2}$ . In the scenario described in Section 2, the kink center is set to the origin, so the translational mode is not excited and the value  $C = 0$  can be assumed in (5.8). Based on the same arguments used for the orthogonal channel, the coefficients of the scattering eigenmodes are assumed to vanish:  $\overline{R}(q) = 0$  in (5.9). Therefore, Eq. (5.8) simplifies to

$$\phi_{2H} = \overline{A} e^{i\overline{\omega} T_0} \text{sech } X_0 \tanh X_0 + \text{c.c.}, \quad (5.10)$$

A particular solution of the non-homogeneous linear differential Eq. (5.7) can be found in the form

$$\phi_{2P} = \phi_2^{(0)} + \phi_2^{(1)} e^{i2\widehat{\omega} T_0} + \text{c.c.}, \quad (5.11)$$

which leads to equations similar to (5.7) for the variables  $\phi_2^{(i)}$  associated to terms  $\overline{F}_2^{(i)}$ . The first of these equations reads

$$[-\partial_{X_0, X_0} - 2 + 6\phi_0^2] \phi_2^{(0)} = -4|\widehat{A}|^2 \text{sech}^2 X_0 \tanh X_0, \quad (5.12)$$

where it has been considered that  $\phi_2^{(0)}$  does not depend on the slow time  $T_0$ . According to Fredholm's alternative, inhomogeneous equations admit bounded solutions if and only if the functions  $\overline{F}_2^{(i)}$  are orthogonal to the corresponding homogeneous solutions. In the case at hand, the homogeneous solution is  $\phi_{2H}^{(0)} = \text{sech}^2 X_0$ , which is orthogonal to  $\overline{F}_2^{(0)}$ . Therefore, the solution of (5.12) can be written as

$$\phi_2^{(0)}(X_0) = -|\widehat{A}|^2 X_0 \text{sech}^2 X_0. \quad (5.13)$$

Note the factor  $X_0 \text{sech } X_0$  in the above expression, which does not oversize the previous term  $\phi_0$  in the  $\epsilon$ -expansion, although they become larger than the difference  $\phi_0 \mp 1$  as  $X_0 \rightarrow \pm\infty$ . This behavior could lead to non-uniformity of these expansions, see [72]. This problem can be solved by noting that  $X_0 \text{sech}^2 X_0$

can be expressed as the derivative of  $\tanh(kX_0)$  with respect to  $k$ . This implies that

$$\tanh[(1 - |\widehat{A}|^2)X_0] \approx \tanh X_0 - |\widehat{A}|^2 X_0 \operatorname{sech}^2 X_0 + o(|\widehat{A}|^2),$$

which means that  $\phi_2^{(0)}$  is responsible for a variation of the kink size.

On the other hand, the differential equation for  $\phi_2^{(1)}$  is

$$[-\partial_{X_0, X_0} - 2 + 6\phi_0^2 - (2\widehat{\omega})^2] \phi_2^{(1)} = -2\widehat{A}^2 \operatorname{sech}^2 X_0 \tanh X_0, \quad (5.14)$$

which must be solved under the symmetry conditions imposed by our problem, which in turn imply that the solution of (5.14) must be an odd function in the variable  $X_0$ . This means that

$$\phi_2^{(1)}(X_0, X_2, \dots; T_2, \dots) = \widehat{A}^2 h(X_0; q_1) + \text{c.c.}, \quad q_1 = 2\sqrt{\sigma^2 - 2}, \quad (5.15)$$

where

$$\begin{aligned} h(X_0; q) &= -\frac{q^2 - 2}{4(q^2 + 1)} \tanh X_0 \\ &\quad + e^{iqX_0} \frac{\pi q}{8(q^2 + 1)} \\ &\quad \times \operatorname{cosech} \frac{\pi q}{2} (q^2 - 2 + 3iq \tanh X_0 + 3 \operatorname{sech}^2 X_0) \\ &\quad + h_1(X_0, q) + h_1(X_0, -q), \end{aligned} \quad (5.16)$$

with

$$\begin{aligned} h_1(X_0, q) &= \frac{-1}{8(q^2 + 1)} (q^2 - 2 - 3iq \tanh X_0 + 3 \operatorname{sech}^2 X_0) \\ &\quad \times \left( {}_2F_1\left[1, \frac{iq}{2}, 1 + \frac{iq}{2}, -e^{2X_0}\right] \right. \\ &\quad \left. - \frac{q}{q - 2i} e^{2X_0} {}_2F_1\left[1, 1 + \frac{iq}{2}, 2 + \frac{iq}{2}, -e^{2X_0}\right] \right). \end{aligned} \quad (5.17)$$

Therefore, the final expression for the first component of the scalar field in the second order approximation  $\phi_2$ , taking into account (5.10), (5.13) and (5.15), is given by

$$\begin{aligned} \phi_2 &= \bar{A} e^{i\widehat{\omega}T_0} \operatorname{sech} X_0 \tanh X_0 - |\widehat{A}|^2 X_0 \operatorname{sech}^2 X_0 \\ &\quad + \widehat{A}^2 e^{i2\widehat{\omega}T_0} h(X_0; q_1) + \text{c.c.} \end{aligned} \quad (5.18)$$

The asymptotic behavior of this field is

$$\lim_{X_0 \rightarrow \infty} \phi_2 \approx \frac{\pi \widehat{A}^2}{2} \frac{\sqrt{\sigma^2 - 2}}{\sinh(\pi\sqrt{\sigma^2 - 2})} \frac{\sqrt{\sigma^2 - 1}}{\sqrt{4\sigma^2 - 7}} e^{i(2\widehat{\omega}T_0 - q_1 X_0 + \delta_1)}. \quad (5.19)$$

From (5.19) it is immediate to see that, as in Section 4, we find that the system emits radiation in the first component of the field with frequency  $2\widehat{\omega}$ . On the other hand, it can be verified that the radiation amplitude obtained in this section has a very similar shape to that calculated in the previous section. In fact, the only appreciable difference between the amplitudes obtained with both perturbative methods is that the one given in (5.19) is just twice the one that can be seen in (4.23).

#### 5.4. Third order approximation: $\psi_3$

At third order we find the following condition for the field  $\phi_2$

$$-\partial_{X_0, X_1} \phi_2 + \partial_{T_0, T_1} \phi_2 = 0.$$

If we substitute the solution (5.18) into the previous equation, the amplitude of the longitudinal shape mode must comply with

$$\partial_{X_1} \bar{A}(X_1, T_1) = \partial_{T_1} \bar{A}(X_1, T_1) = 0,$$

which means that

$$\bar{A} = \bar{A}(X_2, \dots; T_2, \dots).$$

On the other hand, the condition for the second field component at this order reads

$$\partial_{T_0, T_0} \psi_3 + [-\partial_{X_0, X_0} - 2 + \sigma^2 + 2\phi_0^2] \psi_3 = \widehat{F}_3, \quad (5.20)$$

where

$$\begin{aligned} \widehat{F}_3 &= e^{i\widehat{\omega}T_0} [-2\widehat{A} |\widehat{A}|^2 \operatorname{sech} X_0 (3 \operatorname{sech}^2 X_0 + 2h(X_0) \tanh X_0) \\ &\quad - 2i \operatorname{sech} X_0 (\widehat{\omega} \partial_{T_2} \widehat{A} - i \tanh X_0 \partial_{X_2} \widehat{A}) \\ &\quad + 4|\widehat{A}|^2 \widehat{A} X_0 \operatorname{sech}^3 X_0 \tanh X_0] + \text{c.c.} \\ &\quad + e^{3i\widehat{\omega}T_0} [-2\widehat{A}^3 \operatorname{sech} X_0 (\operatorname{sech}^2 X_0 + 2h(X_0) \tanh X_0)] + \text{c.c.} \\ &\quad + e^{i(\widehat{\omega} + \widehat{\omega})T_0} [-4\widehat{A} \widehat{A} \operatorname{sech}^2 X_0 \tanh^2 X_0] + \text{c.c.} \\ &\quad + e^{i(\widehat{\omega} - \widehat{\omega})T_0} [-4\widehat{A} \widehat{A}^* \operatorname{sech}^2 X_0 \tanh^2 X_0] + \text{c.c.} \\ &= \widehat{F}_3^{(0)} e^{i\widehat{\omega}T_0} + \widehat{F}_3^{(1)} e^{3i\widehat{\omega}T_0} + \widehat{F}_3^{(2)} e^{i(\widehat{\omega} + \widehat{\omega})T_0} + \widehat{F}_3^{(3)} e^{i(\widehat{\omega} - \widehat{\omega})T_0} + \text{c.c.} \end{aligned} \quad (5.21)$$

Exploiting the linearity of Eq. (5.20) it can be assumed that

$$\psi_3 = \psi_3^{(0)} e^{i\widehat{\omega}T_0} + \psi_3^{(1)} e^{3i\widehat{\omega}T_0} + \psi_3^{(2)} e^{i(\widehat{\omega} + \widehat{\omega})T_0} + \psi_3^{(3)} e^{i(\widehat{\omega} - \widehat{\omega})T_0} + \text{c.c.} \quad (5.22)$$

If we substitute (5.22) into Eq. (5.20) we can determine the effect of every term  $\widehat{\psi}_3^{(i)}$  on the global solution. For example the ordinary differential equation which sets  $\widehat{\psi}_3^{(0)}$  has the form

$$-\partial_{X_0, X_0} \psi_3^{(0)} + (-2 + \sigma^2 + 2\phi_0^2 - \widehat{\omega}^2) \psi_3^{(0)} = \widehat{F}_3^{(0)}.$$

From the Fredholm alternative to obtain bounded solutions the projection of  $\widehat{F}_3^{(0)}$  on the homogeneous solution must be zero, that is,

$$\begin{aligned} \int_{-\infty}^{\infty} dX_0 \operatorname{sech} X_0 \left[ -2\widehat{A} |\widehat{A}|^2 \operatorname{sech} X_0 (3 \operatorname{sech}^2 X_0 + 2h(X_0) \tanh X_0) \right. \\ \left. - 2i \operatorname{sech} X_0 (\widehat{\omega} \partial_{T_2} \widehat{A} - i \tanh X_0 \partial_{X_2} \widehat{A}) \right. \\ \left. + 4|\widehat{A}|^2 \widehat{A} X_0 \operatorname{sech}^3 X_0 \tanh X_0 \right] = 0, \end{aligned}$$

which leads to the condition

$$i\widehat{\omega} \partial_{T_2} \widehat{A} + \left( \frac{5}{3} + \xi(\sigma) \right) \widehat{A} |\widehat{A}|^2 = 0, \quad (5.23)$$

where

$$\xi(\sigma) = \int_{-\infty}^{\infty} dX_0 h(X_0; q) \operatorname{sech}^2 X_0 \tanh X_0,$$

and  $h(X_0)$  is given in (5.16). Returning to the unscaled amplitude  $\widehat{a} = \epsilon \widehat{A}$  of the orthogonal wobbling amplitude and the original time variable  $t$ , we can write (5.23) as

$$i\widehat{\omega} \frac{\partial \widehat{a}}{\partial t} + \left( \frac{5}{3} + \xi(\sigma) \right) \widehat{a} |\widehat{a}|^2 = 0,$$

which leads to the equation

$$\frac{\partial |a|^2}{\partial t} = -\frac{2 \operatorname{Im} \xi(\sigma)}{\widehat{\omega}} |a|^4,$$

such that

$$|a(t)|^2 = \frac{|a(0)|^2}{1 + \frac{2 \operatorname{Im} \xi(\sigma)}{\widehat{\omega}} |a(0)|^2 t}.$$

The equation determining the field  $\psi_3^{(1)}$  becomes

$$\begin{aligned} -\partial_{X_0, X_0} \psi_3^{(1)} + [-2 + \sigma^2 + 2\phi_0^2 - 9\widehat{\omega}^2] \psi_3^{(1)} &= \widehat{F}_3^{(1)} \\ &= -2\widehat{A}^3 \operatorname{sech} X_0 (\operatorname{sech}^2 X_0 + 2h(X_0) \tanh X_0). \end{aligned} \quad (5.24)$$

We recall that  $\widehat{\eta}_q(x) = e^{iqx}(q + i \tanh x)$  and that the Wronskian associated to these solutions is given by  $\widehat{W}_q = W[\widehat{\eta}_q(x), \widehat{\eta}_{-q}(x)] = 2iq(q^2 + 1)$ . With this notation the expression for  $\psi_3^{(1)}$  extracted from (5.24) can be written as

$$\psi_3^{(1)}(X_0) = \frac{1}{\widehat{W}_{q_2}} \left\{ \widehat{\eta}_{q_2}(X_0) \int \widehat{\eta}_{-q_2}(X_0) \widehat{F}_3^{(1)}(X_0) dX_0 - \widehat{\eta}_{-q_2}(X_0) \int \widehat{\eta}_{q_2}(X_0) \widehat{F}_3^{(1)}(X_0) dX_0 \right\},$$

where  $q_2 = \sqrt{8\sigma^2 - 9}$  because  $(3\widehat{\omega})^2 = 9(\sigma^2 - 1)$ .

On the other hand, from (5.20)–(5.21) the equation for  $\psi_3^{(2)}$  reads

$$-\partial_{X_0, X_0} \psi_3^{(2)} + [-2 + \sigma^2 + 2\phi_0^2 - (\bar{\omega} + \widehat{\omega})^2] \psi_3^{(2)} = \widehat{F}_3^{(2)} = -4\bar{A} \widehat{A} \operatorname{sech}^2 X_0 \tanh^2 X_0. \tag{5.25}$$

In this case the solution is given by

$$\psi_3^{(2)}(X_0, X_2, \dots; T_2, \dots) = \bar{A} \widehat{A} g(X_0; q_3),$$

where  $q_3$  is given in (4.25) and

$$g(X_0; q) = -\frac{q^2}{2(q^2 + 1)} + \operatorname{sech}^2 X_0 + \frac{\pi q^3 e^{iqX_0}}{4(q^2 + 1) \operatorname{sech} \frac{\pi q}{2}} \times (-iq + \tanh X_0) + g_1(X_0, q) + g_1(X_0, -q),$$

with

$$g_1(X_0; q) = -\frac{iq^2(q - i \tanh X_0)}{4(q^2 + 1)} {}_2F_1\left[1, \frac{iq}{2}, 1 + \frac{iq}{2}, -e^{2X_0}\right] + \frac{q^3}{4(q^2 + 1)(q - 2i)} e^{3X_0} \operatorname{sech} X_0 \frac{iq + \tanh X_0}{1 + \tanh X_0} \times {}_2F_1\left[1, 1 + \frac{iq}{2}, 2 + \frac{iq}{2}, -e^{2X_0}\right].$$

We have that the asymptotic behavior for  $X_0 \rightarrow \infty$  is

$$\psi_3^{(2)} \xrightarrow{X_0 \rightarrow \infty} \bar{A} \widehat{A} \frac{\pi q^3}{4(-1 + iq_3) \sinh \frac{\pi q_3}{2}} e^{i(\bar{\omega} + \widehat{\omega})T_0 - q_3 X_0} + \text{c.c.} \tag{5.26}$$

As we can see, this term corresponds to a radiative term, as occurred in Section 4. In the present case, the amplitude obtained is different, although the qualitative behavior obtained from (5.26) is the same as that obtained can extract from (4.26).

### 5.5. Fourth order approximation: $\phi_4$

At fourth order we find the following condition for the field  $\phi_4$

$$\partial_{T_0, T_0} \phi_4 + [-\partial_{X_0, X_0} - 2 + 6\phi_0^2] \phi_4 = -(6\phi_0 \phi_2^2 + 2\phi_2 \psi_1^2 + 4\phi_0 \psi_1 \psi_3 - 2\partial_{X_0, X_2} \phi_2 - \partial_{X_1, X_1} \phi_2 + 2\partial_{T_0, T_2} \phi_2 + \partial_{T_1, T_1} \phi_2) = \bar{F}_4. \tag{5.27}$$

As in previous sections, the non-homogeneous term of this differential equation will present terms with different frequencies, so that

$$\bar{F}_4 = \bar{F}_4^{(0)} + \bar{F}_4^{(1)} e^{i\bar{\omega}T_0} + \bar{F}_4^{(2)} e^{2i\bar{\omega}T_0} + \bar{F}_4^{(3)} e^{2i\bar{\omega}T_0} + \bar{F}_4^{(4)} e^{4i\bar{\omega}T_0} + \bar{F}_4^{(5)} e^{2i\bar{\omega}T_0 + i\bar{\omega}T_0} + \bar{F}_4^{(6)} e^{2i\bar{\omega}T_0 - i\bar{\omega}T_0} + \text{c.c.} \tag{5.28}$$

We will now focus only on the term with frequency  $\bar{\omega}$ , as it will be used to find the decaying law for  $\bar{A}$ . For this frequency, the corresponding differential equation will be the following:

$$-\bar{\omega}^2 \phi_4^{(1)} + [-\partial_{X_0, X_0} - 2 + 6\phi_0^2] \phi_4^{(1)} = -4|\widehat{A}|^2 \bar{A} \operatorname{sech}^3 X_0 \tanh X_0 + 12X_0 |\widehat{A}|^2 \bar{A} \operatorname{sech}^3 X_0 \tanh^2 X_0 - 4|\widehat{A}|^2 \bar{A} \operatorname{sech} X_0 \tanh X_0 g(X_0) - 2i\bar{\omega} \operatorname{sech} X_0 \tanh X_0 \partial_{T_2} \bar{A}$$

$$+ 2 \operatorname{sech}^3 X_0 \partial_{X_2} \bar{A} - 2 \operatorname{sech} X_0 \tanh^2(X_0) \partial_{X_2} \bar{A} = \bar{F}_4^{(1)}(X_0).$$

From Fredholm's alternative we know that in order to obtain bounded solutions, in the previous equation the solution of the homogeneous part must be orthogonal to the inhomogeneous term. This results in the following condition

$$\int_{-\infty}^{\infty} dX_0 \left( \operatorname{sech} X_0 \tanh X_0 \bar{F}_4^{(1)}(X_0) \right) = 0, \tag{5.29}$$

which leads us to the differential equation

$$-5i\bar{\omega} \partial_{T_2} \bar{A} + (3 - 15\mu(\sigma)) \bar{A} |\bar{A}|^2 = 0, \tag{5.30}$$

where

$$\mu(\sigma) = \int_{-\infty}^{\infty} dX_0 g(X_0) \operatorname{sech}^2 X_0 \tanh^2 X_0. \tag{5.31}$$

If  $\widehat{a} = \epsilon \widehat{A}$  and  $\bar{a} = \epsilon \bar{A}$ , then

$$\frac{\partial |\bar{a}|^2}{\partial t} = |\bar{a}|^2 |\widehat{a}|^2 \left( \frac{-6 \operatorname{Im} \mu(\sigma)}{\bar{\omega}} \right). \tag{5.32}$$

Finally, the solution of (5.32) leads to the time evolution law for  $\bar{a}$  being

$$|\bar{a}(t)|^2 = |\bar{a}(0)|^2 (\bar{\omega} \widehat{\omega})^{\frac{3 \operatorname{Im} \mu(\sigma) \widehat{\omega}}{1 \operatorname{Im} \xi(\sigma) \bar{\omega}}} \left( (2|\widehat{a}(0)|^2 \operatorname{Im} \xi(\sigma) t + \widehat{\omega}) \bar{\omega} \right)^{-\frac{3 \operatorname{Im} \mu(\sigma) \widehat{\omega}}{1 \operatorname{Im} \xi(\sigma) \bar{\omega}}}. \tag{5.33}$$

This procedure has some similarities with the one carried out in the previous section, since, for example, the differential Eqs. (5.23) and (5.30) present a very similar form to each other. However, there are also very important differences. For example, in this case we can see how  $\bar{A}$  is affected by  $\widehat{A}$ , while in the calculation of  $\widehat{A}$  something similar does not happen. This is reasonable since we are initially only exciting the discrete mode of the second field, so it makes sense that  $\bar{A}$  dictates the behavior of  $\widehat{A}$ . Note that in this perturbative theory we have managed to reach fourth order. It is also important to note that in (5.28) the frequency terms  $4\widehat{\omega}$  and  $2\widehat{\omega} + \bar{\omega}$  appear, which correspond to the extra radiative terms that we found in Fig. 7.

## 6. Concluding remarks

In this paper we have investigated the interaction between the shape modes associated to the one non-null component kink present in the family of MSTB models. In this case, in addition to a longitudinal shape mode whose eigenfrequency has been denoted by  $\bar{\omega}$ , an orthogonal shape mode is also found whose frequency  $\widehat{\omega}$  is a function of the model parameter  $\sigma$ . For this reason, three different regimes have been distinguished which are delimited by the special values of the model parameter  $\sigma_1$  and  $\sigma_2$  introduced in Section 2. In particular, the evolution of the kink is numerically studied when only the orthogonal shape is initially excited. Following the excitation of the orthogonal shape mode, the longitudinal shape mode and the radiation modes in both the longitudinal and orthogonal channel are also excited for some particular frequencies corresponding to some linear combinations of  $\bar{\omega}$  and  $\widehat{\omega}$ . This demonstrates that the energy stored in orthogonal shape mode can freely excite other vibrational modes. For  $\sigma > \sigma_1$  longitudinal radiation with frequency  $2\widehat{\omega}$  is emitted, that is, twice the eigenfrequency associated with the orthogonal shape mode (and not the longitudinal shape mode as we could have initially inferred from the behavior of the  $\phi^4$  model). For  $\sigma < \sigma_1$  the pattern is much more complex and frequencies such as  $\bar{\omega} + 2\widehat{\omega}$  and  $4\widehat{\omega}$  replace the previously mentioned frequency. This behavior involves the prevalence of higher order terms in

the interaction between the vibrational modes in this regime. On the other hand, for the orthogonal channel the radiation is predominantly emitted with frequency  $\bar{\omega} + \hat{\omega}$  for  $\sigma > \sigma_1$  and  $3\hat{\omega}$  for  $\sigma < \sigma_1$ .

In Sections 4 and 5 the analytical understanding of the previous numerical results have been achieved by applying perturbation theory to our problem in the regime  $\sigma > \sigma_1$ . The approaches used by Manton and Merabet [71] (based on the Lindstedt–Poincaré method) and by Barashenkov and Oxtoby [72] (based on the method of multiple scales) to study the evolution of the wobbling kinks in the  $\phi^4$  model have been considered respectively in each section. With both, similar results are obtained and the non-linear terms responsible for the excitation of the different radiation frequencies found in our numerical simulations are identified. The amplitudes of the radiation are also derived from these analytical procedures and they are found to be in concordance with the numerical results. On the other hand, although the regime  $\sigma < \sigma_1$  has not been analytically addressed the previous study indicates that for the values  $\sigma = \sigma_1$  and  $\sigma = \sigma_2$  some resonances arise. In these cases, some detuning parameters must be introduced in the perturbation theory approach. In addition to this, new higher order terms must be included in the analysis which explain the presence of other excited frequencies. The situation is so complex that the study of these regimes has been postponed for future research.

In summary, the interaction between longitudinal and orthogonal shape modes analyzed in this paper shows some fascinating novel behaviors that open new possibilities for further works. A fascinating idea to unveil more features in the energy transfer mechanism between shape modes is to construct a new two-component scalar field model in which both components exhibit more bound states above the zero mode to investigate how energy flows from one to other higher excited modes. Furthermore, the present investigation extends new perspectives to investigate the scattering between excited topological defects in a two-component real scalar field model.

### Declaration of competing interest

The authors declare that they have no known competing financial interests or personal relationships that could have appeared to influence the work reported in this paper.

### Data availability

No data was used for the research described in the article.

### Acknowledgments

This research was supported by Spanish MCIN with funding from European Union NextGenerationEU (PRTRC17.11) and Consejería de Educación from JCyL through QCAYLE project, as well as MCIN project PID2020-113406GB-I0. A. Alonso-Izquierdo acknowledges the Junta de Castilla y León for financial support under grant SA067G19. This research has made use of the high performance computing resources of the Castilla y León Supercomputing Center (SCAYLE), financed by the European Regional Development Fund (ERDF).

### References

- [1] A. Vilenkin, E.P.S. Shellard, *Cosmic Strings and Other Topological Defects*, Cambridge University Press, Cambridge, 1994.
- [2] T. Vachaspati, *Kinks and Domain Walls: An Introduction to Classical and Quantum Solitons*, Cambridge University Press, Cambridge, 2006.
- [3] T. Yanagisawa, I. Hase, Y. Tanaka, *Phys. Lett. A* 382 (2018) 3483.
- [4] D. Melnikov, A.J. Niemi, A. Sedrakyan, *Sci. Rep.* 9 (2019) 14641.
- [5] D. Melnikov, A.B.F. Neves, *J. Appl. Phys.* 126 (2019) 244701.
- [6] D. Bazeia, M.V. de Moraes, B.F. de Oliveira, *Europhys. Lett.* 129 (2020) 28002.
- [7] B.F. de Oliveira, M.V. de Moraes, D. Bazeia, A. Szolnoki, *Physica A* 572 (2021) 125854.
- [8] A.S. Davydov, *Solitons in Molecular Systems*, D. Reidel, Dordrecht, 1985.
- [9] D. Bazeia, E. Ventura, *Chem. Phys. Lett.* 303 (1999) 341.
- [10] N. Manton, *Topological Solitons*, Cambridge University Press, Cambridge, 2004.
- [11] Y.M. Shnir, *Topological and Non-Topological Solitons in Scalar Field Theories*, Cambridge University Press, Cambridge, 2018.
- [12] L.F. Mollenauer, J.P. Gordon, *Solitons in Optical Fibers—Fundamentals and Applications*, Academic Press, Burlington, 2006.
- [13] T. Schneider, *Nonlinear Optics in Telecommunications*, Springer, Heidelberg, 2004.
- [14] G.P. Agrawal, *Nonlinear Fiber Optics*, Academic Press, San Diego, 1995.
- [15] D.K. Campbell, J.S. Schonfeld, C.A. Wingate, *Physica D* 9 (1983) 1.
- [16] T. Sugiyama, *Progr. Theoret. Phys.* 61 (1979) 1550.
- [17] P. Anninos, S. Oliveira, R.A. Matzner, *Phys. Rev. D* 44 (1991) 1147.
- [18] B.A. Malomed, *J. Phys. A: Math. Gen.* 25 (1992) 755.
- [19] R.H. Goodman, R. Haberman, *SIAM J. Appl. Dyn. Syst.* 4 (2005) 1195.
- [20] R.H. Goodman, *Chaos* 18 (2008) 023113.
- [21] D. Saadatmand, S.V. Dmitriev, D.I. Borisov, P.G. Kevrekidis, M.A. Fatykhov, K. Javidan, *Commun. Nonlinear Sci. Numer. Simul.* 29 (2015) 267.
- [22] I. Takyi, H. Weigel, *Phys. Rev. D* 94 (2016) 085008.
- [23] D. Saadatmand, D.I. Borisov, P.G. Kevrekidis, K. Zhou, S.V. Dmitriev, *Commun. Nonlinear Sci. Numer. Simul.* 56 (2018) 62.
- [24] C. Adam, T. Romanczukiewicz, A. Wereszczynski, *J. High Energy Phys.* 3 (2019) 131.
- [25] A.R. Gomes, F.C. Simas, K.Z. Nobrega, P.P. Avelino, *J. High Energy Phys.* 10 (2018) 192.
- [26] P.G. Kevrekidis, J. Cuevas-Maraver (Eds.), *A Dynamical Perspective on the  $\phi^4$  Model*, in: *Nonlinear Systems and Complexity*, vol. 26, Springer, Cham, 2019.
- [27] C. Adam, K. Oles, T. Romanczukiewicz, A. Wereszczynski, *Phys. Rev. Lett.* 122 (2019) 241601.
- [28] C. Adam, K. Oles, J.M. Queiruga, T. Romanczukiewicz, A. Wereszczynski, *J. High Energy Phys.* 07 (2019) 150.
- [29] C. Adam, K. Oles, T. Romanczukiewicz, A. Wereszczynski, *Phys. Rev. D* 101 (2020) 105021.
- [30] M. Mohammadi, R. Dehghani, *Commun. Nonlinear Sci. Numer. Simul.* 94 (2021) 105575.
- [31] H. Yan, Y. Zhong, Y.X. Liu, K. Maeda, *Phys. Lett. B* 807 (2020) 135542.
- [32] C.F.S. Pereira, G. Luchini, T. Tassis, C.P. Constantinidis, *J. Phys. A* 54 (2021) 075701.
- [33] N.S. Manton, K. Oles, T. Romanczukiewicz, A. Wereszczynski, *Phys. Rev. Lett.* 127 (2021) 071601.
- [34] J.J. Blanco-Pillado, D. Jimenez-Aguilar, J. Urrestilla, J. Cosmol. Astropart. Phys. 01 (2021) 027.
- [35] C. Adam, N.S. Manton, K. Oles, T. Romanczukiewicz, A. Wereszczynski, *Phys. Rev. D* 105 (2022) 065012.
- [36] J. Shieflman, P. Kumar, *Phys. Scr.* 20 (1979) 435.
- [37] M. Peyrard, D.K. Campbell, *Physica D* 9 (1983) 33.
- [38] B.A. Malomed, *Phys. Lett. A* 136 (1989) 395.
- [39] V.A. Gani, A.E. Kudryavtsev, *Phys. Rev. E* 60 (1999) 3305.
- [40] R.H. Goodman, P.J. Holmes, M.I. Weinstein, *Physica D* 161 (2002) 21.
- [41] R.H. Goodman, R. Haberman, *Physica D* 195 (2004) 303.
- [42] V.A. Gani, A.M. Marjaneh, A. Askari, E. Belendryasova, D. Saadatmand, *Eur. Phys. J. C* 78 (2018) 345.
- [43] F.C. Simas, F.C. Lima, K.Z. Nobrega, A.R. Gomes, *J. High Energy Phys.* 12 (2020) 143.
- [44] H. Weigel, *J. Phys.: Conf. Ser.* 482 (2014) 012045.
- [45] V.A. Gani, A.E. Kudryavtsev, M.A. Lizunova, *Phys. Rev. D* 89 (2014) 125009.
- [46] A.M. Marjaneh, V.A. Gani, D. Saadatmand, S.V. Dmitriev, K. Javidan, *J. High Energy Phys.* 07 (2017) 028.
- [47] T. Romanczukiewicz, *Phys. Lett. B* 773 (2017) 295.
- [48] D. Bazeia, A.R. Gomes, K.Z. Nobrega, F.C. Simas, *Phys. Lett. B* 793 (2019) 26.
- [49] F.C. Lima, F.C. Simas, K.Z. Nobrega, A.R. Gomes, *J. High Energy Phys.* 10 (2019) 147.
- [50] I.C. Christov, R.J. Decker, A. Demirkaya, V.A. Gani, P.G. Kevrekidis, A. Khare, A. Saxena, *Phys. Rev. Lett.* 122 (2019) 171601.
- [51] I.C. Christov, R.J. Decker, A. Demirkaya, V.A. Gani, P.G. Kevrekidis, R.V. Radomskiy, *Phys. Rev. D* 99 (2019) 016010.
- [52] I.C. Christov, R.J. Decker, A. Demirkaya, V.A. Gani, P.G. Kevrekidis, A. Saxena, *Commun. Nonlinear Sci. Numer. Simul.* 97 (2021) 105748.
- [53] J.G.F. Campos, A. Mohammadi, *Phys. Lett. B* 818 (2021) 136361.
- [54] D. Bazeia, E. Belendryasova, V.A. Gani, *J. Phys.: Conf. Ser.* 934 (2017) 012032.
- [55] D. Bazeia, E. Belendryasova, V.A. Gani, *Eur. Phys. J. C* 78 (2018) 340.

- [56] D. Bazeia, A.R. Gomes, K.Z. Nobrega, F.C. Simas, *Internat. J. Modern Phys. A* 34 (2019) 1950200.
- [57] F.C. Simas, A.R. Gomes, K.Z. Nobrega, J.C.R.E. Oliveira, J. *High Energy Phys.* 9 (2016) 104.
- [58] T. Romanczukiewicz, *Acta Phys. Polon. B* 39 (2008) 3449.
- [59] A. Halavanau, T. Romanczukiewicz, Ya. Shnir, *Phys. Rev. D* 86 (2012) 085027.
- [60] A. Alonso-Izquierdo, *Physica D* 365 (2017) 12.
- [61] A. Alonso-Izquierdo, *Phys. Rev. D* 97 (2018) 045016.
- [62] A. Alonso-Izquierdo, *Commun. Nonlinear Sci. Numer. Simul.* 75 (2019) 200.
- [63] L.A. Ferreira, P. Klimas, W.J. Zakreswski, *J. High Energy Phys.* 01 (2019) 020.
- [64] A. Alonso-Izquierdo, *Commun. Nonlinear Sci. Numer. Simul.* 85 (2020) 105251.
- [65] Y. Zhong, X.L. Du, Z.C. Jiang, Y.X. Liu, Y.Q. Wang, *J. High Energy Phys.* 02 (2020) 153.
- [66] A. Alonso-Izquierdo, M.A. Gonzalez Leon, J. Martin Vaquero, M. de la Torre Mayado, *Commun. Nonlinear Sci. Numer. Simul.* 103 (2021) 106011.
- [67] C. Adam, K. Oles, T. Romanczukiewicz, A. Wereszczynski, W.J. Zakrzewski, *J. High Energy Phys.* 2021 (2021) 147.
- [68] Fabiano C. Simas, K.Z. Nobrega, D. Bazeia, Adalto R. Gomes, Degeneracy and kink scattering in a two coupled scalar field model in (1, 1) dimensions, 2022, arXiv:2201.03372.
- [69] B.S. Getmanov, *JETP Lett.* 24 (1976) 291.
- [70] H. Segur, *J. Math. Phys.* 24 (1983) 1439.
- [71] N.S. Manton, H. Merabet, *Nonlinearity* 10 (1997) 3.
- [72] I.V. Barashenkov, O.F. Oxtoby, *Phys. Rev. E* 80 (2009) 026608.
- [73] I.V. Barashenkov, The continuing story of the Wobbling Kink, in: *A Dynamical Perspective on the  $\phi^4$  Model*, Springer, Cham, 2019, p. 187.
- [74] A. Alonso-Izquierdo, J. Queiroga-Nunes, L.M. Nieto, *Phys. Rev. D* 103 (2021) 045003.
- [75] A. Alonso-Izquierdo, L.M. Nieto, J. Queiroga-Nunes, *Commun. Nonlinear Sci. Numer. Simul.* 107 (2022) 106183.
- [76] J.G.F. Campos, A. Mohammadi, *J. High Energy Phys.* 2021 (2021) 67.
- [77] C. Montonen, *Nuclear Phys. B* 112 (1976) 349.
- [78] R. Rajaraman, E.J. Weinberg, *Phys. Rev. D* 11 (1975) 2950.
- [79] S. Sarker, S.E. Trullinger, A.R. Bishop, *Phys. Lett. A* 59 (1976) 255.
- [80] J.F. Currie, S. Sarker, A.R. Bishop, S.E. Trullinger, *Phys. Rev. A* 20 (1979) 2213.
- [81] R. Rajaraman, Solitons of coupled scalar field theories in two dimensions, *Phys. Rev. Lett.* 42 (1979) 200.
- [82] K.R. Subbaswamy, S.E. Trullinger, *Phys. Rev. D* 22 (1980) 1495.
- [83] K.R. Subbaswamy, S.E. Trullinger, *Physica D* 2 (1981) 379.
- [84] E. Magyari, H. Thomas, *Phys. Lett. A* 100 (1984) 11.
- [85] H. Ito, *Phys. Lett. A* 112 (1985) 119.
- [86] H. Ito, H. Tasaki, *Phys. Lett. A* 113 (1985) 179.
- [87] A. Alonso-Izquierdo, M.A. Gonzalez Leon, J. Mateos Guilarte, *Nonlinearity* 13 (2000) 1137.
- [88] A. Alonso-Izquierdo, M.A. Gonzalez Leon, J. Mateos Guilarte, *Nonlinearity* 15 (2002) 1097.
- [89] A. Alonso-Izquierdo, J. Mateos Guilarte, *Physica D* 237 (2008) 3263.
- [90] A. Alonso-Izquierdo, *Phys. Scr.* 94 (2019) 085302.



# Capítulo 5

---

## Conclusiones

---

En esta tesis se ha analizado el modo o modos vibracionales que presentan soluciones tipo kink y su relación con otros modos normales. Con este objetivo, se ha conducido una investigación sistemática utilizando simulaciones numéricas y aproximaciones perturbativas para diferentes modelos de teorías de campos escalares en los cuales el mecanismo de transferencia de energía resonante es desencadenado por la interacción entre los modos normales de la solución. Es importante destacar que esta transferencia de energía desempeña un papel fundamental en las propiedades observadas en los diagramas de scattering entre kinks.

En este sentido, en el primer trabajo que conforma esta tesis se investigó la estructura subyacente asociada a las colisiones simétricas entre kinks excitados del modelo  $\phi^4$ . Se analizó de manera directa la influencia de la velocidad y la amplitud inicial de vibración de las soluciones en el proceso de colisión, lo que ha permitido comprender la redistribución de energía entre los modos normales por la transferencia de energía resonante.

Por otro lado, en el segundo trabajo se investigó el proceso de transferencia de energía entre los modos normales en colisiones asimétricas entre kinks del modelo  $\phi^4$ . Con este objetivo se ha tomado dos escenarios asimétricos extremos, que son: colisiones entre (1) kinks vibrantes con fases opuestas y (2) un kink vibrante y un antikink no excitado. En estos escenarios se destacó el impacto de la diferencia de fase entre los kinks vibrantes y la amplitud inicial de vibración sobre la amplitud y velocidad final de las soluciones dispersadas.

Finalmente, en el último trabajo que conforma esta tesis se investigó la interacción entre modos normales en el modelo de dos campos MSTB. Esta investigación muestra la evolución de la solución kink cuando el modo vibracional ortogonal es excitado inicialmente. Adicionalmente, se ha tratado analíticamente la interacción entre los modos normales utilizando aproximaciones perturbativas que han permitido comparar los resultados analíticos con los resultados numéricos.

Las principales conclusiones que han sido alcanzadas en los tres trabajos mencionados anteriormente son las siguientes:

- La estructura fractal dentro del régimen de resonancia del diagrama de velocidad final versus

velocidad inicial se vuelve más intrincada conforme aumenta la amplitud inicial excitación en proceso de colisión simétrica entre kinks del modelo  $\phi^4$ . Este aumento de la complejidad de la estructura fractal ocurre principalmente por (1) la separación de la cola de reflexión y (2) el surgimiento espontáneo de nuevas ventanas en el régimen de resonancia.

- Para valores suficientemente altos de la amplitud inicial en esas colisiones simétricas, los kinks vibrantes pueden alejarse con velocidades mayores que la velocidad inicial. Esto indica que en un proceso de  $n$ -rebotes la última colisión consiste en kinks fuertemente excitados que se aproximan a bajas velocidades. Esto significa que para que los kinks puedan alejarse en el régimen de resonancia debe alcanzarse esta situación.
- En el scattering asimétrico entre kinks del modelo  $\phi^4$  la diferencia de fase entre las soluciones da lugar a una interferencia destructiva en el punto de colisión entre las soluciones. De hecho, la estructura fractal encontrada en el régimen de resonancia parece ser menos intrincada que la observada en colisiones simétricas. Por otro lado, el proceso de scattering entre kink vibrante y antikink no excitado da lugar a una transferencia de energía del modo vibracional de la solución excitada inicialmente a otros modos normales de la solución no excitada, lo que da lugar a resultados similares al scattering simétrico aunque también presenta propiedades particulares.
- Debido a la asimetría presente en la configuración inicial, las velocidades y amplitudes finales de los kinks son diferentes en el scattering mencionado anteriormente. No obstante, para un conjunto discreto de velocidades iniciales la diferencia de amplitud y velocidad final entre ambas soluciones es nula. Utilizando un razonamiento analítico se ha alcanzado una expresión que proporciona este conjunto de velocidades iniciales válida para cualquier escenario.
- En el modelo de dos campos escalares reales MSTB se ha constatado que la excitación del modo vibracional de la componente ortogonal del campo desencadena la excitación de otros modos normales de la componente longitudinal. Adicionalmente, otros modos normales del campo ortogonal también son excitados para algunas frecuencias determinadas, lo que indica que la energía puede ser transferida de un modo normal al otro entre las diferentes componentes del campo.
- Los resultados analíticos alcanzados utilizando aproximaciones perturbativas reproducen los resultados numéricos en el escenario mencionado anteriormente. La interacción entre los modos normales de diferentes componentes del campo fueron tratadas analíticamente utilizando la aproximación perturbativa de Manton y Merabet y la aproximación de Barashenkov y Oxtoby.



